

## Precipitation Strengthening in Al-Mg-Si Alloys

Présentée le 17 décembre 2021

Faculté des sciences et techniques de l'ingénieur  
Laboratoire de modélisation mécanique multi-échelle  
Programme doctoral en mécanique

pour l'obtention du grade de Docteur ès Sciences

par

**Yi HU**

Acceptée sur proposition du jury

Prof. T. Schneider, président du jury  
Prof. W. Curtin, directeur de thèse  
Prof. J. Segurado, rapporteur  
Prof. D. Warner, rapporteur  
Prof. P. Derlet, rapporteur



# Acknowledgements

I would like to first thank Prof. W. A. Curtin who gave me the opportunity to learn and work in his group. He is the one who introduced me to the world of atomistics, dislocations, metallurgy, etc. His rigor in science and critical thinking in research are the most important qualities that I have learned.

I also thank my defense committee, Prof. T. M. Schneider, Prof. P. M. Derlet, Prof. J. Segurado and Prof. D. H. Warner, for reading my thesis, attending my defense, and giving valuable feedback in the defense.

Sincere thanks go to the collaborators and all my past and present colleagues in LAMMM. It is you that help me get acquainted with the field of dislocation and walk me through some of the research difficulties. Dating back to my start in LAMMM, Ali Tehranchi was the first person that lent a hand to me when I started using LAMMPS and debugging with atomistic systems. His help made my transition from continuum to atomistic scale a rather smoother one. I want to thank Rasool Ahmad and Eleanor Mak for the joint efforts on teaching assistant tasks for ME-331 Solid Mechanics. As for my research, the work cannot be done without the productive discussion with Prof. D. Rodney and Dr. B. A. Szajewski, the code  $\mu$ Spectre from Till Junge and the powerful Neural Network Potentials that were developed by various excellent researchers including Prof. R. Kobayashi, Dr. D. Giofre, Dr. A. Glensk, Daniel Marchand and Abhinav Jain. Furthermore, I would like to thank all the visiting professors and postdocs, including Zhaoxuan Wu, Prof. J. Song, Prof. M. Ghazisaeidi, Nikolas Bouklas, Francesco Maresca, Binglun Yin, Markus Stricker, Xiao Zhou, Terrence Moran, Carolina Baruffi, You Rao, Manura Liyanage. It was nice to interact with you and learn from you. I would also like to thank other past and present graduate students in the lab, Wolfram Noehring, Max Hodapp, Predrag Andric, Nag Shankha, Alireza Ghafarollahi, Ankit Gupta, Ali Falsafi, Recep Ekin Kubilay, Xin Liu, Masoud Rahbarniazi. You helped me on various occasions. Lastly, I would like to thank Terrence, Xiao, and Daniel for proofreading parts of my thesis, and Claire for helping me with French version of thesis abstract.

I am also indebted to a lot of friends in Lausanne, who helped me strike a work-life balance (which I am very bad at). I want to thank Bin Lu, with whom I played a lot of tennis and went out for a lot of hikes. Thanks also go to Jianing, Feng Lu, Yue Wang and Yiling Zhang, who finally got me started on skiing. In addition, I want to thank Jianqi, Jian Yang, Yashi, Wenyan,

## Acknowledgements

---

Xiaoyu, Peijia, Heqian and many others. We went out for trips, hikes and dinners. These were all great moments in my PhD.

Last but not the least, I want to express my deepest gratitude to my parents. You are always the source of support and encouragement.

*Lausanne, November 30, 2021*

Yi



# Abstract

Precipitation strengthening is one of the key strengthening strategies in many industrial alloys like aluminum alloys, nickel-based superalloys, etc. The yield strength of alloy is improved by forming precipitates in materials and employing them as obstacles for dislocation movement. In this study, we calibrate Discrete Dislocation Dynamics (DDD) to include one of the essential atomistic information, dislocation core energy, to make quantitative strength predictions. Then we attempt to predict peak-aged strength of Al–Mg–Si alloys using experimental characterizations and via modeling the Orowan mechanism in DDD. Extensive mesoscale studies show that matrix misfit stress has small effects on Critical Resolved Shear Stress (CRSS). In contrast, CRSS depends largely on the precipitate edge-to-edge spacing and the dislocation core energy within 5.4 b. However, with the most faithful mesoscale simulation, the alloy tensile yield strength is overestimated by  $\approx 33\%$ . Detailed analysis of forces on precipitates shows that multiple precipitates are sheared prior to be looped. Then atomistic simulations using the near-chemically-accurate Al–Mg–Si Neural Network Potential are performed to investigate dislocation-precipitate interactions. Results show that a given precipitate can show shearing or looping depending on the relative orientation of the precipitate and dislocation, as influenced by the precipitate internal misfit stresses, direction-dependence of precipitate shearing energies, and dislocation line tension. Analytic models for shearing and calibrated discrete dislocation models of looping can accurately capture the trends and magnitudes of strengthening in most cases. Reasonable quantitative agreement with experiments is then achieved by using the theories together with the more-accurate first-principles material properties. The combination of theories and simulations demonstrated here constitutes a quantitative path for understanding and predicting the role of chemistry and microstructure on alloy strength that can be applied in many different alloys.

keywords: dislocation core energy, non-singular theory, Discrete Dislocation Dynamics, precipitation strengthening, Orowan mechanism, shearing mechanism, atomistic simulation, Neural Network Potential, yield strength prediction



## Résumé

Le renforcement par précipitation est l'une des principales stratégies de renforcement dans de nombreux alliages industriels comme les alliages d'aluminium, les superalliages à base de nickel, etc. La limite d'élasticité de l'alliage est améliorée par la formation de précipités dans les matériaux qui sont utilisés comme des obstacles au mouvement des dislocations. Dans cette étude, nous calibrons la dynamique des dislocations discrètes (DDD) pour inclure une des informations atomistiques essentielles, l'énergie du noyau des dislocations, afin de faire des prédictions quantitatives de la résistance. Nous tentons ensuite de prédire la résistance au vieillissement des alliages Al-Mg-Si en utilisant des caractérisations expérimentales et en modélisant le mécanisme d'Orowan dans la DDD. Des études approfondies à méso-échelle montrent que la contrainte d'inadaptation de la matrice à de faibles effets sur la contrainte de cisaillement résolue critique (CRSS). En revanche, la CRSS dépend largement de l'espacement bord à bord du précipité et de l'énergie du noyau de dislocation dans 5.4 b. Cependant, avec la simulation méso-échelle la plus fidèle, la limite d'élasticité en traction de l'alliage est surestimée de  $\approx 33\%$ . L'analyse détaillée des forces sur les précipités montre que plusieurs précipités sont cisailés avant d'être bouclés. Ensuite, des simulations atomistiques utilisant le potentiel de réseau de neurones Al-Mg-Si quasi chimiquement exact sont réalisées pour étudier les interactions dislocation-précipité. Les résultats montrent qu'un précipité donné peut présenter un cisaillement ou un bouclage selon l'orientation relative du précipité et de la dislocation, influencée par les contraintes d'inadaptation interne du précipité, la dépendance de la direction des énergies de cisaillement du précipité et la tension de la ligne de dislocation. Les modèles analytiques de cisaillement et les modèles calibrés de bouclage des dislocations discrètes peuvent capturer avec précision les tendances et les magnitudes du renforcement dans la plupart des cas. Un accord quantitatif raisonnable avec les expériences est alors obtenu en utilisant les théories avec de plus précises propriétés des premiers principes des matériaux. La combinaison des théories et des simulations démontrée ici constitue une voie quantitative pour comprendre et prédire le rôle de la chimie et de la microstructure sur la résistance des alliages, ce qui peut être appliquée à de nombreux alliages différents.

Mots-clés : énergie du noyau de dislocation, théorie non-singulière, dynamique discrète des dislocations, renforcement de la précipitation, mécanisme d'Orowan, simulation atomistique, mécanisme de cisaillement. Potentiel de réseau neuronal, prédiction de la limite d'élasticité.



# Contents

<b>Acknowledgements</b>	<b>i</b>
<b>Abstract (English/Français/Deutsch)</b>	<b>iii</b>
<b>List of Figures</b>	<b>ix</b>
<b>List of Tables</b>	<b>xi</b>
<b>1 Introduction</b>	<b>1</b>
1.1 Background . . . . .	1
1.2 Continuum Solution and Discrete Dislocation Dynamics . . . . .	3
1.2.1 Volterra Solution and Non-singular Theory . . . . .	3
1.2.2 Discrete Dislocation Dynamics . . . . .	7
1.3 Precipitation Strengthening Mechanisms . . . . .	9
1.3.1 Shearing Mechanism . . . . .	10
1.3.2 Orowan Mechanism and Bacon-Kocks-Scattergood Theory . . . . .	13
1.3.3 CRSS Prediction and Experiment . . . . .	13
1.4 Al-Mg-Si Alloys . . . . .	15
1.5 Thesis Organization . . . . .	16
<b>2 Dislocation Core Energies</b>	<b>19</b>
2.1 Introduction . . . . .	19
2.2 Atomistic Calculation of Dislocation Core Energies . . . . .	21
2.3 Atomistic Core Contributions to Dislocation Line Tension . . . . .	26
2.4 Calibrating Non-singular Theory to Atomistic Core Energies . . . . .	28
2.5 Validation of Atomistically-informed DDD: Dislocation Bow-out . . . . .	31
2.6 Calibration of Partial Dislocation Core Energy with NS Theory . . . . .	36
2.7 Role in Orowan Mechanism . . . . .	41
2.7.1 1D Periodic Simulation Model . . . . .	41
2.7.2 Validation of Bacon-Kocks-Scattergood Theory . . . . .	43
2.7.3 Dislocation Core Energy Contribution to CRSS . . . . .	44
2.8 Discussion . . . . .	45
<b>3 Mesoscale Study of Precipitation Strengthening</b>	<b>47</b>
3.1 Introduction . . . . .	47

## Contents

---

3.2	Pseudo-random Precipitate Microstructures of Peak-aged Al–Mg–Si . . . . .	49
3.3	Misfit Stresses in the Pseudo-random Microstructures . . . . .	52
3.4	DDD Simulations of Dislocation-precipitate Interactions . . . . .	55
3.5	CRSS for Orowan Looping . . . . .	59
3.5.1	CRSS versus Volume Fraction and Misfit Stress . . . . .	59
3.5.2	Role of Microstructure . . . . .	61
3.5.3	Role of Dislocation Core Energy . . . . .	64
3.5.4	Comparison with Experiments . . . . .	66
3.6	Precipitate Shearing . . . . .	66
3.7	Conclusion . . . . .	70
<b>4</b>	<b>Dislocation-Precipitate Interaction at Atomistic Scale</b>	<b>73</b>
4.1	Introduction . . . . .	73
4.2	Theories for Precipitate Shearing and Looping . . . . .	74
4.2.1	Precipitate Shearing . . . . .	74
4.2.2	Precipitate Looping . . . . .	77
4.3	Benchmarking of the Al–Mg–Si Neural Network Potential . . . . .	78
4.4	Simulation Models . . . . .	79
4.4.1	Atomistic Simulations . . . . .	79
4.4.2	Continuum Simulations . . . . .	82
4.5	Validation of Continuum Simulations . . . . .	83
4.5.1	Misfit Strain/Stress Fields . . . . .	83
4.5.2	Dislocation-Precipitate Interactions . . . . .	85
4.6	Atomistic Simulations: Results and Comparison to Theory . . . . .	87
4.6.1	Atomistic Results . . . . .	87
4.6.2	Some Details of Dislocation-precipitate Interaction . . . . .	89
4.6.3	Incremental In-situ Analysis for Atomistic Simulations . . . . .	90
4.6.4	Predictions versus Atomistics . . . . .	92
4.7	Strength Prediction for Al-6xxx . . . . .	96
4.8	Optimal Precipitate Size . . . . .	102
4.9	Conclusion . . . . .	104
<b>5</b>	<b>Summary</b>	<b>107</b>
<b>A</b>	<b>List of Line Tensions</b>	<b>111</b>
<b>B</b>	<b>Introduction of FFT method</b>	<b>117</b>
<b>C</b>	<b>Behler-Parrinello Neural Network Potential</b>	<b>119</b>
<b>D</b>	<b>Simulation with ParaDiS</b>	<b>121</b>
	<b>Bibliography</b>	<b>127</b>

# List of Figures

1.1	Atomistic dislocation, TEM dislocation network, dislocation movement. . . . .	2
1.2	Continuum single dislocation. . . . .	3
1.3	Dislocation network discretization . . . . .	7
1.4	Flowchart of Discrete Dislocation Dynamics. . . . .	9
1.5	Schematics of two basic precipitation strengthening mechanisms. . . . .	10
1.6	Friedel's geometry relationship. . . . .	11
1.7	Force balance for line tension and resisting force. . . . .	11
1.8	Simulation and experiment validation of Orowan and shearing mechanisms. . .	14
1.9	Experimental Al–Mg–Si microstructures from TEM. . . . .	15
2.1	Cylinder model for core energy calculation. . . . .	22
2.2	Dislocation total energy per unit length in a cylinder for various characters (Ni EAM potential) . . . . .	24
2.3	Atomistic dislocation core energy of Cu, Ni, and Al EAM potentials. . . . .	25
2.4	Core energy (at b) contribution to line tension for various EAM potentials. . . .	27
2.5	Bow-out model schematics. . . . .	31
2.6	Comparison of bow-outs between DDD and atomistics for Al EA94 . . . . .	34
2.7	Comparison of bow-outs between DDD and atomistics for Al Mishin99 . . . . .	35
2.8	Atomistic dissociation length vs NS dissociation length. . . . .	38
2.9	Thompson tetrahedron and dissociation of character angle $\theta$ , $(60^\circ - \theta)$ and $(60^\circ + \theta)$ . . . . .	39
2.10	Plot of partial core energy vs character angle. . . . .	41
2.11	BKS simulation model: size test and spacing test. . . . .	42
2.12	Validation of BKS via 1D periodic model with circular precipitate. . . . .	43
2.13	Effects of core energy on CRSS of Orowan mechanism. . . . .	45
3.1	Building block composed of three precipitate orientations. 8 variants of building block. Perturbation of center position of precipitate and the relative position of cut precipitates on a glide plane. . . . .	50
3.2	Example of micro(100) microstructures and comparison with a corresponding experiment. . . . .	50
3.3	Building block of micro(111) microstructures and its relative distance on a glide plane. Comparison with pseudo-random microstructure with large perturbation. .	51

## List of Figures

---

3.4	Examples of normalized RSS for different volume fractions and cross sections. .	54
3.5	From 3D microstructure to a 2D DDD simulation model for both screw and edge dislocations. . . . .	56
3.6	Schematics to show adaptation of DDD to model Orowan mechanism. . . . .	57
3.7	Visualization of DDD simulation for screw/edge and with or without misfit stress.	60
3.8	Dual lattice of the Voronoi tessellation of three typical microstructures with dislocation configurations close to CRSS for different volume fractions. . . . .	62
3.9	Dual lattice of the Voronoi tessellation and dislocation configurations close to CRSS for different microstructures at $f=1.10\%$ . . . . .	63
3.10	Forces at each precipitate compared with the resisting force derived from GSFE.	68
3.11	Schematic of model for shear CRSS prediction. . . . .	69
3.12	DDD analysis after removing shear-favorable precipitates. . . . .	71
4.1	Simplified model for CRSS prediction. . . . .	76
4.2	Atomistic model setup and specifications. . . . .	81
4.3	Comparison of atomistics and DDD CRSS simulation model. . . . .	83
4.4	Elastic strain and RSS of $Mg_5Si_6$ precipitate in Al matrix. . . . .	84
4.5	Atomistic vs DDD for edge and screw at various loads. . . . .	86
4.6	Edge $Mg_5Si_6$ interaction for different cases. . . . .	88
4.7	Screw $Mg_5Si_6$ interaction for different cases. . . . .	89
4.8	Atomistic details of dislocation-precipitate interaction. . . . .	91
4.9	Incremental atomistic study for edge pz case. . . . .	92
4.10	Energy contour of edge pz complicated interaction. . . . .	94
4.11	Plot to find optimal precipitate size. . . . .	104
A.1	Dislocation curve with fixed ends. . . . .	111
A.2	Small bowout. . . . .	114
A.3	Large bowout. . . . .	114
A.4	Periodic sinusoidal bowout. . . . .	115
A.5	BKS bowout. . . . .	115
A.6	Comparison of different line tensions. . . . .	116
B.1	Example FFT calculation compared with FEM. . . . .	118
C.1	Neural Network Potential structure for an atomic environment with N atoms. .	120
D.1	Unwanted simulation detail due to small $a$ . . . . .	123
D.2	Discretization of precipitates. . . . .	124
D.3	Simple example of Orowan looping. . . . .	124



## List of Tables

2.1	Energy prefactor and dislocation core energy convergence with radius. . . . .	23
2.2	Comparison of the atomistic core energy with the default core energy in ParaDiS. . . . .	25
3.1	Experimental precipitate characterizations. . . . .	49
3.2	DFT elastic constants of Al and precipitates from Giofr� et al. . . . .	53
3.3	CRSS for different volume fractions, microstructures. . . . .	59
3.4	Comparison of CRSS result with different core energies. . . . .	65
4.1	Material properties from DFT and NNP16 for Al, Mg <sub>5</sub> Si <sub>6</sub> and Mg <sub>4</sub> Al <sub>3</sub> Si <sub>4</sub> . . . . .	80
4.2	Geometry measurements in atomistics. . . . .	90
4.3	Atomistic results vs. shearing predictions vs. DDD. . . . .	95
4.4	DDD simulations for obtaining random factors. . . . .	98
4.5	DDD simulations with various material properties. . . . .	99
4.6	Uniaxial tensile yield stress prediction for realistic Al-6xxx containing Mg <sub>5</sub> Si <sub>6</sub> precipitates with experimental cross section 2a × 4c at experimental spacing $\bar{L}$ = 125b. . . . .	101



# 1 Introduction

## 1.1 Background

The search for materials which are lightweight yet contain high strength has been a long sought goal for research and industry. Today, this is becoming increasingly important with the new industry emphasis on environmental sustainability. In the field of metallurgy, the development of novel materials is often done through experimenting with different compositions and manufacture processes. To better understand these strengthening mechanisms, new theories are required to characterize the experimentally observed material response. With the advancement of computational tools, another pillar of research using simulations and theories has emerged. Such a research path not only has the ability to clarify details observed in experiments, furthering our understanding of the underlying mechanisms, but also opens the door of exploring new materials and their relevant manufacturing processes. This approach forms the basis of Integrated Computational Materials Engineering (ICME) [90] and the concept of X-Mechanics [27]. Specifically, the theory of dislocations combined with computational tools such as atomistic simulations and Discrete Dislocation Dynamics (DDD) are required for strength prediction in alloys.

In alloys, dislocations are key for predicting a material's strength and understanding its plastic behavior. An example of edge dislocation shown as an extra plane of atoms in the regular crystal is depicted in Figure 1.1a. The dislocation can be also regarded as a line of termination of crystal slip across a glide plane, i.e. the upper right block of atoms are slipped with respect to the bottom right block of atoms shown in Figure 1.1. When the crystal is deformed and the atoms are displaced, the dislocations will advance. By this means, the movement of dislocations plays a critical role in materials plastic deformation and strength. In real materials, dislocations are intertwined and form very complicated networks. These networks require specific modeling tools which will be introduced in Section 1.2.

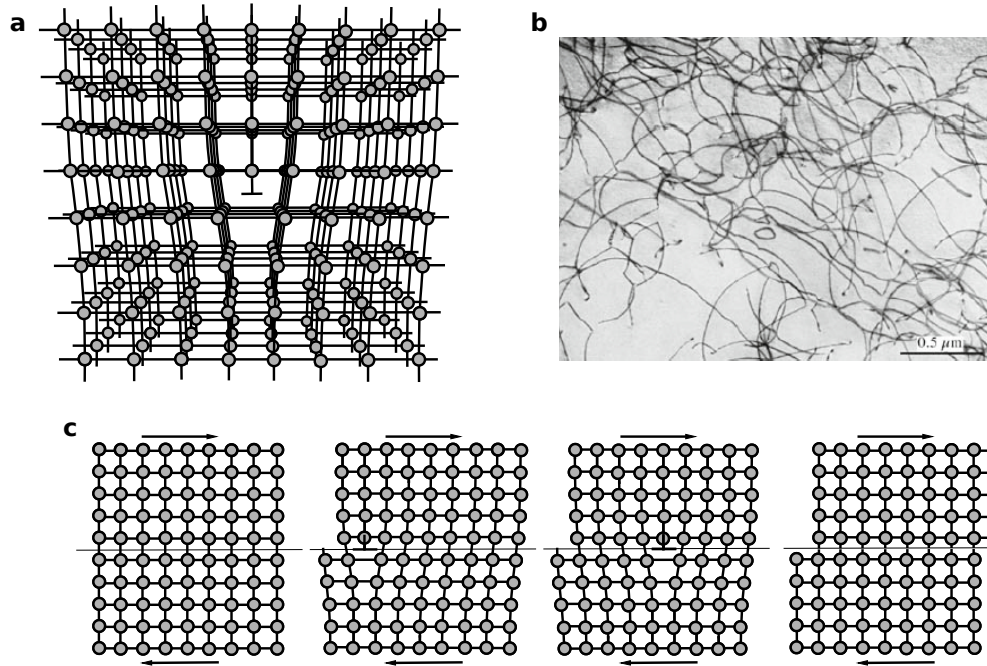


Figure 1.1 – (a) Example of an edge dislocation in a simple crystal. (b) A dislocation network observed experimentally (taken from Figure 1.12 of [18]). (c) Dislocation movement under loading.

In FCC materials, the movement of dislocations is easy, e.g. 10 MPa for pure aluminum. To improve the strength of these FCC metals, we need to include obstacles that can block dislocation movement. There are several types of obstacles that exist in real materials (e.g. solutes, precipitates, etc.). In this work we will focus only on dislocation-precipitate interactions. Formed from special heat treatments, precipitates are ordered phases in a matrix crystal structure. They can be in various shapes (sphere, needle, plate, or cubes) and can be of different types with respect to the matrix crystal, e.g. coherent or incoherent. Coherent precipitates maintain compatibility and have coherent precipitate-matrix interfaces. To overcome such obstacles in the crystal, dislocations can either shear the obstacles or loop around them, referred as shearing and Orowan mechanisms respectively. The basic theories of both mechanisms are presented in Section 1.3.

In this work we will focus on aluminum alloys, one of the most commonly used alloys in industry. In these alloys, precipitation strengthening is often employed. By adding particular alloying elements combined with a specific heat treatment, the strength of aluminum alloys is improved greatly by the formation of precipitates. For example, with the addition of Zn, as found in the common aerospace 7xxx alloys, a tensile yield strength of more than 500 MPa can be achieved. As for the Al–Mg–Si alloys, which are commonly used in the automotive industry, a tensile yield strength of 300 MPa is obtained. A thorough understanding of the underlying precipitation strengthening is thus crucial for new alloy development in the future. To prepare for a detailed investigation of precipitation strengthening in Al–Mg–Si alloys, we review some

of its basic properties in Section 1.4.

## 1.2 Continuum Solution and Discrete Dislocation Dynamics

In a realistic crystal, we often have an enormous number of dislocations, with dislocation density  $10^{12} - 10^{15} \text{ m}^{-2}$  (where dislocation density is defined as the number of dislocation line cross  $1 \text{ m}^2$  or the length of dislocation line in  $1 \text{ m}^3$ ). In these materials, the plastic behavior depends largely on the collective behavior of these complex dislocation networks. In atomistic simulations, just a few number of dislocations can be simulated due to computational constraint. For this reason, we resort to a continuum approach of dislocations which allows for the simulation of these large complex networks by modeling their elastic fields, and the interaction among dislocations is realized through their elastic fields. Of these continuum models there are two primary approaches. The first is the classical Volterra solution [49], which gives a singular elastic field and energy at the dislocation core. The second approach is based on a non-singular theory which is described in [20]. These theories form the basis of the Discrete Dislocation Dynamics codes [110].

### 1.2.1 Volterra Solution and Non-singular Theory

#### Volterra Dislocation

We start our discussion by looking at a single dislocation with a Burgers vector  $\mathbf{b}$ , and line direction  $\xi$  in an infinite perfect lattice (Figure 1.2). In the continuum description, we assume the direction of dislocation  $\xi$ , then the discontinuity  $\mathbf{b}$  across the glide plane is obtained via Burgers circuit in the right-handed sense of  $\xi$  by the convention in [49]. Essentially, for the Volterra dislocation, the following displacement discontinuity over the half plane  $y = 0, x > 0$  is assumed.

$$\begin{aligned} \text{screw} \quad & \lim_{\eta \rightarrow 0, x > 0} u_z(x, -\eta) - u_z(x, \eta) = b \\ \text{edge} \quad & \lim_{\eta \rightarrow 0, x > 0} u_x(x, -\eta) - u_x(x, \eta) = b \end{aligned} \tag{1.1}$$

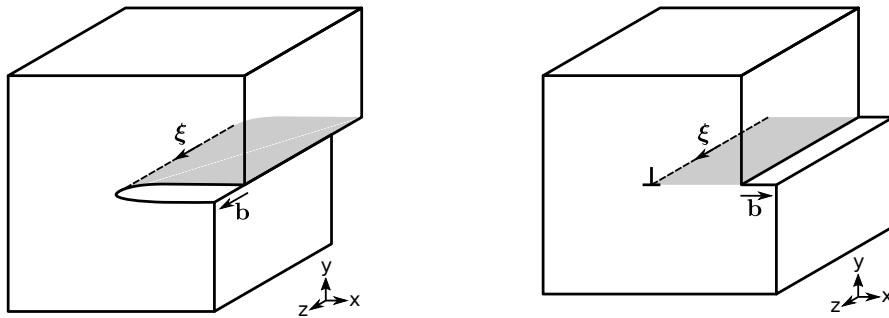


Figure 1.2 – Left: screw dislocation. Right: edge dislocation.

## Chapter 1. Introduction

---

There are basically two ways to solve this problem [28]. The first is to treat the dislocation as an internal boundary, solving for equilibrium equation by assuming an appropriate displacement function and solving for the coefficients [49]. The second approach uses the concept of eigenstrains, utilizing a Green's function to obtain the correction solution [81]. The final solution of a screw and edge dislocation in an isotropic material, with shear modulus  $\mu$  and Poisson ratio  $\nu$ , gives us the following displacement fields

screw	edge	
$u_x = 0$	$u_x = \frac{b}{2\pi} \left[ \tan^{-1} \frac{y}{x} + \frac{xy}{2(1-\nu)(x^2+y^2)} \right]$	(1.2)
$u_y = 0$	$u_y = -\frac{b}{2\pi} \left[ \frac{1-2\nu}{4(1-\nu)} \ln(x^2+y^2) + \frac{x^2-y^2}{4(1-\nu)(x^2+y^2)} \right]$	
$u_z = \frac{b}{2\pi} \tan^{-1} \frac{y}{x}$	$u_z = 0$	

Here the  $\tan^{-1}(y/x)$  is the “two argument arctangent” that expands the region of definition such that the result is in the interval  $[0, 2\pi)$ .

As we know, dislocations interact with each other through elastic stress fields. Thus, we must derive these fields (for screw and edge) using Hook's law.

screw	edge	
$\sigma_{xx} = 0$	$\sigma_{xx} = -\frac{\mu b}{2\pi(1-\nu)} \frac{y(3x^2+y^2)}{(x^2+y^2)^2}$	(1.3)
$\sigma_{yy} = 0$	$\sigma_{yy} = \frac{\mu b}{2\pi(1-\nu)} \frac{y(x^2-y^2)}{(x^2+y^2)^2}$	
$\sigma_{zz} = 0$	$\sigma_{zz} = -\frac{\mu b\nu}{\pi(1-\nu)} \frac{y}{x^2+y^2}$	
$\sigma_{yz} = \frac{\mu b}{2\pi} \frac{x}{x^2+y^2}$	$\sigma_{yz} = 0$	
$\sigma_{xz} = -\frac{\mu b}{2\pi} \frac{y}{x^2+y^2}$	$\sigma_{xz} = 0$	
$\sigma_{xy} = 0$	$\sigma_{xy} = \frac{\mu b}{2\pi(1-\nu)} \frac{x(x^2-y^2)}{(x^2+y^2)^2}$	

The integration of the stress field in a torus area from  $r_c$  to  $R$  gives us dislocation elastic energy per unit length [49]. Equivalently, the elastic energy can be also calculated as the work done by displacing one half of the body relative to the other half. This work is attributed to the surface

traction on the cut plane with  $y = 0, x > 0$  [54].

$$\begin{aligned} \boxed{\text{screw}} \quad E_{\text{el}} &= \int_{r_c}^R \frac{1}{2} \sigma_{yz} b \, dA = \frac{\mu b}{4\pi} \ln \left( \frac{R}{r_c} \right) \\ \boxed{\text{edge}} \quad E_{\text{el}} &= \int_{r_c}^R \frac{1}{2} \sigma_{xy} b \, dA = \frac{\mu b}{4\pi(1-\nu)} \ln \left( \frac{R}{r_c} \right) \end{aligned} \quad (1.4)$$

It should be noted that the above energy does not account for the energy within the radius  $r_c$ . We define this energy as the dislocation core energy  $E_c(\theta)|_{r_c}$ , which is a mathematical quantity, as the choice of core cutoff  $r_c$  is arbitrary. Additionally, the dislocation core energy within  $r_c$  is usually determined by the local atomistic non-linear interactions. In comparison with the mathematical core defined in  $r_c$ , we also observe the underlying atomistic structures of a dislocation core, i.e. physical core. The core structures are different for different crystal systems. In fcc material, a dislocation dissociates into two partials joint by a stacking fault, while in bcc material, a screw dislocation core often has a non-degenerate form. The underlying core structure is associated with the generalized stacking fault surface and can influence Peierls stress [54]. However, such details of dislocation are not important in the current precipitate strengthening problem. A detailed discussion of  $E_c|_{r_c}$  is presented in Chapter 2. In the context of anisotropic elasticity, the pre-logarithm energy factor will change and is often solved by using Stroh's formalism [49]. If we denote the energy prefactor as  $K(\theta)$  ( $\theta$  is dislocation character angle), then the total energy of dislocation per unit length in a cylinder with radius  $R$  can be written as

$$E(\theta) = K(\theta) \ln \left( \frac{R}{r_c} \right) + E_c(\theta)|_{r_c} \quad (1.5)$$

The above continuum theory of dislocations (displacement field (1.2)) has been verified experimentally in [56], particularly in the long range. However, the Volterra solution presented above has two improper features close to the dislocation core: (1) the discontinuity of  $\mathbf{b}$  (disregistry) is uniform on the plane  $y = 0, x > 0$  and (2) the solution field ( $\mathbf{u}$  and  $\boldsymbol{\sigma}$ ) and dislocation energy are singular at the origin. These two features are incorrect, as we know that these features of the dislocation core are resolved at the atomic scale with non-linear interactions. Besides, the field singularity poses problems when calculating dislocation interaction forces at a small distance. A classical way of treating singularity in dislocation interactions is to use an interaction cutoff  $\rho$ , wherein no interaction is modeled. To be consistent in energetics, we set  $\rho = r_c/2$  as documented in [49].

### Non-singular Theory

The Volterra solution of dislocations can work properly in the long-range via elasticity, but there are some drawbacks, such as the singularity and inaccurate description of core behavior. To resolve these issues, other continuum theories have been developed. For example, the Peierls-Nabarro model is capture the atomistic displacement and disregistry by presuming a distribution of Burgers vector on the glide plane. Using this distribution of slip combined with

a misfit energy, one can obtain an analytical solution of the displacement field. Details of the Peierls-Nabarro model can be found in [15, 49]. To eliminate the singularity, one of the classical approaches is to assume an interaction cutoff as mentioned above. Alternatively, non-singular theories can be utilized. Examples of non-singular theories are non-local elasticity [33] and strain gradient elasticity [95]. In this work, we focus on the non-singular theory proposed by [20], which is the basis of the open-source code ParaDiS for Discrete Dislocation Dynamics (DDD) [7].

The primary concept of the non-singular theory presented in [20] is assume a radial Burgers vector distribution  $\tilde{w}(r; a)$  with a regularization parameter  $a$ , then

$$\mathbf{b} = \int \mathbf{b} \tilde{w}(r; a) d^3 \mathbf{x} \quad (1.6)$$

Then the stress field generated by a single dislocation, “tilde field”, is derived as the convolution of the Volterra field in (1.3)

$$\tilde{\boldsymbol{\sigma}}(\mathbf{x}; a) = \boldsymbol{\sigma}(\mathbf{x}) * \tilde{w}(\mathbf{x}; a) = \int \boldsymbol{\sigma}(\mathbf{x} - \mathbf{x}') \tilde{w}(\mathbf{x}'; a) d^3 \mathbf{x} \quad (1.7)$$

This is the field that we need to consider for the dislocation interactions with defects such as solutes, grain boundaries, etc. To account for dislocation-dislocation interactions, a second stress convolution is required, since both dislocations have a distributed Burgers vector. Hence a different stress field for dislocation interactions arises. We denote such field as “non-singular field”

$$\boldsymbol{\sigma}^{\text{ns}}(\mathbf{x}; a) = \tilde{\boldsymbol{\sigma}}(\mathbf{x}) * \tilde{w}(\mathbf{x}; a) = \int \boldsymbol{\sigma}(\mathbf{x} - \mathbf{x}') w(\mathbf{x}'; a) d^3 \mathbf{x} \quad (1.8)$$

with  $w = \tilde{w} * \tilde{w}$ . In Discrete Dislocation Dynamics simulations the interaction calculations are more frequent, and a more efficient evaluation of non-singular field  $\boldsymbol{\sigma}^{\text{ns}}$  is demanded. With a carefully chosen  $w(\mathbf{x}; a)$ , a succinct expressions of the non-singular field can be formulated as

screw	edge	
$\sigma_{xx}^{\text{ns}} = 0$	$\sigma_{xx}^{\text{ns}} = -\frac{\mu b}{2\pi(1-\nu)} \frac{y}{\rho_a^2} \left[ 1 + \frac{2(x^2 + a^2)}{\rho_a^2} \right]$	
$\sigma_{yy}^{\text{ns}} = 0$	$\sigma_{yy}^{\text{ns}} = \frac{\mu b}{2\pi(1-\nu)} \frac{y}{\rho_a^2} \left[ 1 - \frac{2(y^2 + a^2)}{\rho_a^2} \right]$	
$\sigma_{zz}^{\text{ns}} = 0$	$\sigma_{zz}^{\text{ns}} = -\frac{\mu b \nu}{\pi(1-\nu)} \frac{y}{\rho_a^2} \left[ 1 + \frac{a^2}{\rho_a^2} \right]$	(1.9)
$\sigma_{yz}^{\text{ns}} = \frac{\mu b}{2\pi} \frac{x}{\rho_a^2} \left[ 1 + \frac{a^2}{\rho_a^2} \right]$	$\sigma_{yz}^{\text{ns}} = 0$	
$\sigma_{xz}^{\text{ns}} = -\frac{\mu b}{2\pi} \frac{y}{\rho_a^2} \left[ 1 + \frac{a^2}{\rho_a^2} \right]$	$\sigma_{xz}^{\text{ns}} = 0$	
$\sigma_{xy}^{\text{ns}} = 0$	$\sigma_{xy}^{\text{ns}} = \frac{\mu b}{2\pi(1-\nu)} \frac{x}{\rho_a^2} \left[ 1 - \frac{2y^2}{\rho_a^2} \right]$	



with  $\rho_a = \sqrt{x^2 + y^2 + a^2}$ . The “singular field” in (1.3) and “non-singular field” (1.9) converge to the same elastic solution in the long range. The regularization in the solution removes the core singularity and the regularization parameter  $a$  is a similar quantity as the cutoff radius  $r_c$  in the Volterra solution. The comparison of different continuum descriptions is meaningful to get a consistent result [20]. Furthermore, to ensure realistic results, the energetics of these continuum models should match atomistic simulations. A more detailed discussion of energetics and other aspects of the non-singular theory are presented in Chapter 2.

### 1.2.2 Discrete Dislocation Dynamics

Based on the continuum theories of dislocations, Discrete Dislocation Dynamics (DDD) becomes one of the popular mesoscale approaches for simulating complex dislocation networks. Dating back to the 90s, various types of 3D Discrete Dislocation Dynamics have been proposed [7, 96, 125, 39, 30].

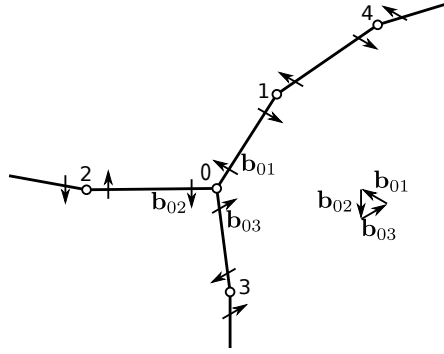


Figure 1.3 – Discretized network with Burgers vector balanced.

Basically, dislocation lines are discretized into linear segments with nodes (Figure 1.3) and the movements of these segments are driven by the forces on each segment under an assumed mobility law. The forces on a dislocation segment  $\mathbf{l}_{ij}$  with a Burgers vector  $\mathbf{b}_{ij}$  consist of forces induced by externally applied load  $\boldsymbol{\sigma}^{\text{app}}$ , elastic forces (long-range elastic interaction forces  $\mathbf{f}_{ij}^{kl}$  due to segment  $kl$  and elastic self-forces  $\mathbf{f}_{ij}^{\text{el}}$ ) and core energy forces  $\mathbf{f}_{ij}^{\text{core}}$ . Additionally, we can include other forces, due to interfaces and boundaries, or osmotic forces resulting from vacancies. In summary, the force  $\mathbf{f}_{ij}$  on a dislocation segment  $ij$  can be expressed with

$$\mathbf{f}_{ij} = \mathbf{f}_{ij}^{\text{app}} + \mathbf{f}_{ij}^{\text{el}} + \mathbf{f}_{ij}^{\text{core}} \quad (1.10)$$

And for each component, we have

$$\begin{aligned} \mathbf{f}_{ij}^{\text{app}} &= (\boldsymbol{\sigma}^{\text{app}} \mathbf{b}_{ij}) \times \mathbf{l}_{ij} \\ \mathbf{f}_{ij}^{\text{el}} &= \mathbf{f}_{ij}^{\text{s}} + \sum_{kl \neq ij} \mathbf{f}_{ij}^{kl} \\ \mathbf{f}_{ij}^{\text{core}} &= - \frac{\partial E_c ||\mathbf{l}_{ij}||}{\partial \mathbf{l}_{ij}} \end{aligned} \quad (1.11)$$

where the core energy  $E_c$  is defined above within a cutoff radius  $r_c$ . One of the most computationally expensive step in DDD is the interaction force calculation  $\sum_{kl \neq ij} \mathbf{f}_{ij}^{kl}$ . This is a result of the long-range segment-segment interactions which can become very complex [20]. In practice, various numerical techniques are used to improve the simulation efficiency [7]. A common way to treat the  $1/r$  interaction is to employ a Fast Multipole Method (FMM), where the stresses from distant dislocation segments can be calculated efficiently. However, the stress of a dislocation segment has a complicated form, which is further reduced by using a Taylor expansion of the stress expression. Moreover, great care must be taken in using different approximations (Taylor expansion approximation and multiple moment approximation in FMM), and one needs to strike a balance between efficiency and accuracy (Appendix D). More recent DDD performs these FMM force calculations via GPUs [13], further increasing the computational efficiency.

With the segment forces and appropriate mobility coefficient  $\mathbf{B}(\mathbf{l}_{ij}, \mathbf{b}_{ij})$ , the kinematics of dislocation segments can be determined via a crystal-specific mobility law

$$\mathbf{B}(\mathbf{l}_{ij}, \mathbf{b}_{ij}) \mathbf{v}_{ij} = \mathbf{f}_{ij} \quad (1.12)$$

Here a simple linear mobility function is assumed, with the mobility coefficient,  $\mathbf{B}(\mathbf{l}_{ij}, \mathbf{b}_{ij})$  depending on the the orientation of the dislocation segment, the Burgers vector and the slip plane it resides on. The parameters can be obtained from atomistics [89]. To get the position of dislocation segments, we then integrate to solve (1.12). Due to the complicated forces and an evolving geometry, the solution (position of the nodes) can oscillate even for simple problems. Recent advances have been devoted to resolve this issue [109].

During the simulation, multiple topology changes can occur, greatly influencing the results as presented in [7]. These topology changes include dislocation annihilation, dissociation, jog formation, cross-slip, etc. To improve the simulation efficiency while maintaining resolution, local refinement and coarsening of dislocation lines are implemented. Efficient implementation of all sorts of topology changes requires collision detection algorithm and operations for geometry changes [7]. Specific geometry operations are added, when more physics and critical mechanisms are incorporated [107].

Equipped with all the techniques and developments described above, Discrete Dislocation Dynamic has become a useful tool for studying material strengthening mechanisms [65] via virtual material testing [37, 31] without the expense associated with atomistic modeling [131]. A simplified flowchart of the Discrete Dislocation Dynamics simulation is presented in Figure 1.4. In later chapters of the thesis, we will show how to embed the dislocation core energy in DDD, and model dislocation-precipitate interactions.

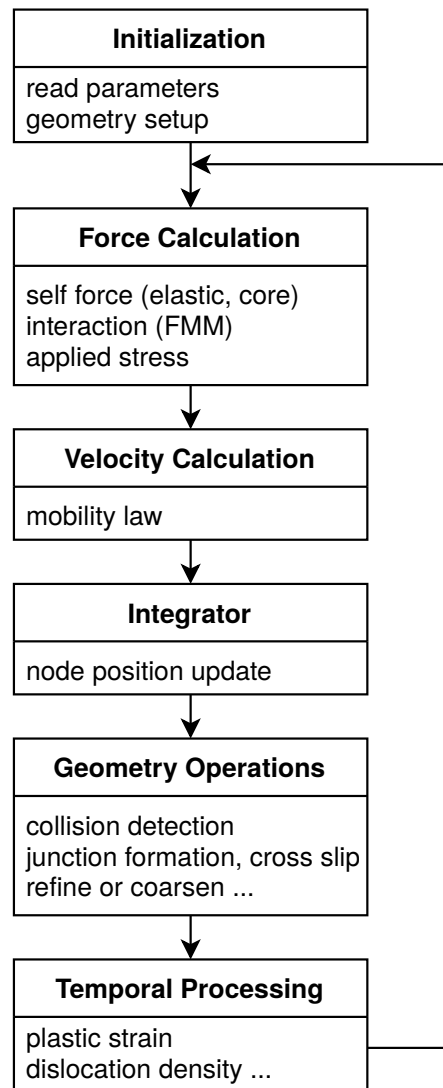


Figure 1.4 – Simplified procedure of Discrete Dislocation Dynamics simulation.

### 1.3 Precipitation Strengthening Mechanisms

Precipitates are important strengthening phases in alloys. In manufacturing, they are formed by special heat treatments, i.e. dissolution of solute element at high temperature, rapid quenching to room temperature for forming supersaturated solid solution and then aging at a medium temperature to obtain a finer microstructure. The temperature and the duration of aging time is crucial for precipitation strength development. If the aging time is too long, it will lead to over-aging, where precipitates coarsen and the material strength is reduced. Typical applications of precipitation strengthening are nickel-based superalloys and aluminum alloys.

In precipitate-strengthened materials, precipitates serve as obstacles to impede the dislocation motion, resulting in an increase in the Critical Resolved Shear Stress (CRSS). Specifically,

there are two possible strengthening mechanisms for precipitates (Figure 1.5): (1) a shearing mechanism, where the dislocation cuts the precipitate, and (2) an Orowan mechanism, where the dislocation wraps around the precipitate forming a loop. With precipitate volume fraction  $f$ , and assuming a circular precipitate with radius  $r$ , the CRSS scales with  $\sqrt{r}$  for shearing, and  $1/r$  for Orowan looping [84]. Given the CRSS associated with each mechanism, the minimum required CRSS will control this interaction. For peak-aged alloys, these two mechanisms have the same CRSS. We present the derivation of the scaling of CRSS for both mechanism in the following section.

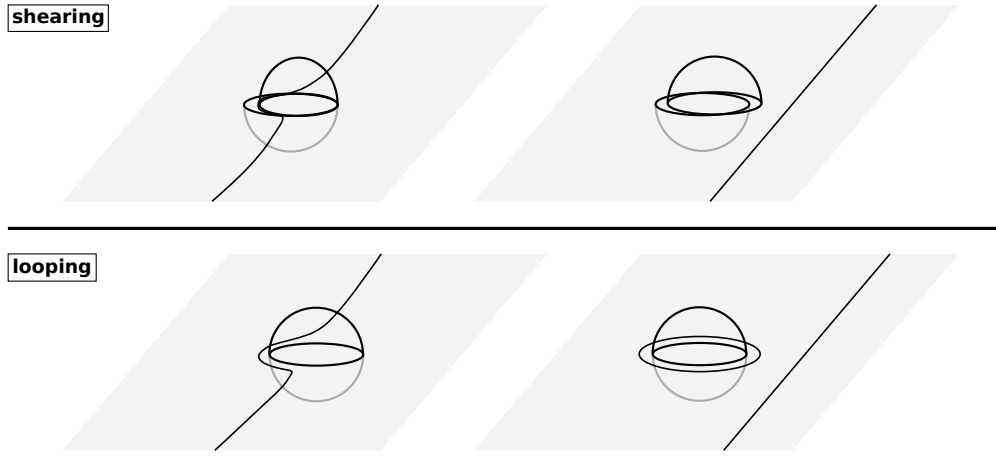


Figure 1.5 – Schematics of two basic dislocation-precipitate interaction mechanisms.

### 1.3.1 Shearing Mechanism

We focus our discussion on a chosen slip plane and assume circular precipitates with an identical radius  $r$  in the following derivations. We start with a simple ordered arrangement of precipitates. The average precipitate edge-edge spacing is defined as  $L$ , and the average precipitate center-center spacing is  $\bar{L}$ . Then the average area fraction  $f$  is

$$f = \frac{\pi r^2}{\bar{L}^2} \quad (1.13)$$

Here we do not differentiate the notation of the average area fraction and the volume fraction, since the average area fraction is actually the same as the volume fraction.

We first introduce Friedel statistics presented in [42, 5], then use this to derive the CRSS prediction for precipitate shearing.

The Friedel statistics is derived for random weak obstacles. By “weak” obstacles we mean that the critical cusp angle  $\phi_c$  (the spanned angle of two dislocation arms at a precipitate) is relatively large when compared with Orowan looping (which is zero), and small dislocation bow-out. This allows for an area equivalence, i.e. the area swept by dislocation to the next precipitate (gray area on the right of Figure 1.6) is equal to the area occupied by a single

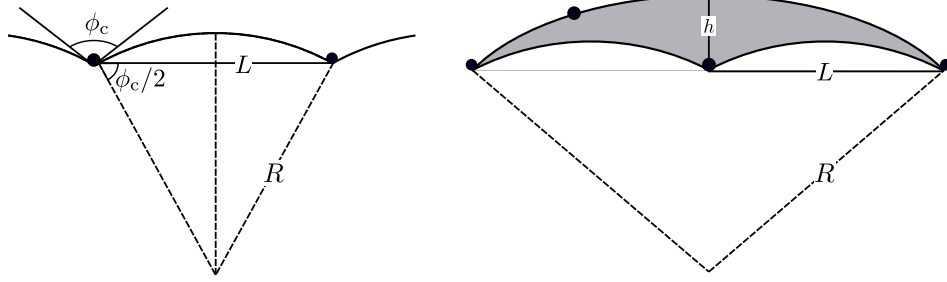


Figure 1.6 – Geometry relationships for “weak” obstacle. The right figure gives area equivalence.

precipitate,  $\bar{L}^2$  (precipitate center-center spacing). Supposing a swept distance is  $h$  and precipitate edge-edge spacing  $L$ , then the area equivalence is

$$Lh = \bar{L}^2 \quad (1.14)$$

For a circular arc geometry, with radius  $R$  in Figure 1.6, the geometrical relationship becomes

$$\begin{aligned} R \cos \frac{\phi_c}{2} &= \frac{L}{2} \\ (R - h)^2 + L^2 &= R^2 \end{aligned} \quad (1.15)$$

This yields the cusp angle

$$\cos \frac{\phi_c}{2} = \frac{h}{L} \quad (1.16)$$

With the area equivalence in (1.14), we have the relationship between the precipitate edge-edge spacing  $L$  and the precipitate center-center spacing  $\bar{L}$

$$\left( \frac{\bar{L}}{L} \right)^2 = \cos \frac{\phi_c}{2} \quad (1.17)$$

Equation (1.17) is the essential relationship in Friedel’s statistics, meaning that the edge-edge spacing  $L$  is larger than the actual center-center spacing for weak obstacles.

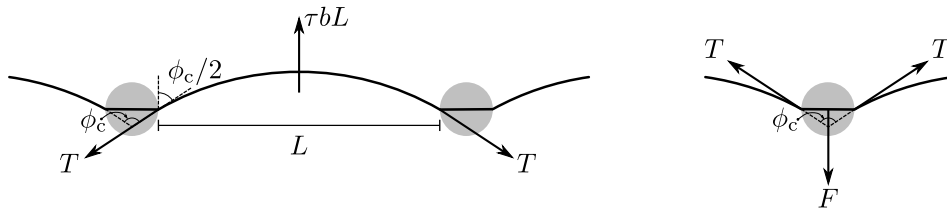


Figure 1.7 – Force balance for bow-out dislocation arc (left) and the individual precipitate (right).

Now we consider the force on a dislocation line and an individual precipitate. For the dislocation curve, at the critical state shown in Figure 1.7a, the critical cusp angle  $\phi_c$ , the Critical

## Chapter 1. Introduction

---

Resolve Shear Stress  $\tau_c$  can be expressed by the following

$$\tau_c = \frac{2T \cos(\phi_c/2)}{bL} \quad (1.18)$$

Using the above, the critical force balance between precipitate resisting force  $F$  and the line tension  $T$  on the precipitate has the following relationship

$$F = 2T \cos \frac{\phi_c}{2} \quad (1.19)$$

where the resisting force is supplied by the Generalized Stacking Fault Energy (GSFE)  $\gamma$ , i.e.  $F = 2r\gamma$ . Hence the critical cusp angle for shearing is derived as

$$\cos \frac{\phi_c}{2} = \frac{r\gamma}{T} \quad (1.20)$$

To obtain the CRSS, we use (1.18) and first replace the edge-edge spacing  $L$  using (1.17) and (1.13), then substitute the critical cusp angle with (1.20)

$$\begin{aligned} \tau_c &= \frac{2T}{bL} \cos \frac{\phi_c}{2} \\ &= \frac{2T}{b\bar{L}} \left( \cos \frac{\phi_c}{2} \right)^{\frac{3}{2}} \\ &= \frac{2T}{b\bar{L}} \left( \frac{r\gamma}{T} \right)^{\frac{3}{2}} \\ &= \frac{2T}{br\sqrt{\pi/f}} \left( \frac{r\gamma}{T} \right)^{\frac{3}{2}} \\ &= \frac{2}{\sqrt{\pi}} \frac{\gamma^{3/2}}{b\sqrt{T}} \sqrt{fr} \end{aligned} \quad (1.21)$$

If the line tension  $T$  is treated as a constant material quantity, then we have  $\tau_c \propto \sqrt{r}$ . This is the correct scaling as previously reported in [84].

It should be noted that if we do not utilize Friedel statistics (and the assumptions therein) then we do not obtain the essential relationship shown in (1.17). Thus the scaling  $\tau_c \propto \sqrt{r}$  no longer holds. If we use the approximation  $L \approx \bar{L}$  and the critical cusp angle in (1.20), then  $\tau_c$  has no dependence on  $r$

$$\begin{aligned} \tau_c &= \frac{2T}{b\bar{L}} \cos \frac{\phi_c}{2} \\ &= \frac{2T}{br\sqrt{\pi/f}} \left( \frac{r\gamma}{T} \right) \\ &= \frac{2}{\sqrt{\pi}} \frac{\gamma\sqrt{f}}{b} \end{aligned} \quad (1.22)$$

This CRSS is independent of the geometry and random arrangement of precipitates, and can

be thought as a direct balance between the applied loading and the precipitate resistance, namely  $\tau_c b \bar{L} = 2r\gamma$ .

#### 1.3.2 Orowan Mechanism and Bacon-Kocks-Scattergood Theory

In Orowan mechanism for very strong precipitates, dislocations loop around precipitates, and CRSS is attained when the cusp angle is  $\phi_c = 0^\circ$ . Therefore, from the force balance on the dislocation curve (1.18), we have

$$\tau_c = \frac{2T}{bL} \quad (1.23)$$

If  $T = 0.5\mu b^2$ , the above expression reduces to the critical Orowan stress of  $\tau_c = \mu b/L$ . Using  $L \approx \bar{L}$  and substituting (1.13), then

$$\tau_c = \frac{2T}{\sqrt{\pi}b} \frac{\sqrt{f}}{r} \quad (1.24)$$

This is the often cited scaling  $\tau_c \propto (1/r)$  [84].

In the Bacon-Kocks-Scattergood theory [9] (BKS), the authors attempted to predict CRSS for a randomly field of spherical obstacles. In this random system, the critical cusp angle,  $\phi_c$ , is no longer zero, since the dislocation lines can fold and pass more easily through the array. Then they found the critical cusp angle  $\phi_c$  via a comparison of a “triplet configuration” with a penetrable precipitate. Additionally, they postulated (but not proved) a more realistic line tension model, which involves dislocation branch interaction.

$$T = A\mu b^2 \left( \ln \frac{\bar{D}}{b} + B \right) \quad (1.25)$$

where  $A = 1/4\pi$  for the edge and  $A = 1/4\pi(1 - \nu)$  for the screw,  $B$  is a constant and related to the dislocation core energy at  $b$ , and  $\bar{D}$  is the harmonic average of diameter  $D = 2r$  and  $L$ , i.e.  $\bar{D} = (D^{-1} + L^{-1})^{-1}$ . After applying Friedel statistics in (1.17), they obtained the following formula as (there are also other similar formulas in their paper)

$$\tau_{\text{BKS}} = \left( \frac{\ln(D/b)}{\ln(L/b)} \right)^{1/2} \frac{\mu b \ln(D/b)}{L} \frac{1}{2\pi} \quad (1.26)$$

In general, the randomness will reduce the prediction of CRSS from periodic model. The above BKS prediction has been verified by both simulations and experiments [78, 101].

#### 1.3.3 CRSS Prediction and Experiment

All of the above described CRSS predictions (1.21), (1.22) and (1.24) produce the scaling  $\tau_c \propto \sqrt{f}$ , demonstrating that the strength increases with a higher precipitate density. Furthermore, the shearing  $\tau_c$  increases with larger shearing energy  $\gamma$ , while in the Orowan mechanism  $\tau_c$  scales with line tension  $T$ . However, relying on Friedel statistics in both shearing prediction

(1.21) and BKS prediction (1.26) might not be appropriate, since precipitates are basically large obstacles and can not be deemed as “weak”. So the geometrical relationship in (1.17) may not hold. Irregardless, the line tension quantity is often related to the dislocation geometry, as shown in BKS line tension (1.25) (or Appendix A). so treating it as a constant material property might also not hold.

Now we focus on finding the optimal precipitate size, which is attained when shearing mechanism gives the same CRSS as Orowan mechanism. By equating (1.21) with (1.24) we find  $r_{\text{opt}} = T/\gamma$ . In fact, when  $r_{\text{opt}} = T/\gamma$ , all three CRSS predictions (1.21), (1.22) and (1.24) are equal. This simple formula for optimal  $r$  is reasonable, when the critical cusp angle  $\phi_c = 0^\circ$  in the right plot of Figure 1.7. In this case, the line tension is balanced with the shearing resisting force,  $2T = 2r_{\text{opt}}\gamma$ . This optimal radius as  $r_{\text{opt}} = T/\gamma$  gives us good guidance for peak-aging. This is demonstrated for the Al–Mg–Si alloys in Chapter 4, where the line tension is  $T = 8.08 \times 10^4 \text{ MPa} \cdot \text{\AA}^2$  and an approximate GSFE of precipitate is  $\gamma = 450 \text{ mJ/m}^2$ . Then the optimal radius is  $r_{\text{opt}} = 1.8 \text{ nm}$  on the slip plane. As will be shown in later Chapter 3, the actual precipitate diameter on the slip plane  $D = 3 \text{ nm} < 2r_{\text{opt}}$ . This point confirms that the precipitates are in the shearing mechanism regime.

Aside from the theoretical analysis of the precipitation strengthening, previous simulations and experiments in Mohles et al. [78] are also worth mentioning. Their results involving spherical precipitates on glide planes are replotted here in Figure 1.8. In particular, the looping CRSS is well predicted, as seen from the simulation on the left of Figure 1.8. However, the  $\sqrt{r}$  scaling underestimates the strength. As for the optimal radius  $r_{\text{opt}}$ , the theory seems to deliver a reasonable result. In their experimental result on the right of Figure 1.8, the BKS prediction (with a coefficient) can explain some of the simulation cases, but does a poorer job of matching experimental results (solid markers).

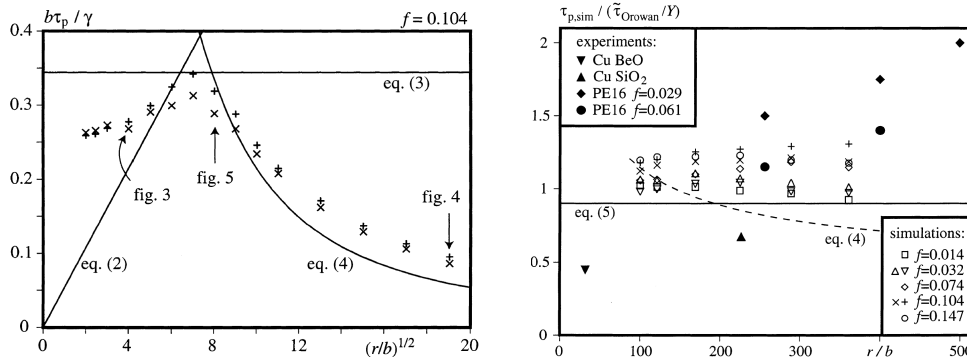


Figure 1.8 – Simulation and experiment results of spherical precipitates reported in [78]. The left figure shows the simulations of different virtual random systems. The right figure shows various experimental results, where eq.(5) in the plot represents the BKS prediction as our (1.26), and eq.(4) is the simple prediction (1.24).

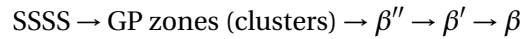
We emphasize here that the above analysis of precipitation strengthening is based on spherical precipitates. However, in real materials, different precipitate geometries are present, such



as cuboidal precipitates in Ni-based super alloys, disc-like precipitates in Al–Cu alloys and needle-shaped precipitates in Al–Mg–Si alloys. It has been demonstrated that a change of this morphology can have a significant influence on the strengthening of a material [85, 99].

## 1.4 Al–Mg–Si Alloys

For Al–Mg–Si alloys, the summed atomic weight content of Mg and Si ranges from 0.8% to 1.2%, with its strength primarily attributed to precipitation strengthening. As is noted above, heat treatments are often utilized to form precipitates in alloys for strength improvement. Specifically for T6 tempered Al 6061 alloy, the material is heated to over 500 °C and then quenched rapidly to room temperature, forming a Supersaturated Solid Solution (SSSS). A subsequent artificial aging at 175 °C for 8 h is realized to finally obtain a finer precipitate microstructure in the material [8]. The time and temperature of artificial aging is crucial, since peak-aging is the target. The precipitation process in Al–Mg–Si is understood as [4]



where the major strengthening phase for peak-aged alloy is thought to be  $\beta''$ . This metastable phase is needle-shaped and shares a common axis with the Al matrix as shown in Figure 1.9. The crystallography structure of  $\beta''$  is monoclinic and often possess a 11-atom “eye” structure as shown on the right of Figure 1.9 [3]. Different variants of  $\beta''$  are  $\text{Mg}_5\text{Si}_6$ ,  $\text{Mg}_5\text{Al}_2\text{Si}_4$ ,  $\text{Mg}_4\text{Al}_3\text{Si}_4$  and the primitive unit cell of  $\beta''$  contains 22 atoms.

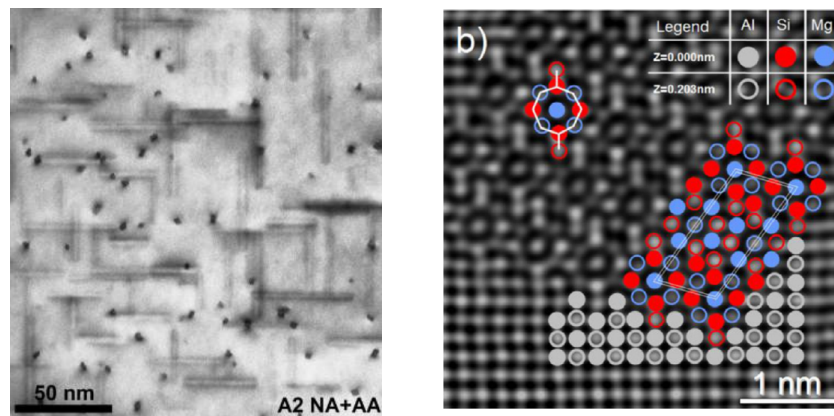


Figure 1.9 – Microstructure of Al–Mg–Si alloy (left) [124] and  $\text{Mg}_5\text{Si}_6$  crystal structure [87].

In industry fabrication, many factors like the element content ratio, room temperature storage, etc. can influence the final product. Experiments [72] have addressed the effects of different Mg/Si ratios and reported that Si-rich Al–Mg–Si alloy has a finer precipitate structure resulting in a higher hardness. Also, natural aging (due to room temperature storage) has a strong effect on material hardness [124], which can be circumvented by adding small amounts of Cu (0.1%) [124, 74].

With the respect of strengthening mechanisms in Al–Mg–Si alloys, direct observation of dislocations and precipitates is often difficult. This is especially true when considering the shearing mechanism, which requires a very high resolution. Recent experimental methods [25] has enabled an elaborate investigation of in-situ deformation mechanism of precipitate. These results nicely complement previous experimental work [97], where the authors show that the non-shear to shear transition is possible in Al–Mg–Si alloys at a diameter 2.5-3 nm.

In parallel to the above experimental work, there have been several modeling efforts trying to build models for precipitation process together with strength predictions [83, 10]. However, these models involve calibrated coefficients which are sometime heuristic and lacks fundamental atomistic knowledge. Nevertheless, they are still of great technological importance for fast prototyping and development. In contrast, the current thesis is dedicated to a deeper understanding of the precipitation strengthening processes on variety of scales in the hopes that this work will help design new materials with broader applications.

### 1.5 Thesis Organization

The current thesis starts with the study of dislocation core energy, then attempts to predict the strength of Al–Mg–Si by conduction a mesoscale study, and investigates the strengthening mechanism at atomistic scale. The thesis is organized as follows.

**Chapter 2:** We describe the methodology of quantifying dislocation core energy and its incorporation in Discrete Dislocation Dynamics. We validate the calibrated DDD by comparing with multiscale simulations in a bow-out model. The importance of dislocation core energy is examined in the context of the Orowan mechanism with the Bacon-Kocks-Scattergood theory.

**Chapter 3:** Mesoscale simulations with key experimental information are performed to predict the peak-aged Al–Mg–Si yield strength. A method of creating pseudo-random microstructures is proposed. The misfit stresses associated with the microstructures are calculated to incorporate into later mesoscale simulations. The current Discrete Dislocation Dynamics code ParaDiS is adapted to include dislocation-precipitate interactions for the Orowan mechanism. Then various aspects of the precipitation strengthening at mesoscale are carefully studied. We estimate the yield strength of peak-aged material with different material parameters and dislocation core energies. The force analysis on individual precipitates are performed to probe the real dislocation-precipitate interaction mechanism.

**Chapter 4:** We use the latest Neural Network Al–Mg–Si potential to study of dislocation-precipitate interactions. The strengthening theories are reviewed and extended with atomistic information about dislocation geometry. Continuum calculations are validated for 1. misfit stress/strain calculation and 2. dislocation-precipitate interactions, which are prepared for later theoretical predictions. Atomistic simulation results are analyzed in detail for various cases, and we compare our CRSS predictions with atomistic simulations (corrected by image forces), which show good agreement. In addition, realistic tensile yield strength calcula-

tion based on the acquired atomistic knowledge and first-principle material properties were performed. At the end of this chapter, a method of finding the optimal precipitate size is presented.

**Chapter 5** summarizes all the findings in the current research and presents several possible directions for future work within the field of precipitation strengthening.

Various technical details and useful information are documented in the appendices.



## 2 Dislocation Core Energies

This chapter is adapted from the following article, with permission from the coauthors and the publisher.

**Yi Hu**, B. A. Szajewski, D. Rodney, and W. A. Curtin. Atomistic dislocation core energies and calibration of non-singular discrete dislocation dynamics. *Modelling and Simulation in Materials Science and Engineering*, 28(1):015005, Nov. 2019. ISSN 0965-0393. doi: 10.1088/1361-651X/ab5489.

### 2.1 Introduction

The total energy of a dislocation can be conceptually partitioned into two parts [49]: an elastic energy contribution due to the elastic deformations introduced by the dislocation and an inelastic energy contribution occurring in the dislocation core region, loosely defined as the region where the non-linear/non-convex energy landscape of the material and discreteness of the lattice structure influence the dislocation structure and fields. The elastic energy dominates the total energy of an infinite straight dislocation, diverging in an infinite medium, often leading to approximations that neglect the inelastic core energy. However, when the dislocation density is high, dislocation segments are short and close to one another, and/or when the dislocation radius of curvature is in the sub-micron scale of 100nm and below, the atomistic core energy contribution cannot be neglected a priori.

As introduced in Section 1.2.1, in most mesoscale models the singularity at the origin is circumvented by using a heuristic cutoff radius or a regularized field theory [20]. Details of the actual dislocation core structure and energy are usually neglected, although occasionally the dissociated structure of glissile fcc dislocations is incorporated by treating each partial dislocation as a separate dislocation line [75]. A core energy may also be introduced [7], but is treated as a parameter, while a regularized core model automatically imposes some core energy that is not necessarily directly related to any atomistic quantity. Multiscale methods, which aim to combine both atomistic and continuum descriptions simultaneously in different

regions of the material [29, 128] also require a careful calibration of the continuum description to the atomistic dislocations, including the core energy. Accurate computation of the core energy and precise calibration of the non-singular continuum theory are the topics of this chapter.

There are two basic approaches to computing the dislocation core energy. One method uses a single straight dislocation in a cylindrical geometry. This method is mentioned in [49] but has not been widely used. We use this method here because (i) it is easy to implement, (ii) requires no additional corrections, (iii) has a controllable accuracy and easy convergence assessment because the scaling of the far-field elastic energy versus distance is known analytically, and (iv) it is easy to calibrate non-singular theory to the atomistic results. The other method uses a dislocation dipole geometry [19]. The dipole method has been preferred by many researchers when using first principles methods [26, 66] because the periodicity enables accurate computation of the total system energy. The dipole method has also been employed in molecular statics studies [132, 45]. The dipole method requires corrections for the periodic images, which can be computed numerically in anisotropic elasticity. This method is thus accurate if the dislocations interact solely through the elastic fields, which must be verified by convergence studies.

There have also been significant efforts to describe the dislocation core region itself through approximate (non-atomistic) models, e.g. [95, 14, 47, 44]. These elegant methods help bridge the gap between atomistic dislocations and their continuum counterparts, but do not usually ensure that the total dislocation energy is preserved in making such a transition. Thus, the specific determination of the core energy and its precise introduction into a higher-scale method has not generally been achieved, with the exception of the recent work of Geslin et al. [44]. Therefore, in the current work, we execute a straightforward strategy for computing the dislocation core energy in a full atomistic environment, discuss the calibration of non-singular theory to atomistics, and demonstrate that the atomistically-calibrated non-singular theory can provide good predictions of the evolving curvature of a dislocation over scales of  $\sim 25\text{-}50$  nm. This work largely resolves previous discrepancies between the atomistics and DDD studies using an approximate core-energy representation [118] and demonstrates a general methodology that can be applied to any system described by interatomic potentials.

The remainder of this chapter is organized as follows. In the next section, we introduce the basics of dislocation energies and the atomistic simulation method, and compute the dislocation core energies for  $\mathbf{b} = a[\bar{1}10]/2$  dislocations in the fcc metals Al, Cu, and Ni. In Section 2.3, we present the resulting atomistic core contributions to the dislocation line tension. In Section 2.4, we discuss how to incorporate the atomistic core energy into the non-singular theory of dislocations [20]. In Section 2.5, we define the bow-out dislocation test problem and compare predictions of DDD using non-singular theory [7] and atomistics, drawing attention to the role of the regularization parameter in the non-singular theory. In Section 2.6, we compute the atomistic core energies for the  $\mathbf{b}_s = a[\bar{2}11]/6$  Shockley partial dislocations in fcc materials as appropriate for use in continuum-level models. In Section 2.8,

we discuss our results and restate our major conclusions.

## 2.2 Atomistic Calculation of Dislocation Core Energies

For an infinite straight dislocation, the total dislocation energy within a cylinder of radius  $R$  centered on the dislocation line can be expressed as

$$E(\theta) = K(\theta) \ln \left( \frac{R}{r_c} \right) + E_c(\theta)|_{r_c} \quad (2.1)$$

where  $\theta$  is the character angle of the dislocation and  $E_c$  is the core energy defined at a chosen cutoff radius  $r_c$ . The separation between elastic and core energies is always defined with respect to some chosen cutoff; for straight dislocations, there is no strict nor unique partition of the total energy into these two components. The goal of calibrating the core energy is to capture the correct total dislocation energy at large  $R \gg b$ , independent of the chosen cutoff  $r_c$ . The coefficient  $K(\theta)$  is fully determined by the anisotropic elastic constants, dislocation Burgers vector  $\mathbf{b}$ , and dislocation line direction can be computed for any particular material using the Stroh formalism [115]. Note that the dislocation is treated as a full undissociated dislocation, and thus the core energy as defined here includes, for fcc dislocations, the energies of the two partial dislocations, their interactions, and the stacking fault energy, as well as all non-linear contributions. Inclusion of all of these effects into the core energy is consistent with most DDD simulations that treat the dislocation as a single undissociated dislocation; the core energies of the partial dislocations in fcc metals are presented in Section 2.6.

We compute the core energy  $E_c(\theta)$  atomistically by first measuring the total dislocation energy as a function of  $R$  in an atomistic simulation. We then extrapolate the far-field elastic energy back to the chosen cutoff radius  $r_c$ . Here, we choose  $r_c = b$ . The core energy at any other chosen cutoff  $r_c$  can then be obtained with no further approximation by writing the total energy as

$$\begin{aligned} E(\theta) &= K(\theta) \ln \left( \frac{R}{b} \right) + E_c(\theta)|_b \\ &= K(\theta) \ln \left( \frac{R}{r_c} \right) + K(\theta) \ln \left( \frac{r_c}{b} \right) + E_c(\theta)|_b \\ &= K(\theta) \ln \left( \frac{R}{r_c} \right) + E_c(\theta)|_{r_c} \end{aligned} \quad (2.2)$$

That is, a term  $K(\theta) \ln(r_c/b)$  is subtracted from the elastic energy and added to the core energy; the total energy remains unchanged.

A schematic of the simulation setup is shown in Figure 2.1. The atomistic simulation model is a cylindrical disk of outer radius  $R_{\max}$  aligned along the dislocation line direction. Periodic boundary conditions are imposed along the dislocation line direction. Fixed displacement boundary conditions are applied to atoms on an outer annulus of the cylindrical disk. Specif-

ically, to the cylinder of radius  $R_{\max}$  we add an annulus of atoms of thickness  $d_{\text{bd}}$  equal to twice the cutoff distance of the chosen interatomic potential. The position of the atoms in this annular domain are held fixed at the positions predicted by the anisotropic elastic solution for a Volterra dislocation at the origin as obtained using Stroh's formalism. The outer boundary condition is thus exactly the field associated with a singular core; differences due to core dissociation are dipolar in nature and so do not affect the boundary conditions if  $R_{\max}$  is large enough. All atoms within  $R_{\max}$  are then relaxed fully to their zero-force positions, yielding the minimum-energy structure for the dislocation.

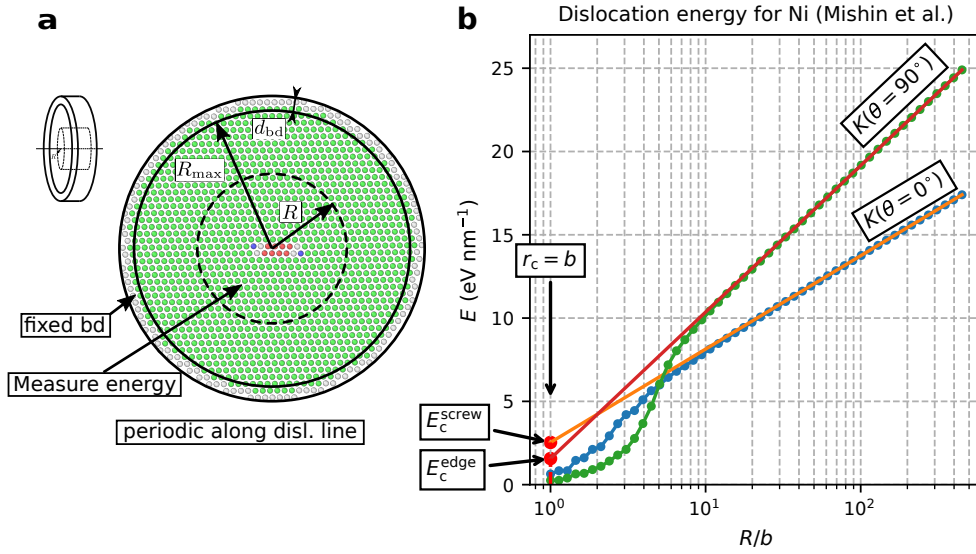


Figure 2.1 – (a) Schematic of the simulation model with simulation size  $R_{\max} + d_{\text{bd}}$ , outer boundary layer thickness  $d_{\text{bd}}$ , and radius  $R$  for measuring energy, as indicated. This is an artificially small  $R_{\max}$  used only to show actual atoms, which are colored using common neighbor analysis so that the dissociated core of the fcc edge dislocation is evident at this scale. (b) Total energy within radius  $r \leq R$  for screw and edge dislocations computed using the Mishin Ni EAM potential [76]. The dislocation core energy at cutoff  $r_c = b$  is obtained by extrapolating the elastic response at large  $R$  back to  $R = b$ , as indicated.

The details of the atomistic calculations are as follows. We measure the total atomic energy of those atoms within radius  $R$  as a function of  $R$  measured from the geometrical center of the dislocation core. We compute the energy at 50 different values of  $R$  from  $b$  to, typically,  $R_{\max} = 450b$  with equal spacing in  $\ln(R/b)$ . At each  $R$ , there are  $N$  atoms within  $R$  and we subtract the reference total energy  $NE_0$  where  $E_0$  is the energy per atom of an unstrained fcc crystal (the cohesive energy). The resulting total dislocation energy in the region  $r \leq R$  is then obtained. In Figure 2.1 an example demonstrating the energy versus  $\ln(R/b)$  for screw and edge dislocations in Ni obtained using the Mishin potential [76] is shown.

According to elasticity theory (2.1), for  $R$  much larger than the core region, the total energy versus  $\ln(R/b)$  should be linear with a slope of precisely  $K(\theta)$ . The measured slopes computed



## 2.2. Atomistic Calculation of Dislocation Core Energies

from the simulation results at radius  $R$ , using the last 10 points including  $r = R$ , are shown in table 2.1 for various  $R$ . For  $R = 100b$ , the error in  $K(\theta)$  is  $\approx 1\%$ , decreasing to  $\approx 0.1\%$  at  $R = R_{\max} = 500b$ . While these errors seem small, it is crucial to recognize that the core energy is obtained by extrapolating back to  $R = b$ , and the error in extracting the core energy is thus greatly magnified. Table 2.1 shows the extrapolated core energy using the  $K(\theta)$  estimated from the simulations at various  $R$ . The core energy converges with increasing  $R$ . Setting the core energy at  $R = 500b$  as a standard core energy, we can compute the error for core energies computed at smaller  $R$ . For the edge dislocation the error in the core energy at  $R = 100b$  is  $\approx 10\%$ . The error reduces to less than 1% at  $R = 400b$ . Thus, it is necessary to use radii of  $450b$  or larger to make accurate core energy estimates. Fortunately, atomistic computations at these sizes are not computationally challenging when using EAM and MEAM potentials.

Table 2.1 – Elasticity coefficient  $K(\theta)$  and estimated dislocation core energy as a function of radius  $R$ , for edge and screw dislocations using the Mishin Ni EAM potential (Mishin et al. [76]). At each  $R$ , the  $K(\theta)$  is computed by measuring slope of the the last 10 points in the energy plot and is compared to the exact value predicted by anisotropic elasticity. The estimated core energy evaluated at cutoff  $r_c = b$  is shown for each  $R$ , showing the convergence of the core energy to a reliable value at the largest  $R$  values.

$R_{\max}$ (b)	$\theta = 90^\circ$			$\theta = 0^\circ$		
	$K(\theta)/(b^2/4\pi)$ (GPa)	$K(\theta)$ error	$E_c(\theta)$ (eV/nm)	$K(\theta)/(b^2/4\pi)$ (GPa)	$K(\theta)$ error	$E_c(\theta)$ (eV/nm)
100	124.966	0.88 %	1.193	79.827	1.02 %	1.797
200	124.464	0.48 %	1.254	79.326	0.39 %	1.859
300	124.275	0.33 %	1.282	79.181	0.20 %	1.880
400	124.180	0.25 %	1.297	79.113	0.12 %	1.891
500	124.086	0.17 %	1.313	79.069	0.06 %	1.899
elasticity	123.870	–	–	79.019	–	–

Extending the analysis across the full range of dislocation character angles, we use a simulation system size  $R_{\max} = 450b$  to achieve sufficient accuracy for  $E_c(\theta)$ . For each character angle, the appropriate periodic distance along the dislocation line must be determined from crystallography and used, increasing the size of the atomistic system. Nonetheless, the maximum number of atoms in any simulation in this chapter is 15 million atoms for character angle at  $47.8^\circ$ , still computationally accessible. The computed total energy versus  $\ln(R/b)$  for all character angles studied here is shown for Ni in Figure 2.2.

Extrapolation using the slope  $K(\theta)$  yields the associated core energy for each character angle as shown in Figure 2.3 for the Mishin Cu, Ni, and Al potentials [76] and the Ercolessi-Adams Al potential [32]. The general trends are similar across the different metals. The behavior observed for the Mishin Al potential is notably different from those of the other three potentials, however. This suggests that this potential should be used with caution for the intermediate character angles and especially the commonly-studied  $30^\circ$  case. For Cu, the screw core energy

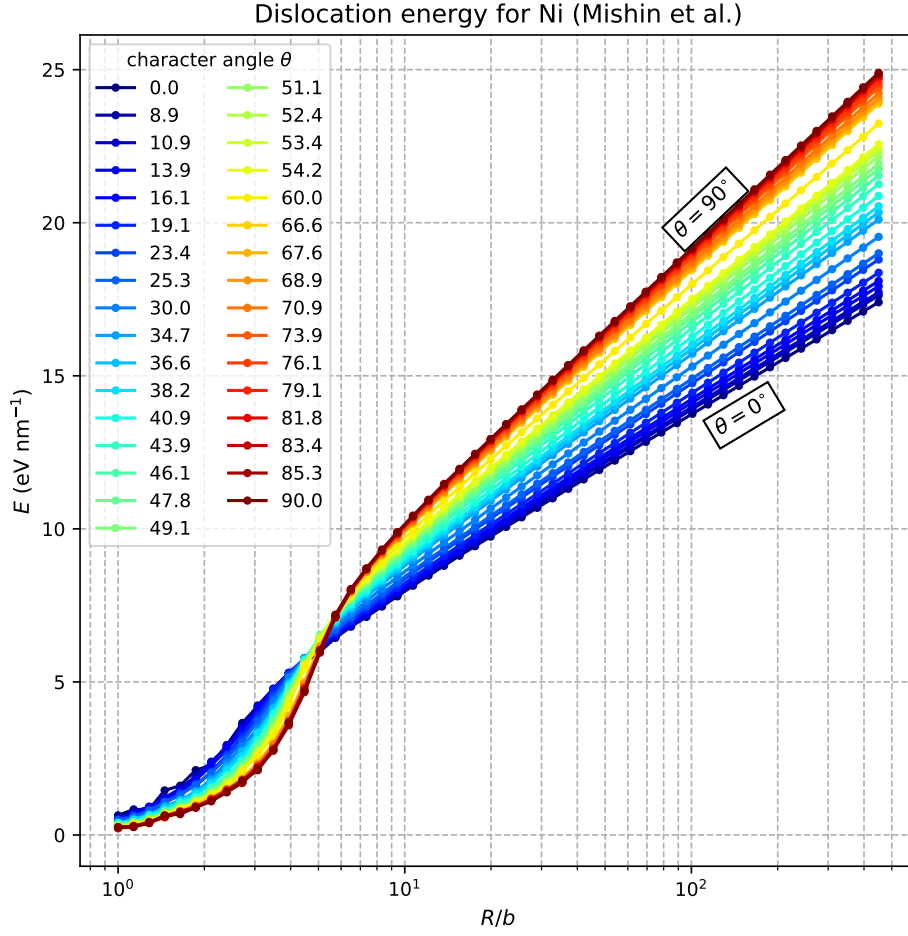


Figure 2.2 – Total dislocation energy versus radius  $R \leq 450b$  for 33 different dislocation character angles (units in degrees), using the Mishin EAM Ni potential (Mishin et al. [76])

at  $r_c = b$  is negative but this has no physical importance as it is simply the correction needed, as a core energy, to ensure that the total dislocation energy is identical to the atomistic result. Selecting a larger cutoff  $r_c > b$  would render the core energy positive as shown in (2.2) with no change in total energy or physics of the problem. The magnitudes of the core energies differ, but the screw core energies at  $r_c = b$  scale roughly with the shear moduli of the different metals. In the DDD code ParaDiS, the default core energy is  $\mu b^2 / 4\pi \ln(r_c / 0.1b) (\cos^2 \theta + \sin^2 \theta / (1 - \nu))$  [38]. Table 2.2 shows the atomistic and ParaDiS core energies for screw and edge dislocations at  $r_c = b$ . The differences are significant, especially for the edge dislocations. The non-singular theory in ParaDiS has additional core energy contributions as discussed in detail below, so the comparison in Table 2.2 is not a precise quantitative comparison but the significant differences strongly motivate improved core models for ParaDiS calibrated to atomistics, which is a main focus of this chapter.

For a compact representation of the core energies, Figure 2.3 also shows numerical fits to the

## 2.2. Atomistic Calculation of Dislocation Core Energies

Table 2.2 – Comparison of the atomistic core energy with the default core energy in ParaDiS.

(eV/nm)	$\theta = 0^\circ$		$\theta = 90^\circ$	
	atomistic	ParaDiS	atomistic	ParaDiS
Cu Mishin[76]	1.071	3.088	-0.044	5.314
Ni Mishin[76]	2.535	5.312	1.566	8.472
Al Ercolessi-Adams[32]	0.810	2.862	0.463	4.370
Al Mishin[76]	1.262	2.609	1.198	4.020

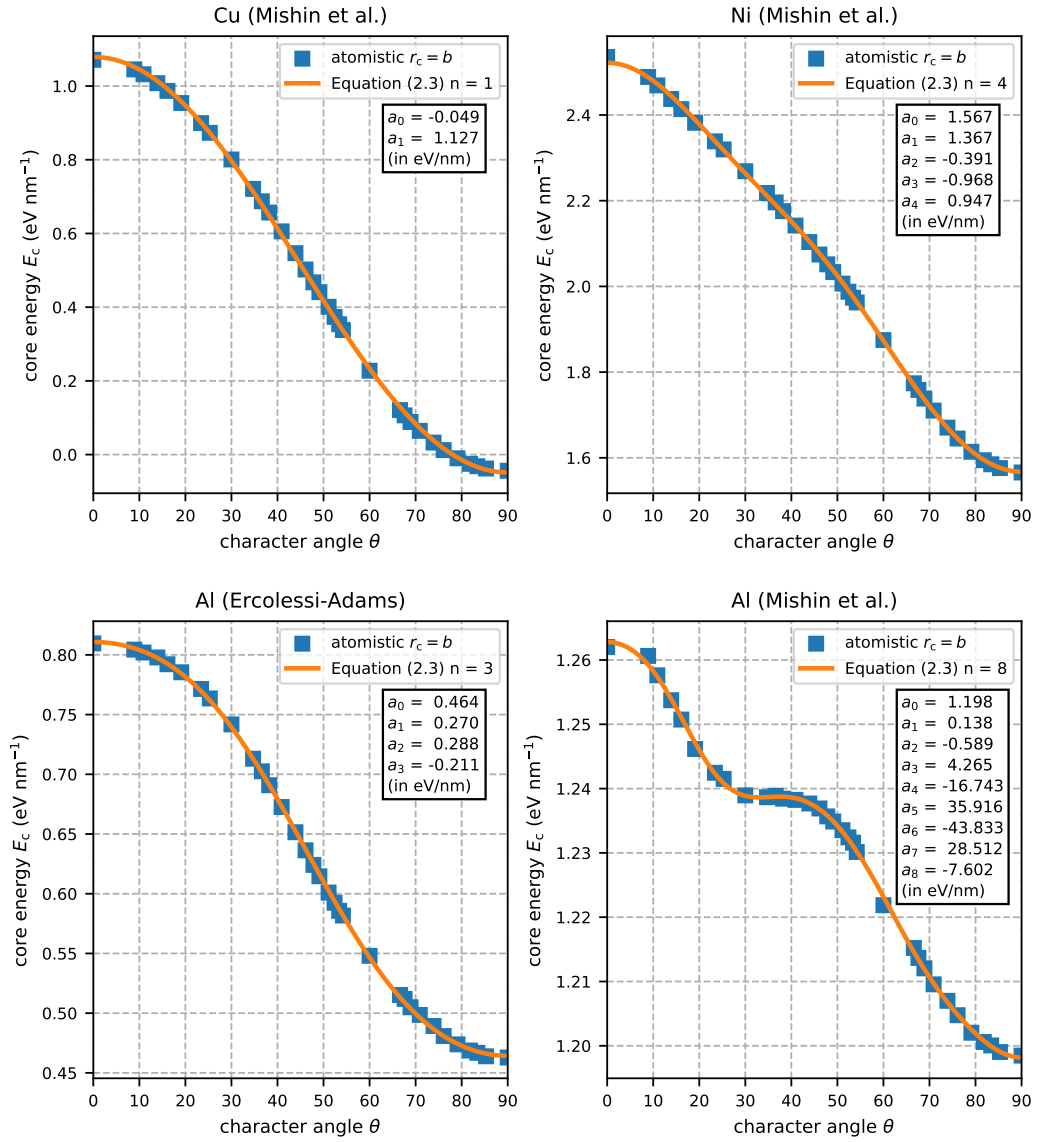


Figure 2.3 – Atomistic core energy for the full dislocation at cutoff  $r_c = b$  for Cu, Ni, and Al metals as a function of character angle. The solid line shows a fit to an approximate form (2.3) with coefficients  $a_i$ ,  $i = 0 \dots n$  as indicated.

atomistic core energies at  $r_c = b$  using a form consistent with the symmetries of the problem [45] as

$$E_c^{\text{fit}}(\theta) = a_n(\cos^2 \theta)^n + a_{n-1}(\cos^2 \theta)^{n-1} + \dots + a_0 \quad (2.3)$$

The non-zero coefficients in the fit for each material are indicated in each figure. The simple decomposition of the core energy into screw and edge components as  $E_c^{\text{fit}}(\theta) = E_s \cos^2 \theta + E_e \sin^2 \theta$  might be valid for some potentials, e.g. the Cu Mishin potential, but the more precise functional form of (2.3) easily obtained and is generally needed to capture the curvature of core energy, which contributes to the line tension (see section 2.3).

### 2.3 Atomistic Core Contributions to Dislocation Line Tension

The behavior of curved dislocations is often discussed using the concept of line tension. The line tension of a dislocation is often interpreted simply as a force per unit line length of dislocation due to the change of dislocation geometry. Such an approximate concept is very useful for baseline analytic models of moderately complex dislocation geometries, capturing the general scaling of behavior versus total dislocation length. Strictly, the line tension is a configurational force for a given dislocation geometry. As such, the line tension is defined as the change of dislocation energy with respect to the change in dislocation length due to an infinitesimal change in the dislocation geometry while maintaining an overall parametric configuration of the dislocation. Denoting the dislocation geometry by the configuration label  $X$ , the line tension  $T_X$  is expressed in terms of the change in total dislocation energy  $W$  divided by the change of total dislocation length  $L$ ,

$$T_X = \frac{\delta W}{\delta L} \quad (2.4)$$

A proper line tension is thus defined for each specific type of dislocation geometry  $X$  (e.g. circular loop, small triangular bow-out, small sinusoidal bow-out) [50]. If a dislocation geometry is composed of different parts, the change in total dislocation energy  $W$  involves changes in the self energy of each part plus the elastic interactions among the different parts. In previous work, the line tension was evaluated in the context of elasticity theory accounting only for the change in total elastic dislocation energy. The change in dislocation core energy is often neglected. However, an accurate line tension requires the contribution due to the core energy. This was recently confirmed [44] by analyzing the thermal fluctuations of dislocations in MD simulations. This work showed that the fluctuation spectra can be explained using linear elasticity for the long-range interactions supplemented by a core line tension to account for short-range core effects.

If the interaction energy is neglected, the line tension of a geometry can be expressed using

### 2.3. Atomistic Core Contributions to Dislocation Line Tension

the self energy of a dislocation per unit length  $E$  as

$$T_{\text{self}} = E + \frac{\partial^2 E}{\partial \theta^2} \quad (2.5)$$

A standard derivation can be found in [49], and a more general derivation is given in [64]. Since the dislocation core energy  $E_c$  is one component of the dislocation self energy, the core energy contribution to the dislocation line tension is

$$T_c = E_c + \frac{\partial^2 E_c}{\partial \theta^2} \quad (2.6)$$

The core energy contributions to the line tension for the materials studied here are shown in

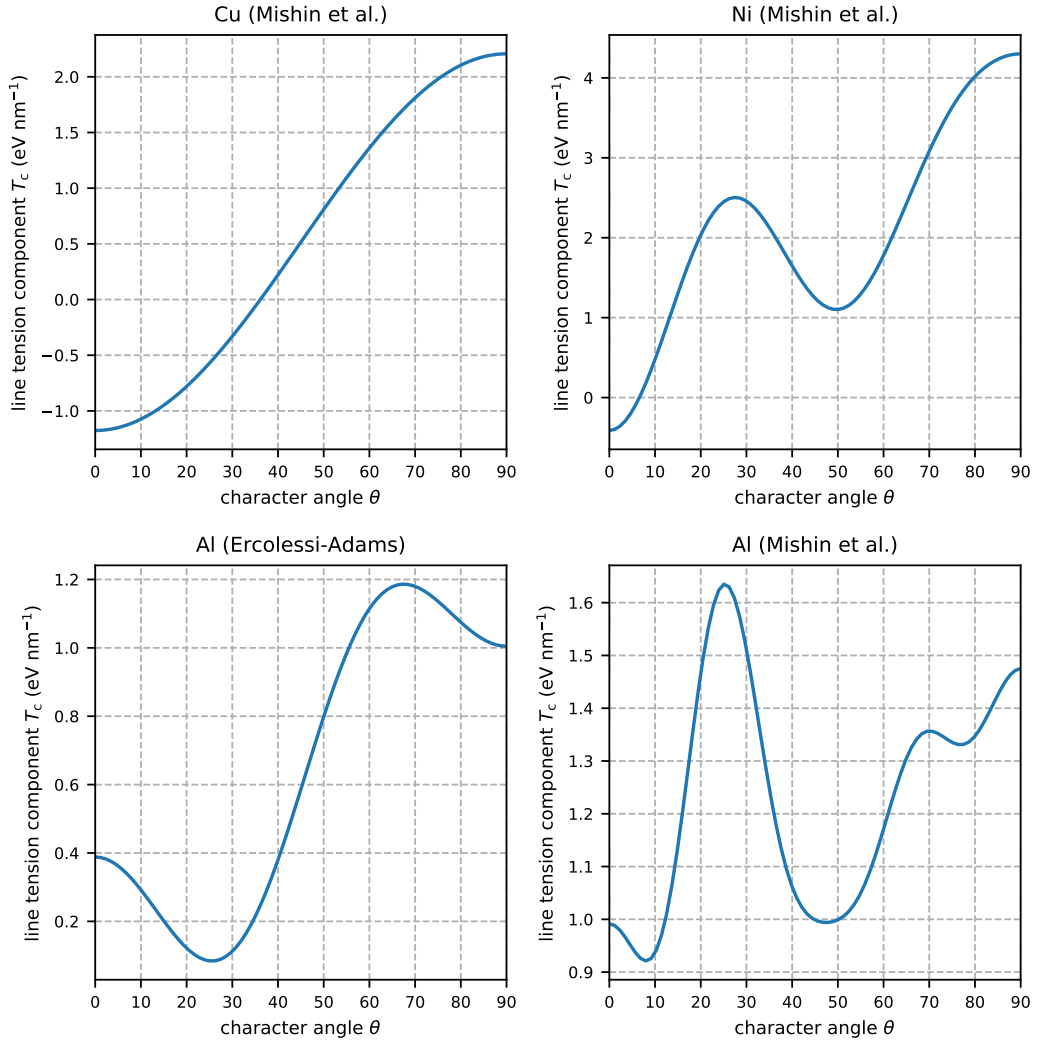


Figure 2.4 – Line tension calculation using (2.6) and the core energy approximation in (2.3) with the fitted parameters given in Figure 2.3. The cutoff radius is  $r_c = b$ .

Figure 2.4. We see that the line tension contribution from the core energy can vary substantially in magnitude as the dislocation character is varied, and can be a rather complex function of the character angle. Importantly, even when the core energy might be reasonably described by the decomposition  $E_c^{\text{fit}}(\theta) = E_s \cos^2 \theta + E_e \sin^2 \theta$  (e.g. Ni, Al), the line tension contribution from core energy can have a more complex dependence on character angle due to the inclusion of the curvature of the core energy expressed in (2.6). These results pertain to the chosen cutoff  $r_c = b$ . Increasing the cutoff distance embeds more “elastic” energy into the “core energy”. These elastic contributions scale with  $K(\theta) \ln(r_c/b)$  (see (2.2)) and so make the core contribution increasingly follow the trend of the elastic term with  $K(\theta)$ . However, the underlying dependence of the total line tension on the core contribution computed at  $r_c = b$  (Figure 2.4) does not disappear.

To examine the relative importance of the core and elasticity contributions to the line tension at  $r_c = b$ , we consider the periodic sinusoidal bow-out geometry. This geometry was studied by Lothe [68] for a Volterra dislocation in an isotropic elastic material; a more general derivation is presented in the supplement of [44] within a non-singular theory. The elastic contribution to the line tension is

$$T_{\text{elas}}^{\text{sine}} = \frac{\mu b^2}{4\pi(1-\nu)} \left[ 2(1-\nu \sin^2 \theta) \ln \left( \frac{L}{2\pi e^{\gamma_0} \rho} \right) - (1-\nu \cos^2 \theta) \ln \left( \frac{L}{2\pi e^{\gamma_0-1/2} \rho} \right) \right] \quad (2.7)$$

where  $\gamma_0$  is the Euler-Mascheroni constant and  $e^{\gamma_0} \approx 1.78$ . To relate eq. (2.7) to our atomistic analysis, the interaction cutoff  $\rho$  must be set to  $\rho = \frac{1}{2} r_c$  [49]. To make a quantitative comparison, we consider the Al Mishin potential [76] with isotropic shear modulus  $\mu_s = 28.7$  GPa and Poisson’s ratio  $\nu_s = 0.348$  (see Section 2.5) and typical dislocation densities of deformed metals of  $10^{12} \sim 10^{15} \text{ m}^{-2}$  corresponding to dislocation lengths between forest intersections of  $30 \sim 1000$  nm. For the edge dislocation, the relative contribution of the core energy to the elastic energy,  $T_c/T_{\text{elas}}^{\text{sine}}$ , is 2.11 at 30 nm and 0.57 at 1000 nm. Thus the core contribution for the edge is significant over the entire range of metallurgically-relevant lengths and strengthening processes (see, for instance, [121]). For screw dislocation, the core contributions are 0.15 at 30 nm and 0.07 at 1000 nm, and so are less important in general. Thus, if accurate predictions for metallurgical plasticity phenomena are to be made using dislocation-based analyses, the contribution of the core energy is essential.

## 2.4 Calibrating Non-singular Theory to Atomistic Core Energies

With the importance of the core energy established, we now address how to calibrate the non-singular dislocation theory of Cai et al. [20] that is implemented in the DDD code ParaDiS to the “true” atomistic result.

A non-singular isotropic theory was proposed by Cai et al. [20] to eliminate the energy and stress divergences at the singular core of the Volterra dislocation. This was accomplished by assuming that the dislocation Burgers vector is spatially distributed over all space according

to a radial distribution function  $\tilde{w}(r; a)$  satisfying

$$\mathbf{b} = \int \mathbf{b} \tilde{w}(r; a) d^3\mathbf{x} \quad (2.8)$$

where  $a$  is introduced as the regularizing length scale that characterizes the spread of the Burgers vector. The stress field due to the Burgers vector distribution  $\tilde{w}(\mathbf{x}; a)$  is then expressed as the convolution of  $\tilde{w}(\mathbf{x}; a)$  with the classical Volterra solution  $\sigma_{\alpha\beta}(\mathbf{x})$  as

$$\tilde{\sigma}_{\alpha\beta}(\mathbf{x}; a) = \int \sigma_{\alpha\beta}(\mathbf{x} - \mathbf{x}') \tilde{w}(\mathbf{x}'; a) d^3\mathbf{x}' \quad (2.9)$$

In DDD simulations, the chief quantity of interest is not the local stress but the interaction force between different dislocation segments. In non-singular theory, this involves the interaction between the two spread cores and thus, a double convolution. The associated stress field  $\sigma_{\alpha\beta}^{\text{ns}}$  that yields the correct Peach-Koehler force,  $d\mathbf{F} = \sigma^{\text{ns}} \mathbf{b} \wedge d\mathbf{L}$  on an elementary segment  $d\mathbf{L}$  of a dislocation of Burgers vector  $\mathbf{b}$ , is called the non-singular field, and is given as [20]

$$\sigma_{\alpha\beta}^{\text{ns}}(\mathbf{x}) = \int \sigma_{\alpha\beta}(\mathbf{x} - \mathbf{x}') w(\mathbf{x}'; a) d^3\mathbf{x}' \quad (2.10)$$

where  $w(\mathbf{x}; a)$  is the convolution of  $\tilde{w}(\mathbf{x}; a)$  with itself, i.e.

$$w(\mathbf{x}; a) = \int \tilde{w}(\mathbf{x} - \mathbf{x}'; a) \tilde{w}(\mathbf{x}'; a) d^3\mathbf{x}' \quad (2.11)$$

An analytical expression for  $w(\mathbf{x})$  was derived as [20]

$$w(\mathbf{x}; a) = \frac{15}{8\pi a^3 (r^2/a^2 + 1)^{7/2}} \quad (2.12)$$

and analytic results for the non-singular stress fields of edge, screw and linear combinations of any dislocation character could also be obtained.

The elastic energy of a dislocation is computed, with  $S_{ijkl}$  the compliance tensor, as

$$E = \frac{1}{2} \int S_{ijkl} \tilde{\sigma}_{ij} \tilde{\sigma}_{kl} dv \quad (2.13)$$

This requires the stress field  $\tilde{\sigma}_{\alpha\beta}$  rather than the non-singular field,  $\sigma_{\alpha\beta}^{\text{ns}}$ . An exact analytic form for  $\tilde{w}(\mathbf{x}; a)$  and thus  $\tilde{\sigma}_{\alpha\beta}$  is not available. However, it was found [20] that a very good analytic approximation to  $\tilde{w}(\mathbf{x}; a)$  is

$$\tilde{w}(\mathbf{x}; a) \approx (1 - m) w(\mathbf{x}; a_1) + m w(\mathbf{x}; a_2) \quad (2.14)$$

with  $a_1 = 0.9038a$ ,  $a_2 = 0.5451a$ ,  $m = 0.6575$ . Therefore, using (2.14) in (2.9) and noting the definition in (2.10),  $\tilde{\sigma}_{\alpha\beta}(\mathbf{x})$  is approximated as

$$\tilde{\sigma}_{\alpha\beta}(\mathbf{x}; a) \approx (1 - m) \sigma_{\alpha\beta}^{\text{ns}}(\mathbf{x}; a_1) + m \sigma_{\alpha\beta}^{\text{ns}}(\mathbf{x}; a_2) \quad (2.15)$$

## Chapter 2. Dislocation Core Energies

With the analytical solutions for  $\sigma_{\alpha\beta}^{\text{ns}}$  of the infinite straight non-singular dislocations in hand, the approximation for  $\tilde{\sigma}_{\alpha\beta}(\mathbf{x})$  can be computed. For the screw dislocation, the non-singular stress field is

$$\sigma_{\theta z}^{\text{ns}} = \frac{\mu b}{2\pi} \frac{r}{\rho_a^2} \left( 1 + \frac{a^2}{\rho_a^2} \right) \quad (2.16)$$

where  $\rho_a = \sqrt{x^2 + y^2 + a^2}$ . Employing the relation (2.15),  $\tilde{\sigma}_{\theta z}$  can be computed and the non-singular energy per unit length follows as

$$E(\theta = 0^\circ) = \int_0^R \frac{(\tilde{\sigma}_{\theta z})^2}{2\mu} 2\pi r dr = \frac{\mu b^2}{4\pi} \left[ \ln\left(\frac{R}{a}\right) + 0.49445 \right] \quad (2.17)$$

The final result is given for the proper limiting case  $R \gg a$ . For the edge dislocation, the total energy is calculated using a similar procedure as

$$\begin{aligned} E(\theta = 90^\circ) &= \int_0^R r dr \int_0^{2\pi} d\theta \left[ \frac{1}{2\mu} \tilde{\sigma}_{xy}^2 + \frac{1}{2\mu(1+\nu)} \left( \tilde{\sigma}_{xx}^2 + \tilde{\sigma}_{yy}^2 - 2\nu \tilde{\sigma}_{xx} \tilde{\sigma}_{yy} - \tilde{\sigma}_{zz}^2 \right) \right] \\ &= \frac{\mu b^2}{4\pi(1-\nu)} \left[ \ln\left(\frac{R}{a}\right) + \frac{0.24445 - 0.25\nu - 0.49445\nu^2}{1-\nu^2} \right] \end{aligned} \quad (2.18)$$

The leading terms for each case coincide with the elastic strain energy obtained from the classical Volterra solution with cutoff  $r_c = a$ . There is then an additional constant energy for both (2.17) and (2.18); within the general formulation of equation (2.2), this constant could be interpreted as an effective core energy embedded in NS theory that is associated with the regularization of the core region.

In the singular and non-singular isotropic theories, the dislocation energy for any character angle can be decomposed into screw and edge components. So only the above results for the screw and edge dislocation are required to consider all character angles. As noted earlier, ParaDiS allows for an additional core energy term proportional to the elastic energy [38] but we have seen above that this term itself does not match atomistics. Furthermore, this term was found insufficient for capturing the behavior for the bow-out of atomistic dislocations [118].

The non-singular dislocation energy follows the general form of (2.1). Taking the regularization parameter  $a$  equal to the cutoff radius  $r_c$ , the total energy of an infinite straight dislocation line in non-singular theory can be made to match the atomistic result by adding the true atomistic core energy while subtracting the additional constant energy appearing in non-singular theory. Operationally, we add a core energy correction to the non-singular energy of

$$\begin{aligned} E_c^{\text{corr}}(\theta) &= E_c|_{r_c}(\theta) - K(\theta) \ln\left(\frac{r_c}{a}\right) - \left( \frac{0.49445\mu b^2}{4\pi} \right) \cos^2 \theta \\ &\quad - \left( \frac{\mu b^2}{4\pi(1-\nu)} \frac{0.24445 - 0.25\nu - 0.49445\nu^2}{1-\nu^2} \right) \sin^2 \theta \end{aligned} \quad (2.19)$$

with  $E_c|_{r_c}(\theta)$  expressed with  $E_c|_b(\theta)$  as in (2.2), where  $E_c|_b(\theta)$  is represented using (2.3).



With this correction, the total energy of the non-singular theory matches the true atomistic energy. We introduce the above correction by revising the definition of the core energy function in ParaDiS using the functional form for the atomistic core energy shown in Figure 2.3. In the actual implementation, we modified the self force due to the core energy accordingly.

## 2.5 Validation of Atomistically-informed DDD: Dislocation Bow-out

We now examine a canonical dislocation problem, periodic dislocation bow-out, to assess the accuracy of DDD relative to full atomistic simulations for curved dislocations. We use the non-singular theory as implemented within the ParaDiS code [7] but augmented with the atomistically-informed core energy via the correction of (2.4).

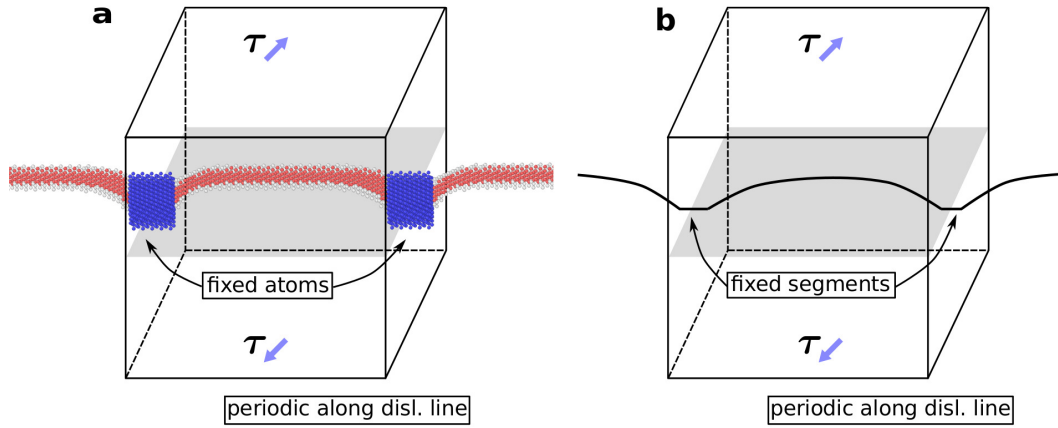


Figure 2.5 – Atomistic bow-out simulation (a) is carried out with a multiscale scheme [93], while the DDD simulations (b) are performed in a large simulation box with periodic boundary condition along the dislocation line. The dislocation bows out in the slip plane rendered in gray in the figures. In the schematic atomistic simulation the atoms are colored by common neighbor analysis showing the stacking fault, partial dislocations and the fixed atoms; note that the schematic is not to scale.

The geometry of the bow-out problem is shown schematically in Figure 2.5. In the atomistic simulations, a single dislocation is pinned periodically by fixing a small group of atoms at the zero-stress core structure. The system is then subjected to an applied shear stress, which causes the dislocation to bow-out in between the pinning points. The simulations were reported previously [118], and were performed in a multiscale simulation that eliminates all spurious image forces that can arise in finite-size periodic simulations [93, 117]; key details are as follows. Creation of a dislocation in the atomistic region of the multiscale simulation is achieved by displacing all atoms according to the Volterra solution and then relaxing the entire multiscale system under zero displacements on the outer boundary of the system. Loading is then applied by imposing displacement boundary conditions on the outer surface of the continuum region to create the desired homogeneous pure shear stress acting on the glide plane in the direction of glide. The simulations are performed using explicit dynamics at  $T=0K$ .

The pinning obstacles in the bow-out problem are created by fixing all atoms within a small cubic volume  $1 \text{ nm}^3$  centered on the dislocation core and with periodicity  $L$ . The interactions of the dislocation with these rigid obstacles has been estimated to be equivalent to an applied shear stress of less than 3 MPa [118], which is small relative to the loads applied here. The full shape of the bowed-out dislocation is measured at each applied load, for both initial screw and edge dislocations. The center line of the dislocation is then determined as the mid-point between the centers of the two partial dislocations identified using the common neighbor analysis. The corresponding DDD problem is also shown in Figure 2.5. The fixed atoms of the atomistic simulation are replaced by fixed segments of dislocation. The remaining dislocation line can bow-out in response to the applied load.

The bow-out geometry seems to be a clean geometry for measuring significant changes in dislocation curvature, and thus testing the accuracy of DDD across a range of dislocation character angles. The line tension also generally scales linearly with the maximum bow-out, enabling differences in bow-out to be interpreted in terms of approximate differences in line tension. A similar bow-out geometry was recently used [44] to test the measurement of the core line tension at finite temperature from the thermal fluctuations of straight dislocations. The simulation were, however, carried out only in the range of small bow-out amplitudes induced by thermal fluctuations.

Current DDD codes based on analytical expressions of dislocation interactions are mainly limited to elastically isotropic materials. Cubic metals are generally elastically anisotropic, and so direct comparisons between atomistic simulations and DDD are best performed for nearly-isotropic atomistic models. For this reason, our comparison is restricted to Aluminum modeled with two EAM potentials, [32] and [76]. For both potentials the Zener anisotropy  $A = 2C_{44}/(C_{11} - C_{12})$  values are  $A=1.31, 1.21$  respectively. Al is thus fairly isotropic and the effects of anisotropy may be modest. Future studies using a new anisotropic version of ParaDiS or DDD frameworks based on eigenstrains [12] can avoid this small difference and extend the study to strongly anisotropic systems such as Ni and Cu. Here, for DDD, we must select appropriate isotropic elastic constants for the weakly-anisotropic Al. We employ the Scattergood and Bacon effective material moduli [106] defined as  $\mu_s = 4\pi K(0^\circ)/b^2$  and  $\nu_s = 1 - K(0^\circ)/K(90^\circ)$ . This estimate has been investigated recently [119] and shown to reproduce well the line tension of straight dislocations with different characters.

The non-singular DDD method also involves the regularization parameter  $a$ . For consistency of the energies in DDD with those of the atomistic simulations, this parameter must be taken equal to the cutoff parameter  $r_c$  used in the calibration of the atomistic core energy, which sets the partition between the elastic and core contributions to the dislocation energy. We use the atomistic core energy determined at  $r_c = b$  and then, for any choice of  $a$ , we set  $r_c = a$  and use the relation in (2.2) to get the corresponding core energy at  $r_c = a$ , then we correct it using (2.4) for NS theory (notice that  $r_c = a$  gives no  $K(\theta) \ln(r_c/a)$  term). For a straight dislocation, this partitioning is artificial; the total energy is preserved for any choice of  $r_c = a$ . However, for curved dislocations, the choice of  $a$  may affect the short-range interactions between

dislocation segments and so may therefore affect the equilibrium dislocation geometry. In addition, non-asymptotic terms (e.g. higher order terms as  $\frac{a^2}{R^2}$ ) in the total energy may enter into the DDD problem. In the following section, we thus probe these features numerically by investigating the effect of different regularization parameters  $a$  on the predicted dislocation bow-out. Setting  $a = r_c$  in ParaDiS and introducing the atomistic core energy as in (2.4), we predict the bow-out in DDD for four values of  $a$  ( $a = b, eb, 2eb, 4eb$ , where  $e = 2.713$  is the natural logarithm base) to include the value  $a = eb$  considered in earlier work [118].

In most cases, deviations between atomistic and ParaDiS DDD simulations are due to a sharper angle predicted by DDD near the pinning points. In these regions, the dislocation shape is influenced by the periodic interactions with nearby segments, which may be influenced by dislocation partial dissociation distance and the DDD treatment of the dislocation as a perfect dislocation. Also, fixing the atomic positions in the pinning regions of the atomistic simulations disrupts locally the elastic behavior of the medium and may affect the way the dislocation segments interact on either side of the obstacles. These details cannot be resolved, and we thus focus attention more on the overall extent of bow-out.

Results for the Ercolessi-Adams potential are shown in Figures 2.6. Overall, the DDD simulations are in good agreement with the atomistic results. The differences in bow-out distance at the peak - which are approximately proportional to the line tension - are typically within 5 Å across all cases. Furthermore, the influence of  $a$  is, overall, fairly small especially at small  $a$ . This indicates that the calibration to the atomistic core energy captures the dominant energetic effects for curved dislocations over a range of curvatures. The agreement for  $a = 2eb$  is perhaps slightly better across all cases relative to other choices. In particular, at the highest load of 73.9 MPa for the screw dislocation, the DDD configuration is unstable for  $a = b$  but is stable and in very good agreement with atomistics for  $a = 2eb$ . Using an even larger value of  $a = 4eb$  leads to less bow-out, i.e. higher line tension, and some underprediction of the bow-out at higher loads. The value  $a = 2eb$  thus provides the best match for the Ercolessi-Adams Al potential. While not directly relevant to the value of  $a$ , the dissociation distances of the current potential are  $3.5b$  and  $7.0b$  for screw and edge bow-out respectively. The best regularization parameter  $a = 2eb$  lies in this range.

For the Mishin potential, similar trends are found as shown in Figure 2.7. There is a deviation for the screw dislocation at stresses only slightly larger than the Peierls stress of the straight screw dislocation; this arises because the operative Peierls stress, based on loading and unloading simulations and discussed in detail by Szajewski et al. [118], is a strong function of the curvature at low curvature (low stress) while the DDD predictions use the operative Peierls stress that is appropriate for higher curvatures. There is also a systematic deviation in the bow-out for the 50 nm edge case, largely independent of  $a$ . The Mishin Al potential has the most unusual core contributions to the line tension (see Figure 2.3), which may contribute somehow to the larger deviations as compared to the EA potential. Otherwise, the dependence of the bow-out on  $a$  remains modest, while the value  $a = 4eb$  provides the best overall agreement with simulations relative to other choices studied, with notably better predictions for the screw

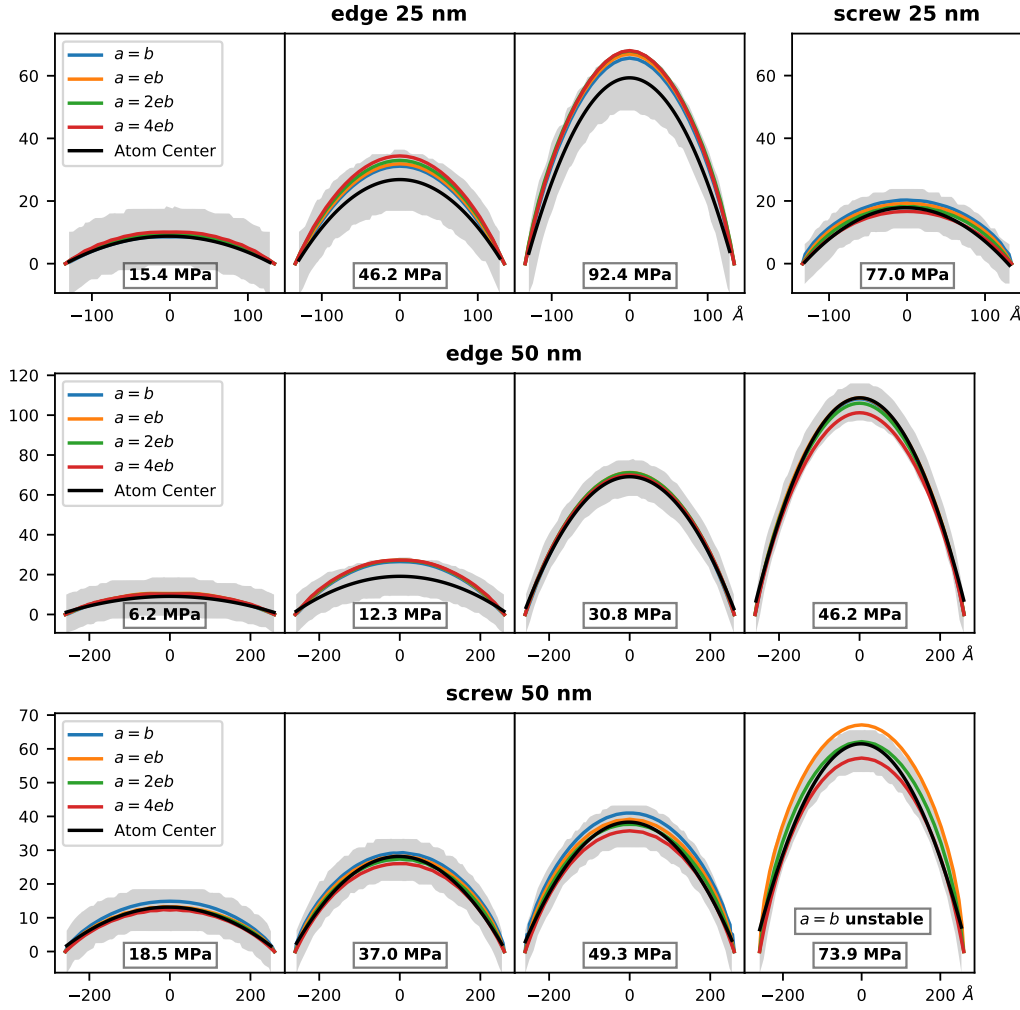


Figure 2.6 – Comparison of atomistic simulations and ParaDiS simulations for the Ercolessi-Adams Al potential [32] using different regularization parameters  $a$  noted on the figure. The grey areas show the stacking faults. Simulations use the effective elastic moduli according to [106]. An optimal  $a = 2eb$  is found for the bow-out problem using this potential.

dislocation across all loads. Using this potential, the dissociation distances are  $3.5b$  and  $6.3b$  for screw and edge bow-out case. The optimal parameter  $a = 4eb$  does not lie in this range, but the results with  $a = 2eb$  also give relative good results and lie within the range of dissociation.

Overall, the regularization parameter  $a$  has a fairly small influence on the dislocation bow-out. This is important because the atomistic simulations and calibration of NS theory do not depend on the value of  $a$ , and so  $a$  cannot be determined. The insensitivity of our results to  $a$  thus implies that reasonable values of  $a$  can be used with limited concern for the creation of significant error. However, as seen here for the bow-out problem, the applied stress at the point of an instability, which may be interpreted as a strength value for some process, may be affected by the choice of  $a$ . For both Al potentials studied here, based on our comparisons

## 2.5. Validation of Atomistically-informed DDD: Dislocation Bow-out

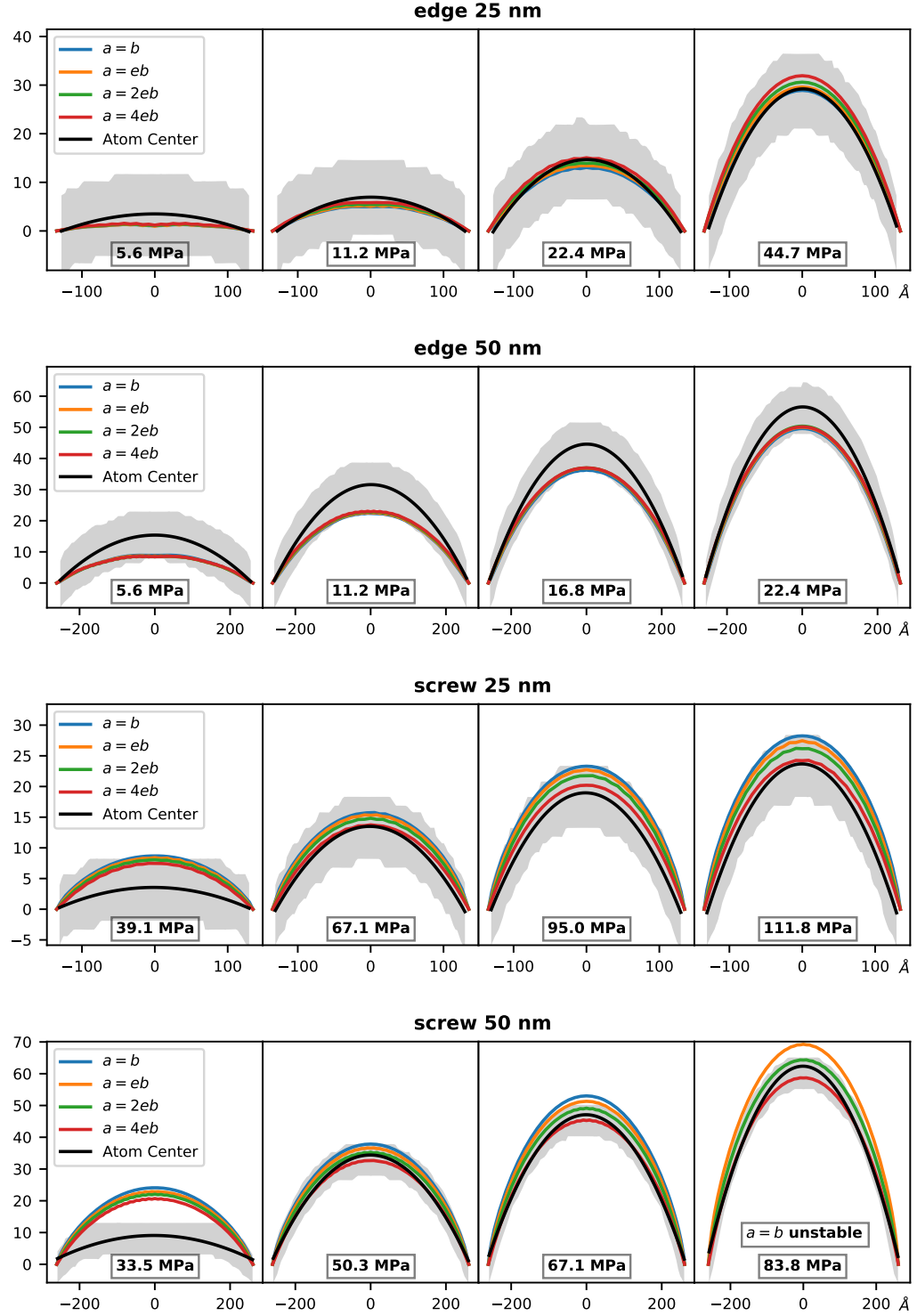


Figure 2.7 – Comparison of atomistic simulations and ParaDiS simulations for the Mishin Al potential [76] using different regularization parameters  $a$  noted on the figure. The grey areas show the stacking fault. Simulations use an effective effective moduli [106]. An optimal  $a = 4eb$  is found for the bow-out problem using this potential. The lower loading cases are strongly influenced by the Peierls stress discussed in [118]. Applying an operative Peierls stress does not give good agreement with atomistics.

with the atomistic simulations, we recommend values of  $a = 2 - 4eb$ .

Analyzing dislocation fluctuations for the Mishin potential at  $T = 300$  K, Geslin et al [44] found optimal values of  $a = 1.2b$  and  $a = 2b$  for screw and edge dislocations, respectively. Since DDD implementations require a single value of  $a$ , independent of the dislocation character, a global optimal value of  $a = 1.25b$  was found to reproduce both the long-wavelength fluctuations and the dislocation bow-out at small applied stresses, at  $T = 300$  K. These optimal values of  $a$  are smaller than found here. However, the fluctuation method involves rather small amplitudes of atomistic bow-out and the finite temperature study likely reduces the relevant Peierls stress. These aspects make direct comparisons between our study and that of Geslin et al. difficult. The relatively weak dependence of our results on the value of  $a$ , especially at small bowouts typical of those used by Geslin et al. suggests that any differences arising between the atomistic calibrations of Geslin et al. and the present work may not have significant quantitative influence on the accurate study of dislocation behaviors at the continuum level.

The results for bow-out here differ substantially from those found previously using the standard ParaDiS core energy implementation as a fitting parameter [118]. Specifically, Szajewski et al. found that fitting of the core energy to the simulations for atomistic edge bow-out then led to very poor predictions of the bow-out for screw dislocations. The details embedded in the atomistic core energy are thus necessary if DDD studies are to be adequately representative of atomistic results.

## 2.6 Calibration of Partial Dislocation Core Energy with NS Theory

In fcc metals, a full dislocation dissociates into two partial dislocations with a stacking fault in between. So far in this chapter, we have considered the energetics of the dissociation process as part of the core energy of the full dislocation. The reason is that DDD studies rarely include the dissociation phenomenon due to the high computational cost of resolving the nanoscale partial separation. However, there are scenarios [100] where it is important to simulate the behavior of individual partial dislocations or the dissociated full dislocation within a DDD framework [75]. Therefore, in this section we compute the atomistic core energy for partial dislocations as a function of partial dislocation character in the context of NS theory.

From (2.17) and (2.18), we write the elastic energy in NS theory for any character angle  $\theta$  as

$$E^{\text{ns}}(\theta) = K^{\text{ns}}(\theta) \ln\left(\frac{R}{a}\right) + C(\theta) \quad (2.20)$$

with the energy factor  $K^{\text{ns}}(\theta)$  and additional term  $C(\theta)$  expressed as

$$K^{\text{ns}}(\theta) = \frac{\mu b^2}{4\pi} \left[ \cos^2 \theta + \frac{\sin^2 \theta}{(1-\nu)} \right], \quad C(\theta) = \frac{\mu b^2}{4\pi} \left[ C_s \cos^2 \theta + \frac{C_e \sin^2 \theta}{(1-\nu)} \right] \quad (2.21)$$

where  $C_s$  and  $C_e$  are the constants in (2.17) and (2.18).

## 2.6. Calibration of Partial Dislocation Core Energy with NS Theory

To derive the partial core energy, we need to calculate the interaction energy of the two partials within NS theory. Following [127], the interaction energy for partials separated by  $r_{12}$  is the work done by the displacement of one partial with partial Burgers vector  $\mathbf{b}_{2p}$  moving against the stress field  $\boldsymbol{\sigma}_{1p}^{\text{ns}}$  of the second partial from large separation  $R$  to separation  $r_{12}$ . We decompose the partial Burgers vector into screw and edge component as  $\mathbf{b}_{2p} = \mathbf{b}_{2ps} + \mathbf{b}_{2pe}$ . From isotropic elasticity, the stress field can be written as  $\boldsymbol{\sigma}_{1p}^{\text{ns}} = \boldsymbol{\sigma}_{1ps}^{\text{ns}} + \boldsymbol{\sigma}_{1pe}^{\text{ns}}$  representing the field associated with the screw and edge components of the Burgers vector. We denote the dislocation line direction as  $\boldsymbol{\xi}$  and employ the stress field of a straight dislocation in [20] to obtain the Peach-Koehler force on the other dislocation. Then the interaction energy can be derived as

$$\begin{aligned} W_{12}^{\text{ns}} &= \int_{r_{12}}^R \left( (\boldsymbol{\sigma}_{1ps}^{\text{ns}} + \boldsymbol{\sigma}_{1pe}^{\text{ns}}) \cdot (\mathbf{b}_{2ps} + \mathbf{b}_{2pe}) \right) \times \boldsymbol{\xi} \cdot d\mathbf{s} \\ &= \frac{\mu b_{1ps} b_{2ps}}{4\pi} \left[ \ln \left( \frac{R^2 + a^2}{r_{12}^2 + a^2} \right) + a^2 \left( \frac{1}{r_{12}^2 + a^2} - \frac{1}{R^2 + a^2} \right) \right] + \frac{\mu b_{1pe} b_{2pe}}{4\pi(1-\nu)} \ln \left( \frac{R^2 + a^2}{r_{12}^2 + a^2} \right) \end{aligned}$$

We note that in equation (2.22) the partial Burgers vectors correspond to  $|\mathbf{b}_{1p}| = |\mathbf{b}_{2p}| = |\mathbf{b}|/\sqrt{3}$ . Combining the logarithm terms in (2.22), we rewrite the interaction energy as

$$W_{12}^{\text{ns}} = K_{12}^{\text{ns}} \ln \left( \frac{R^2 + a^2}{r_{12}^2 + a^2} \right) + C_{p12} \quad (2.22)$$

with the  $K_{12}^{\text{ns}}$  as the prelogarithmic factor and  $C_{p12}$  as the constants due to NS theory.

The total dislocation energy consists of the interaction energy, the stacking fault energy over length  $r_{12}$ , and the partial core energies  $E_{cp}$ . In NS theory, the total energy is thus

$$\begin{aligned} E &= E_{p1} + E_{p2} + W_{12} + \gamma_{\text{sf}} r_{12} \\ &= \left( K_{p1}^{\text{ns}} \ln \left( \frac{R}{a} \right) + C_{p1} + E_{cp1}^{\text{ns}} \right) + \left( K_{p2}^{\text{ns}} \ln \left( \frac{R}{a} \right) + C_{p2} + E_{cp2}^{\text{ns}} \right) \\ &\quad + \left( K_{12}^{\text{ns}} \ln \left( \frac{R^2}{r_{12}^2 + a^2} \right) + C_{p12} \right) + \gamma_{\text{sf}} r_{12} \\ &= K^{\text{ns}} \ln \left( \frac{R}{a} \right) + \left( K_{12}^{\text{ns}} \ln \left( \frac{a^2}{r_{12}^2 + a^2} \right) + \gamma_{\text{sf}} r_{12} + C_{p1} + C_{p2} + C_{p12} \right) + E_{cp1}^{\text{ns}} + E_{cp2}^{\text{ns}} \end{aligned}$$

where (2.20) and (2.22) are used, and we take the appropriate limit of large  $R \gg a$ .

Calculation of the partial core energy in (2.23) requires knowledge of the equilibrium partial dissociation distance  $r_{12}$ . The equilibrium dissociation distance in NS theory minimizes the total dislocation energy, i.e. satisfies  $\frac{\partial E}{\partial r_{12}} = 0$ , leading to

$$-\frac{2K_{12}^{\text{ns}} r_{12}}{r_{12}^2 + a^2} - \frac{\mu b_{1s} b_{2s}}{2\pi} \frac{a^2 r_{12}}{(r_{12}^2 + a^2)^2} + \gamma_{\text{sf}} = 0 \quad (2.23)$$

The NS value for  $r_{12}$  is always smaller than the value  $K_{12}/\gamma_{sf}$  derived from singular theory (obtained by setting  $a = 0$  in NS theory). More importantly, for Al, both the NS and singular theory estimates are not in good agreement with atomistic simulations, as shown in Figure 2.8. Better agreement is obtained for materials with lower stable stacking fault energies, such as Cu and Ni, with correspondingly larger  $r_{12}$  values. Additionally, for these more anisotropic materials, an anisotropic elastic analysis needs to be carried out. However, the difference between atomistic and NS predictions for  $r_{12}$  immediately implies that the derived partial core energies are only effective core energies that include some contributions associated with the stacking fault energy and elastic interactions. However, within the closed system of a DDD simulation using the NS description of partial dislocations, the use of the NS value for  $r_{12}$  is the only self-consistent approach that will also accurately capture the total dislocation energy.

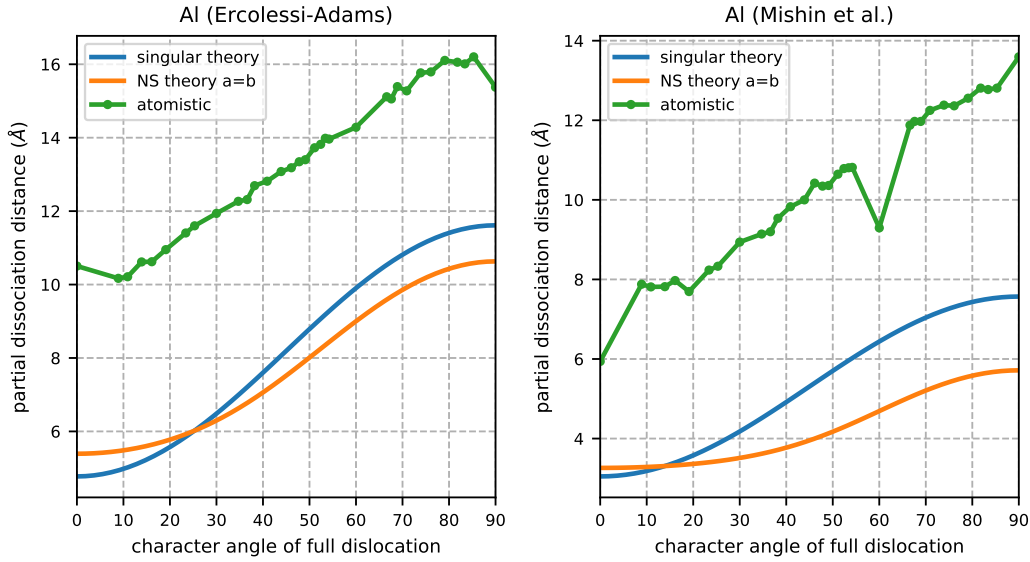


Figure 2.8 – Comparison between the dissociation distance measured in atomistic simulations and predicted from (2.23) with the singular ( $a = 0$ ) and non-singular ( $a = b$ ) theories.

Using the NS dissociation distance and the dissociation geometry shown by the Thompson tetrahedron (Figure 2.9), we reformulate equation (2.23) as

$$E(\theta) = K^{ns}(\theta) \ln\left(\frac{R}{a}\right) + M(\theta) + E_{cp}^{ns}(\theta - 30^\circ) + E_{cp}^{ns}(\theta + 30^\circ) \quad (2.24)$$



## 2.6. Calibration of Partial Dislocation Core Energy with NS Theory

with the notation

$$\begin{aligned}
 M(\theta) &= K_{12}^{\text{ns}}(\theta) \ln \left( \frac{a^2}{r_{12}^2 + a^2} \right) + \gamma_{\text{sf}} r_{12}(\theta) + C_{\text{p1}}(\theta) + C_{\text{p2}}(\theta) + C_{\text{p12}}(\theta) \\
 C_{\text{p1}}(\theta) &= \frac{\mu b^2}{12\pi} \left( C_s \cos^2(\theta - 30^\circ) + \frac{C_e}{1-\nu} \sin^2(\theta - 30^\circ) \right) \\
 C_{\text{p2}}(\theta) &= \frac{\mu b^2}{12\pi} \left( C_s \cos^2(\theta + 30^\circ) + \frac{C_e}{1-\nu} \sin^2(\theta + 30^\circ) \right) \\
 C_{\text{p12}}(\theta) &= \frac{\mu b^2}{12\pi} \left( \frac{a^2}{r_{12}^2 + a^2} \cos(\theta - 30^\circ) \cos(\theta + 30^\circ) \right) \\
 C_s &= 0.49445, \quad C_e = \frac{0.24445 - 0.25\nu - 0.49445\nu^2}{1 - \nu^2}
 \end{aligned} \tag{2.25}$$

Subtracting the overall elastic energy contribution that is independent of the partials and dissociation, the total dislocation core energy is

$$E_{\text{ct}}(\theta) = M(\theta) + E_{\text{cp}}^{\text{ns}}(\theta - 30^\circ) + E_{\text{cp}}^{\text{ns}}(\theta + 30^\circ) \tag{2.26}$$

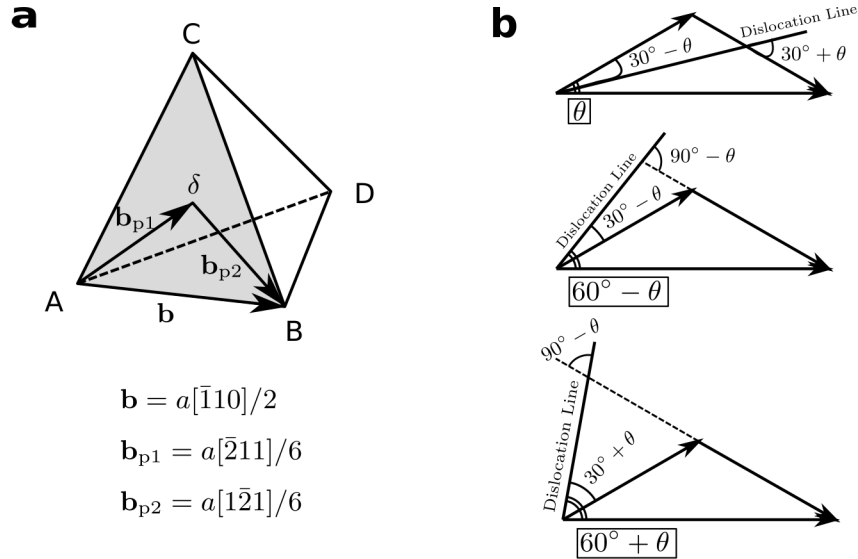


Figure 2.9 – (a) Thompson tetrahedron ABCD. A perfect dislocation with Burgers vector  $\mathbf{b}$  dissociates into two partial dislocations having Burgers vectors  $\mathbf{b}_{\text{p1}}$  and  $\mathbf{b}_{\text{p2}}$  on the same slip plane. (b) Three different perfect dislocation orientations  $\theta$ ,  $(60^\circ - \theta)$  and  $(60^\circ + \theta)$  are used to extract the partial core energies.

To solve for the partial core energy  $E_{\text{cp}}^{\text{ns}}(\theta)$  on the left hand side of (2.26), we examine the dislocation dissociation geometry and search for common partial dislocation orientations. For a dislocation with character angle  $\theta$ , the associated partial dislocations have character angles  $(30^\circ - \theta)$  and  $(30^\circ + \theta)$ . The full dislocation orientations on the right of Figure 2.9 lead to

the following set of equations

$$\begin{aligned}
 E_{\text{cp}}^{\text{ns}}(30^\circ - \theta) + E_{\text{cp}}^{\text{ns}}(30^\circ + \theta) &= E_{\text{ct}}(\theta) - M(\theta) \\
 E_{\text{cp}}^{\text{ns}}(30^\circ + \theta) + E_{\text{cp}}^{\text{ns}}(90^\circ - \theta) &= E_{\text{ct}}(60^\circ + \theta) - M(60^\circ + \theta) \\
 E_{\text{cp}}^{\text{ns}}(30^\circ - \theta) + E_{\text{cp}}^{\text{ns}}(90^\circ - \theta) &= E_{\text{ct}}(60^\circ - \theta) - M(60^\circ - \theta)
 \end{aligned} \tag{2.27}$$

Summing the last two equations in (2.27) and subtracting the first equation, we obtain the partial core energy at character angle  $(90^\circ - \theta)$  as

$$E_{\text{cp}}^{\text{ns}}(90^\circ - \theta) = \frac{1}{2} [E_{\text{ct}}(60^\circ - \theta) + E_{\text{ct}}(60^\circ + \theta) - E_{\text{ct}}(\theta) - M(60^\circ - \theta) - M(60^\circ + \theta) + M(\theta)] \tag{2.28}$$

Substituting  $(90^\circ - \theta)$  with  $\theta$ , we rewrite the above equation as

$$E_{\text{cp}}^{\text{ns}}(\theta) = \frac{1}{2} [E_{\text{ct}}(\theta - 30^\circ) + E_{\text{ct}}(\theta + 30^\circ) - E_{\text{ct}}(90^\circ - \theta) - M(\theta - 30^\circ) - M(\theta + 30^\circ) + M(90^\circ - \theta)] \tag{2.29}$$

In the above derivation, the symmetry and periodicity properties of the dislocation core energy are used, i.e.  $E_{\text{c}}(\theta) = E_{\text{c}}(-\theta)$ ,  $E_{\text{c}}(\theta) = E_{\text{c}}(180^\circ - \theta)$  for both partial and full core energies. Hence with the full core energy approximation in Figure 2.3, the elastic interaction energy factor  $K_{12}^{\text{ns}}$  from (2.22), the solved dissociation estimation  $r_{12}$  in (2.23) and the stable stacking fault energy  $\gamma_{\text{sf}}$ , the NS partial core energy as a function of partial character is computed for the two Al potentials as shown in Figure 2.10.

For comparison, we also compute the partial core energy using the singular theory (Volterra dislocation,  $a = 0$ ). The NS correction additional  $C_{\text{p1}}$ ,  $C_{\text{p2}}$ ,  $C_{\text{p12}}$  vanish and we re-introduce the cutoff radius  $r_{\text{c}}$  as in equation (2.1). Using the dissociation distance from singular theory, we obtain the partial core energy versus character for the two Al potentials as shown in Figure 2.10.

The two approaches yield surprisingly similar core energies for pure edge partials but increasingly different values as the character changes toward pure screw. Neither analysis is preferable over the other - they differ due to the different self-consistent treatments of the dislocation (non-singular and singular) - and both are ultimately calibrated to the correct total energy of the full dislocation.

The inclusion of partial dislocations into DDD simulations may have some implications for dislocation network evolution. Some years ago, the study of dislocation junction structures and their destruction under load [69] showed some agreement between atomistic and DDD predictions. However, the critical resolved shear stresses for junction destruction differed, which may be due to the absence of an atomistically-calibrated core energy in the DDD method. Other work embedding atomistic information into DDD only used the atomistic stacking fault energy investigated in [75] and inclusion of an accurate core energy may further improve the quantitative agreement between atomistic simulations and DDD. However, for anisotropic materials, the full comparison requires the use of an anisotropic DDD code.

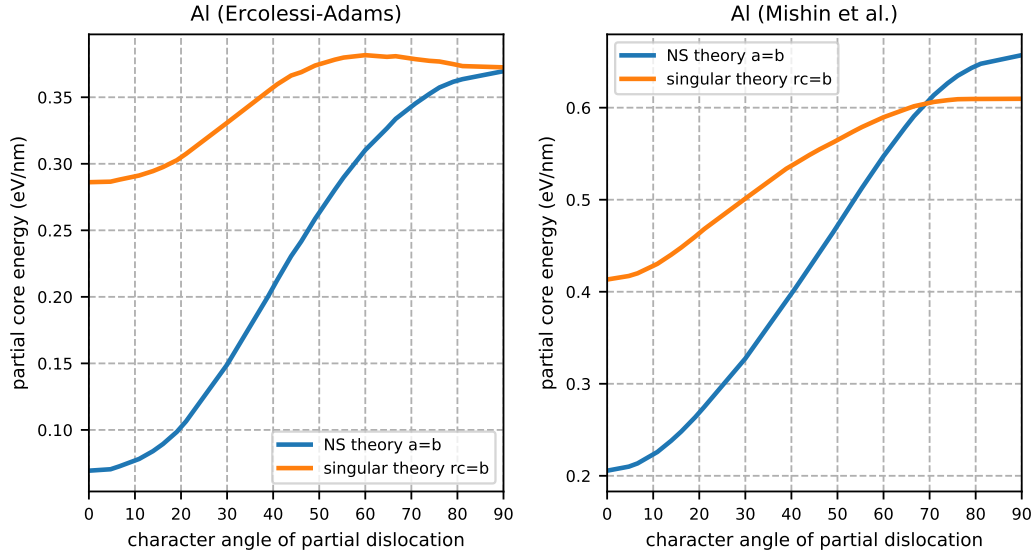


Figure 2.10 – Partial core energy using two Al potentials calibrated from both the singular and non-singular theories. The approximations for the full core energy in Figure 2.3 were used.

## 2.7 Role in Orowan Mechanism

In the above sections we calculated dislocation core energies (both full and partial) and integrated in the non-singular theory based code ParaDiS. The importance of core energy in line tension and matching atomistic simulations is clarified. Now we investigate the role of core energy in the Orowan mechanism. This will later be connected to our study on precipitation strengthening.

### 2.7.1 1D Periodic Simulation Model

A Simple 1D periodic bow-out model is utilized to investigate the effects of dislocation core energy on the Orowan mechanism. Specifically, multiple precipitates (both circles and squares) are placed in a line, for the case of screw and edge dislocations. These configurations are shown in Figure 2.11. Two sets of simulations were conducted. The first set varied the size of the precipitates, while holding the center-to-center spacing constant as  $1000b$ . The second set held the size constant while varying spacing. When modeling circular precipitates the simulation resembles the Bacon-Kocks-Scattergood theory (BKS) [9], with the addition of periodic boundary conditions. In this study, only the Orowan mechanism is considered, i.e. dislocations are restricted from entering the precipitate domain. During the simulation a constant strain rate is applied to the system. We monitored the stress versus plastic strain, and the CRSS is the maximum measured stress.

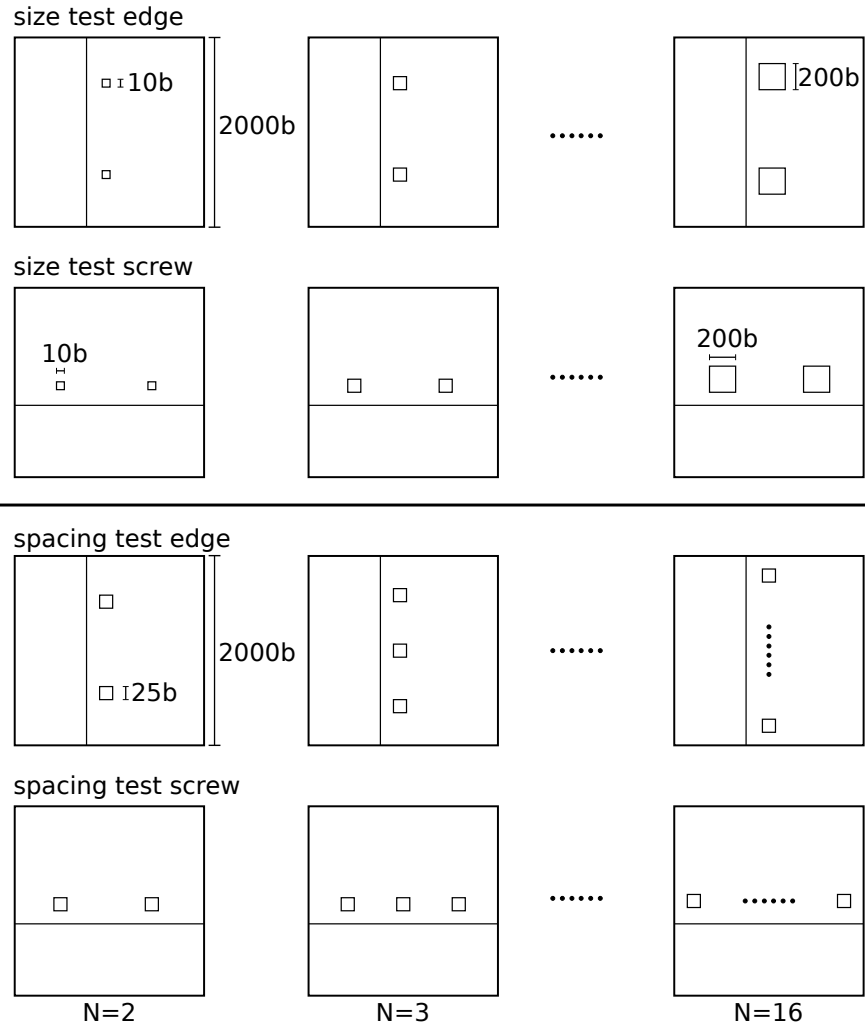


Figure 2.11 – Size test and spacing test models for various cases. Size test starts with 10b and ends with 200b in diameter D, while spacing test starts with 2 precipitates (center-center spacing 1000b) till 16 precipitates (center-to-center spacing 125b) with fixing size of 25b in D. The precipitate shape in the simulation can be either square or circle.

In these simulations, material parameters are varied to observe the effects of core and elastic energy on the CRSS. We first validate the 1D BKS theory by using different shear moduli in the simulations and use a zero core energy in ParaDiS, i.e.  $E_{core}=0$ . For the investigation of the effects of dislocation core energy on the CRSS, only the core energy was accounted for during simulations. This is achieved by setting the parameter for elastic interaction energy to zero in ParaDiS, i.e.  $elasticinteraction=0$ .

### 2.7.2 Validation of Bacon-Kocks-Scattergood Theory

In the original BKS theory [9], as reviewed in Section 1.3, the CRSS for edge and screw dislocations are

$$\begin{aligned}\tau^{\text{edge}} &= \frac{\mu b}{2\pi L} \left[ \ln \frac{\bar{D}}{b} + B \right] \\ \tau^{\text{screw}} &= \frac{\mu b}{2\pi(1-\nu)L} \left[ \ln \frac{\bar{D}}{b} + B \right]\end{aligned}\quad (2.30)$$

where

$L$  = edge-to-edge spacing

$D$  = diameter of circle

$\bar{D} = (1/L + 1/D)^{-1}$

To reproduce BKS result, we simulate circular precipitates while varying the shear modulus (5GPa, 10GPa, 32GPa) and maintaining a zero core energy (i.e.  $E_{\text{core}}=0$ ). A relative small regularization parameter of  $a=0.4b$  is required to avoid local instability. The results of both size and spacing tests are presented in Figure 2.12.

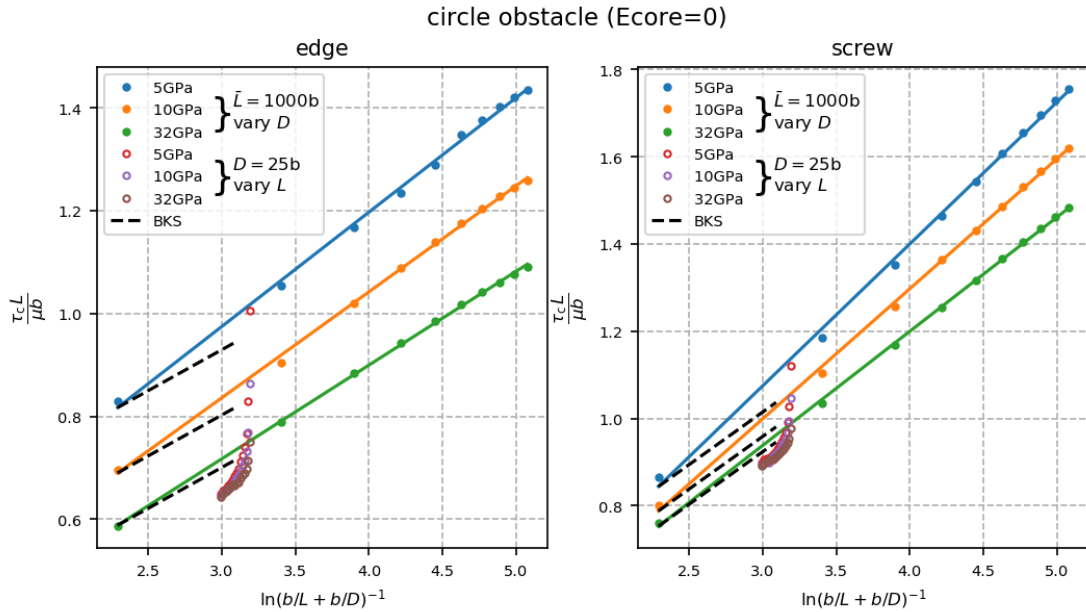


Figure 2.12 – Size ( $\bar{L} = 1000b$  and vary  $D$ ) and spacing test ( $D = 25b$  and vary  $L$ ) with different  $\mu$  and  $E_{\text{core}}=0$ . Linear regression of  $\tau_c L / (\mu b)$  against  $\ln(\bar{D}/b)$  is carried out. Black dash lines are for the theoretical BKS slopes.

As is shown in Figure 2.12, the slopes of the data fit show a large deviation from the BKS theory, with the magnitude of the shear modulus being inversely proportional to this deviation. For many common structural alloys where the shear modulus is often greater than 20 GPa (such as aluminum  $\mu = 25$  GPa), utilizing the BKS theory is valid. Since in the current simulation

setting, all dislocation interaction and forces scale with shear modulus (and we also normalize CRSS with the corresponding shear modulus), the slope deviations might come from the inaccuracy in DDD, limited approximating order of interaction stress, or insufficient multipole expansion order. However, these points require further testing.

In the spacing test, with  $E_{\text{core}}=0$  and  $D$  held fixed at 25 b, the results shown in Figure 2.12 are concentrated in a small region. Although this data deviates from the linear regression of the size test data, the last point of each simulation set converges to this line. This is because the last simulation only has two precipitates, the same number as the size test simulations. Additionally, the spacing test results show better convergence with varying shear moduli, for the data points almost overlap after scaled with shear modulus, and the initial part of the data (small  $L$ ) seems to converge to the predicted BKS slopes. For each shear modulus, the corresponding spacing test results are lower than the size test result as shown in Figure 2.12. The systematic reduction of strength can be attributed to increased precipitates density, making overcoming precipitates more probable. The increased convergence of spacing tests towards the BKS theory implies that a minimum of 5 precipitates in a 1D periodic model are optimal. This level is more consistent with real systems, which contain many precipitates.

We emphasize here that we intentionally choose a very large simulation domain 2000 b to eliminate the spurious image effect, as we found out that an infinite dislocation can move automatically in the absence of external loading.

### 2.7.3 Dislocation Core Energy Contribution to CRSS

In this section we examine the role of dislocation core energy on CRSS for Orowan mechanism. Simulating the precipitate size tests at a shear modulus  $\mu = 32$  GPa, a more broader range of  $\ln(\bar{D})$  can be observed. In these tests we simulate different precipitate shapes (i.e. circle and square) utilizing different material settings for the study of different aspects of the problem. In particular, we have three types of simulations: one is using the elastic and atomistic energetics, noted as “full” in Figure 2.13, another type of simulations involves elastic energy and the default ParaDiS core energy, noted as “full default”, and the other type of simulations has only a characterized atomistic core energy using Al EA94 potential, noted as “core Hu” in the plot.

The results of these simulations are shown in Figure 2.13. The first thing we note here is that results seem to be independent of precipitate shape as the dislocation-precipitate interaction appears very similar. The second point is that using different regularization parameter  $a$  (different energy partition) gives almost identical result, seen from the overlapping of data points. This ensures that CRSS prediction will be reliable once all the energetics are included in the simulation. However, we still need to be cautious with regard to our choice of  $a$ , as this can influence the local stability as discussed in Appendix D. Then we notice that the simulation with all energetics has a BKS slope as before, and by adding a dislocation core energy an increase in strength is observed. If the default dislocation core energy is used

(denote as “full default” in the Figure), the resulting CRSS is considerably higher than using fully atomistic results. Moreover, for a more technological important scale as  $\ln(\bar{D}/b) \approx 3$  ( $D = 25b$  and  $L = 100b$ ), the core energy at 1.3 b contribute about 60% of the strength, and the core energy at 5.4 b makes up almost all the predicted CRSS. This again demonstrates that a proper dislocation core energy is required for realistic strength prediction, complementing the line tension discussion in Section 2.3.

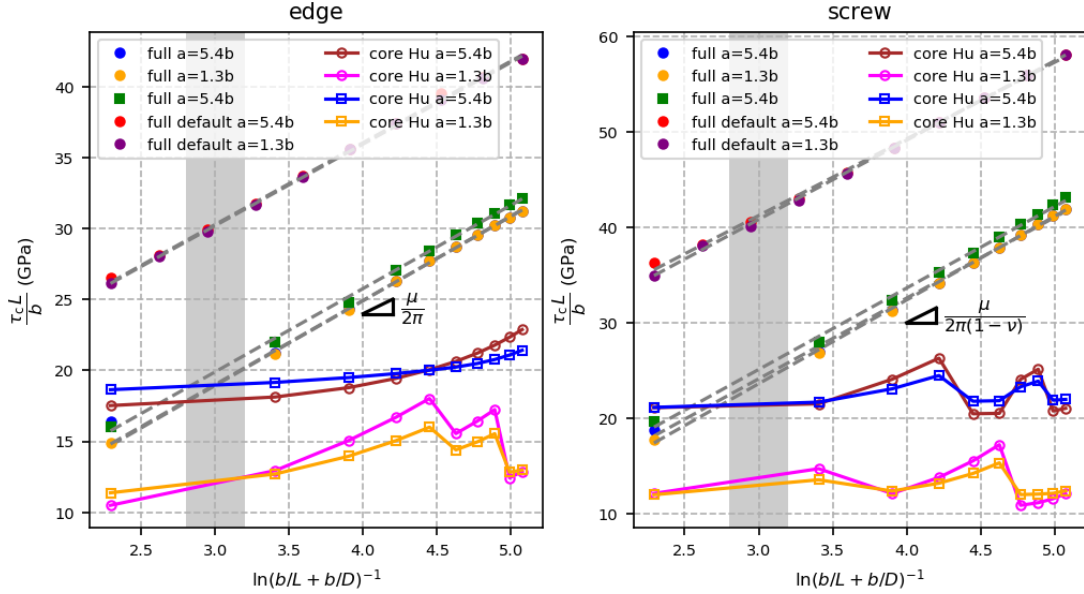


Figure 2.13 – All size tests ( $\bar{L} = 1000b$  and vary  $D$ ) for  $\mu = 32$  GPa with different simulation options. The shapes of markers represent the shapes of precipitates. The solid markers are simulations with full energetics (elasticity + core), while the hollow ones are with partial energetics (atomistic core energy only). Specifically, “full” is simulation with elasticity and atomistic core energy from Al EA94 potential. “full default” is simulation with elasticity + ParaDiS default core. And “core Hu” is the simulation with only atomistic core energy (from Al EA94) at different  $a$ .

## 2.8 Discussion

In this chapter, atomistic simulations have been used to compute the dislocation core energy at cutoff scale  $r_c = b$  as a function of character angle for Al, Cu, and Ni as described by well-established interatomic potentials. The core energy at any other cut-off can be determined analytically, with all choices preserving the total (elastic + core) dislocation energy. The proper incorporation of the atomistic core energy into the non-singular theory of dislocations for any value of the NS regularization parameter  $a$  has been presented and implemented in the DDD code ParaDiS. Comparisons of the calibrated DDD predictions against full atomistic studies have been shown for the problem of dislocation bow-out. Over a range of lengths, loads, and dislocation types, the calibrated DDD model for nearly-isotropic Al is in good

agreement with simulations. Only modest variations in the DDD bow-out are found as a function of the NS regularization parameter  $a$ , although the values  $a = 2eb \sim 4eb$  give the best agreement with atomistic simulations for Al using two different interatomic potentials. We further demonstrated how to compute the core energies for partial dislocations in fcc metals based on the total energies computed atomistically and the stable stacking fault energy.

The present method of calibration does not, in principle, involve any approximations. The accuracy of the core energy quantity can be controlled and reduced while the calibration of NS theory is precise within the context of NS theory. Comparisons of atomistics and DDD so far do involve the assumption that the weak anisotropy of Al is not quantitatively important, and results show that there is some residual dependence of the DDD results on  $a$  that is outside the scope of the calibration. However, these issues are not unique to the present method of determining the core energy itself, but rather to the more general issues of the implementations in DDD. The calibration of partial core energies does involve the use of the NS partial separation, which differs from the atomistic value, but this is consistent for implementations of DDD using NS. Core corrections for NS theory of partial dislocation interactions must also be included. However, the methodology for computing partial core energies from simulations of full dislocations is generally valid, and our results here could be applied to DDD models using singular descriptions [125, 96] or improved non-singular models [95, 14].

Additionally, the importance of dislocation core energy is clarified in the context of Orowan mechanism. Bacon-Kocks-Scattergood theory [9] is first validated via various tests. The gained experience of size test and spacing tests is useful for future simulations and predictions. After these simulations, a careful investigation of different simulation setups demonstrated that a calibrated dislocation core energy is required for realistic predictions.

The careful calibration of the core energy to a particular atomistic potential, as present here, drives simulation studies toward more-quantitative results. Core energy contributions to DDD influence the predicted critical stresses for dislocations to cut or loop precipitates and to break dislocation junctions, and so will enable better quantification between DDD and atomistic studies. In addition, careful calibration now enables more-reliable execution of coupled multiscale methods that have atomistic resolution in critical small domains with DDD resolution in much larger domains [2, 51, 22], where high consistency between atomistic and DDD representations of dislocations is essential. Finally, the accurate study of the core energies of different interatomic potentials of the same metal provides an understanding of one source of uncertainty in atomistic predictions of dislocation phenomena relative to the real metal.



## 3 Mesoscale Study of Precipitation Strengthening

This chapter is adapted from the following article, with permission from the coauthors and the publisher.

**Yi Hu** and W. A. Curtin. Modeling peak-aged precipitate strengthening in Al–Mg–Si alloys. *Journal of the Mechanics and Physics of Solids*, 151:104378, June 2021. ISSN 0022-5096. doi: 10.1016/j.jmps.2021.104378.

### 3.1 Introduction

The strength of Al–Mg–Si alloys is mainly attributed to precipitation strengthening. Experimental studies probe the alloy strength as a function of processing conditions (aging time and temperature) to identify peak-aged conditions at which the strength is a maximum. The precipitation process in Al–Mg–Si under the T6 heat treatment sequence is (i) annealing at a high temperature to create a solid solution state, (ii) quenching to room temperature, (iii) heat treatment at about 180°C for 10 hours, and (iv) cooling to room temperature [86]. If the aging treatment in step (iii) is shorter or longer, the material is under- or over-aged. The overall precipitation process from under-aged to over-aged condition is understood to be GP zones (clusters)  $\rightarrow \beta'' \rightarrow \beta' \rightarrow \beta$  [4]. Peak strengthening is obtained when the  $\beta''$  precipitates dominate in a fine-scale microstructure [73, 72].

We know that there are two basic precipitation strengthening mechanisms (Section 1.3), i.e. shearing mechanism ( $\propto \sqrt{r}$ ) and Orowan mechanism ( $\propto 1/r$ ), and an optimal precipitate size is achieved when two mechanisms deliver the same CRSS. Quantitatively, the strength should also depend on volume fraction, precipitate microstructure, misfit stresses caused by the lattice and elastic mismatch between coherent precipitates and the matrix, elastic mismatch effects on the dislocation motion, and any residual solute strengthening in the matrix. All of these processes are, in principle, thermally-activated (and thus temperature- and strain-rate-dependent) [21]. Therefore, all these effects need to be considered carefully in any attempt to understand or model experiments.

Because of its technological importance, the key phases in Al–Mg–Si alloys are well-studied [3] including composition dependence [72] and the effects of processing on the precipitate microstructure [124]. Complementary simulation studies have computed precipitate properties and precipitates embedded in the Al matrix using first-principles methods [87, 46]. Without accurate interatomic potentials (but see Kobayashi et al. [60] and [58]), atomistic simulations of dislocation/precipitate interactions in Al–Mg–Si alloys have not been reported, although similar studies exist using approximate potentials for Al–Cu [112] and Mg–Al alloys [35, 120]. It has been more common to use mesoscale Discrete Dislocation Dynamics (DDD) to examine Orowan looping, but usually focused on idealized microstructures with spherical [77, 80] or ellipsoidal inclusions [1], often without misfit stresses or elastic mismatch effects. In parallel, analytical models based on basic mechanisms have been used to fit the strength of Al–Mg–Si alloys [83, 10] but involve empirical parameters that limit predictive capability.

The general issues for computations in Al–Mg–Si are (1) can the peak-aged strength be predicted accurately without fitting and (2) if so, can computations provide some guidance for alloy development? Here, we address the first question using state-of-the-art methods. Specifically, we take advantage of the peak aging condition and study the Orowan mechanism in realistic peak-aged microstructures of  $\beta''$  precipitates. We incorporate accurate misfit strains, neglect the (small) elastic mismatch effects, and neglect solute strengthening since nearly all the Mg and Si additions are in the precipitates. We find that misfit stress effects on Orowan looping are small but that the dislocation core energy is very important for quantitative results. With atomistically-calibrated core energies, which are much lower than the default core energy in the widely used DDD code ParaDiS, we find that the CRSS for Orowan looping is  $\approx 50\%$  above experiments using  $T=0$  K core energies and  $33\%$  above experiments using a  $T=300$  K core energy. This suggests that precipitate shearing at a lower CRSS controls the peak-aged strength. A preliminary analysis of shearing is made and the estimated CRSS is in better agreement with experiments, motivating future work on detailed modeling of precipitate shearing even at peak-aging.

The current chapter is organized as follows. In Section 3.2, we describe our method for creating realistic pseudo-random precipitate microstructures for peak-aged Al–Mg–Si. Section 3.3 presents the calculation of the misfit stresses in these microstructures. In Section 3.4, we discuss the design and execution of mesoscale simulation of dislocation motion through the precipitate microstructures using Discrete Dislocation Dynamics simulations. Section 3.5 presents simulation results, analysis of the features controlling the strengthening, and comparisons with experiments. Section 3.6 presents initial analyses of the shearing mechanism and the associated CRSS. The final section summarizes our main findings.

### 3.2 Pseudo-random Precipitate Microstructures of Peak-aged Al–Mg–Si

Existing TEM studies reveal that the  $\beta''$  precipitates have a monoclinic crystal structure [3]. They form as needle-like precipitates aligned with the fcc Al cubic axes, with the orientation relationship

$$\mathbf{a} = [100]_{\beta''} \parallel [203]_{\text{Al}}, \quad \mathbf{b} = [010]_{\beta''} \parallel [010]_{\text{Al}}, \quad \mathbf{c} = [001]_{\beta''} \parallel [\bar{3}01]_{\text{Al}}$$

There are three possible precipitate orientations corresponding to the precipitate  $\mathbf{b}$  aligned along the matrix  $[100]$ ,  $[010]$ , and  $[001]$  directions, respectively. There are also three main precipitate compositions ( $\text{Mg}_5\text{Si}_6$ ,  $\text{Mg}_5\text{Al}_2\text{Si}_4$ ,  $\text{Mg}_4\text{Al}_3\text{Si}_4$ ) with slightly different crystal dimensions and elastic constants; these differences are marginal within the study performed here. Experiments at peak aging [124] provide information on the precipitate dimensions (cross-sectional area  $A$  on  $\{100\}$  planes and length  $l$ ) and volume fraction  $f$ . Table 3.1 shows relevant experimental data on the precipitates and microstructures. The precipitates form by a process of nucleation and growth, as solutes in the matrix diffuse to the precipitates, and then grow further by Ostwald ripening. This formation process suggests that the microstructure is not random but instead has precipitate spacings that are more narrowly distributed around the mean value. These considerations motivate our creation of pseudo-random microstructures as follows.

Table 3.1 – List of experimental characterization of  $\beta''$  phases in [124, 70], and the corresponding simulated precipitate dimensions and building block sizes. The length for each lattice vector of precipitate is from  $\text{Mg}_5\text{Si}_6$  for reference.

$f$	precipitate type	experiment		simulated precipitate in lattice unit			$l_c$ (nm)
		$A$ (nm <sup>2</sup> )	$l$ (nm)	$\mathbf{a}$ $[203]_{\text{Al}}$ (15.14 Å)	$\mathbf{b}$ $[010]_{\text{Al}}$ (4.08 Å)	$\mathbf{c}$ $[\bar{3}01]_{\text{Al}}$ (6.93 Å)	
0.66%	$\text{Mg}_5\text{Si}_6$	7.5	22.5	2	55	4	41.9
1.10%	$\text{Mg}_4\text{Al}_3\text{Si}_4$	8.1	37.8	3	93	3	43.8
1.10%	$\text{Mg}_4\text{Al}_3\text{Si}_4$	8.1	37.8	2	93	4	42.1
1.60%	$\text{Mg}_5\text{Si}_6$	21.2	25	3	61	8	46.5

Our initial building block for a realistic microstructure is a cubic cell based on the experimental precipitate dimensions and volume fraction. Three precipitates, one for each orientation, are placed in a cubic cell such that periodic replication of the cell in all three cubic directions gives equal spacings among all precipitates and their periodic images. At precipitate volume fraction  $f$  and number of density  $\rho$  [124], the edge length of the cubic cell is  $l_c = \sqrt[3]{3Al/f}$  or  $l_c = \sqrt[3]{3/\rho}$ . There are 8 variants of this fundamental building block, as shown in Figure 3.1 (b), created by rotations and/or reflections of the basic cell.

Pseudo-random microstructures labelled as micro(100) are then created as  $3 \times 3 \times 3$  assemblies

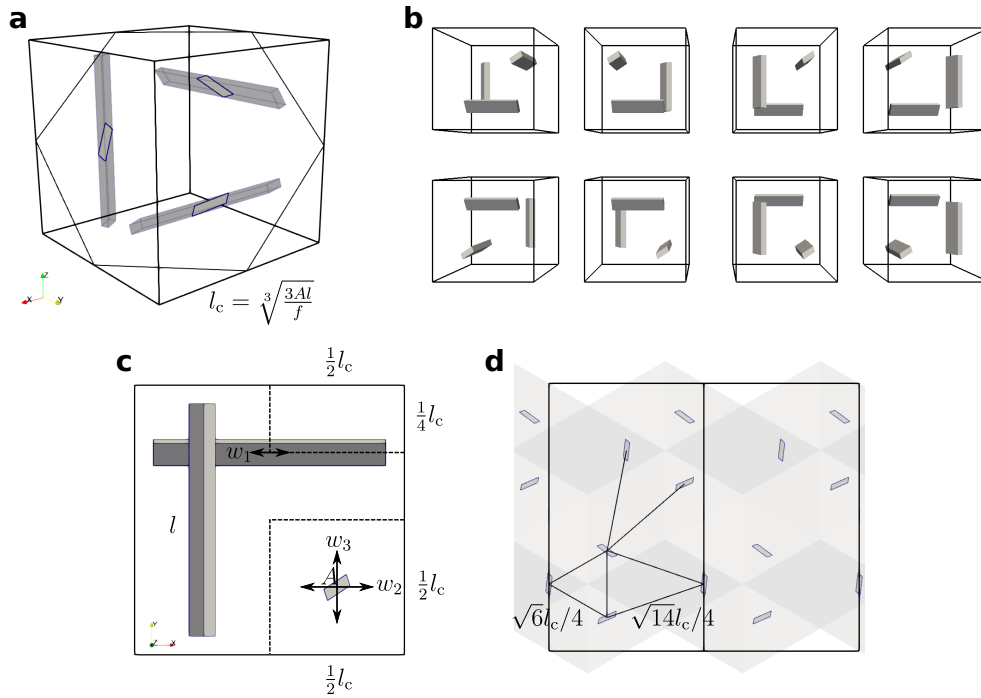


Figure 3.1 – (a) Building block of the micro(100) pseudo-random structure with three equispaced precipitates aligned in three axis directions, with  $A$  the precipitate cross sectional area,  $l$  the precipitate length, and  $l_c$  the edge length of the cubic cell. (b) The 8 equivalent variants of the fundamental building block. (c) In-plane projection of the building block for micro(100) showing the range of random perturbations  $w_1$ ,  $w_2$  and  $w_3$  added to each precipitate position. (d) Precipitate structure of an ideal single-variant unperturbed micro(100) structure on a (111) slip plane, showing two different precipitate spacings.

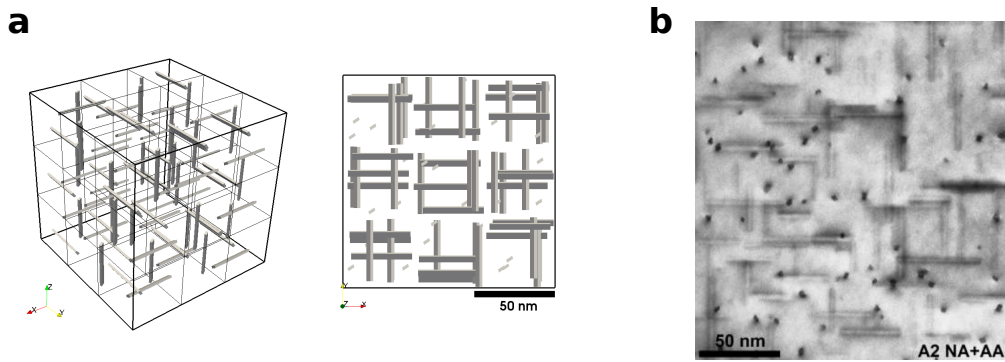


Figure 3.2 – (a)  $3 \times 3 \times 3$  pseudo-random precipitate model with micro(100) corresponding to the alloy denoted A2 (NA+AA) in [124]. (b) Corresponding experimental micrograph in [124]. The scale bars in (a) and (b) are the same.

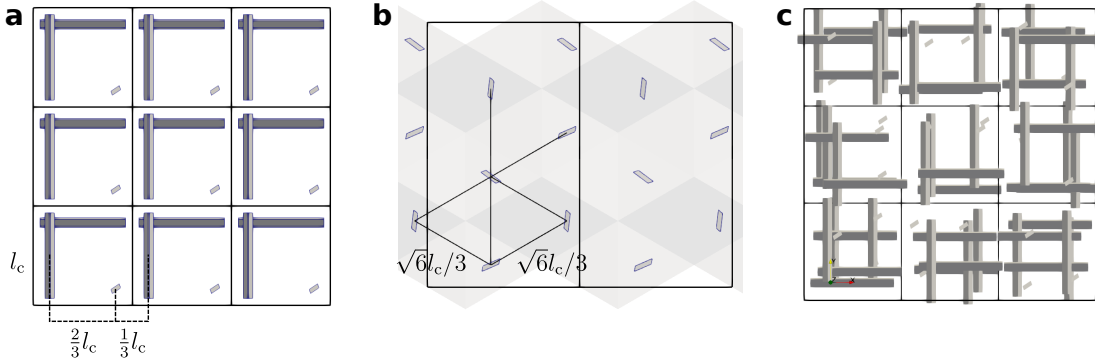


Figure 3.3 – (a) Precipitate structure of an ideal single-variant unperturbed micro(111) showing two different precipitate spacings in the (100) projection. (b) The same microstructure but on the (111) plane, showing equal precipitate spacing on the (111) plane. (c) Projection of a full  $3 \times 3 \times 3$  micro(111) microstructure generated with large perturbations of the individual precipitates.

containing 27 of the initial building blocks with variants randomly chosen from the 8 possibilities shown in Figure 3.1 (b). Further, we perturb the center position of each precipitate in each building block in the [100], [010] and [001] directions as indicated by the  $w_i$  and their ranges shown in Figure 3.1(c). These perturbations are limited only by the restrictions that each precipitate remains in its original cubic cell and that the precipitates do not overlap. In an infinite non-periodic microstructure, the average precipitate area fraction on (111) slip planes is exactly equal to the volume fraction  $f$ . The perturbations imposed here generate microstructures having precipitate area fractions on the (111) slip planes very near  $f$  (e.g. between 1.0% and 1.2% for a microstructure with average  $f=1.10\%$ ). Furthermore, for simulations below, we then study slip only on (111) planes having the correct average precipitate area fraction.

Figure 3.2 shows one example of a pseudo-random microstructure created in this manner, corresponding to the volume fraction and dimensions from experiment [124] with a micrograph from the experiment also shown. The visual correspondence is good. However, when the precipitates are not permitted to extend outside the individual building block, there are regions of zero precipitate along the building block boundaries. These create similar regions on the (111) slip planes of the microstructure. Figure 3.1(d) further shows that the equal spacing of the periodic precipitates in the cubic directions leads to two different length scales on the (111) planes where the dislocations glide. This might affect dislocation behavior as well.

To rectify possible issues with the above micro(100) structures, we have created a second family of microstructures denoted as micro(111). As shown in Figure 3.3, the precipitate spacings in the cubic direction of micro(111) are unequal but the precipitate spacings on the (111) planes are equal. Furthermore, we consider perturbations in which the precipitates can extend outside of their individual blocks, eliminating the precipitate-free regions along

the block boundaries (Figure 3.3(c)). The micro(111) structures again have nearly-average precipitate area fractions on all (111) planes, and simulations are performed on (111) planes very near the average area fraction.

Finally, while we report below only small sample-to-sample variations in the strength at size  $3 \times 3 \times 3$ , indicating sufficient sampling, we also created several micro(100) structures of size  $5 \times 5 \times 5$  to examine convergence. We also studied several microstructures with random placement of precipitate cross-sections on the (111) plane.

Using the above general procedure, specific microstructures based on experimental studies were created as shown in Table 3.1. The primary microstructure has  $f = 1.10\%$  with  $\text{Mg}_4\text{Al}_3\text{Si}_4$  precipitates corresponding to the alloy denoted A2(NA+AA) in Ref. [124]. For the low Mg concentration (0.443 at.%) in this alloy,  $\text{Mg}_4\text{Al}_3\text{Si}_4$  is the only possible composition at  $f = 1.10\%$  and the residual solute concentration are  $c_{\text{Mg}}^{\text{sol}} = c_{\text{Mg}} - 4f/11 = 0.043$  at.% and  $c_{\text{Si}}^{\text{sol}} = 0.402$  at.% so that residual solute strengthening is negligible. For this system, we consider two different precipitate shapes ( $2\mathbf{a} \times 4\mathbf{c}$  and  $3\mathbf{a} \times 3\mathbf{c}$ ) having similar cross-sectional area but different shape. To evaluate the effect of volume fraction, we created microstructures with  $f = 0.66\%$  and  $f = 1.60\%$  using the properties of  $\text{Mg}_5\text{Si}_6$ . The first case is similar to the A3 alloy (particularly, A3\_36h\_175°C) in [74] but with a slightly larger cross sectional area. The second case is similar to the alloy in Ref. [70] with a shorter length and larger cross-section area. While we use different precipitate compositions for different cases, the differences among them are negligible for our determination of the CRSS for Orowan looping.

### 3.3 Misfit Stresses in the Pseudo-random Microstructures

The nanoscale  $\beta''$  precipitates remain coherent with the Al matrix. The mismatch in size and shape of the precipitates relative to the closest corresponding region of Al atoms leads to the creation of misfit stresses in the matrix and the precipitates. This is observed in both previous experiments and DFT calculations [123]. It is thus necessary to determine the misfit strains throughout the microstructure and then incorporate those misfit stresses into simulations of dislocation motion through the microstructure.

The misfit stress field  $\boldsymbol{\sigma}$  throughout a specified microstructure is calculated using a fast-fourier transform (FFT) method as follows. First, the precipitate misfit strain  $\bar{\boldsymbol{\epsilon}}$  is computed relative to the underlying Al lattice. In general, the precipitate lattice vectors  $\mathbf{a}_p$  are related to the matrix lattice vectors  $\mathbf{a}_m$  by  $\mathbf{a}_m = \bar{\mathbf{F}}\mathbf{a}_p$ , where  $\bar{\mathbf{F}}$  is the transformation deformation gradient. The precipitate misfit strain is then  $\bar{\boldsymbol{\epsilon}} = \frac{1}{2}[\bar{\mathbf{F}}^T + \bar{\mathbf{F}}] - \mathbf{I}$ . The linear-elastic stress-strain relationships for the matrix and precipitates are

$$\begin{cases} \boldsymbol{\sigma} = \mathbf{C}_m \boldsymbol{\epsilon} & \text{in } \Omega_m \\ \boldsymbol{\sigma} = \mathbf{C}_p (\boldsymbol{\epsilon} - \bar{\boldsymbol{\epsilon}}) & \text{in } \Omega_p \end{cases} \quad (3.1)$$

where  $\mathbf{C}_p$  and  $\mathbf{C}_m$  are the elastic constants of the precipitates and the Al matrix, respectively.

### 3.3. Misfit Stresses in the Pseudo-random Microstructures

We use the first-principles-computed values of Giofré et al. [46] as shown in Table 3.2. The misfit stresses are obtained by solving the equilibrium equation  $\nabla \cdot \boldsymbol{\sigma} = \mathbf{0}$  within the entire periodic pseudo-random microstructural simulation cell.

Table 3.2 – Elastic constants obtained by first principle calculation in [46]. These elastic constants are used in eigenstress calculation.

[GPa]	$C_{11}$	$C_{22}$	$C_{33}$	$C_{44}$	$C_{55}$	$C_{66}$
Al	106.1				31.9	
Mg <sub>5</sub> Si <sub>6</sub>	98.4	84.6	88.0	21.9	29.1	51.2
Mg <sub>5</sub> Al <sub>2</sub> Si <sub>4</sub>	107.1	94.7	99.1	26.9	36.3	49.4
Mg <sub>4</sub> Al <sub>3</sub> Si <sub>4</sub>	106.7	96.5	97.1	25.9	35.6	46.3
$C_{12}$	$C_{13}$	$C_{23}$	$C_{15}$	$C_{25}$	$C_{35}$	$C_{46}$
	55.9			0.		
	50.0	47.7	45.7	8.2	5.8	5.4
	40.3	45.6	43.0	-13.1	4.3	11.9
	46.5	48.0	48.8	9.3	5.7	9.3

Taking advantage of the periodicity, we use a new fast-fourier transform (FFT) spectral solver [59] (see the Appendix) that discretizes the full structure into  $N$  pixels with each pixel assigned the appropriate elastic constants. The discrete FFT stress field has oscillations at the scale of the pixels. These are first reduced in size scale by using a fairly high resolution of  $N = 301$  corresponding to a pixel size of  $2.3b$  where  $b = 2.851 \text{ \AA}$  is the Al Burgers vector. We then apply a smoothing filter to reduce the remaining oscillations to a level that should have no effect on subsequent dislocation simulations. To be specific for the smoothing filter, the stress value of a chosen pixel is calculated by averaging it with its 6 neighbors.

The misfit stresses create Peach-Koehler forces  $\mathbf{F} = (\boldsymbol{\sigma} \mathbf{b}) \times \mathbf{t}$  acting on a dislocation with line direction  $\mathbf{t}$ . Glide of dislocations with Burgers vector  $\mathbf{b} = [\bar{1}10] a/2$  on the (111) plane with normal vector  $\mathbf{n}$  leads to a Peach-Koehler glide force  $\mathbf{F}_g = (\mathbf{n} \cdot (\boldsymbol{\sigma} \mathbf{b}))(\mathbf{n} \times \mathbf{t})$ . Thus, we compute the resolved shear stress (RSS) field  $\mathbf{n} \cdot (\boldsymbol{\sigma} \mathbf{b})/|\mathbf{b}|$  that exerts forces in the glide plane acting normal to the dislocation line direction. Examples of the RSS field are presented in Figure 3.4 for several microstructures. The RSS values in the matrix can be large - reaching  $\pm 600 \text{ MPa}$  - but only very locally around the precipitates. Each precipitate has little interaction with other precipitates, and so all precipitates with the same orientation have nearly the same RSS. The sign of the RSS depends on the chosen  $\mathbf{n}$  and  $\mathbf{b}$ , which are a matter of convention and are shown in each figure. These features will rationalize our conclusion that the role of misfit stresses on Orowan strengthening is quite small.

Inside the precipitates, the magnitude and sign vary significantly with both orientation and shape, as seen in detailed views in Figures 3.4. These fields, while not important for Orowan looping, can thus assist or impede precipitate shearing as discussed in Section 3.6. Experi-

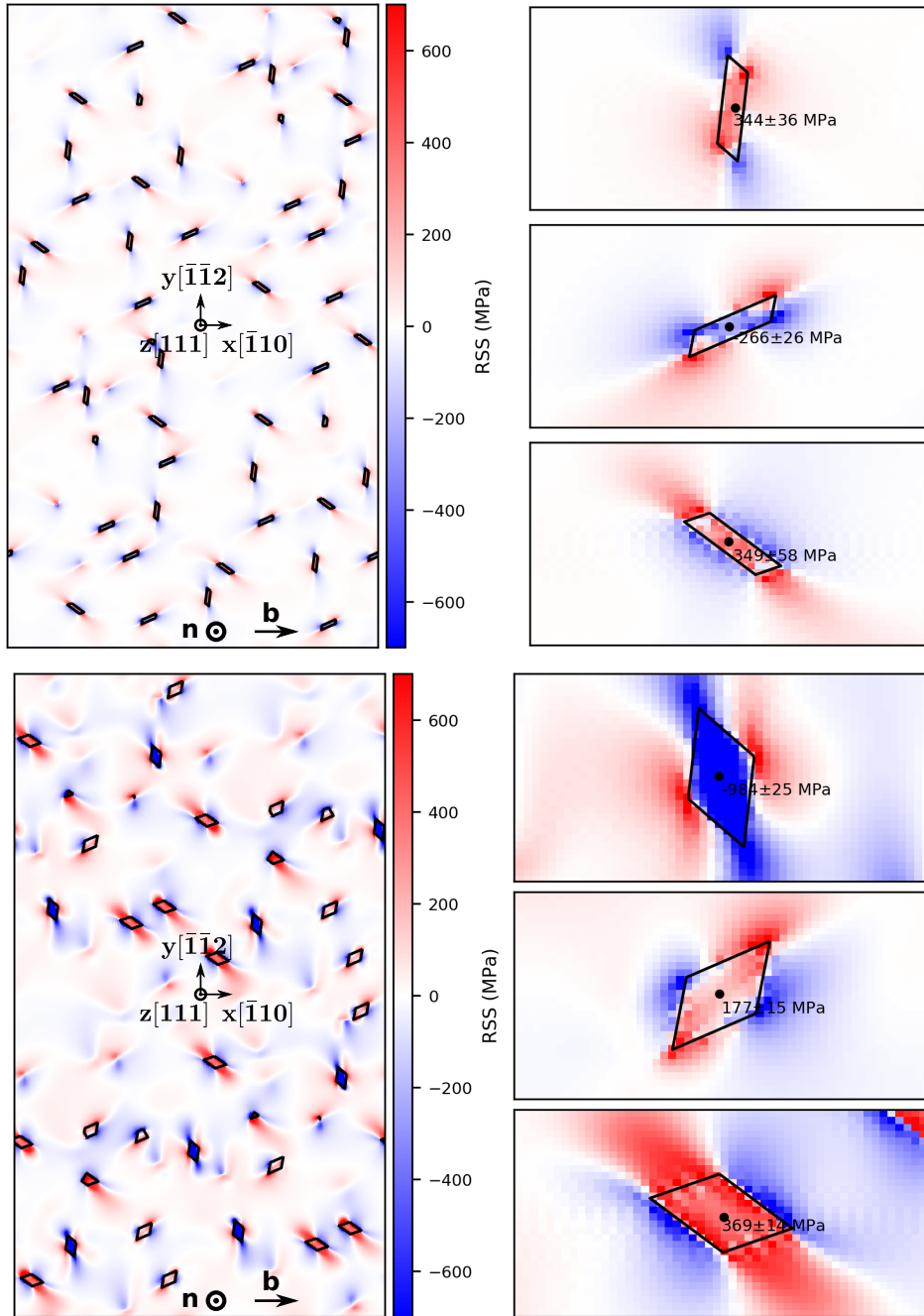


Figure 3.4 – Normalized Resolved Shear Stresses (RSS) due to precipitate misfit strains acting on a screw dislocation, as computed for two different microstructures (precipitate dimensions  $3a \times 3c$  at  $f = 1.10\%$ , and  $3a \times 8c$  at  $f = 1.60\%$ ). The RSS are large very near the precipitates but decay rapidly with distance, as expected. The sign of the RSS varies with precipitate orientation, dislocation type, and chosen (111) slip plane. The average and standard deviation of the RSS inside the different precipitates are indicated, and play a role in precipitate shearing.



mental measurements show large internal strains in the precipitates [123], consistent with our results.

### 3.4 DDD Simulations of Dislocation-precipitate Interactions

The motion of a dislocation through the precipitate field of the pseudo-random microstructures is modeled using the non-singular theory [20] for Discrete Dislocation Dynamics (DDD) as implemented in the open-source code ParaDiS [7]. Generically, DDD methods discretize continuum dislocation lines into linear segments, compute the long-range elastic interactions among all segments, and evolve the discretized dislocations according to the total driving force on each segment (Section 1.2.2). The total driving force includes contributions from (i) an applied stress, (ii) the elastic interactions among segments, (iii) the self forces due to elasticity and dislocation core energy of individual segments, (iv) the image forces due to interactions with elastically-mismatched precipitates [49], and (v) the misfit stresses (RSS) created by the combination of lattice and elastic mismatch of the precipitates. Implementation requires careful attention to a range of details, as discussed below.

For a DDD simulation in ParaDiS, we first select a (111) glide plane from the 3d microstructure. Noting that the microstructure periodicity is different on a (111) plane, we replicate the full 3d precipitate microstructure to obtain a periodic microstructure on the chosen (111) plane, as indicated in Figure 3.5 (a). ParaDiS simulations are then performed within some even-larger periodic cubic cell. We insert our periodic (111) glide plane microstructure into such a cubic cell with the glide plane and desired dislocation line direction aligned with the cubic axes of the ParaDiS cell. A single dislocation is then introduced along the desired line direction, and sufficient periodic images along the line direction are added. Note that the absence of precipitate microstructure outside the actual (111) domain along the dislocation glide direction is unimportant. This outer region is simply a large surrounding elastic domain that prevents undesired image effects in ParaDiS while having no effect at all on the motion of the dislocation through the microstructured region. Examples of the (111) plane models within the larger ParaDiS cell, for both screw and edge dislocations, are shown in Figure 3.5 (b) and (c). With periodic boundary conditions imposed in all directions within ParaDiS, we verify that the image forces on an infinite straight dislocation line are less than 3 MPa for the ParaDiS cell dimensions of over 1200b used here.

With a primary focus on Orowan looping on the glide plane, we treat the precipitates as impenetrable obstacles. Because the elastic moduli of the precipitates are generally close to those of the Al matrix, and because the cost of computing image forces due to the difference in elastic moduli is extremely high [39], we neglect this effect. Then, the effect of the precipitates is entirely constrained to the glide plane of the dislocation. A precipitate is a region where the dislocation cannot be present while creating a spatially-varying misfit RSS outside the precipitate. We represent the precipitates by using prismatic loops along the exact boundary of the precipitates in the glide plane. The stress field created by a prismatic loop in the glide plane

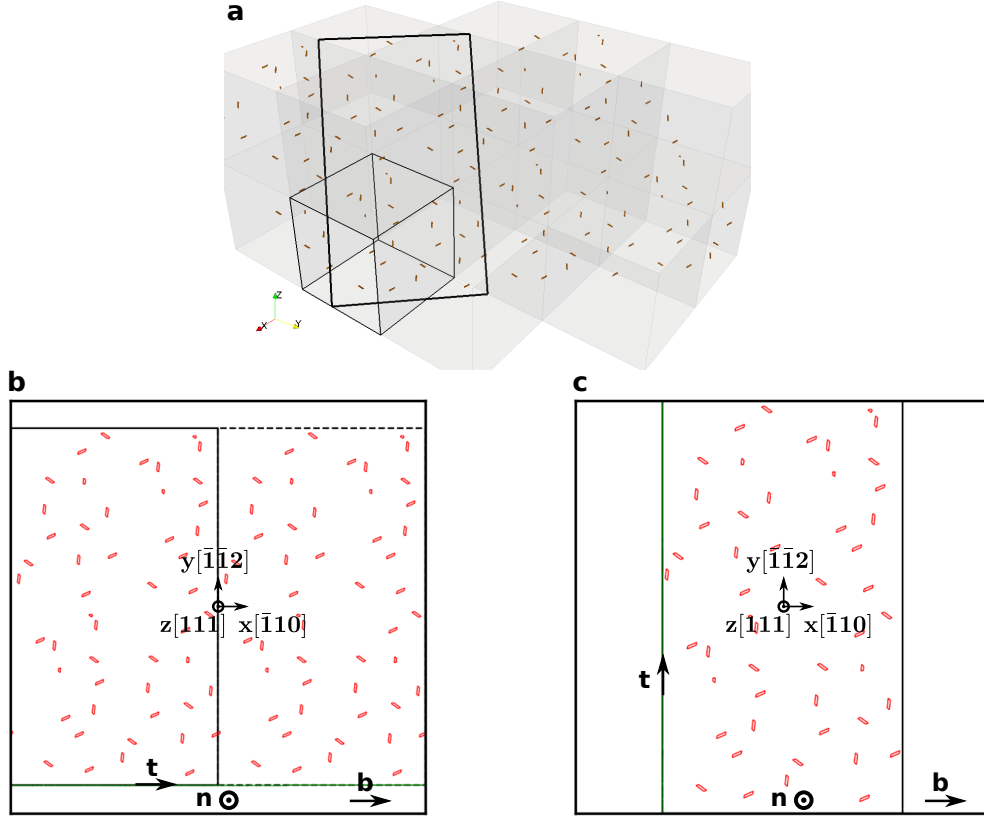


Figure 3.5 – (a) Periodicity of a (111) simulation plane as created from replication of an underlying  $3 \times 3 \times 3$  microstructure, with precipitates intersecting the chosen glide plane shown. (b) Microstructure on the (111) plane for a DDD simulation for screw dislocation. The Burgers vector, line direction, and initial straight screw dislocation are shown. Red polygons show the boundaries of the cut precipitates in this glide plane. (c) as in (b) but for an edge dislocation.

of the dislocation generates exactly zero driving force for the mobile dislocation on the same glide plane. Nonetheless, we explicitly set the forces to zero in ParaDiS by labelling nodes of the prismatic loops as “precipitate” and setting any interaction forces involving “precipitate” nodes to zero. The prismatic loop is thus fully fixed during the simulation. As a discretized lattice dislocation approaches a discretized prismatic loop (a precipitate), any node that comes within a pre-defined collision distance of  $0.2b$  of the precipitate loop is assigned essentially zero velocity. The lattice dislocation thus conforms to the precise shape of the precipitate as it attempts to glide around it, with no spurious interactions and no numerical instabilities. A schematics of such strategy is presented in Figure 3.6.

The matrix RSS calculated in the Section 3.3 is imported in the DDD simulation as a static field. For each concerned dislocation segment, the imposed matrix misfit RSS is calculated as the average of pixel RSS where the two end nodes reside. In our simulation, the dislocation

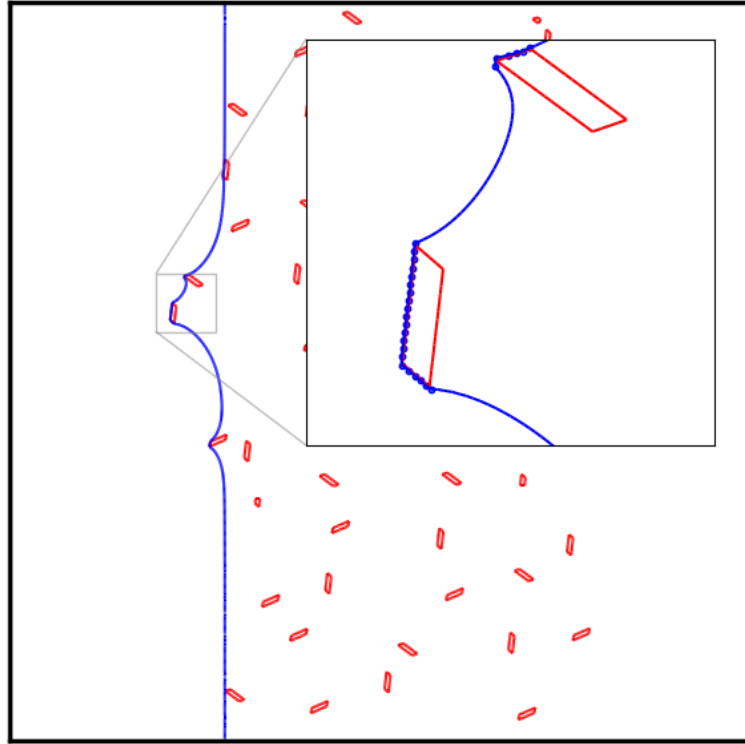


Figure 3.6 – Snapshot of the discretized dislocation interactions with precipitates in the DDD simulation. Dislocation nodes are pinned when they are within a distance  $0.2b$  of the prismatic segments that define the precipitate. The nodes shown in the inset are those pinned at the precipitate in this configuration.

segment length is between  $1b$  to  $2b$  ( $\text{minSeg} = 1$ ,  $\text{maxSeg} = 2$ ) and the resolution of misfit RSS is  $2.3b$ , thus the current interpolation scheme is reasonable.

Most previous modeling of precipitates imposes some high artificial stress on the dislocations in the region occupied by precipitates [98, 39, 77, 65]. This avoids the need to determine when the dislocation reaches the precipitate boundary. However, as mentioned in [77], this method can cause numerical problems at the precipitate boundary. Agesen et al. [1] use the exact geometry with dislocation nodes pinned at the precipitate interface, most similar to our approach. Work by Al–Cu [102, 103] used a very different method wherein the precipitate is fully modeled and the entire glide dislocation loop is represented by a discretized eigenstrain, enabling a full 3d FFT model. However, this treatment of the dislocation is more approximate and we prefer to use actual dislocation lines gliding in a 2d plane with control of the dislocation core energy, at the cost of neglecting the small dislocation/precipitate image interactions.

In addition to treatment of the dislocation-precipitate interactions, the simulations require material parameters such as the Burgers vector, elastic constants, dislocation core energy, non-singular regularization parameter “ $a$ ”, and dislocation mobility. We are examining only stable quasistatic solutions and so the mobility parameter is not important aside from being small

enough to ensure numerical stability; we use the small value of 0.05b/s. ParaDiS performs automatic re-meshing and refinements of the time steps. The baseline elastic properties are taken from an EAM potential for Al [32] with Bacon-Scattergood effective isotropic material moduli [106]  $\mu = 32.0$  GPa,  $\nu = 0.34$ .

The term core energy is imprecise. A dislocation only has a total self-energy but it is convenient to conceptually partition that energy into an “elastic” contribution and an “inelastic” or core contribution at the arbitrary but convenient reference length  $b$  as [53]. So the total energy of a dislocation can be written in terms of dislocation character  $\theta$  as (see also Section 1.2.1 and Section 2.2)

$$E(\theta) = K(\theta) \ln \left( \frac{R}{b} \right) + E_c(\theta)|_b \quad (3.2)$$

where  $K(\theta)$  is an elastic parameter; for an isotropic material,  $K(\theta) = \frac{\mu b^2}{4\pi} (\cos^2 \theta + \frac{1}{1-\nu} \sin^2 \theta)$ . The above total energy can also be determined at any other reference length  $a$  as

$$E(\theta) = K(\theta) \ln \left( \frac{R}{a} \right) + K(\theta) \ln \left( \frac{a}{b} \right) + E_c(\theta)|_b \quad (3.3a)$$

$$= K(\theta) \ln \left( \frac{R}{a} \right) + E_c(\theta)|_a \quad (3.3b)$$

thereby defining a core energy quantity at scale  $a$ . In non-singular dislocation theory,  $a$  is the non-singular regularization parameter. To calibrate non-singular theory to an atomistic calculation of the total energy within a radius  $R \gg a$  requires subtracting an additional constant self-energy term that appears in non-singular theory and then adding an energy such that the total energy within radius  $R \gg a$  exactly matches the atomistic total energy [53]. The total self-energy is then independent of the choice of regularization parameter  $a$ . Nonetheless, comparisons of ParaDiS and atomistic simulations of dislocation bow-out show that some values of  $a$  are slightly better than others. Here, we use the calibration of Hu et al. [53] to atomistic Al as described by the Ercollessi-Adams EAM potential, for which  $a = 5.4b$  was found optimal; other calibrations are considered in Section 3.5.3.

We load the system with a resolved shear stress  $\tau$  on the glide plane to move screw dislocations in the positive y direction and edge dislocations in the positive x direction. The critical resolved shear stress (CRSS) for Orowan looping is obtained by incrementing the applied stress. If the change in maximum advance of the dislocation in the glide direction is less than 0.1b for 300 time steps, we increment the load by 5 MPa. When a stress increment exceeds the CRSS, the dislocation moves forward through the remaining sections of the microstructure. The CRSS  $\tau_c$  is then in between two load increments differing by 5 MPa, and is quoted as the mean value with an uncertainty of  $\tau_c \pm 2.5$  MPa. Figure 3.7 shows examples of the edge and screw dislocations just below and just above  $\tau_c$  in one typical microstructure.

### 3.5 CRSS for Orowan Looping

#### 3.5.1 CRSS versus Volume Fraction and Misfit Stress

Simulations of Orowan looping in our realistic micro(100) microstructures were performed at volume fractions 0.66%, 1.10% and 1.60% using  $\mu = 32.0$  GPa,  $\nu = 0.34$  and the Ercolessi-Adams core energy at cut-off  $5.4b$  [53]. For each volume fraction, two micro(100) pseudo-random structures were created (Section 3.2) using precipitate dimensions in Table 3.1. In particular, we use a more-rectangular cross section  $3\mathbf{a} \times 3\mathbf{c}$  for  $f = 1.10\%$  to mimic experiments (see Fig.4 in [124])) while for volume fractions  $f = 0.66\%$  and  $f = 1.10\%$  we use an equiaxed more-diamond-like shape; we address any shape effects subsequently. Four different (111) glide planes were studied for each microstructure. The averaged CRSS values for edge and screw dislocations over all simulations are shown in Table 3.3 along with the standard deviations.

Table 3.3 – Simulated CRSS values for various microstructures and volume fractions  $f$  as indicated. The first three rows are simulated using 4 different glide planes in each of 2 different  $3 \times 3 \times 3$  pseudo-random microstructures while the last 4 rows are calculated using 4 different glide planes in 1 pseudo-random microstructure.

$f$	microstructure	precipitate dimension $\mathbf{a} \times \mathbf{c}$	CRSS (MPa)			
			with misfit stress		without misfit stress	
			screw	edge	screw	edge
0.66%	micro(100)	$2 \times 4$	$123 \pm 10$	$109 \pm 14$	$113 \pm 13$	$103 \pm 13$
1.10%	micro(100)	$3 \times 3$	$164 \pm 25$	$140 \pm 8$	$158 \pm 21$	$139 \pm 7$
1.60%	micro(100)	$3 \times 8$	$161 \pm 22$	$147 \pm 14$	$147 \pm 13$	$120 \pm 11$
1.10%	micro(100)	$2 \times 4$	-	-	$151 \pm 19$	$135 \pm 16$
1.10%	micro(111)	$3 \times 3$	-	-	$143 \pm 10$	$128 \pm 5$
1.10%	micro(111) (large perturb)	$3 \times 3$	-	-	$165 \pm 14$	$141 \pm 9$
1.10% (5x5x5)	micro(100)	$3 \times 3$	-	-	$160 \pm 14$	$136 \pm 6$

Comparing the screw and edge simulations, the CRSS for the screw dislocation is only slightly higher (20 MPa) than the CRSS for the edge dislocation across all cases. A much higher strength for the screw is expected based on standard elasticity models [9] where the screw line tension is much larger than that of the edge. However, for precipitates at the nanoscale, the CRSS is controlled mainly by the core energy contribution to the line tension, which is only slightly larger for the screw than for the edge [53]. Thus, the typical conclusion drawn from standard models can be misleading when applied to nanoscale precipitate structures. Also, as shown below, the typical precipitate edge-edge spacing at the CRSS is also slightly larger for the screw as compared to the edge, further reducing the differences in strength.

Examining the effects of misfit stresses, Table 3.3 shows that the matrix misfit stresses have

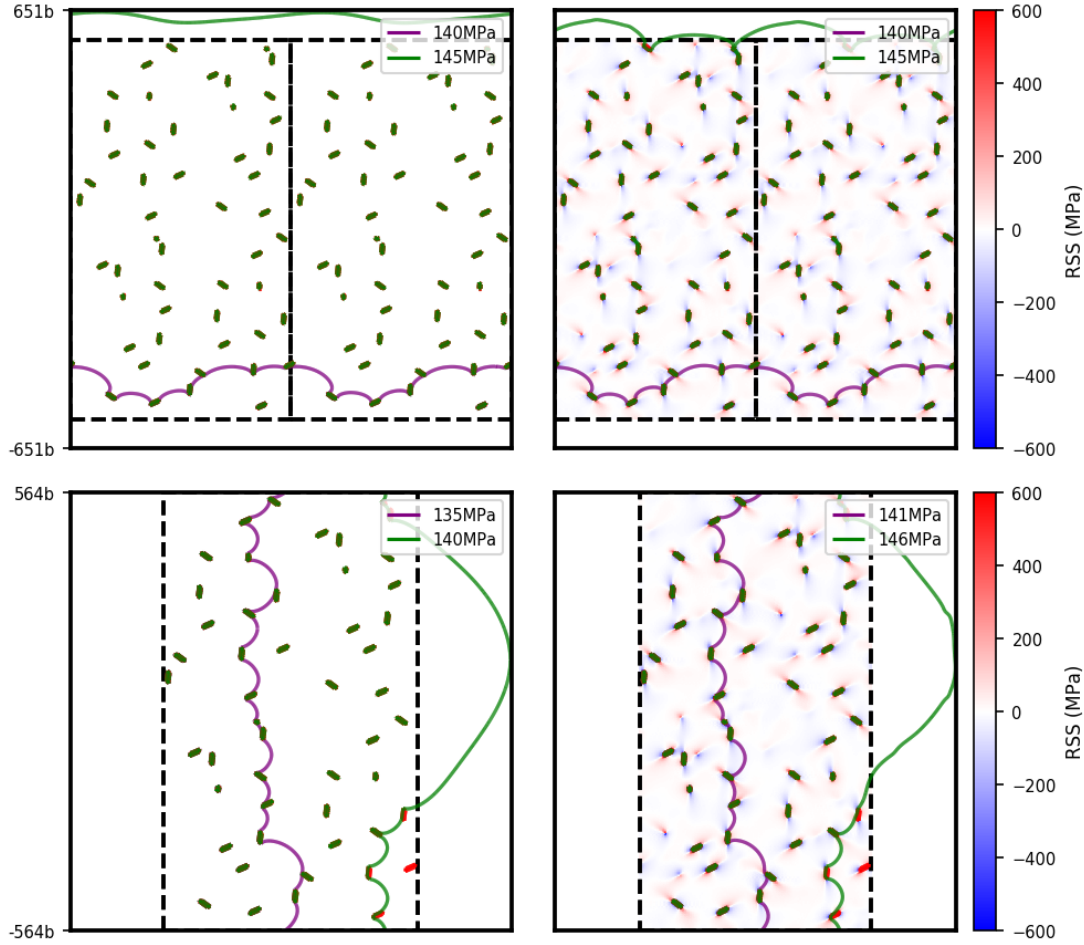


Figure 3.7 – DDD configurations for screw (top) and edge (bottom) simulations at stresses just before and just after Orowan looping for one particular  $f = 1.10\%$  microstructure and glide plane, and for simulations with and without misfit stresses. The misfit stresses have minimal effect on the critical dislocation configuration.

almost no effect on the averaged CRSS for both edge and screw, especially for  $f = 0.66\%$  and  $1.10\%$ . Visualization of the critical configurations in typical cases for edge and screw are shown in Figure 3.7 and are essentially identical with and without misfit stresses. This is consistent with the very local misfit stress fields shown in Figure 3.4. For  $f = 1.60\%$ , the misfit stresses increase the CRSS slightly ( $\approx 14$  MPa for the screw and  $27$  MPa for the edge) due to the larger size and more-equiaxed shape that lead to larger misfit stresses in the matrix extending over a slightly longer range. Reversing the line direction to change the sign of the PK force due to RSS field leads to no statistically-different results. Overall, the effects of the matrix misfit stresses are small relative to the total CRSS and so are not crucial for reasonable determination of the CRSS in the typical peak-aged alloy ( $f = 1.10\%$ ). This also implies that a loss of such misfit (or coherency) stresses that may arise for larger precipitates in the overaged regime may not be a significant contribution to any decrease in strength for Orowan looping.

With costly-to-compute misfit stresses of little importance, we now focus on results computed without misfit stress in Table 3.3 and examine the role of geometry. The strength increases significantly from  $f = 0.66\%$  to  $1.10\%$  but decreases upon a further increase in  $f$  to  $1.60\%$ . The latter effect is unexpected in traditional models. However, as known from classic analyses of Orowan strengthening [9], the CRSS should scale as  $\tau_c \propto 1/L$  where  $L$  is the edge-to-edge spacing of precipitates. We have performed a Voronoi tessellation of our microstructures to extract the average center-to-center precipitate spacing  $\bar{L}$  in the entire microstructure and the average edge-to-edge precipitate spacing  $L$  along the actual dislocation at the CRSS. We also measure the edge-to-edge distance  $D$  across the precipitates pinning the dislocation at the CRSS. Examples of these geometric measurements are shown in Figure 3.8. The microstructure with  $f = 1.10\%$  has the smallest  $L$  while the microstructures with  $f = 0.66\%$  and  $f = 1.60\%$  have larger and comparable  $L$ . This is due to the fact that the  $f = 1.60\%$  microstructure consists of precipitates with a larger area and shorter length, as compared to  $f = 1.10\%$ . The strength is controlled by  $L$ . Analysis shows that, across all microstructures, the dislocation is pinned in a configuration that has a  $L < \bar{L}$  with, typically,  $L = (0.79 \pm 0.18)\bar{L}$  (screw) and  $L = (0.67 \pm 0.08)\bar{L}$  (edge). The strength of the  $f = 1.10\%$  microstructure is thus higher than that of both  $f = 0.66\%$  and  $f = 1.60\%$  mainly because it has a smaller  $L$ . The difference in strength between  $f = 0.66\%$  and  $f = 1.60\%$  is then mainly due to the (smaller) effect of the precipitate size  $D$  at comparable  $L$ . These results demonstrate that volume fraction is not an appropriate measure for estimating strength. The size and shape of the precipitates, and the effects of that geometry on the precipitate microstructure on the relevant dislocation glide planes, are the main microstructural determinants of the strength.

The emergence of an operative edge-to-edge spacing  $L = (0.73 \pm 0.15)\bar{L}$  (average of screw and edge) across many simulations is interesting, but as yet not quantitatively explained. It seems, however, natural that the dislocation will be pinned in the strongest possible configurations, corresponding to some  $L < \bar{L}$ . This finding is in contradiction to the analysis of Friedel [42] for weak point-pinning obstacles, invoked also in the BKS theory [9]. Friedel found that the dislocation will find paths with *longer* average segments ( $L > \bar{L}$ ) in a random microstructure. However, this result in the weak-pinning limit does not apply for Orowan looping.

#### 3.5.2 Role of Microstructure

Here we examine the CRSS for Orowan looping across a wider range of microstructures. Due to the high cost of computing the misfit stresses, their minimal effect on the CRSS, and our interest in comparisons among structures, we consider only systems with zero misfit stresses and focus on  $f=1.10\%$ .

To assess any size dependence of our finite-size simulations, we simulated Orowan looping in a larger  $5 \times 5 \times 5$  pseudo-random micro(100) microstructure (see Table 3.3). The CRSS is statistically identical to the results for the  $3 \times 3 \times 3$  microstructure. This, as well as the small sample-to-sample strength variations among the  $3 \times 3 \times 3$  microstructures, indicates that this

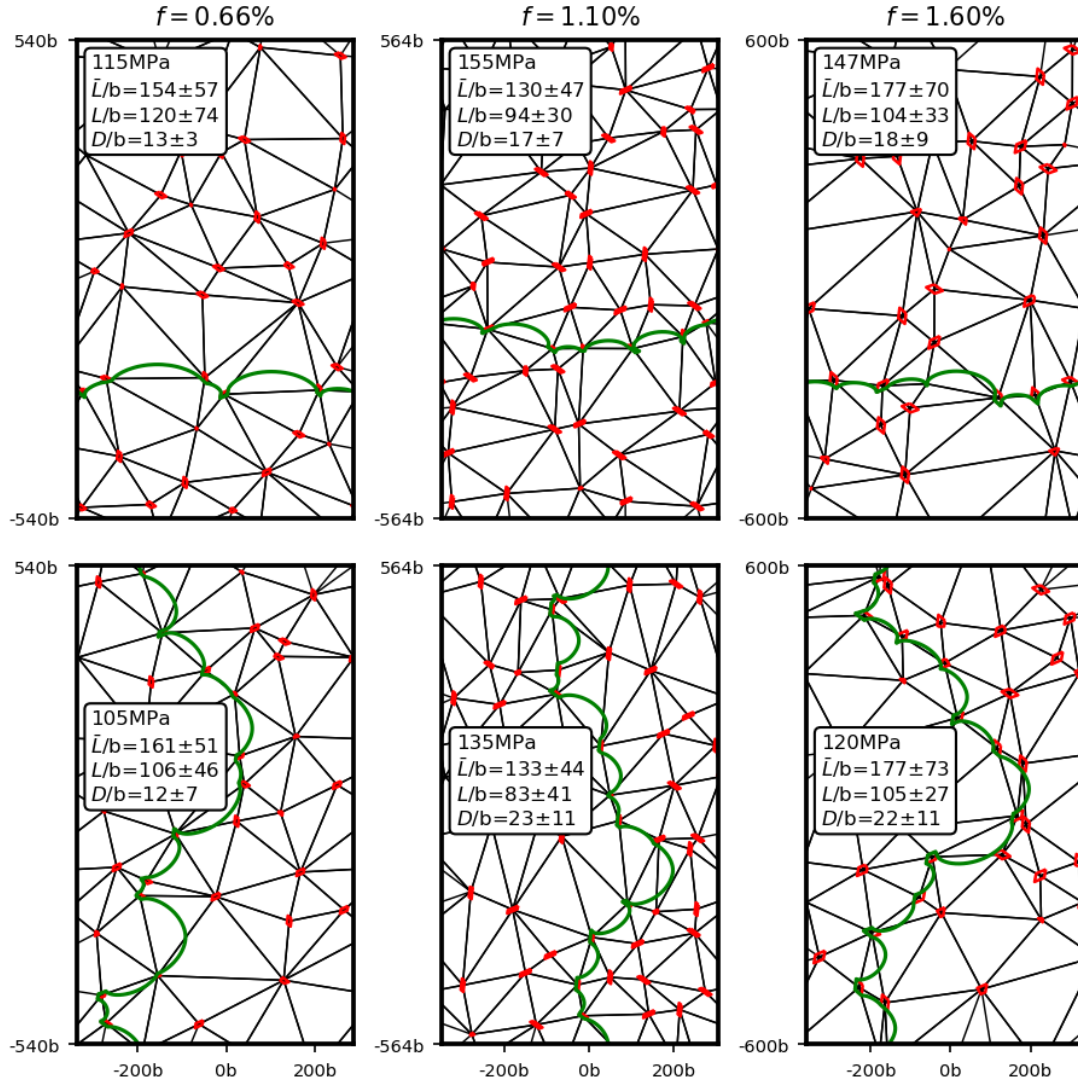


Figure 3.8 – Dual lattice of the Voronoi tessellation of three typical microstructures at  $f=0.66\%$ ,  $1.10\%$ , and  $1.60\%$ , with the average center-to-center precipitate spacing  $\bar{L}$  and average edge-to-edge precipitate distance  $L$  at the CRSS indicated. The dislocation configuration at the simulated CRSS is shown by the green line for screw (upper) and edge (lower) simulations.



size is sufficiently representative. The slow convergence with increasing size found for weak point-pinning obstacles [88] does not apply to the present strong-obstacle problem.

We next compare results using the equiaxed diamond-like  $2\mathbf{a} \times 4\mathbf{c}$  cross-section to the previous rectangle-like  $3\mathbf{a} \times 3\mathbf{c}$  cross-section. Results in Table 3.3 show that the difference is minimal, verifying that the effect of the average precipitate cross-section size is small. The microstructures have the same average spacing  $\bar{L}$  and, more importantly, the same average critical edge-to-edge spacing  $L$  at the CRSS that is the main feature controlling strength.

Turning to the micro(111) microstructures, the CRSS for the case where precipitates do not extend outside the building block shows strengths very slightly lower than the micro(100) (see Table 3.3). The dislocation configuration at the CRSS for a typical case is shown in Figure 3.9 along with the Voronoi tessellation. For this geometry, we find  $\bar{L} = 125b$  and  $L = 89b$ , the latter just slightly larger than for the micro(100) cases and hence consistent with a slightly smaller CRSS. With larger perturbations enabling precipitates to cross building block boundaries, and thus partially eliminating precipitate-free channels, the CRSS is statistically identical to that for micro(100) (see Table 3.3). The dislocation configuration at the CRSS for a typical case is shown in Figure 3.9. For this geometry, the  $\bar{L}$  and  $L$  are  $128b$  and  $84b$ , essentially identical to those found for micro(100), rationalizing the similar strengths.

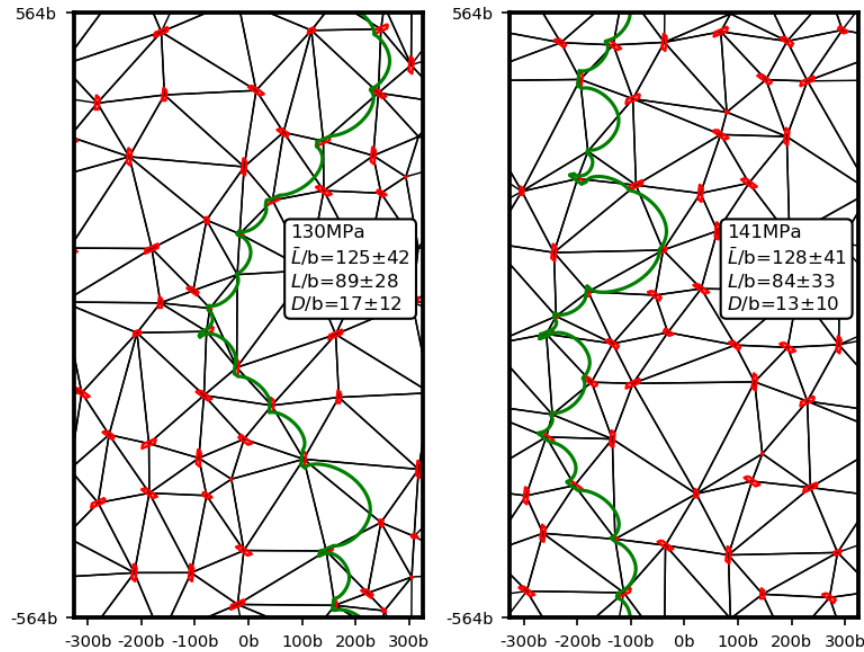


Figure 3.9 – Dual lattice of the Voronoi tessellation of typical micro(111) structures at  $f=1.10\%$  without (left) and with (right) large perturbations. The average center-to-center precipitate spacing  $\bar{L}$  and average edge-to-edge precipitate distance  $L$  at the CRSS for an edge dislocation are shown. The dislocation configuration at the simulated CRSS is shown by the green line.

Finally, we also created several random microstructures in which precipitate cross-sectional shapes were placed randomly, but without overlaps, within the domain at area fraction  $f = 1.10\%$ . We do not believe the purely random microstructure is appropriate for these materials, but a comparison remains interesting. The CRSS for Orowan looping in these random microstructures are statistically identical to those obtained for our pseudo-random microstructures.

From all of these studies, we conclude that the simulated CRSS for Orowan looping is quite robust across variations in the microstructure. The CRSS is thus controlled by a combination of precipitate size, shape, and volume fraction that determines  $\bar{L}$  and  $L$ , with minimal secondary effects of (i)  $D$  and (ii) larger-scale differences between micro(100) and micro(111). The relative insensitivity to these microstructural aspects is important for enabling comparisons with experiment below.

#### 3.5.3 Role of Dislocation Core Energy

The classic BKS analysis of Orowan looping was based on an elasticity analysis, imposing an arbitrary cut-off length  $r_0$  in the calculation of self-energies [9]. The total dislocation energy was then implicitly embedded in the choice of  $r_0$  but its effects were not directly investigated. In ParaDiS and other DDD codes, the inelastic contributions to the total dislocation energy are either neglected or introduced as an additional core energy in an ad-hoc manner, and again the effects of the choice of this core energy on phenomena are rarely examined. Here, we demonstrate the role of a chosen core energy on the CRSS for Orowan looping and, moreover, the importance of retaining an accurate (i.e. atomistic) total dislocation energy for the nanoscale strengthening in Al-6xxx.

Specifically, in addition to the Ercolessi-Adams atomistic energy, we study several other core energy choices. Atomistically, we consider the core energy derived from the Mishin EAM potential [76] at  $T=0K$  [53] and, using an entirely different analysis, at  $T=300K$  by Geslin et al. [44] who found  $a = 1.2b$  as optimal in calibrating to ParaDiS. We then also consider the ParaDiS default core model  $E_c(\theta) = \frac{\mu b^2}{4\pi} \ln(\frac{a}{0.1b})(\cos^2 \theta + \frac{1}{1-\nu} \sin^2 \theta)$ , while noting that there is an additional contribution to the total energy in the non-singular theory that is also automatically included [53]. Finally, we examine a hybrid model as follows. We use the Ercolessi-Adams atomistic core energy measured at  $a = 5.4b$  but then compute all segment-segment elastic interactions in ParaDiS using a much lower shear modulus  $\mu = 10$  GPa. This hybrid model thus suppresses the effects of long-range elastic interactions beyond  $a = 5.4b$ . The material parameters for all of these test cases are shown in Table 3.4. The screw and edge core energies are all quoted at the common value of  $a = b$  for comparison purposes. The full character-dependent core energies  $E_c(\theta)$  that dictate the core contributions to the dislocation line tension  $\Gamma_c = E_c(\theta) + \partial^2 E_c(\theta) / \partial \theta^2$  are used in the DDD simulations. DDD results that preserve the total atomistic energy are essentially independent of  $a$  (see Section 2.7.3).

Results for the CRSS of the  $f = 1.10\%$  micro(100) case averaged over 4 different glide planes are

Table 3.4 – Material parameters and dislocation core energies used in parametric studies of the CRSS for Orowan looping. Shear modulus and Poisson ratio are obtained by Bacon-Scattergood effective properties. Dislocation core energies are quoted at  $a = b$ . The core energy for [44] is recovered from their line tension calibration, and the NS additional term is added back for consistent comparison [53]. The value of  $a$  used in ParaDiS for each case is shown. The CRSS for the  $f = 1.10\%$   $3 \times 3 \times 3$  micro(100) structure is then shown for each case.

core model	$\mu$ (GPa)	$\nu$	$E_c, a = b$ (eV/nm)		$a$	CRSS (MPa)	
			screw	edge		screw	edge
Ercolessi-Adams, T=0K [53]	32.0	0.34	0.810	0.463	5.4b	158±21	139±7
Mishin, T=0K [53]	28.7	0.35	1.262	1.198	1.2b	157±24	140±14
Mishin, T=300K [44]	28.7	0.35	0.939	0.732	1.2b	138±23	124±13
ParaDiS [7]	32.0	0.34	2.972	4.504	1b	289±26	254±18
Hybrid	10.0	0.33	0.810	0.463	5.4b	135±12	133±8

shown in Table 3.4 for the different core models. Use of the T=0K core energy from the Mishin potential yields statistically identical results to those using the Ercolessi-Adams potential. The core energies for edge and screw do differ slightly (see Table 3.4), but Orowan looping involves the full line tension  $\Gamma$  and so differences between edge and screw are not sufficient for a quantitative comparison. The use of the Geslin et al. calibration to the Mishin potential at 300K [44] leads to a modest decrease in the CRSS of 16-21 MPa. All the atomistically-calibrated results are thus quite comparable. In contrast, use of the default ParaDiS core energy model leads to a huge increase, nearly doubling the CRSS for Orowan looping while still using the Ercolessi-Adams elastic constants.

Finally, the limited role of the long-range elastic energies is demonstrated by the hybrid model (reduced-modulus simulation that retains the Ercolessi-Adams core energy at  $a = 5.4b$ ). The CRSS for this hybrid model is reduced by only 23 MPa (15%) for the screw and only 6 MPa (5%) for the edge. Standard elasticity-based models and simulations would show that all strengths scale directly with  $\mu$ . While the core energy has some interplay with  $\mu$  and  $a$ , results of Hu et al. [53] for Al, Cu, and Ni show that the core energies at a fixed  $a$  are not directly proportional to the corresponding shear moduli. Accurate modeling, relative to atomistic models, thus requires a proper calibration of a core energy contribution to the total dislocation energy versus character for a chosen scale  $a$ . Accurate results for the CRSS of Orowan looping here requires an accurate representation of the energy within  $a = 5.4b$  (independent of its partitioning between elastic and core contributions), with long-range elastic interactions having a very small effect.

### 3.5.4 Comparison with Experiments

In commercial Al-6061, Ozturk et al. examined both the yield strength and the hardness as a function of aging time [92]. When the precipitate microstructure is well-formed (around peak aging), they showed that the tensile yield stress (in MPa) was quantitatively equal to 3 times the Vickers Hardness,  $\sigma_y = 3HV$ . This is essentially the relationship between yield and hardness derived by Taylor for an elastic/perfectly-plastic material. This relationship presumably applies well to this system because the work-hardening rate is quite low around the peak aged condition. Using this validated relationship, the measured hardness of 97 kg/mm<sup>2</sup> in the A2(NA+AA) alloy studied by Wenner et al. [124] corresponds to a tensile yield stress of 291 MPa. The peak-aged strength in Al-6061 measured by Ozturk et al., but without any microstructural information, was comparable at 275 MPa. For an alloy denoted as A12 having a microstructure with  $f = 1.2\%$  containing longer (69 nm) and larger-area (12.2 nm<sup>2</sup>) precipitates, Mariaora et al. [74] report a peak-aged hardness of 104 kg/mm<sup>-2</sup> corresponding to a yield stress of 312 MPa. Thus, all results on peak-aged materials are fairly similar.

The Orowan looping strengths for screw and edge dislocations in the representative  $f = 1.10\%$   $3 \times 3 \times 3$  pseudo-random microstructures using the Ercolessi-Adams EAM Al T=0K elastic constants, core energy [32, 53], and misfit stresses are 164 MPa and 140 MPa, with an average of 152 MPa. Using a Taylor factor of 3.06 for an untextured large-grain polycrystal, we thus estimate the tensile strength as 465 MPa. We have shown that this strength is robust against a range of microstructural differences and atomistically-calibrated core energies at T=0K, and is much smaller than the CRSS coming from a default ParaDiS simulation. Nonetheless, this result is significantly higher ( $\approx 50\%$ ) than the experimental strengths of  $\approx 300$  MPa.

The experiments are at room temperature. Using the average reduction in CRSS of 17.5 MPa found when using the room temperature core energy of Geslin et al. [44] for the Mishin potential [76], the predicted strength is reduced to 411 MPa. This improves the agreement with experiment but remains roughly 33% higher than experiments. Thermal activation of precipitate strengthening at finite T and experimental strain rates is usually quite small, as revealed by standard Haasen plots [6], and so is unlikely to explain this remaining difference.

Overall, we conclude that the modeling of Orowan looping using realistic precipitate microstructures, state-of-the-art computational methods, and atomistically-calibrated dislocation core energies, results in a non-negligible *over-prediction* of the room-temperature strength of peak-aged Al–Mg–Si alloys. Our findings indicate that, while Orowan looping may provide an upper bound for the yield stress, the yield stress at peak aging is not quantitatively determined by Orowan looping. This finding is in contrast to standard metallurgical wisdom.

## 3.6 Precipitate Shearing

In the previous sections, we have modeled Orowan looping with what we believe is the highest degree of realism at above-atomistic scales. We have not included dislocation dissociation into

two partial dislocations separated by a stacking fault ribbon nor elastic mismatch effects, both of which are computationally demanding and not likely to bridge the gap between experiments and simulations. As a result, we deduce that precipitate shearing is most likely occurring and is the controlling mechanism even at peak aging. This deduction is actually consistent with very recent experimental TEM observations of multiply-sheared precipitates in this alloy [23], but is not consistent with the traditional textbook view of the strengthening at peak aging. Here, we therefore make a preliminary examination of precipitate shearing.

The critical material parameter for precipitate shearing is the generalized fault energy corresponding to shearing of the precipitate by Al  $[110]a/2$ -type dislocations gliding on  $(111)$ -type planes. This information has heretofore been unknown, making assessment of shearing impossible in this alloy. These generalized fault energies were recently computed, however, for the three  $\beta''$  precipitates using first-principles Density-Functional Theory [58]. Across all the  $[110]a/2$  Al Burgers vectors projected onto the  $(51\bar{1})$  and  $(112)$  planes in  $\beta''$  that align nearly perfectly with the Al  $(111)$  slip planes, a typical accessible shearing fault energy can be estimated as  $\gamma_f = 450 \text{ mJ/m}^2$ .

We first consider the shearing in terms of forces. For a dislocation shearing into a rectangular precipitate along an edge of length  $D$ , the force required to overcome the fault energy is  $F = \gamma_f D$ . For the precipitates here with typical precipitate dimension  $D = \sqrt{A} = 3 \text{ nm}$  and  $\gamma_f = 450 \text{ mJ/m}^2$ , the typical necessary force is  $F = 1.35 \text{ nN}$ . Figure 3.10 shows the total forces acting on the precipitates at the critical stress for Orowan looping as computed by DDD. The individual nodal forces are concentrated at the precipitate corners (not shown), with the forces along the straight pinned regions comparatively small. This is expected since these (configurational) forces are dominated by the core energy and line tension concentrated in regions of high curvature or high angle change. The total force exceeds the estimated shearing force of  $F = 1.35 \text{ nN}$  in 10 of 17 precipitates for the edge and 4 of 12 precipitates for the screw. Thus, the DDD results indicate that significant precipitate shearing could occur prior to Orowan looping.

The above analysis does not include the effects of the misfit stresses inside the precipitate. We thus now examine an overall energy balance for the shearing of an average precipitate that accounts for the applied stress, the internal precipitate misfit stress, and the shearing energy cost as follows. For simplicity, we consider the cutting of a square  $D \times D$  precipitate parallel to the edge of the precipitate. A single precipitate is cut with the dislocation pinned at the neighboring precipitates as shown schematically in Figure 3.11. An analysis of cutting diagonally starting at the apex of the square leads to a more-complex result where thermal activation must be considered but final quantitative results at experimental temperatures and strain rates are quite similar to those of the analysis we show now.

As shown in Figure 3.11, when the dislocation cuts the precipitate over an incremental distance  $dx$  the two adjacent dislocation segments of length  $L_s$  in the matrix bowout such that the applied stress  $\tau$  does work on the system of  $\tau b L_s dx$ . Work of  $\tau_{\text{misfit}} b D dx$  is also done by the

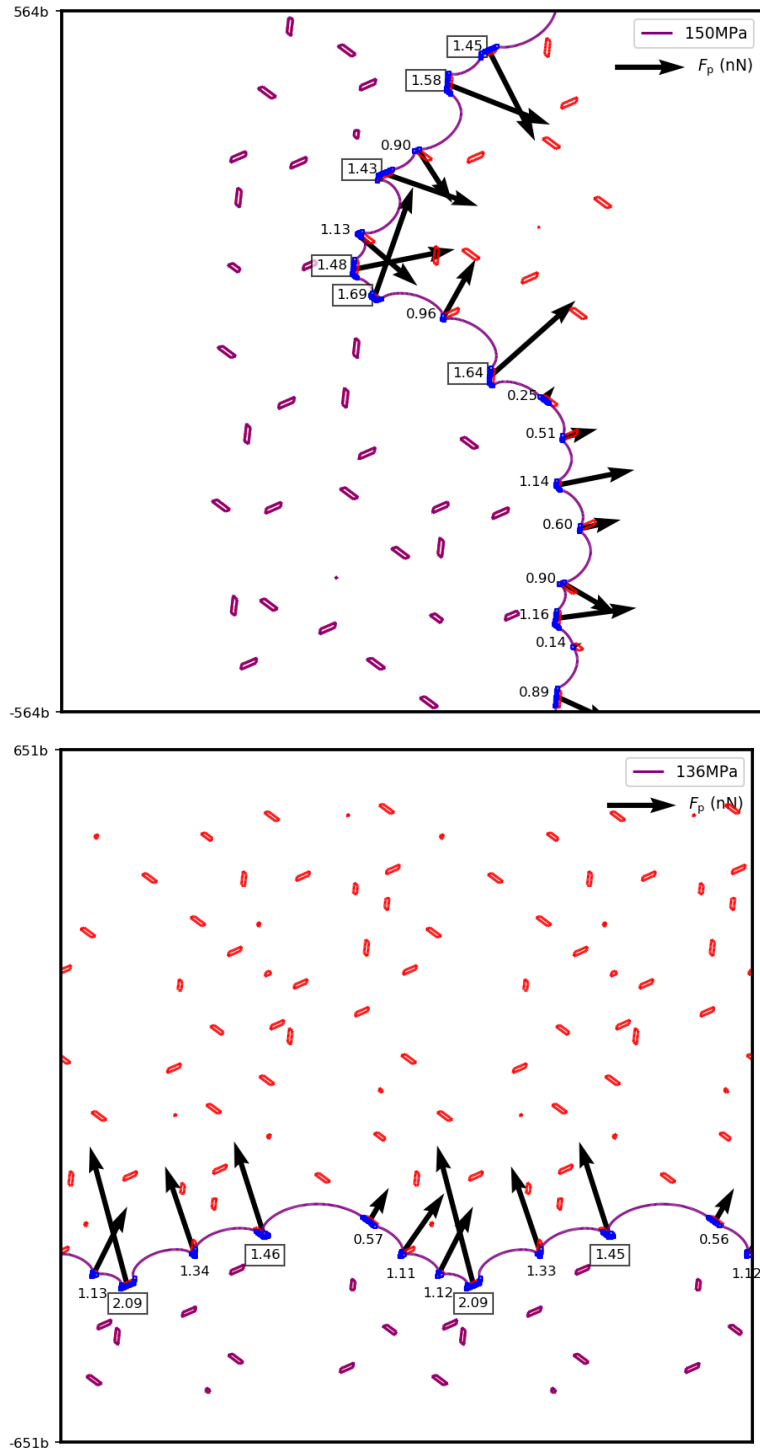


Figure 3.10 – Forces  $F_p$  exerted by the dislocation on each precipitate as computed in DDD, for edge (top) and screw (bottom) dislocations at the CRSS for Orowan looping. These forces are to be compared with the critical value for shearing of  $\gamma_f D = 1.35$  nN, with values shown in boxes exceeding this value.

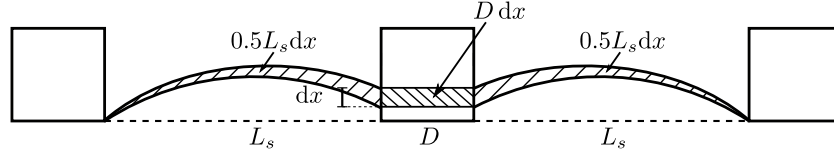


Figure 3.11 – Shearing of a precipitate by a dislocation, showing the incremental areas swept by the dislocation for an advance by distance  $dx$  inside the precipitate.

*internal* precipitate misfit stress  $\tau_{\text{misfit}}$ . We consider those precipitates where the sign of the misfit stress assists the cutting. Finally, the energetic cost of creating the additional area of faulted precipitate is  $\gamma_f D dx$ . Precipitate shearing is achieved at the stress for which the net incremental energy cost is zero,  $\tau b L_s dx + \tau_{\text{misfit}} b D dx - \gamma_f D dx = 0$ . This leads to the critical stress (strength for precipitate shearing) of

$$\tau_c = \frac{\gamma_f D - \tau_{\text{misfit}} b D}{b L_s} \quad (3.4)$$

In appropriately-oriented precipitates, the internal precipitate misfit stress can act as an effective reduction of the fault energy, lowering the strength for shearing. Once these precipitates shear and the dislocation advances, the remaining precipitates will either shear or be by-passed by Orowan looping at this stress; this will be examined by DDD below.

We apply the above analysis using values for alloy A2(NA+AA) of  $D = 3$  nm, precipitate center-to-center distance  $\bar{L} = \sqrt{6} l_c / 3 = 35.8$  nm, and hence  $L_s = \bar{L} - D$ ,  $b = 2.851$  Å, and  $\gamma_f = 450$  mJ/m<sup>2</sup>. The sign of the misfit RSS depends on Burgers vector and line direction, and so only some of the precipitates will assist shearing but the absolute magnitude of the shearing is clear, with an average of 347 MPa for screw dislocations and 266 MPa edge dislocations. The predicted CRSS values for shearing are 113 MPa for the screw and 120 MPa for the edge. Taking the average of 116.5 MPa corresponds to a tensile yield stress of  $\sigma_y = 356$  MPa, which is much closer to experiments. Local statistical fluctuations or a reduction of the GSFE energies with temperature [122] would reduce the CRSS, while dislocation pinning at smaller values of  $L_s$  would increase the CRSS; these are beyond the scope of the present analysis.

We can then use DDD to verify that the CRSS due to shearing of favorable precipitates would allow subsequent Orowan looping and/or shearing of any remaining precipitates. This is done by approximately mimicking the consequences of precipitate shearing as follows. We perform a DDD simulation in which all precipitates that would be cut with the assistance of the internal precipitate misfit stresses are removed at the start of the simulation. This leaves a microstructure with 1/3 fewer precipitates for the edge and 2/3 fewer precipitates for the screw. In such a modified  $f = 1.10\%$  micro(100) microstructure, the average CRSS values for the residual Orowan looping are 105 MPa and 103 MPa for screw and edge dislocations. These reductions are consistent with larger precipitate spacing  $\bar{L}$  due to fewer precipitates, and we find the corresponding critical  $L$  values to have a ratio  $L/\bar{L}$  similar to those in the original microstructures. Most importantly, these values for looping are lower than the estimated CRSS

values for the initial shearing so that the initial shearing would control the CRSS. Finally, at the CRSS for looping in these modified microstructures, the forces acting on the unsheared precipitates are shown in Figure 3.12 and some of them can again exceed the shearing resistance  $\gamma_f D + |\tau_{\text{misfit}}| bD$  even though the remaining misfit stresses now inhibit shearing. Thus, after shearing of the initial shearable precipitates, both shearing and looping are estimated to enable dislocation motion through the remainder of the precipitates in the microstructure.

Overall, this preliminary theoretical and simulation study of shearing indicates that the CRSS in peak-aged Al-6xxx should be controlled by precipitate shearing rather than Orowan looping, and that the estimated CRSS values are closer to experimental strengths.

## 3.7 Conclusion

We have presented a detailed analysis of dislocation motion through realistic precipitate microstructures in Al-6xxx (Al-Mg-Si) alloys at the peak-aging condition with the goal of making quantitative connection with experiments.

We first examined Orowan looping as the controlling strengthening mechanism, since Orowan looping and precipitate shearing are believed to give the same strength at peak-aging. We created realistic pseudo-random precipitate microstructures, calculated the misfit stress fields, and examined dislocation motion using Discrete Dislocation Dynamics. We found that (i) matrix misfit stresses have little influence on the CRSS for looping, (ii) the CRSS for screw and edge are quite similar, in contrast to classic elasticity models [9], (iii) the CRSS is controlled by a critical edge-to-edge precipitate spacing  $L$  that is smaller than the average spacing  $\bar{L}$  with  $L/\bar{L} \approx 0.73$ , in contrast to the weak-pinning Friedel model, with other microstructural features of less importance, and (iv) dislocation core energies dominate over longer-range elastic energies so that calibrated atomistic core energies are essential for quantitative results. With a room temperature atomistic core energy, we predict a tensile yield strength that remains 33% above the experimental value. The Orowan looping mechanism is thus only an approximate upper bound for the tensile yield strength in this peak-aged alloy.

Analysis of the DDD-computed forces on precipitates and the resisting forces derived from precipitate generalized stacking fault energy shows that many precipitates could be sheared prior to Orowan looping. An energy-based prediction of precipitate shearing that includes the effects of the internal precipitate misfit stresses then leads to an estimated CRSS that is closer to experiments.

Overall, this chapter demonstrates a number of new findings that indicate that classical and continuum analyses quantitatively fail when applied to nanoscale microstructures such as peak-aged Al-6xxx. Accurate modeling requires detailed microstructures, calibrated dislocation energies, relevant misfit stresses, and realistic precipitate shearing energies. Fortunately, all of these new aspects are computationally accessible, so that the general methodology introduced here can be widely applied to Al and other alloys that rely on nanoscale precipitation to



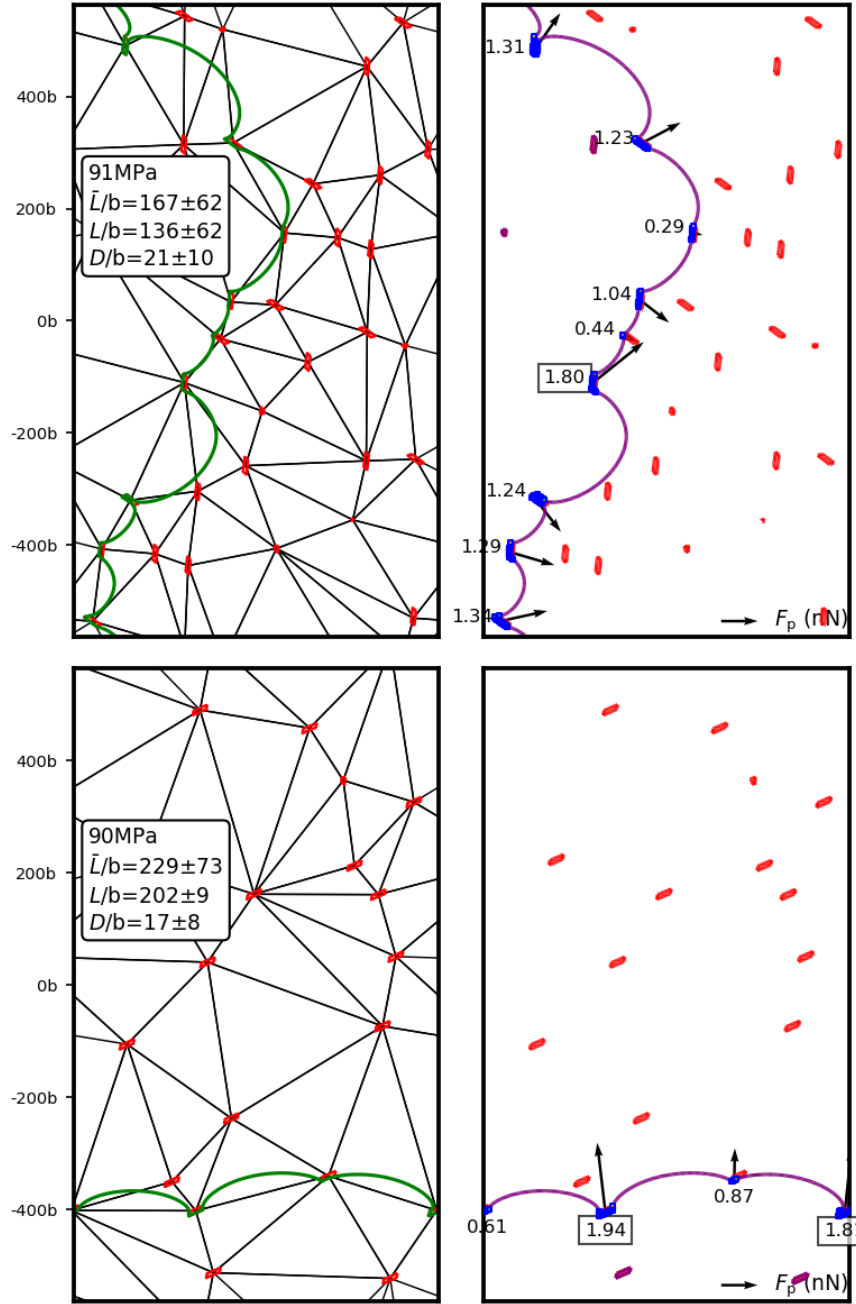


Figure 3.12 – DDD simulations of dislocation motion through microstructures where the shearable precipitates have been removed, for edge (above) and screw (below) cases. Left figures show the critical configuration and relevant spacings. Right figures show the forces acting on the precipitates at the critical configuration, with boxed values above the critical resisting force  $\gamma_f D + |\tau_{\text{misfit}}| b D$  (1.65 nN for edge and 1.58 nN for screw, respectively).

### **Chapter 3. Mesoscale Study of Precipitation Strengthening**

---

achieve strengths that make them technologically valuable. The present approach can further be used to understand how strength can be optimized by modifications to microstructure or chemistry of precipitates, thus providing guidance to future alloy development.

## 4 Dislocation-Precipitate Interaction at Atomistic Scale

This chapter is adapted from the following article, with permission from the coauthors and the publisher.

**Yi Hu** and W. A. Curtin. Near-chemically-accurate modeling of precipitate strengthening in Al-6xxx alloys. *in preparation*. 2021.

### 4.1 Introduction

In the Al–Mg–Si alloys (Al–6xxx series), the peak strength is achieved by the formation of metastable needle-shaped  $\beta''$  precipitates through a controlled heat treatment starting from the solutionized alloy [86]. Dislocations moving through the alloy must bypass the  $\beta''$  precipitates by Orowan looping or by shearing of the precipitates, or by some combination of these phenomena. These phenomena are controlled by a range of material and microstructure properties: the size, shape, and volume fraction of the precipitates, the coherency or misfit stresses induced in the matrix and precipitates, the energies required to shear the precipitates along the (111)-type glide planes of the operative dislocations in fcc Al, and the line tension of those dislocations. This level of complexity - competing mechanism dependent on microstructure and chemistry - poses a daunting challenge for any a priori prediction of the alloy strength or the guided design of higher-performing alloys. The goal of the present chapter is to demonstrate a path to address this challenge through a combination of modeling methods and theories, using the Al-6xxx alloys as the demonstration platform.

Given the importance of the general problem of understanding the microstructure/property relationships in precipitation-strengthened alloys, there has naturally been extensive theoretical and simulation work over the years. The prevailing basic models predict that, for a fixed precipitate volume fraction and for circular precipitate cross-section of radius  $r$  on the glide plane, the Critical Resolved Shear Stress (CRSS) scales with  $1/r$  for Orowan looping and  $\sqrt{r}$  for shearing [84]. The lower of the two strengths determines the CRSS, and the peak-aged condition is attained when the two CRSS are equal. This widely accepted wisdom has been

verified by simulations and experiments of spherical precipitates [78] (reviewed in Section 1.3). Various precipitation strengthening models exist [82, 34, 10] but do not include much physical atomistic detail and often with extensive experimental calibrations. Quantitative predictions require far more chemical and mechanical details. Several recent atomistic studies have been reported for Al–Cu alloys [111, 36, 63] but the interatomic potentials used have some artifacts [71]. Thus, to date, there has been no reliable atomistic study that incorporates all the necessary alloy details accurately and with no comparisons to independent theory or higher scale simulation models.

For Al–Mg–Si alloys, extensive experiments have identified the precipitate structures, orientations, and compositions [3, 72, 124]. Experiments show that there is a shearing to looping transition in Al-6xxx alloys [97] and a recent study shows that precipitates are actually sheared for peak-aged Al–Mg–Si alloys [24]. First principles calculations of precipitate properties and some energetic aspects of precipitate nucleation have been presented [87, 46]. Our recent work has studied Orowan looping in realistic microstructures using an atomistically-calibrated discrete dislocation model [52]; analysis therein also suggests that precipitate shearing occurs in the peak-aged microstructure. Furthermore, an Al–Mg–Si Neural Network Potential has been developed that predicts many alloy and precipitate properties in good agreement with first principles, including the relevant shearing energies for  $\beta''$  precipitates [58].

The above recent efforts now enable the present work, which is a detailed atomistic study of dislocation-precipitate interactions in Al-6xxx alloys with comparisons to calibrated discrete dislocation models, comparisons to theories, and ultimately predictions relevant to real alloys. The remainder of this chapter is organized as follows. We first present theories of precipitate shearing and looping in Section 4.2. Benchmark properties of the Al–Mg–Si Neural Network Potential are presented in Section 4.3 followed by discussion of the simulation methods and models in Section 4.4. We then quantitatively assess the continuum misfit stresses and calibrated DDD models versus direct atomistic simulations in Section 4.5. Detailed analysis of atomistic simulations and theoretical predictions of the CRSS are presented in Section 4.6, largely validating the theories. In Section 4.7, we connect our results to real alloys, culminating in a prediction of the peak-aged yield stress for Al-6xxx. Finally, we summarize major findings of this scope of work.

## 4.2 Theories for Precipitate Shearing and Looping

### 4.2.1 Precipitate Shearing

Using the  $\beta''$  precipitate shapes and orientations as an example, precipitate shearing can be analyzed using an energetic analysis. There are three in-plane orientations of this precipitate on the (111)-type glide planes of Al which we discuss later and denote as  $p_x$ ,  $p_y$ , and  $p_z$ . We start with the configuration associated with the  $p_x$  and  $p_y$  orientations as shown in Figure 4.1, with center-to-center precipitate spacing  $\bar{L}$ . We neglect the complex matrix Resolved Shear

## 4.2. Theories for Precipitate Shearing and Looping

Stress (RSS) field to achieve a general analytic result. A dislocation shearing the precipitate does so by a minimum-energy path. Inside the precipitate, the dislocation orients itself to align with the minimum span distance  $D$  so as to minimize the incremental sheared area as the dislocation advances. We consider the simple case where  $D$  is constant through much of the precipitate; the analysis can be generalized to other shapes. Outside the precipitate, the dislocation in the matrix adopts the lowest perimeter/area ratio to minimize the elastic or line energy relative to the work done by the applied stress over the area swept by the dislocation. In a simple line tension model with line tension  $T$ , this shape is a circular arc. The dislocation then advances through the precipitate by a rigid gliding of this configuration. The stress required to advance the dislocation is determined by an energy balance for an incremental advance  $dx$  in the glide direction. Similar to Ref. [79], the energy contributions are (i) the work  $-\tau b \bar{L} dx$  done by the applied stress on the dislocation over the incremental swept area, (ii) the work  $\tau_p b D dx$  done by the RSS field inside the precipitate where we take the sign of the RSS to be positive when acting in the direction of the applied field, and (iii) the energy cost  $\gamma D dx$  to shear the precipitate. At the CRSS  $\tau_c$ , the incremental energy change is zero,  $\tau_c b \bar{L} dx + \tau_p b D dx - \gamma D dx = 0$ , leading to

$$\tau_c = \frac{(\gamma/b - \tau_p)D}{\bar{L}} \quad (4.1)$$

The CRSS for shearing thus scales linearly with the precipitate span  $D$  (which can be generalized to be the largest  $D$  when traversing the precipitate in the glide direction) and inversely with the center-to-center precipitate spacing  $\bar{L}$ . The shearing energy and RSS combine to give an effective net resistance to shearing. Note that, in the above model, the dislocation line tension is irrelevant - the shape of the bowed-out loop in the matrix is irrelevant because it is constant during the shearing motion (and generalizing, essentially constant over each increment  $dx$  even if it changes during the shearing process, e.g. for a circular precipitate).

When the precipitate orientation is such that the span  $D$  for shearing in the glide direction is very large, the CRSS from the above model is then high. The dislocation can thus seek a lower-energy path. This is the case for edge dislocations intersecting the pz precipitate; the geometry and dislocation configuration are shown in Figure 4.1b. The dislocation again seeks to shear the precipitate along the shortest possible direction inside the precipitate, which is now parallel to line direction. The dislocation motion can involve forward glide in the matrix by distance  $h$  and lateral glide of the dislocation through the precipitate by distance  $\Delta$ . Again, the initial shearing of the precipitate corners has a low energy cost and so analysis starts with the dislocation having sheared up to the span  $D$ . For analysis, the entire dislocation line is divided into four sections (Figure 4.1b): a segment of length  $D$  shearing the precipitate; a segment of length  $\Delta$  along the precipitate edge; two advancing segments of length  $h$ ; and a circular arc connecting to the two advancing segments.

Extending the standard analysis of circular bow-out within a line tension model (e.g. see [126]), the total energy of the above geometry is written as the sum of the dislocation shearing energy, the total dislocation line energy, the work done by the applied field over the total swept area,

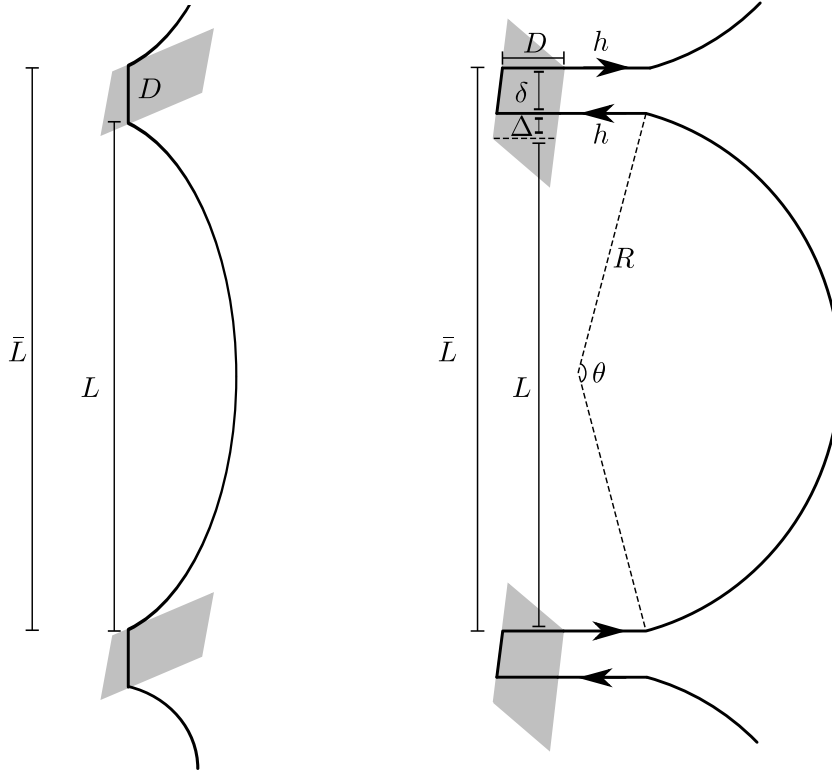


Figure 4.1 – Simplified model for CRSS prediction. Left: edge px/py interaction, Right: edge pz interaction.

and an additional interaction energy between the two straight segments of length  $h$  separated by distance  $\delta = \bar{L} - L - \Delta$ . The total energy is thus

$$E(\Delta, h, \tau) = (\gamma - \tau_p b) D \Delta + TS + W(h, \delta) - \tau b (A + D \Delta) \quad (4.2)$$

where  $A$  and  $S$  are swept area and dislocation length in the matrix,  $W(h, \delta)$  is the interaction energy between the short dislocation segments [49] of

$$W(h, \delta) = \frac{\mu b^2}{2\pi} \left( \sqrt{h^2 + \delta^2} - \delta + h \ln(\sqrt{h^2 + \delta^2} - h) - h \ln \delta \right) \quad (4.3)$$

For this geometry, and in the line tension model, we further have

$$\begin{aligned} S &= 2h + R\theta - \Delta \\ A &= (L + \Delta)h + \frac{1}{2}R^2(\theta - \sin\theta) \\ R &= \frac{T}{\tau b} \\ \theta &= 2 \sin^{-1} \left( \frac{\Delta + L}{2R} \right) \end{aligned} \quad (4.4)$$

## 4.2. Theories for Precipitate Shearing and Looping

For a specified precipitate geometry ( $D$ ,  $L$ ,  $\bar{L}$ ) and material properties ( $T$ ,  $\gamma$ ,  $\tau_p$ ), the total energy thus depends only on the load  $\tau$  and dislocation configurational variables ( $\Delta$ ,  $h$ ).

In the absence of a shearing energy and internal RSS  $\tau_p$ , the above analysis always shows lateral extension  $\Delta$  at any applied load. Thus, as expected, in the absence of a precipitate, the geometry of Figure 4.1 is never realized - it is unstable. It is thus only the cost of precipitate shearing that leads to dislocation pinning and a CRSS, as physically expected.

For a given load  $\tau$ , we then seek configurations  $\Delta$ ,  $h$  that are local minima of the total energy. At low loads,  $\Delta = 0$ ,  $h = 0$  is always a local minimum. With increasing load the energy barrier between the local minimum at ( $\Delta = 0$ ,  $h = 0$ ) and lower energy configurations at finite ( $\Delta$ ,  $h$ ) decreases, reaching zero at the Critical Resolved Shear Stress. Results for this model depend on the detailed geometry and material properties. We thus defer analysis until we apply the model to the specific cases simulated atomistically.

Absent from the above analyses are several other possible effects. First, the dislocation core energy inside the precipitate will differ from that in the matrix; if larger, this can prevent initial penetration into the precipitate. Second, as mentioned, the work done by the matrix RSS is neglected. Third, the dissociated nature of the fcc dislocations is neglected. The GSFE for shearing by one Shockley partial may be larger than for shearing by a full Burgers vector, and that will either inhibit penetration by the first partial or require the dislocation to constrict to a compact structure before penetration, costing energy. Analysis of the GSFE at the slip corresponding to the partial Burgers vector and application of the energy balance to the partial dislocation enables some assessment of this process.

### 4.2.2 Precipitate Looping

Orowan looping has a long history of investigation, mainly numerical starting with the classic work of Bacon, Kocks, and Scattergood (BKS) [9]. For a Frank-Read (FR) source, numerical work using both Discrete Dislocation Dynamics methods [30, 40] and atomistic simulations [129] have shown that the CRSS of Orowan looping is

$$\tau = \frac{2T}{bL} \quad (4.5)$$

where  $T$  is the line tension and  $L$  the source length. With estimate  $T = 0.5\mu b^2$ , (4.5) simplifies to the Orowan stress  $\mu b/L$ . For a periodic bowout geometry, BKS fit their DDD results to the slightly more nuanced numerical form

$$\begin{aligned} \tau^{\text{edge}} &= \frac{\mu b}{2\pi L} \left[ \ln\left(\frac{\bar{D}}{b}\right) + B \right] \\ \tau^{\text{screw}} &= \frac{\mu b}{2\pi(1-\nu)L} \left[ \ln\left(\frac{\bar{D}}{b}\right) + B \right] \end{aligned} \quad (4.6)$$

where  $\bar{D} = (D^{-1} + L^{-1})^{-1}$  and  $B$  is some constant. This form was aimed at including the attraction of periodic loops across the precipitate span  $D$ . With  $T$  scaling typically as  $\mu b(\ln(\bar{D}/b) + B)$ , the CRSS for the FR source and BKS models have the same dominant scaling of  $\mu b/L$ .

The major trends for the CRSS for looping are thus the linear scaling with line tension  $T$  and the inverse scaling with spacing  $L$ . The inverse scaling with  $L$  is thus nearly identical to the scaling for shearing derived above. The remaining dependencies are much weaker, more subtle, and not derived. Thus, in this work, we execute calibrated DDD simulations for the specific geometries studied atomistically and compare them with the corresponding atomistic simulations. This provides a precise comparison, rather than using any approximation that was fitted to simulations using other treatments of the dislocation mechanics [118].

### 4.3 Benchmarking of the Al–Mg–Si Neural Network Potential

A set of Al–Mg–Si Neural Network Potentials have been reported and thoroughly discussed in [58]. These NNPs used the Behler-Parrinello scheme [11] and were trained against over 5000 representative atomistic structures computed via first-principles density-functional theory (DFT). The training was performed using the open source code n2p2 [113] and atomistic simulations used n2p2 with its interface to the LAMMPS [94] code for Molecular Statics simulations. The complete set of potentials can be found on Materials Cloud [57]. Here we use the NNP16 potential that was determined to be among the most accurate overall and which is currently being used to study natural aging in Al-6xxx alloys [58].

Various baseline properties as predicted by NNP16 for both the Aluminum matrix and relevant  $\beta''$  precipitates are shown in Table 4.1 along with the reference DFT values. The elastic constants for the monoclinic  $\beta''$  precipitates are given for an orientation with lattice vectors  $\mathbf{c} \parallel [\bar{3}01]_{\text{Al}}$  as the 3 axis and  $\mathbf{b} \parallel [010]_{\text{Al}}$  as the 2 axis. Agreement with the DFT reference values is broadly good, with a few exceptions. First, the Al elastic constant  $C_{44}$  and associated isotropic shear modulus are both larger than DFT by  $\approx 20\%$ , and DFT itself is slightly higher than experimental values. This affects the dislocation line tension and hence the stresses for Orowan looping. Second, the  $\mathbf{b}$  lattice constant for  $\text{Mg}_5\text{Si}_6$  is too small by  $\approx 3\%$ , which generates larger misfit stresses for this precipitate and thus could influence both looping and shearing.

Of crucial importance for precipitate shearing are the Generalized Stacking Fault Energies (GSFE) for shearing of the precipitates embedded in the Al matrix [58]. The in-situ precipitates have a needle-shape structure with the  $\mathbf{b}$  axis aligned with one of the cubic axes of fcc Al matrix. We thus label the precipitates according to this axis, with the “px” precipitate having  $\mathbf{b} \parallel [100]_{\text{Al}}$  and similarly for “py” and “pz” precipitates. We will model slip along the Al (111) glide plane with Burgers vectors of  $[1\bar{1}0]_{\text{Al}}$  and its negative  $[\bar{1}10]_{\text{Al}}$ . The relevant slip energies  $\gamma$  are not local minima in the GSFE, unlike the antiphase boundaries in simple intermetallics, and are shown for each precipitate and Burgers vector combination encompassing all six possibilities. While several of the NNP16 shearing energies agree well with DFT, others are too large by



$\approx 20\%$ ; this will affect the stress levels for shearing.

Finally, to calibrate the DDD model requires the atomistic dislocation core energy as a function of dislocation character angle  $\theta$ . The method is described in [53]. The core energy at the reference radius  $b$  (magnitude of the Al Burgers vector) are  $E_c(\text{screw}) = 0.100 \text{ eV}/\text{\AA}$  and  $E_c(\text{edge}) = 0.078 \text{ eV}/\text{\AA}$ . For comparison, the core energy for Al as calculated using the long-standing Ercolessi-Adams EAM potential is  $E_c(\text{screw}) = 0.081 \text{ eV}/\text{\AA}$  and  $E_c(\text{edge}) = 0.046 \text{ eV}/\text{\AA}$ .

The NNP16 for Al–Mg–Si is thus not perfect relative to DFT, but these NNPs are far superior to any traditional existing alloy potentials currently available. Thus, we can perform full atomistic simulations to observe important phenomena, interpret those phenomena using quantitative theories, and then apply the theories using more-accurate DFT material parameters as needed to make connections to real alloys.

## 4.4 Simulation Models

### 4.4.1 Atomistic Simulations

Atomistic models of  $\beta''$  precipitates embedded in an Al matrix with and without an initial dislocation in the Al matrix are constructed in several steps using the AtomsK package [48]. First, a cuboidal cell of Al matrix oriented with axes  $x = [1\bar{1}0]_{\text{Al}}$ ,  $y = [11\bar{2}]_{\text{Al}}$ , and  $z = [111]_{\text{Al}}$  is created. For calculations of misfit stresses, a perfect Al fcc lattice is used with periodicity in all three directions. For calculations involving a dislocation, the periodic array of dislocation geometry (PAD) [91] is used wherein an edge/screw dislocation is inserted into the cell with periodicity along the line direction and glide direction and free boundaries along the surfaces normal to the glide plane. Second, a precipitate “needle patch” is constructed by creating a slice of the precipitate of length  $\mathbf{b}_{\text{Al}}$  within a thin square-shape slice of Al matrix (Figure 4.2a), all atoms are relaxed holding the outer boundaries fixed, and a stacking of these identical slices creates an embedded precipitate of length  $41|\mathbf{b}_{\text{Al}}|$ . Third, the “needle patch” is rotated into the matrix cell coordinate system and inserted into the larger cell, removing the corresponding Al atoms in the same volume (same number of layered slices, same number of atoms). An example of the resulting construction is shown Figure 4.2b. A final relaxation of all atoms consistent with the boundary conditions (fully periodic or mixed) is performed with the conjugate gradient method and convergence to a force norm of  $1 \times 10^{-2} \text{ eV}/\text{\AA}$ .

In the absence of a dislocation, the misfit stress field in the Al matrix is calculated using the Elastic Strain modifier in *ovito* [116]. The fields inside the precipitate are more subtle due to the complex crystal structure and the inability to compute virial stresses within *n2p2*. We thus compute the strain field over the central precipitate unit cell (22 atoms) within the larger precipitate needle as follows. The three lattice vectors  $\mathbf{a}, \mathbf{b}, \mathbf{c}$  of the perfect are known. In the in-situ relaxed precipitate, these vectors are deformed to  $\mathbf{a}' = \mathbf{F}\mathbf{a}$ ,  $\mathbf{b}' = \mathbf{F}\mathbf{b}$ , and  $\mathbf{c}' = \mathbf{F}\mathbf{c}$ , respectively, where  $\mathbf{F}$  is the deformation gradient. Determining  $\mathbf{F}$  from the measured  $\mathbf{a}', \mathbf{b}', \mathbf{c}'$ , the elastic strain is then computed as  $\boldsymbol{\epsilon} = \frac{1}{2}[\mathbf{F}^T + \mathbf{F}] - \mathbf{I}$ . Any desired strain components in the

Table 4.1 – Material properties from DFT and NNP16 for Al,  $\text{Mg}_5\text{Si}_6$  and  $\text{Mg}_4\text{Al}_3\text{Si}_4$ .

	$\text{Mg}_5\text{Si}_6$		$\text{Mg}_4\text{Al}_3\text{Si}_4$	
	DFT	NNP16	DFT	NNP16
a (Å)	15.12	15.34	15.12	15.13
b (Å)	4.08	3.96	4.13	4.08
c (Å)	6.93	6.93	6.61	6.64
$\beta$ (°)	110.20	109.24	106.61	105.95
$C_{11}$ (GPa)	105.76	104.21	114.18	114.49
$C_{22}$ (GPa)	90.18	81.91	104.49	95.52
$C_{33}$ (GPa)	87.50	84.26	103.91	108.18
$C_{44}$ (GPa)	16.89	20.38	21.49	27.09
$C_{55}$ (GPa)	32.83	24.50	34.26	32.86
$C_{66}$ (GPa)	30.33	31.58	23.30	31.45
$C_{12}$ (GPa)	49.24	63.53	45.87	49.07
$C_{13}$ (GPa)	50.07	48.96	47.76	49.62
$C_{23}$ (GPa)	46.36	44.70	48.90	44.23
$C_{15}$ (GPa)	-10.79	-8.34	-4.11	-5.01
$C_{25}$ (GPa)	6.16	1.69	5.87	1.37
$C_{35}$ (GPa)	8.76	4.18	6.56	4.08
$C_{46}$ (GPa)	1.42	9.11	-0.12	2.20

$\gamma$ (mJ/m <sup>2</sup> )		$\text{Mg}_5\text{Si}_6$		$\text{Mg}_4\text{Al}_3\text{Si}_4$	
precip orient	shear in $[1\bar{1}0]$	DFT	NNP16	DFT	NNP16
px	+	454	579	413	569
	–	640	609	605	612
py	+	600	756	543	627
	–	507	637	511	657
pz	+	537	547	575	506
	–	509	587	460	508

	Al	
	DFT	NNP16
a (Å)	4.040	4.041
$C_{11}$ (GPa)	112.5	122.5
$C_{12}$ (GPa)	61.0	63.4
$C_{44}$ (GPa)	34.0	40.7
$\mu_s$ (GPa)	29.6	34.8
$\nu_s$	0.35	0.33

coordinate system of the overall simulation cell can then be determined.

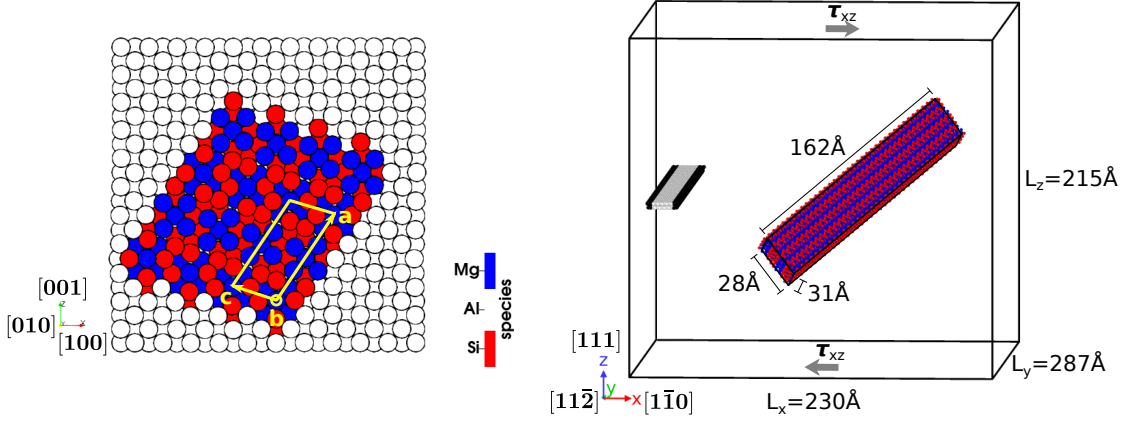


Figure 4.2 – Left: embedded precipitate ( $2a \times 4c$  lattice unit) model with orientation relationship. Right: example dislocation-precipitate interaction model (edge-px) with dimension specifications.

To measure the Critical Resolved Shear Stress (CRSS) required to move the dislocation through the periodic array of precipitates, we apply, in the PAD geometry, a shear stress  $\tau_{xz}$  by applying a force  $f = \tau_{xz} L_x L_y / N$  in the  $+x$  direction on all atoms within the NNP cutoff distance  $10.6 \text{ \AA}$  of the top surface, and forces  $-f$  on atoms near the bottom surface, where  $N$  is the number of atoms on which forces are applied in the top/bottom layer. At a specified  $\tau_{xz}$ , Molecular Statics with the FIRE minimizer is performed until the force norm is reduced to  $1 \times 10^{-2} \text{ eV/\AA}$ , individual atomic forces are verified to be smaller than  $1 \times 10^{-4} \text{ eV/\AA}$  and usually much smaller. If the dislocation has not passed the precipitate, the load is increased. If the dislocation has passed the precipitate, we return to the prior load and use a smaller load increment. Results here are accurate to within 5 MPa.

Simulations of bowing dislocations in the PAD geometry have a spurious image force, as analyzed in detail in [117]. This image force always opposes the applied force, scales inversely with the simulation volume, depends on the aspect ratios of the simulation cell, and is different for edge and screw dislocations. The magnitude of the image force then scales linearly with the extent  $h$  of the bowout. Simulation cost scales with the number of atoms, and the NNP is more costly than simpler EAM-type potentials, and so there are trade-offs in cost versus spurious image forces. Here, we use a precipitate center-to-center spacing, along the dislocation line direction, of  $100b$ , approaching the peak age spacing of  $125b$ . We then choose the other dimensions to have aspect ratios (glide direction/normal direction) of 1.07 and 1.15 for the edge and screw, respectively, that are close to the optimal aspect ratios [117]. The image

stresses are then estimated in terms of the dislocation bowout height  $h$  as

$$\begin{aligned}\tau_{\text{img}}^{\text{edge}} &\approx -\left(\frac{\mu b}{L_y}\right)\left(\frac{4h}{45L_y}\right)\bar{\tau}_{\text{img}}^{\text{edge}}\left(\frac{L_x}{L_z}, \frac{L_x L_z}{L_y^2}\right) \\ \tau_{\text{img}}^{\text{screw}} &\approx -\left(\frac{\mu b}{L_x}\right)\left(\frac{4h}{45L_x}\right)\bar{\tau}_{\text{img}}^{\text{screw}}\left(\frac{L_y}{L_z}, \frac{L_y L_z}{L_x^2}\right)\end{aligned}\quad (4.7)$$

where  $\bar{\tau}_{\text{img}}$  is a coefficient depending on the box dimension ratios e.g.  $L_x/L_z$  and  $L_x L_z/L_y^2$ . For the simulations here,  $\bar{\tau}_{\text{img}}^{\text{edge}} = 2.33$  and  $\bar{\tau}_{\text{img}}^{\text{screw}} = 0.75$ . In each simulation, we measure the bowout height  $h$  at the CRSS and compute a corrected CRSS by subtracting the estimated image stress, which is typically -20 MPa or  $\approx 10\%$  of the simulated CRSS.

### 4.4.2 Continuum Simulations

To use theories or continuum models or higher-scale models, and thus avoid the very costly and system-specific atomistic simulations, we must verify their accuracy by careful comparisons to atomistic studies. Such verification then provides confidence that these lower-cost, more general theories and methods can be applied to a wider range of systems (alloys, microstructures).

In this work, we will compare (i) continuum calculations of the misfit strain/stress fields and (ii) DDD simulations of non-shearing dislocation-precipitate interactions to atomistic simulations.

Continuum calculations of the misfit strains and stresses use a precipitate embedded in a periodic cell that is aligned with the axes of the precipitate. The precipitate misfit eigenstrain  $\bar{\epsilon}$  is computed from the lattice mismatch between the precipitate and Al matrix in the standard manner [52]. The Fast Fourier Transform solver [59] is then used to solve the equilibrium equation  $\nabla \cdot \boldsymbol{\sigma} = \mathbf{0}$  of linear elasticity, where

$$\begin{cases} \boldsymbol{\sigma} = \mathbf{C}_m \boldsymbol{\epsilon} & \text{in } \Omega_m \\ \boldsymbol{\sigma} = \mathbf{C}_p (\boldsymbol{\epsilon} - \bar{\boldsymbol{\epsilon}}) & \text{in } \Omega_p \end{cases} \quad (4.8)$$

with periodic boundary conditions. The resulting stress and strain tensor fields inside and outside the precipitate are then rotated into the coordinate system of the atomistic model. The Resolved Shear Stress (RSS) that exerts Peach-Koehler forces on the dislocation is then computed as  $\mathbf{n} \cdot (\boldsymbol{\sigma} \mathbf{b})/|\mathbf{b}|$ .

To study the accuracy of continuum simulations of dislocation-precipitate interactions, we use a DDD model having the exact same geometry on the glide plane, i.e. the same precipitate center-to-center spacing  $\bar{L}$  and precipitate shape (right of Figure 4.3). We neglect effects due to matrix/precipitate elastic mismatch, justified due to the small mismatch in the elastic constants so that only in-plane details are needed. We also assume elastic isotropy for Al, which has a Zener anisotropy ratio  $A=1.4$  that is near enough to isotropic. Details of the

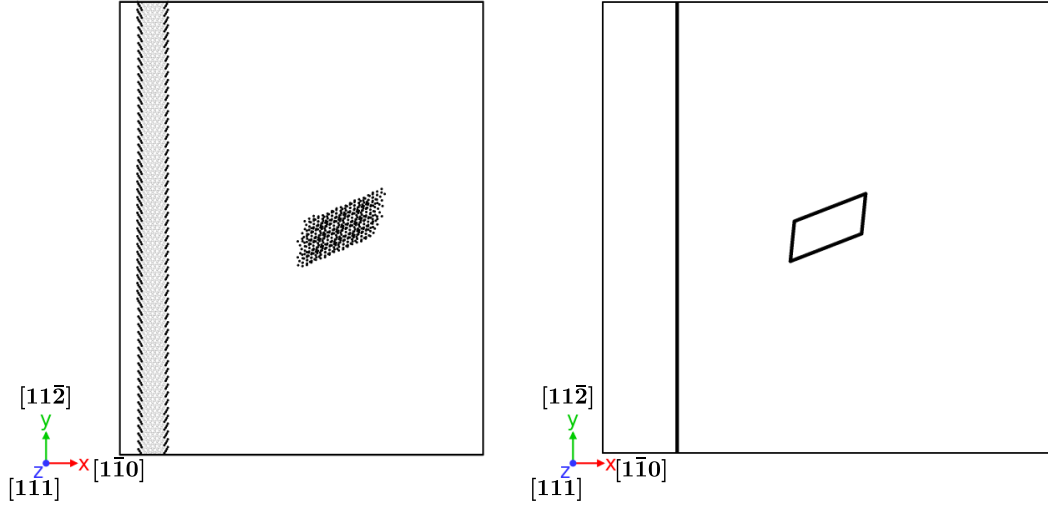


Figure 4.3 – CRSS calculation model (px oriented precipitate) for atomistics (left) and DDD (right). Atoms of the slip planes are shown with FCC atoms removed.

implementation within the framework of the ParaDiS code are given in [52]. The misfit RSS field, whether from the atomistic or continuum calculations above, is imported into the DDD simulation. Finally, we use the atomistically-calibrated dislocation core energy following the method in [53]. The DDD simulation cell is designed to minimize any image forces. We use a strain rate loading and monitor the stress versus plastic strain (plastic displacement) and the CRSS is measured as the maximum stress; the strain rate is slow enough that the CRSS is the same as that obtained by quasistatic tests that reach equilibrium at each load step.

## 4.5 Validation of Continuum Simulations

We first demonstrate that continuum simulations can represent the atomistic misfit fields and dislocation-precipitate configurations. This validation serves as basis for subsequent strengthening models and further mesoscale DDD simulations.

### 4.5.1 Misfit Strain/Stress Fields

The relevant strain component  $\epsilon_{xz}$  for dislocation motion in coordinates aligned with the dislocation glide geometry ( $x = [1\bar{1}0]_{Al}$ ,  $y = [11\bar{2}]_{Al}$ ,  $z = [111]_{Al}$ ) are shown for the atomistic Al matrix in the left column of Figures 4.4 for the px, py, and pz  $Mg_5Si_6$  precipitates. Also shown is the atomistic strain/stress in the central unit cell of the precipitate and the full RSS computed from the strain tensor and precipitate elastic constants. The right column of Figures 4.4 shows the corresponding results from the continuum simulation using the same scale. The matrix strain fields  $\epsilon_{xz}$  have notably different patterns for the three orientations. The continuum results show the same general magnitudes, but differ somewhat in orientation and spatial

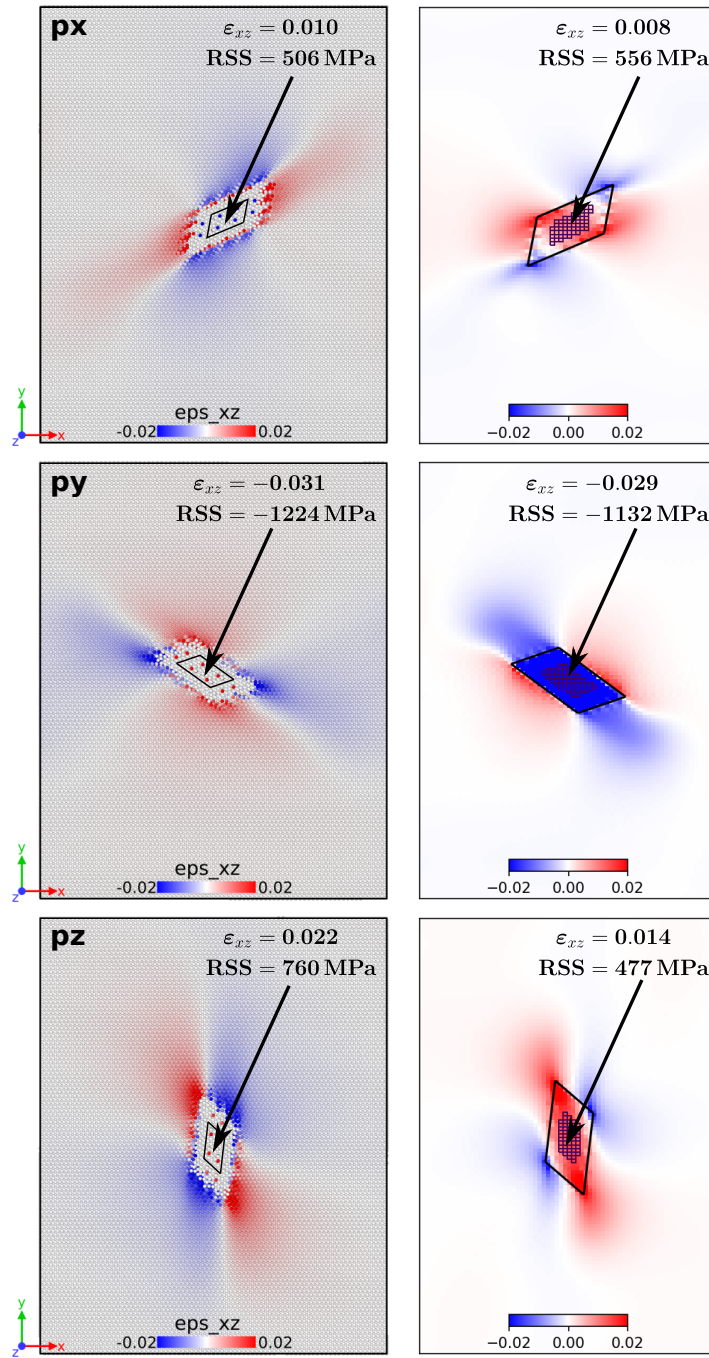


Figure 4.4 – Elastic strain and RSS of  $\text{Mg}_5\text{Si}_6$  precipitate in Al matrix (sliced in the middle). Left: calculation from relaxed precipitate embedded in a perfect lattice, Right: FFT calculation of precipitate in a large cubic box.

extent. For px, the continuum fields are slightly rotated toward the sharp corners as compared to the atomistic fields, and the region of negative strains is more localized. For py, there are more obvious differences with the atomistic fields now more rotated toward the sharp corners and having the negative strains in a smaller spatial extent. For pz, the strain fields are more similar but with some differences. These differences in matrix strain fields lead to some small differences in the detailed Peach-Koehler forces on the dislocations as they approach and move around the precipitate; this will be quantified below.

The strain  $\epsilon_{xz}$  and RSS in the central unit cell of the precipitates are also shown in Figure 4.4. The continuum result is the spatial average of the continuum field over the area of the central unit cell. The continuum results for px and py agree very well with the atomistic results, capturing both the magnitudes - reaching 1 GPa in the py case - and the difference in sign between px and py, which is expected to affect dislocation shearing. The RSS for the pz orientation is only 2/3 the value found in the full atomistic simulation. We have made more complete comparisons of the entire strain tensors, and for the  $\text{Mg}_4\text{Al}_3\text{Si}_4$  precipitates; the continuum results generally follow the trends and magnitudes of the atomistic results but a few strain components can be poorly predicted.

Finally, we note that the atomistic stress states near the precipitate/matrix interface are very difficult to characterize, especially near the sharp corners of the precipitates. These stresses may affect dislocation motion along the interfaces and/or initial shearing into the precipitates in ways that are not quantifiable. We will find, however, that we can reasonably understand the observed behaviors in spite of these truly atomistic issues.

### 4.5.2 Dislocation-Precipitate Interactions

To examine the accuracy of the calibrated DDD simulations in detail, we examine the atomistic and continuum predictions of the dislocation configurations at stresses below the initiation of any shearing (since shearing is not permitted in the DDD simulations). The DDD simulations can be executed using the atomistic or continuum RSS fields (or zero RSS, not shown here). Figure 4.5 compares the dislocation configurations for the px, py, and pz orientations for the edge dislocation and the px and pz orientations for the screw dislocation at single values of the applied stress as indicated. The atomistic dislocations show the region of the two partial dislocations and intervening stacking fault while the DDD, which treats the dislocation as compact, shows only this line. The atomistic displacements inside the precipitate are also shown, verifying the limited shearing at these loads. The atomistic and DDD simulations are shown at the same applied stress; the image forces in the atomistic simulation artificially suppress dislocation bowout by a small amount so the atomistic bowout should be slightly smaller than that seen in the continuum model. Overall, the continuum DDD calculations in the presence of the atomistic RSS fields are in excellent agreement with the atomistic simulations. The continuum dislocation shows a slightly larger bowout in all cases, indicating that the calibrated line tension may be slightly lower than the operative or effective line tension

in the fully atomistic setting. Details of the configurations very near/along the precipitate are slightly different, due in part to the differences in RSS fields near the precipitate and the neglect of elastic mismatch and anisotropy in the DDD. There is also some small variation due to small amounts of precipitate shearing in the corners of the precipitate, most notably for the px screw case and to a lesser extent the pz edge case. The DDD configurations using the continuum RSS are notably different: there is much more bowout for the px and pz edge cases and much less bowout for the py edge and px screw cases. These differences do not necessarily translate into significant effects in the CRSS (to be seen below) but bowing is particularly relevant for Orowan looping and so the differences cannot be neglected a priori.

These results are the first, to our knowledge, to quantitatively compare DDD simulations to atomistic simulations of dislocation-precipitate interactions, and at scales close to those pertaining to experiments. The use of an atomistically-calibrated dislocation core energy is essential to achieving this level of fidelity. The simulations also reveal that accurate matrix RSS fields are required to capture the dislocation configurations well; otherwise differences would be erroneously attributed to inaccuracies of the DDD method (calibrations, neglect of core structure; non-singular regularization approach in ParaDiS, etc.).

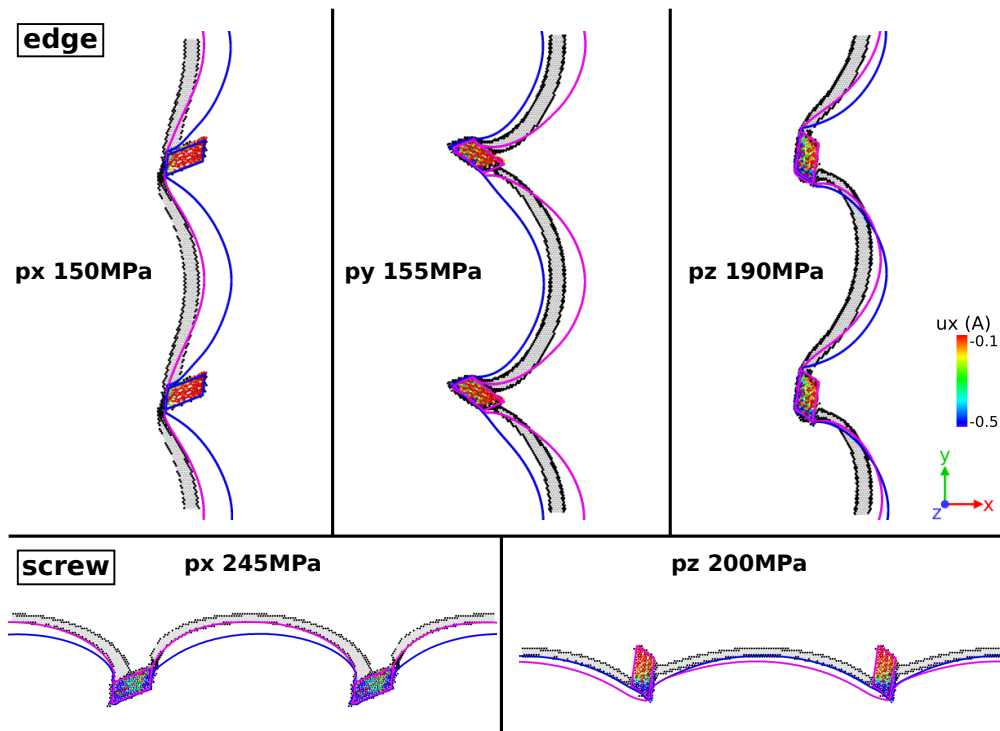


Figure 4.5 – Converged atomistic and DDD simulations for various “ $+\tau$ ” cases. Only non-fcc atoms (from CNA) on the central slip plane are plotted and colored with displacements. Purple line is DDD simulation using atomistic matrix RSS. Blue line is DDD with FFT matrix RSS.



## 4.6 Atomistic Simulations: Results and Comparison to Theory

Here, we present and discuss the atomistic simulations of dislocations moving past  $\beta''$  precipitates of dimensions  $2\mathbf{a} \times 4\mathbf{c}$  and center-to-center spacing  $\bar{L} = 100b$ , with a focus on the  $\text{Mg}_5\text{Si}_6$  precipitates. We then compare these detailed results to predictions of models for shearing and DDD simulations of looping, enabling validation of the theories and models.

### 4.6.1 Atomistic Results

Figure 4.6 and 4.7 shows atomistic configurations at a sequence of increasing loads for each of the different precipitate orientations and the positive and negative Burgers vectors (shearing to the right, “ $+\tau$ ”, and to the left, “ $-\tau$ ”, respectively). Only non-fcc atoms on the slip planes are shown to highlight the dislocation and precipitate, and colors indicate the displacements of precipitate atoms. Results are shown at two loads below the CRSS and one load just above CRSS where the dislocation is shearing or looping.

For the edge px case, Figure 4.6 shows shearing for  $+\tau$  but looping for  $-\tau$  even though the nominal geometry is identical. Thus, shearing versus looping depends on crystallographic, misfit, and direction-dependent precipitate shearing energies. Figure 4.4 shows that the RSS inside the precipitate assists  $+\tau$  shearing and opposes  $-\tau$  shearing while the shearing energy for  $+\tau$  shearing is slightly lower than for  $-\tau$  (Table 4.1), rationalizing a shift toward looping for the  $-\tau$  case. In both cases, the matrix RSS tends to oppose looping. Remarkably, the atomistic CRSS for the two loading directions are nearly identical.

For the edge py case, the situation is reversed. Figure 4.6 shows looping for  $+\tau$  but shearing for  $-\tau$ , again in spite of the nominally identical geometries. The py orientation has a much larger RSS value inside the precipitate, which opposes  $+\tau$  shearing and assists  $-\tau$  shearing, while the shearing energy for  $+\tau$  shearing is 20% higher than for  $-\tau$  (Table 4.1). In this case, the matrix RSS assists looping for  $+\tau$  and opposes looping for  $-\tau$ . These features all qualitatively rationalize the difference in observed phenomenon. With these larger differences, the difference in CRSS is also larger. And the CRSS for py  $-\tau$  shearing is larger than the px  $+\tau$  shearing while the py  $+\tau$  looping is smaller than the px  $-\tau$  looping.

For the edge pz case, both  $+\tau$  and  $-\tau$  show basically the same lateral shearing behavior, and at very similar CRSS values (Figure 4.6). The shearing energies are quite similar but the RSS in the precipitate is larger than px and so should assist shearing for  $+\tau$  and oppose it for  $-\tau$ . The matrix RSS has little effect on the looping. Theory (below) will indicate that this case is controlled by looping but that shearing follows upon reaching the looping instability, rationalizing the similarities between the two loading directions.

The same shearing/looping transition is seen for the edge px  $\text{Mg}_4\text{Al}_3\text{Si}_4$  precipitate, and at nearly the same CRSS values. The shearing energies are very close to those of  $\text{Mg}_5\text{Si}_6$  as are the effects of the matrix RSS on looping, but the internal RSS are smaller. In this case, the

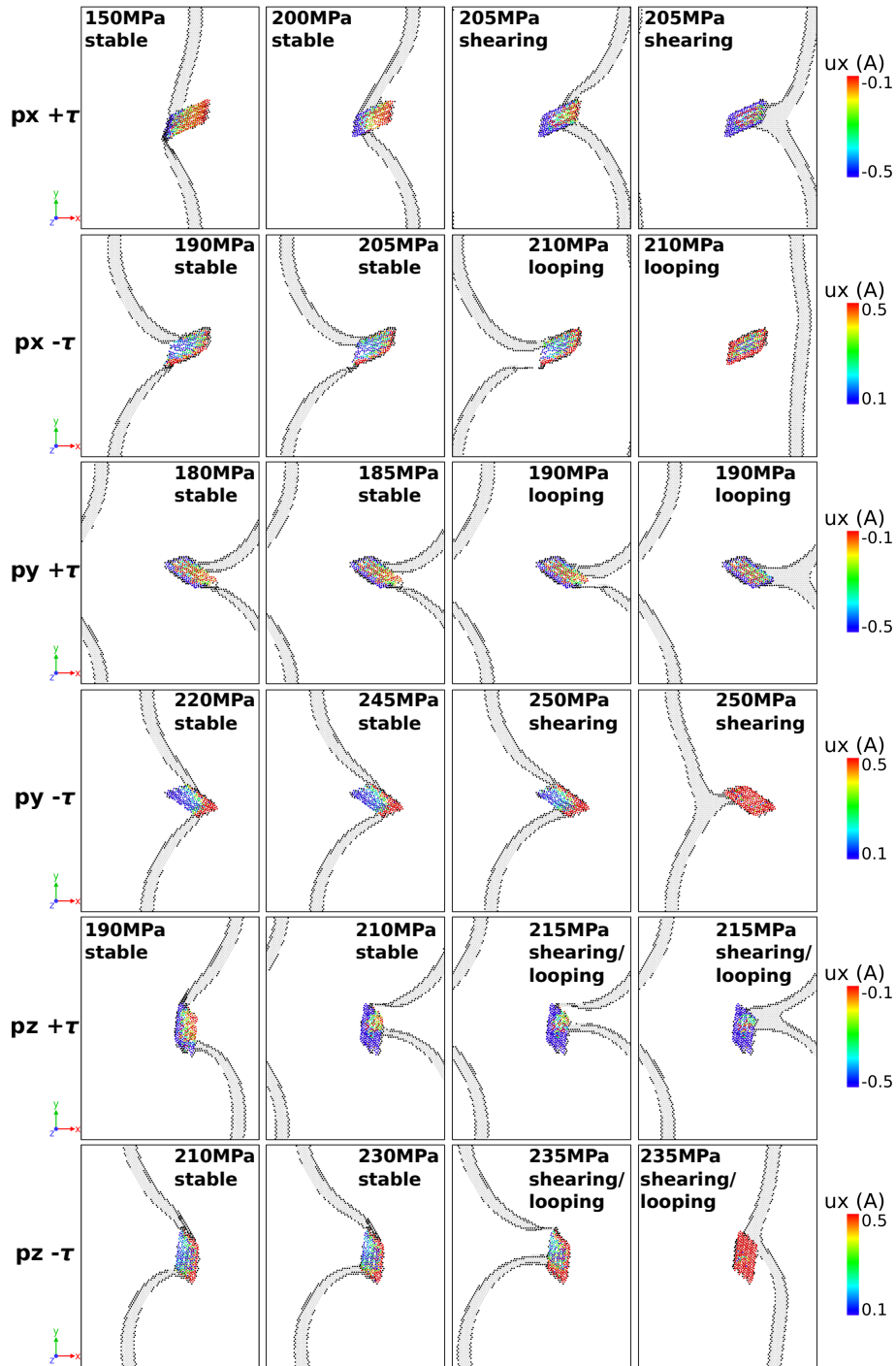


Figure 4.6 – Edge  $Mg_5Si_6$  interaction for different cases.

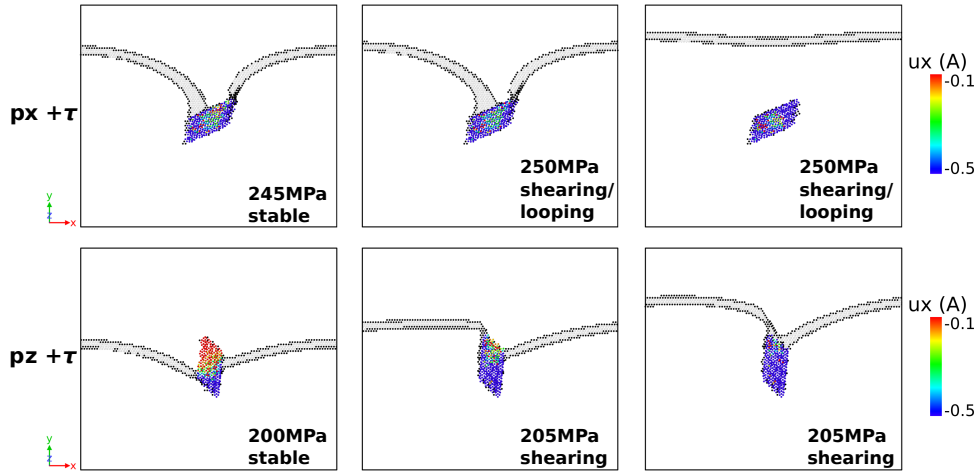


Figure 4.7 – Screw  $\text{Mg}_5\text{Si}_6$  interaction for different cases.

similarity of the two CRSS values is better understood but the shearing/looping transition is much more subtle.

The results for screw/precipitate interactions are shown in Figure 4.7. The geometry is a rotation of the edge/precipitate, e.g. the screw px case resembles the edge pz case, and the screw pz is similar to the edge px case. Specifically, in the screw px interaction, the dislocation cuts the corner and then moves laterally for the shorter span. Then two neighboring branches interact with the central part of precipitate undisplaced, which is eventually like a looping process. The screw dislocation in the pz case cuts the precipitate along the shorter span and the CRSS is very similar to the result for the edge px case. The screw py interaction is not presented in Figure 4.7, since the screw dislocation cross-slip under a much lower loading, due to large shearing energies and RSS for  $\text{Mg}_5\text{Si}_6$  py case (Table 4.1 and Figure 4.4). The predictions in Table 4.3 for screw py case also show significant high CRSS for both shearing and looping, implying that it is very hard to overcome the precipitate on the concerned glide plane.

Across all precipitates orientations and directions of loading, the CRSS values are remarkably close independent of mechanism, being within the range 187-228 MPa (image-force corrected values), with one case at 244 MPa. These results indicate that for the peak-aged  $\beta''$  precipitates in Al-6xxx, the alloy is indeed very close to equality of looping and shearing. We can state this because although the simulations are at spacing  $\bar{L} = 100b$  slightly smaller than experiments, the theory shows that both mechanism have the same dominant  $1/\bar{L}$  scaling of the CRSS.

### 4.6.2 Some Details of Dislocation-precipitate Interaction

In this section we mention some of the observed atomistic details. The representative phenomena are listed in Figure 4.8, where fcc atoms (from CNA) as well as Mg/Si atoms are removed

for better presentation. These phenomena are not limited to the listed plots, and they arise in other simulations, so these details are probably not potential artifacts.

In particular, for the shearing interaction cases (Figure 4.8a), a small interface defect at one end of dislocation can emerge during shearing, and it can be absorbed with an increased load. In looping case (e.g. edge  $py + \tau$ ) there are always two long arms attaching to the precipitate, which is often seen in Orowan mechanism. These two arms have screw character angle, and one of them cross-slips to another plane. The cross-slipped segment is constrained and hinder its later movement and interaction with the other arm. Another cross-slip takes place for screw  $py$  case (not for screw  $px/pz$ ), and it happens for different precipitate sizes and different box sizes. As is seen in Figure 4.8, an interface defect is formed at one side of precipitate, probably triggered by the large negative RSS field. Then the screw dislocation transforms to another plane and expand the cross-slipped area laterally. According to the orientation relationship, the cross-slipped screw dislocation and  $py$  is one of the other interaction cases, i.e. screw  $px$  or screw  $pz$ . Hence, in the later yield stress calculation, we only consider screw  $px$  and screw  $pz$  and their average.

We emphasize here that these atomistic details do not have very strong effects for our model predictions. The presentation here is for completeness.

### 4.6.3 Incremental In-situ Analysis for Atomistic Simulations

The in-situ analysis is based on the converged result at 190 MPa and 210 MPa for edge  $pz$  shown in Figure 4.9. We first employ the DXA algorithm in `ovito` to detect full dislocation geometry in each case. Then relevant geometry quantities such as radius of curvature  $R$ , the swept area  $dA$ , and the dislocation length change  $dS$  can be calculated. Subsequently we estimate the dislocation line tension as  $T = \tau b R$ . Note that the line tension here is a local expression and we embed dislocation interactions in this quantity. Incrementally, the following energy balance holds from 190 MPa to 210 MPa.

$$(\gamma - \tau_p b) D \Delta \sin \theta + T dS = \tau b dA \quad (4.9)$$

where  $\Delta$  denotes for the sliding distance of dislocation along the precipitate edge and  $\theta$  as precipitate edge inclination. The quantity  $D \Delta \sin \theta$  is to measure the swept area in the precipitate.

Table 4.2 – Geometry quantities measured in atomistics. (length in Å unit, area in Å<sup>2</sup> unit).

measure		numerical calculation		estimates	
b	2.857	R (190 MPa)	148.8	$R \cdot dS$	1.21e4
D	25.1	dS	81.4	dA/S1	36.8
$\Delta \sin(\theta)$	18.0	dA	1.04e4		
S (190 MPa)	282.8				

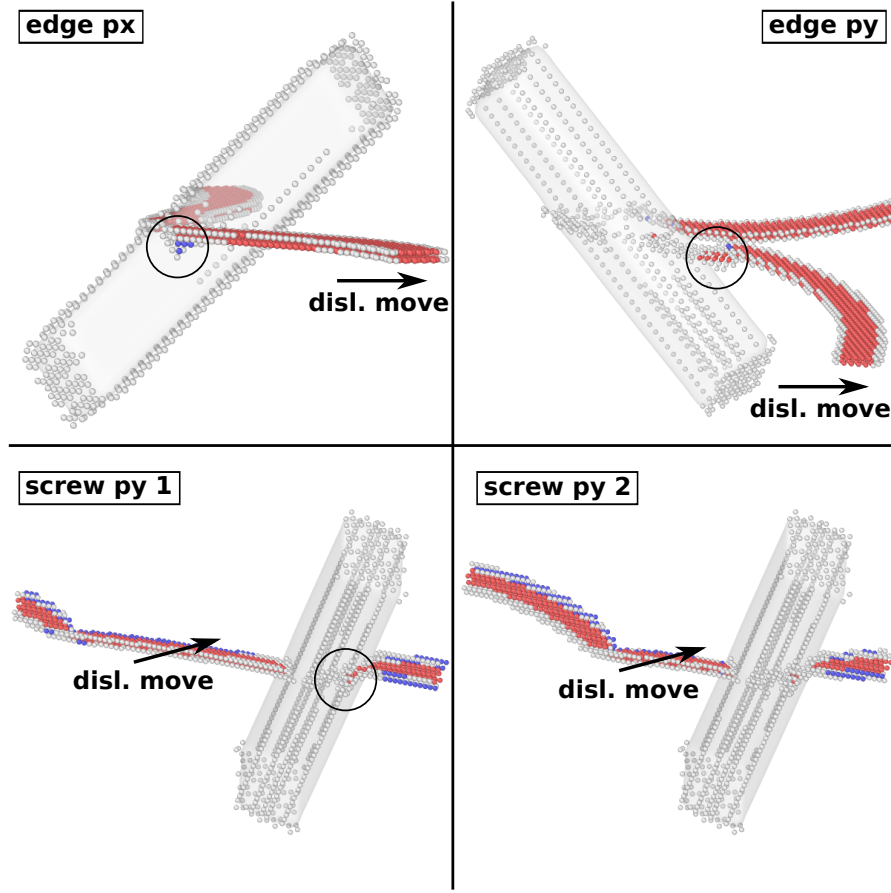


Figure 4.8 – Atomistic detail of dislocation-precipitate interaction. Various details are highlighted with circles. (a) An interface defect is generated during shearing, (b) one of long branches in looping is a screw segment that cross-slips to another plane. (c) (d) screw py case always cross-slips at a lower load (120 MPa in the plot), starting with an interface defect.

From the measured geometry quantities presented in Table 4.2 we have  $T = 8.08 \times 10^4 \text{ MPa}/\text{\AA}^2 = 5.041 \text{ eV/nm}$ . Substituting the NNP16 GSFE  $\gamma = 548 \text{ mJ/m}^2$  for pz (Table 4.1) and the obtained atomistic RSS 760 MPa in Figure 4.4. We have the following estimate of the applied stress  $\tau$  as

$$\begin{aligned} \tau &= \frac{(\gamma - \tau_p b) D \Delta \sin \theta + T dS}{b dA} \\ &= \frac{(5480 - 760 \times 2.857) \times 25.1 \times 18.0 + 8.08 \times 10^4 \times 81.4}{2.857 \times 1.04 \times 10^4} \text{ MPa} \\ &= 50 + 225 \\ &= 275 \text{ MPa} \end{aligned} \tag{4.10}$$

The calculate value is larger than 210 MPa. However, if we ignore the shearing part of the  $\tau$ , the calculated value is closer. It implies that the current pz case is more prone to be governed

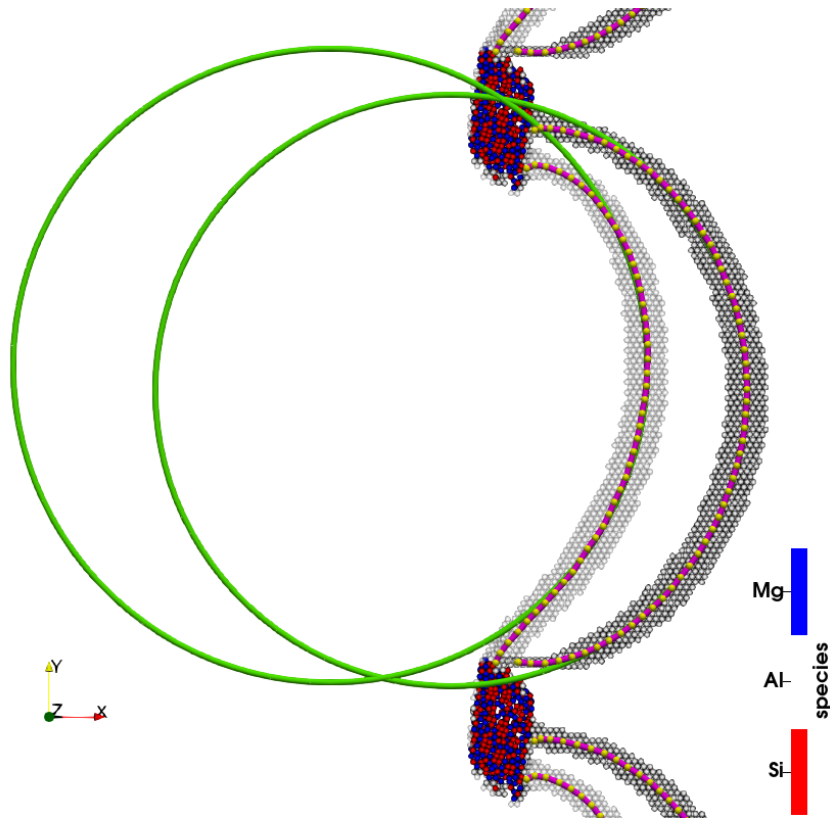


Figure 4.9 – Both final stable states at 210 MPa (dark gray) and 190 MPa (light grey) are plotted (for each loading two simulation images are plotted to show full dislocation geometry). Big yellow dots and purple lines are obtained from DXA analysis. Center parts of dislocation lines are fitted to circles (green).  $R$  changes from 148.8 Å (190 MPa) to 139 Å (210 MPa). A slight change, which is consistent with the change in loading  $\tau$ .

by Orowan mechanism.

### 4.6.4 Predictions versus Atomistics

We now examine predictions of the shearing theory and DDD looping simulations for each individual case. The shearing theory uses the NNP16 shearing energy, the measured RSS in the center of the precipitate, the span length  $D$  for each geometry and loading direction. The looping simulations use the calibrated core energy and matrix residual stress fields. Table 4.3 shows the predictions, where the RSS values from atomistics, continuum, and zero RSS are all shown to reveal the roles of the RSS in the predictions. For the atomistic RSS values, the lowest CRSS, indicating the predicted operative mechanism, is highlighted in bold.

For the edge px case, the theories predict the observed change from shearing to looping with loading direction. Quantitatively, the  $+\tau$  prediction of shearing is too low for both atomistic and continuum precipitate RSS values. The CRSS for looping is predicted to be higher than

#### 4.6. Atomistic Simulations: Results and Comparison to Theory

---

the measured shearing strength when using the atomistic matrix RSS, verifying the shearing behavior. For the  $-\tau$  case, the shearing is strongly disfavored due to the precipitate RSS and looping is easier than for  $+\tau$ . The role of the matrix RSS hinders looping in both cases. The matrix RSS should act similarly to hinder shearing (although the configurations differ somewhat, the dislocation moves through the same matrix field in both shearing and looping). Thus, if the effect of matrix RSS on looping is used to account for matrix RSS effects on shearing, then the predicted CRSS for the  $+\tau$  case would be 176 MPa, in very good agreement with the simulations, while the  $-\tau$  shearing would be hindered even further and not affect the prediction of looping.

For the edge py case, the theories again predict the observed change from looping to shearing with change in loading direction. For the  $+\tau$  case, the predicted looping stress is in excellent agreement with the atomistic result. The matrix RSS assists the looping by reducing the CRSS by 26 MPa. The  $-\tau$  prediction of shearing is now far too low using either atomistic or continuum RSS values in the precipitate. However, the looping simulation, with a much higher CRSS than DDD without matrix RSS, shows that the matrix RSS increases the looping stress by +44 MPa. If this hindering effect is added to the shearing prediction, the predicted CRSS is 153 MPa, but this remains far lower than the simulation value. One possible reason for this could be that the internal precipitate stress measured in the center of the precipitate is an overestimate for the entire cross-section. With zero internal RSS, the shearing prediction is 242 MPa and matrix RSS effects would increase the CRSS to 286 MPa, far above the atomistic result. This indicates that the operative precipitate RSS may need to be more-accurately determined.

Before discussing the edge pz case, we examine the  $\text{Mg}_4\text{Al}_3\text{Si}_4$  edge px case. The theory again predicts the observed mechanism and the CRSS values are in good agreement with the atomistics when the atomistic RSS values are used. The role of precipitate RSS here is quite small because the NNP16 error in the  $\mathbf{b}$  lattice constant is much smaller, reducing the RSS values overall relative to those for  $\text{Mg}_5\text{Si}_6$ . If we apply the increase of 35 MPa due to the matrix RSS for looping to the predicted shearing stress, as done above, the shearing prediction does become larger (219 MPa) than the atomistic result (194 MPa) but remains close to the simulated looping stress so that shearing is still likely to happen. These results again support the qualitative and quantitative predictions of the theories.

We note that the effects of the continuum matrix RSS are generally smaller than those of the atomistic matrix RSS. Thus, theories fully based on non-atomistic modeling of the RSS will have some quantitative errors in predictions.

We now examine the edge pz case, which shows the lateral shearing mechanism (Figure 4.6). Applying the theory for px and py shearing to pz immediately shows that the direct shearing along the much longer span  $D$  would require an extremely high CRSS. Thus, the dislocation finds the alternative lower-energy path involving lateral shearing or looping. Examining Table 4.3, we find that it is the looping predictions that are in excellent agreement with the atomistic results, with a negligible effect of matrix RSS. This is because the lateral shearing

theory applied to this geometry and material parameters predicts a looping-like instability that then drives shearing, as discussed next.

Application of the lateral shearing theory for pz requires an accurate line tension. By fitting the stable atomistic configurations at two applied stresses to a circular arc and using the relation  $T = \tau bR$ , we obtain  $T = 0.504 \text{ eV}/\text{\AA}$  (4.6.3). Application of the theory with the precipitate RSS  $\tau_p = 760 \text{ MPa}$ ,  $\gamma = 547 \text{ mJ/m}^2$ ,  $D = 25.1 \text{ \AA}$ , and  $L = 236.4 \text{ \AA}$  is then executed for increasing values of  $\tau$ . Figure 4.10a shows the constant energy contours of  $E(\Delta, h)$  at 210 MPa, the average value at which atomistic shearing occurs. There is the local minimum at  $\Delta = 0, h = 0$  and increasing energies away from this value until at values around  $\Delta = 1 \text{ \AA}$ ,  $h = 22 \text{ \AA}$  the energy starts to decrease. Thus, the initial state is very stable and there is an 1.35 eV immense energy barrier in reaching the regime of instability (shearing, dislocation expansion). Increasing the load to 230 MPa,  $\Delta = 0, h = 0$  remains a local minimum but the energy landscape is very flat and there is a small energy barrier to achieving an instability for  $h + \Delta > 4 \text{ \AA}$ . At  $\Delta = 9.5 \text{ \AA}$ , the angle  $\theta$  reaches  $\pi$ , and the analysis predicts no solutions, corresponding to a looping instability. The local stability at  $h = 0, \Delta = 0$  is lost entirely at 239 MPa, which is exactly the Orowan or looping instability  $\tau_c = 2T/(Lb)$ , showing that the theory is predicting on Orowan instability that then enables shearing to occur as the system follows the steepest downhill energetic path. Changing the sign of the precipitate RSS then has no effect on this instability. These results indicate that the CRSS for the pz orientation, while showing shearing, is closely connected to a looping instability that is predicted to occur at slightly higher CRSS. In fact (Table 4.3), the actual looping simulations are then found to agree very well with the atomistic results, and with negligible effects of the matrix RSS. This supports the conjecture that this lateral shearing is essentially a looping process, with shearing occurring as a tangential phenomenon rather than a controlling phenomenon.

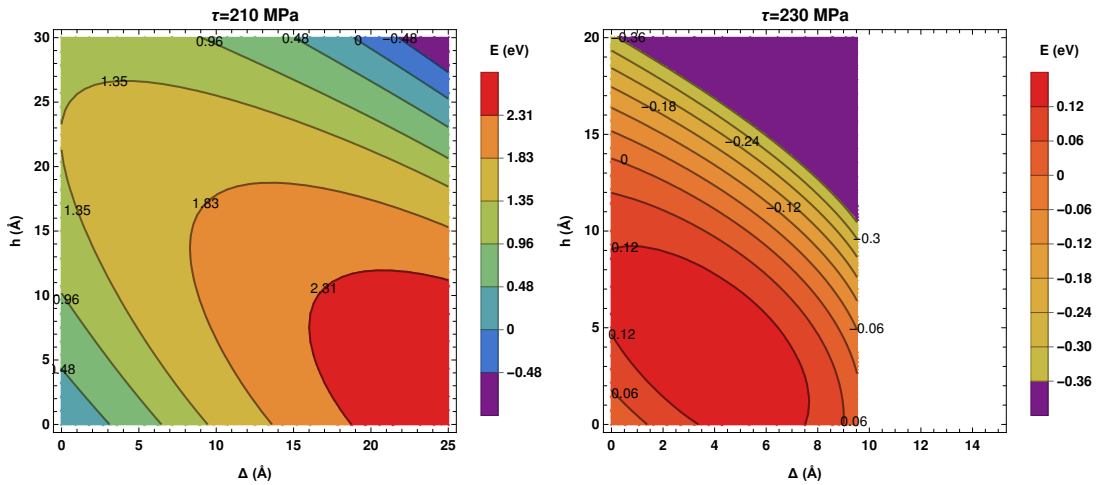


Figure 4.10 – Energy contour plot at different loads. The reference energy level for each plot is  $E(0, 0, \tau)$ .



Table 4.3 – Atomistic calculation of CRSS (in MPa) compared with shear prediction (model) and loop simulation (DDD). Image force effect is subtracted for atomistics according to [117]. Model prediction and DDD simulations use different RSS field. Bold values are lower value of the two predictions with atomistic RSS.

CRSS (MPa)	precipitate type		atomistic simulation				shear prediction with precipitate RSS			loop simulation with matrix RSS		
			simulation result			image corrected	atom	FFT	zero	atom	FFT	zero
edge	Mg <sub>5</sub> Si <sub>6</sub>	px	+ $\tau$	shear	202.5	187	<b>144</b>	139	192	208	186	176
			- $\tau$	loop	207.5	187	250	255	202	<b>190</b>	176	173
		py	+ $\tau$	loop	187.5	162	419	409	287	<b>160</b>	201	186
			- $\tau$	shear	247.5	228	<b>109</b>	119	242	230	175	186
		pz	+ $\tau$	shear	212.5	203	239	239	239	<b>214</b>	205	216
			- $\tau$	shear	232.5	215	239	239	239	<b>220</b>	223	212
	Mg <sub>4</sub> Al <sub>3</sub> Si <sub>4</sub>	px	+ $\tau$	shear	212.5	194	<b>184</b>	159	189	211	193	176
			- $\tau$	loop	207.5	187	208	232	203	<b>188</b>	177	173
		py	+ $\tau$	loop	192.5	173	273	263	238	<b>176</b>	184	186
			- $\tau$	shear	222.5	204	214	224	249	<b>201</b>	173	186
screw	Mg <sub>5</sub> Si <sub>6</sub>	px	+ $\tau$	shear	247.5	244	<b>231</b>	216	297	272	269	257
		py	+ $\tau$	cross-slip		-	566	553	387	<b>336</b>	267	270
		pz	+ $\tau$	shear	202.5	200	<b>101</b>	126	168	239	246	217

Similarly, we now examine the screw cases. For the screw px prediction, we apply again the analysis of (4.2). Using the geometry quantities  $D = 27.2 \text{ \AA}$ ,  $L = 244.9 \text{ \AA}$  and line tension  $T = \tau bR = 0.968 \text{ eV/\AA}$ , we predict a CRSS of 398 MPa, much larger than the DDD simulations, hence the screw px case is controlled by the Orowan mechanism. If we use the simple shearing model to predict CRSS in this case with the larger span  $D = 41.9 \text{ \AA}$  and atomistic RSS as 506 MPa, the calculated CRSS is 223 MPa. It is closer to the corrected atomistic CRSS. And from the displacement plot on the glide plane, the most of atoms are sheared (with just a few strong pinning atoms in red color). So the mechanism is likely to be shearing, although it is very similar with the edge pz case. The screw pz case is purely shearing, as seen in Figure 4.7. However, the shearing prediction with the atomistic precipitate RSS is only 101 MPa. Again, the matrix RSS contribution, of 22 MPa as inferred from the loop simulation, would increase the prediction slightly. The RSS is 760 MPa (Figure 4.4) and the shearing energy is  $547 \text{ mJ/m}^2$ , relative smaller than the other cases. The shearing front in Figure 4.7 for 200 MPa is more tilted than the edge px case and might increase the CRSS, an effect ignored in the model (4.1). While the prediction is low, shearing is still favored over looping.

### 4.7 Strength Prediction for Al-6xxx

The prior sections have demonstrated atomistic details of the shearing and looping processes as a function of precipitate orientation and type, mainly for edge dislocations. The atomistic results have been used to assess the quantitative accuracy of the theory for shearing and the DDD simulations for looping. Broadly, good agreement is achieved in almost all cases when the effects of matrix RSS are included in the shearing predictions; only the edge py  $-\tau$  and screw pz  $+\tau$  cases are not well-captured. And the looping predictions with atomistic matrix RSS and atomistic core energies are very accurate, comparing with the atomistic results. For the shearing predictions, the predicted values are smaller as compared with atomistics, since some of the matrix RSS effect is missing and the characterization of precipitate RSS may not be very accurate.

In spite of the use of the most advanced and quantitative interatomic potential for Al-Mg-Si to date, the matrix and precipitate properties of NNP16 still have differences with respect to the DFT references, which are expected to be close to the true  $T=0 \text{ K}$  alloy properties. The studies here are also on a periodic array of identical precipitates, and at a scale  $\bar{L} = 100b$  slightly smaller than experiments. To make connections of our results to real Al-6xxx thus requires using the most accurate material properties and making corrections for different precipitate spacing and randomness effect, as guided by the shearing theory and the DDD looping simulations.

#### Correction for precipitate spacing

The major correction to connect atomistics to experiments is in the center-to-center spacing. Due to computational cost, the atomistic CRSS are computed at  $\bar{L} = 100b$ . The typical

experimental spacing is  $\bar{L}_r = 125$  b (for precipitate volume fraction 1.10%, see [52]). Theory for both shearing and looping shows the CRSS to scale with  $1/\bar{L}$ , and so the atomistic CRSS values must be corrected by a factor  $\alpha_L = \bar{L}/\bar{L}_r = 0.8$ .

### Correction for random vs. periodic precipitate arrangement and matrix RSS

The difference in Orowan looping between periodic and random precipitate arrangements has been extensively studied [9, 41, 61]. The major conclusion has been that the CRSS is reduced due to the arrangement, an idea originally based on an analogy with the effects of randomness on strengthening by point-pinning obstacles in a line tension model [42]. The detailed analysis of Hu et al. on realistic Al-6xxx microstructures [52] shows several additional features that are not considered in the historical analyses: (i) the randomness lessens the effects of the matrix RSS and (ii) the edge-edge precipitate spacing  $L$  of the actual dislocation at the observed CRSS is the controlling quantity, and is  $L \approx 0.7\bar{L}$ ; this counteracts the traditional reduction of CRSS due to the random arrangement. To quantify the difference in looping CRSS between the periodic and realistic arrangements, we complement our previous simulations of looping in realistic microstructures with simulations of looping in a 1D periodic model at the experimental precipitate spacing  $\bar{L} = 125$  b using the exact same details (especially the DDD calibration to the Al Ercolessi-Adams EAM potential [32] and the  $2a \times 4c$  precipitate cross-section) with and without the matrix RSS fields as calculated with DFT material properties. In addition to simple periodic arrays of px, py, or pz orientations, we also model periodic arrays of several mixed orientations (px, py, pz) and (px, pz, py) again with the same precipitate spacing.

For both edge and screw, results in Table 4.4 show that the role of the matrix RSS is fairly small for the periodic arrays. The mixed cases, executed without residual stresses, show a CRSS that is very close to the average of the three CRSS values for the px, py, and pz arrays. Thus, in the periodic geometry, the effects of different orientations are averaged out. Comparing the CRSS for the mixed 1d periodic case to the previous full 2d realistic microstructure result with the same spacing, we find that the CRSS values for the edge dislocation are essentially identical while those for the screw are slightly ( $\approx 10\%$ ) lower in the true random case. Based on these results, we compute a correction factor for the realistic microstructures relative to the periodic arrays as  $\alpha_r^{\text{screw}} = 0.90$  for the screw and  $\alpha_r^{\text{edge}} = 139/136 = 1.02$  for the edge.

### Correction for matrix and precipitate RSS

Although there are some effects of the matrix RSS in atomistics or DDD for certain cases presented in Table 4.3 due to the smaller periodic geometry, the matrix RSS effects in a pseudo-random system are reduced since the randomness and the positive/negative signs of the matrix RSS lead to some cancellations. The RSS fields are also local around each precipitate, and hence diminishing as the precipitate spacing increases.

## Chapter 4. Dislocation-Precipitate Interaction at Atomistic Scale

Table 4.4 – DDD simulation of 1D periodic model compared with the previous 2D pseudo-random result (both with EA 94 material properties) at different center-center spacings. “mix1” is precipitate order as px, py, pz. “mix” is px, pz, py order. The “mix” case for 2D random is from [52]. RSS fields are calculated with DFT material properties (Al,  $\text{Mg}_5\text{Si}_6$ ).

CRSS (MPa)	$\tilde{L}$ (center-center)	orientation	screw		edge	
			no RSS	with RSS	no RSS	with RSS
1D periodic	100b	px	226	233	153	168
		py	236	238	163	184
		pz	190	221	190	187
		average	217	231	169	180
		mix1	216	-	167	-
		mix2	220	-	163	-
	125b	px	178	187	127	135
		py	195	194	128	130
		pz	154	173	152	152
		average	176	184	136	139
		mix1	171	-	132	-
		mix2	171	-	131	-
2D random	125b	mix	158	164	139	140

We recall, furthermore, that the lattice mismatch of between Al and  $\text{Mg}_5\text{Si}_6$  as predicted by NNP16 is significantly larger than that given by DFT, increasing the RSS fields in the NNP16 simulations. The NNP16 predictions for the  $\text{Mg}_4\text{Al}_3\text{Si}_4$  precipitate showed much better agreement, and the looping simulations showed that the effects of the matrix RSS are quite small for this precipitate. This further motivates the neglect of the matrix RSS in making predictions for real alloys. Hence the matrix RSS can be neglected in the random arrangements.

The RSS inside the precipitates is important shearing, and so we use the RSS calculated from DFT material properties since they are closer to the real material properties.

### Correction for shearing energy

For each precipitate orientation, there is some difference between the shearing energies predicted by NNP16 and the DFT reference, as shown in Table 4.1. Thus, for each case, there is a correction factor  $\alpha_{\text{sf}} = \gamma_{\text{DFT}} / \gamma_{\text{NNP}}$  that ranges from 0.725 to 1.05 across all the different cases, with most cases having a ratio smaller than 1 and an overall average ratio of 0.88 for the  $\text{Mg}_5\text{Si}_6$  precipitates.

### Correction for line tension

The theory and DDD simulations for Orowan looping show that the dislocation line tension is a critical material parameter. The line tension has contributions due to the matrix elastic properties and the dislocation core energies. The NNP16 potential has a larger isotropic shear modulus (34.8 GPa) than computed in DFT (29.6 GPa; see Table 4.1) and the T=0 K DFT value is slightly larger than the experimental value of 28 GPa at room temperature. The core energy is unfortunately unobtainable outside of interatomic potentials. In the mesoscale work [52], we demonstrated that the CRSS for Orowan looping was accurately captured using the total dislocation energy within a radius  $5.4b$ ; this total energy includes “core” and “elastic” energies that cannot be uniquely separated. The line tension within this radius for the NNP16 potential is  $0.237 \text{ eV}/\text{\AA}$  for the edge and  $0.598 \text{ eV}/\text{\AA}$  for the screw. The EA EAM potential, with a lower isotropic shear modulus 32 GPa, also has lower line tensions at radius  $5.4b$  of  $0.207 \text{ eV}/\text{\AA}$  for the edge and  $0.483 \text{ eV}/\text{\AA}$  for the screw. DDD simulations calibrated to the EA potential of the periodic px, py, and pz orientations at  $\bar{L} = 100b$  show looping strengths that scale closely with these differences in line tension. However, the line tension extracted from analysis of the atomistic pz simulations of the edge was much larger,  $0.504 \text{ eV}/\text{\AA}$ , reflecting expected long-range elastic interactions as well as the character-dependency of the line tension that should enter into the line tension. While these analyses do not provide a definitive correction factor for the line tension, we believe that a correction  $\alpha_{lt} = 28/34.8 = 0.80$  based on the shear modulus is the most reasonable estimate. This correction factor is used for correction of DDD looping predictions as well as predictions of the complex shearing case, e.g. edge pz case, where line tension  $T$  is involved.

Table 4.5 – DDD simulation of  $2a \times 4c$  Mg<sub>5</sub>Si<sub>6</sub> center-center spacing  $\bar{L} = 100b$ , with  $a=5.4b$  and calibrated dislocation core energies.

material	$\mu$ (GPa)	$\nu$	$E_c + E_c'' _{5.4b} (\text{eV/nm})$		type	screw (MPa)	edge (MPa)
			screw	edge			
NNP16	34.8	0.33	5.98	2.37	px	257	176
					py	270	186
					pz	217	216
half core	34.8	0.33	2.99	1.19	px	144	93
					py	142	100
					pz	121	121
EA94	32.0	0.34	4.83	2.07	px	226	153
					py	236	163
					pz	190	190

### Tensile strength for realistic Al-6xxx

With the various factors above related to length scales, randomness, and real vs. NNP material properties, as shown in Table 4.6, we now make predictions that apply to the real Al-6xxx alloy at peak aging. For each orientation and loading direction, we predict a CRSS for each process and select the lower value to be the controlling CRSS. We then average over all cases for edge and screw, respectively, and then average the edge and screw results. This leads to a final “corrected” CRSS  $\tau_c^{\text{corr}}$ .

The tensile yield prediction for  $\text{Mg}_5\text{Si}_6$   $\text{Mg}_4\text{Al}_3\text{Si}_4$  are 122 MPa and 126 MPa, quite similar because the DFT shearing energies and RSS are similar. The uniaxial tensile yield stress for an untextured polycrystal is then obtained by multiplying the CRSS by the standard Taylor factor of 3.06, and averaging both precipitate types, to yield  $\sigma_y = 372$  MPa. The typical uniaxial yield stress for peak-aged Al-6xxx is around 300 MPa, and so our prediction overestimates the experiments by  $\approx 24\%$ .

Issues that may contribute to the difference between experiments and theory are as follows. First, the predictions use  $T=0\text{K}$  DFT-computed quantities. There are likely finite-temperature effects, especially reductions in the precipitate shearing free energies with increasing temperature similar to the reductions in stacking fault energies at room temperature found for both Al and Ni using good EAM interatomic potentials [122]. Shearing is otherwise largely athermal - that is, the energy barriers for shearing at stresses below the  $T=0\text{K}$  CRSS quickly become large and inaccessible over experimental time and temperature scales. Looping is also athermal, beyond effects due to elastic moduli and dislocation core energy. We have already made some correction for the finite-temperature elastic modulus that affects the line tension. Another likely factor is the size distribution of precipitates. Smaller precipitates (smaller  $D$ ) are easier to shear. Once sheared, there are then longer distances  $L$  between the remaining precipitates of average and larger sizes. The average sized precipitates can then likely be sheared or looped at lower stresses, followed by the larger size precipitates. The role of randomness in the microstructure also remains uncertain - the dislocation may find easier paths through the precipitate field. Our results here are based on our earlier DDD studies that, while statistically representative of the realistic microstructure, may still be too small and remain periodic, possibly overestimating pinning at “strong” environments that could be overcome if much longer line lengths are examined. This discussion thus points to addressing precipitate size distributions, simulation size scales, and finite-temperature shearing as the main directions for further assessment, and these will likely reduce the CRSS toward the experimental values measured at room temperature.

Table 4.6 – Uniaxial tensile yield stress prediction for realistic Al-6xxx containing  $\text{Mg}_5\text{Si}_6$  precipitates with experimental cross section  $2\mathbf{a} \times 4\mathbf{c}$  at experimental spacing  $\bar{L} = 125\mathbf{b}$ . Both shearing and looping predictions are executed for different precipitate orientations and loading directions. The shearing predictions are obtained via validated theory (from (4.1) or (4.2)) and the looping predictions are based on DDD simulations. Precipitate RSS  $\tau_p$  is calculated with DFT material properties.

	case	$D$ (Å)	$\bar{L}$ (Å)	$\tau_p$ (MPa)	$\gamma$ (mJ/m <sup>2</sup> )	$\tau_m$ (MPa)	$T$ (eV/Å)	$\tau_c$ (MPa)	$\alpha_r$	average (MPa)	CRSS (MPa)
edge	px + $\tau$ shear (4.1) loop	27.2	357.1	315 -	454 -	0 0	- 0.403	<b>121</b> 142	1.02	119	122
	px - $\tau$ shear (4.1) loop	27.2	357.1	315 -	640 -	0 0	- 0.403	242 <b>139</b>			
	py + $\tau$ shear (4.1) loop	31.1	357.1	-667 -	600 -	0 0	- 0.403	300 <b>150</b>			
	py - $\tau$ shear (4.1) loop	31.1	357.1	-667 -	507 -	0 0	- 0.403	<b>120</b> 150			
	pz + $\tau$ shear (4.2) loop	54.4	357.1	675 -	537 -	0 0	- 0.403	191 <b>174</b>			
	pz - $\tau$ shear (4.2) loop	54.4	357.1	675 -	509 -	0 0	- 0.403	191 <b>171</b>			
screw	px + $\tau$ shear (4.1) loop	41.9	357.1	315 -	454 -	0 0	- 0.774	<b>187</b> 207	0.8	125	
	px - $\tau$ shear (4.2) loop	41.9	357.1	315 -	640 -	0 0	- 0.774	354 <b>207</b>			
	pz + $\tau$ shear (4.1) loop	25.1	357.1	675 -	537 -	0 0	- 0.774	<b>106</b> 175			
	pz - $\tau$ shear (4.1) loop	25.1	357.1	675 -	509 -	0 0	- 0.774	216 <b>175</b>			

In our previous modeling of yield strength due to Orowan looping [52], and using a finite temperature core energy, we obtained  $\sigma_y = 411$  MPa. Thus, the inclusion of shearing processes here leads to a slightly lower strength than pure Orowan looping. In that prior work, we also investigate the forces exerted on precipitates, showing that several precipitates would be sheared prior to looping. We then estimated the strength as  $\sigma_y = 356$  MPa based on typical shearing mechanism with the DFT material properties. The current prediction of 373 MPa Table 4.6 is quite close to this previous estimate, but here we have encompassed all the atomistic knowledge and validation of theories.

The shearing models discussed here can also be used to introduce shearing into the Discrete Dislocation Dynamics models. Specifically, at each step of a DDD simulation, the theories here can be applied to each precipitate to determine if, at the current load and the spacings of the two bowing loops on either side of the precipitate, the precipitate should be sheared. If so, then the precipitate can be removed from the simulation (which is equivalent to allowing the dislocation to pass through the precipitate) and the DDD simulation is then relaxed to the next new configuration.

### 4.8 Optimal Precipitate Size

In Section 1.3 we derived two simple formulas for CRSS predictions for the Orowan and shearing mechanisms. Then by equating two predictions, a simple formula for optimal precipitate size (assuming an equivalent circular shape on the glide plane, and the radius is  $r$ ) is obtained

$$r_{\text{opt}} = \frac{T}{\gamma} \quad (4.11)$$

The above relationship implies that the optimal precipitate size is achieved when the dislocation line tension  $T$  is balanced with a resistant force via the Generalized Stacking Fault Energy (GSFE)  $\gamma$ . Once a proper estimate of line tension  $T$  and  $\gamma$  is found, then we can suggest an optimal precipitate size.

The GSFE of a precipitate is a fixed material property that can be quantified by either first principle calculations (DFT) or molecular statics (MS) at 0 K [58]. In contrast, the dislocation line tension  $T$  is a much more complicated quantity. As described in Section 2.3, the dislocation line tension depends not only on the material properties such as the shear modulus, poisson ratio, and dislocation core energy, but also on the dislocation geometry. For the current precipitation strengthening problem, the dominating geometry is the dislocation bow-out. If a specific matrix material is chosen (or a potential is used), and the material properties such as  $\mu$ ,  $\nu$ , and  $E_c$  are fixed, then the dislocation line tension can be treated as a function of the precipitate edge-edge spacing  $L$  and radius  $r$ , i.e.  $T(L, r)$ , if assuming a circular shape on a glide plane. The following formula for dislocation line tension is proposed by the BKS theory as described in Section 1.3

$$T = A\mu b^2 \left( \ln \frac{\bar{D}}{b} + B \right) \quad (4.12)$$



with  $A = 1/4\pi$  for edge, and  $A = 1/4\pi(1 - \nu)$  for screw,  $B$  is a constant related to the dislocation core energy at  $b$ , and  $\bar{D}$  is the harmonic average of diameter  $D = 2r$  and  $L$ , i.e.  $\bar{D} = (D^{-1} + L^{-1})^{-1}$ . This expression may be useful in describing systems with simple precipitate geometries such as circles or squares, as shown in Section 2.7.2. But, with the addition of a more complicated geometry, e.g. parallelogram for the current needle-shaped precipitate, there may not be a simple form of  $T$ . Moreover, the precipitate radius,  $r$ , is also hard to characterize for a more complex shape.

Fortunately, simulations can be utilized in determining the dislocation line tension. An in-situ characterization procedure was presented for atomistic simulations. Such characterizations require a stable dislocation configuration at a given load  $\tau$  (preferably close to the CRSS) and its radius of curvature  $R$ . Under these conditions  $T = \tau bR$ . It should be noted that in such a characterization process we actually embed all the dislocation interactions in this quantity. In other words, we assume an equivalent dislocation line having the same strength  $T$  as the original dislocation geometry (periodic bow-outs, etc.) but without interactions between dislocation segments.

However, atomistic simulations are inherently computationally expensive. To avoid this expense, Discrete Dislocation Dynamics (DDD) can be utilized to examine the dislocation line tension. As is demonstrated earlier in this chapter, with an atomistically informed dislocation core energy, we can not only match the atomistic dislocation geometry quite well, but also have a fairly good prediction of the CRSS. Simply put, Discrete Dislocation Dynamics simulations reliably produce results consistent with atomistic simulations. Therefore, we can obtain an accurate prediction of line tension  $T$  from critical stable configurations of DDD simulations.

After extensive DDD simulations and characterizations, we can have a similar plot as Figure 4.11. Here  $T$  is obtained using the characterization methods described above, and  $F$  is the resisting force which can be calculated as  $F = \gamma D$ , where  $D$  is the transverse precipitate distancing. An optimal precipitate size is obtained at the intersection of these two curves.

Once we have determined optimal precipitate size, we need to fabricate the alloy containing this specific size of precipitate, which is another challenging task. This requires experimental experience and/or other simulation techniques such as the phase field method [67].

In the above design process, there are many assumptions buried in the derivation. For example, the optimal design equation (4.11) holds only when the breaking angle for Orowan looping is  $0^\circ$ , which is not true for the random case. Another assumption is that the shearing scales  $\propto \sqrt{r}$  due to the use of Friedel statistics. This assumes that the precipitates be “weak”, which may not be true for strong precipitate here. Nevertheless, the simulations in [78] for sphere precipitates tend agree with the results predicted by (4.11). To find the optimal precipitate size with other geometries, we need to conduct extensive simulations for precipitates with the required shapes. These simulations should mirror the spherical simulations performed in [78] enabling both looping and shearing mechanisms. Although the equation (4.11) is not fully established, we can still utilize it to observe general trends. For the optimal precipitate

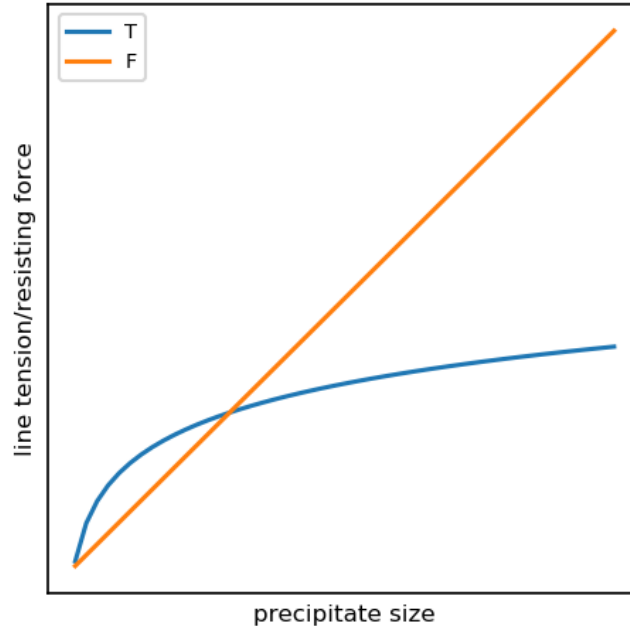


Figure 4.11 – Line tension  $T$  and resisting force  $F$  vs precipitate size.

size, the dislocation line tension and GSFE supported resistance must have some form of equilibrium, which can be more complicated than the simple form of (4.11).

## 4.9 Conclusion

In this study, a near-chemically-accurate Al–Mg–Si Neural Network Potential is used to investigate precipitation strengthening problem in this alloy. The precipitation strengthening mechanisms in the alloy are understood thoroughly through careful atomistic simulations, continuum simulations and theory studies. The major findings are: (i) both precipitate shearing and looping occurs in atomistic simulations, observed in mesoscale study [52], (ii) GSFE and RSS are both important for strengthening mechanism, i.e. large impeding RSS and GSFE can incur looping, (iii) theoretical shearing predictions, combined with DDD simulations, can correctly predict the strengthening mechanisms and match most of the atomistic CRSS, (iv) DDD simulations with atomistically calibrated core energies and atomistic RSS can match atomistic dislocation configuration quite well, (v) with the knowledge gained through atomistics and theory, a reasonable uniaxial tensile yield strength for the real material was achieved.

The excellent agreement of the dislocation geometry from atomistic and mesoscale simulations as well as CRSS calculation in terms of Orowan mechanism implies that an atomistically calibrated mesoscale simulations can achieve atomistic accuracy. This motivates further development of Discrete Dislocation Dynamics to encompass all the possible dislocation-precipitate interactions. Furthermore, we can use the atomistically calibrated DDD to acquire

the critical line tension. By comparing this with the critical GSFE, we can obtain an optimal precipitate size which guides precipitate formation.



## 5 Summary

In an effort to gain a thorough understanding of precipitation strengthening in Al–Mg–Si alloys, and gain the capacity to accurately predict strength increases, a range of problems were addressed on several scales .

The first issue addressed was the calculation of dislocation core energy [53]. This energy was required as an input for the mesoscale DDD simulations in order to make quantitative predictions of strengthening. In contrast to the dipole model [26], which needs an image effect correction, we turned to a straightforward flat cylinder model for core energy calculation. To integrate such a dislocation core energy into Discrete Dislocation Dynamics, we worked out the energetics of a single dislocation in non-singular theory, where an additional term was discovered which is not included in the singular theory. This term needs to be considered when embedding the atomistic dislocation core energy into the DDD code. With proper energetic analysis of partial dislocations and geometry relationships, the characterization of partial dislocation core energy is also feasible. The validation of this calibrated DDD (with full dislocation core energy) was performed by simulating the bow-out problem with comparison to atomistic results. These results confirmed that with a proper calibrated dislocation core energy, atomistic accuracy can be achieved. It should be noted that a regularization parameter  $a = 2\text{ eb} - 4\text{ eb}$  is suggested. Moreover, the dislocation core energy is demonstrated to be very important for nanoscale problems, such as precipitation strengthening. Evidence of this was found in line tension estimations and CRSS calculations within the context of Orowan mechanism. An important point is that dislocation core energy within  $1.3\text{ b}$  contributes 60% of the CRSS and dislocation core energy within  $5.2\text{ b}$  gives almost the full CRSS for the concerned scale in Al–Mg–Si, as a default dislocation core energy can overestimate the CRSS (double the result of atomistic energetics).

The study of dislocation core energy in various contexts is a stepping stone towards solving more sophisticated problems, e.g. precipitation strengthening [52]. As acknowledged by canonical metallurgy wisdom [114, 84], precipitates can either be sheared or looped by a dislocation. In a process of alloy manufacturing, the strength of an alloy first increases and then decreases as the growth of precipitates, corresponding to a shearable to non-shearable

transition [97]. When an alloy is optimally aged, shearing and looping mechanisms provides equal strengthening (CRSS). Based on this logic, we modeled Orowan looping in Discrete Dislocation Dynamics with experimental characterizations of peak-aged alloys (volume fraction, cross section, precipitate length). First, a method for creating pseudo-random microstructures was proposed. Then the mesoscale simulation tool DDD was adapted to include the dislocation-precipitate interaction. With these modeling strategies, we simulated a range of systems with various experimental characterizations. The systematic investigation of different simulation conditions, such as with or without misfit stress, different microstructures, different volume fractions, and different material properties provided a lot of insight into precipitation strengthening for the current complex geometries. The key findings are: 1. the effect of misfit stress is marginal, 2. precipitate edge-edge spacing controls CRSS and it is about 70% of center-center spacing, 3. dislocation core energy is crucial in prediction. However, with the most state-of-the-art modeling strategies and atomistic dislocation core energy, we still overestimated the material uniaxial tensile yield strength by about 33%-50%. This motivated us to look at dislocation-precipitate interaction in detail, paying special consideration to the forces on individual precipitates. Comparing the applied force from the mobile dislocation and the resisting force supplied by Generalized Stacking Fault Energy proves that shearing happens at various locations. The predicted yield strength based on shearing mechanism is closer to the experimental yield strength. This shows that even for peak-aged Al-Mg-Si alloys, shearing controls its strength.

Now the question is what really happens in atomistic simulations during the dislocation-precipitate interaction? Intricate experiments have been developed to observe these interactions at atomistic scale [24], providing evidence for shearing. Here, we used atomistic simulations to confirm this point. These simulations were made possible by the newly developed Al-Mg-Si Neural Network Potential [58]. For the current dislocation-precipitate interaction problem, we carried out molecular statics simulations using this potential. The simulation result shows that both dislocation shearing and looping can take place depending on precipitate shearing energy and precipitate RSS, which are associated with precipitate orientations and loading directions. Shearing theories and looping simulations with calibrated (and validated) DDD demonstrated the ability to accurately predict the controlling mechanism and CRSS for most cases. Based on these validated theories and simulations, reasonable uniaxial tensile yield stress predictions were achieved using more accurate first-principle material properties. We also demonstrated that Discrete Dislocation Dynamics with atomistic core energy and atomistic misfit stress field can reproduce both atomistic dislocation and atomistic CRSS for looping. It was then reveals that mesoscale simulations can achieve atomistic accuracy with the essential atomistic information. Hence we can utilize DDD for estimating dislocation line tension in a bow-out geometry with high fidelity, which is a quantity rather difficult to characterize. Together with a calculated Generalized Stacking Fault Energy (either from DFT or MS), an optimal precipitate size can be solved  $r = T(r)/\gamma$ .

The careful study above deepens our understanding of precipitation strengthening and will contribute to future research within this field. The possible directions of such a research effort

---

are listed below.

- Since Discrete Dislocation Dynamics simulation can achieve atomistic accuracy with a much smaller computation cost than atomistic simulations, it then needs further development to include all possible dislocation-precipitate interactions, e.g. shearing mechanism, or cross-slip. Prior efforts are devoted to the Ni-based superalloys [43, 55], which has a relatively regular geometry. Recent work done by [104] has tackled the shearing problem of more disc-like precipitates in Al–Cu alloys. However, systematic simulations are demanded to extract the scaling of shearing and looping mechanisms for complex realistic geometries. Such investigation can be either in a periodic setting or random setting, from which we can determine random factors for various cases.
- As noted by various researchers [35, 105, 62], the dislocation-precipitate interaction process can be thermally activated, i.e. CRSS can be reduced due to finite temperature. This effect should also be understood in the current alloy system, particularly in combination with shearing and looping mechanism. This might require Nudged Elastic Band (NEB) calculations for calculating the energy barrier. Eventually, with a finite temperature effect included, we are able to predict alloy strength in a more realistic condition and close the gap between simulation and experiment.
- The ultimate goal of this study is to obtain an optimal precipitate size. A simple scheme of finding the optimal size is proposed in Section 4.8. Such procedures need to be examined carefully and validated by simulations or experiments. There are many assumptions and details in this scheme that should be clarified in future work, before application to other alloy systems. As mentioned in Section 4.8, we can employ other simulation techniques such as phase field modeling [67] to make a fully virtual material design. This modeling strategy would be more fundamental than previous work [83, 10], which relies on a lot of parameters and coefficients that are either heuristic or calibrated from experiments.

In summary, we have addressed several problems ranging from dislocation core energy, mesoscale dislocation-precipitate interaction, and atomistic precipitation strengthening mechanisms. The key issues in precipitation strengthening were carefully examined with results presented clearly. These results are not only useful for the alloy system examined here, but also could guide research into other systems with higher geometrical complexity. Although much research is still needed, the multiscale bottom-up approach of material design shows very good prospect for the future.





# A List of Line Tensions

## General Derivation of Line Tension due to Self Energy

We first reproduce the derivation in [64] in detail. In contrast to the derivation in [49], the derivation here does not assume an a priori geometry, thus is general for self energy. A curved

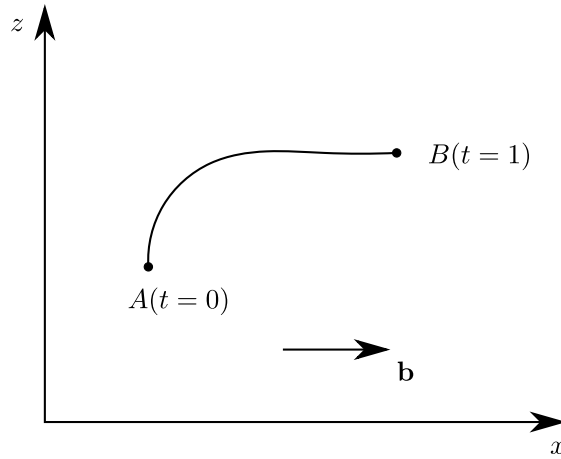


Figure A.1 – Dislocation curve with fixed ends.

dislocation is connected to fixed ends A and B (Figure A.1). The dislocation line lies on the  $xz$ -plane with the Burgers vector  $\mathbf{b}$  parallel to the  $x$  axis. The dislocation line is parameterized by  $t$ , i.e.  $(x(t), z(t))$ ,  $t = 0$  for A,  $t = 1$  for B. The energy per unit length for character  $\theta$  is denoted as  $E(\theta)$ . And we know the tangent of the dislocation line can be expressed by

$$\tan \theta(t) = \frac{z'(t)}{x'(t)} \quad (\text{A.1})$$

When ignoring the interaction energy, the dislocation self energy is (including the elastic and core energy)

$$U^d = \int_A^B E[\theta(t)] ds \quad (\text{A.2})$$

## Appendix A. List of Line Tensions

---

Assuming virtual displacement as  $\delta \mathbf{r}(t) = (\delta x(t), \delta z(t))$ , the potential energy due to the external loading is

$$- \int_A^B \mathbf{f}^0(t) \cdot \delta \mathbf{r}(t) ds \quad (\text{A.3})$$

where  $\mathbf{f}^0(t)$  is the Peach-Koehler force  $\mathbf{f}^0(t) = (\mathbf{b} \cdot \boldsymbol{\sigma}) \times \boldsymbol{\xi}$ . If only the force in xz-plane is considered. Then  $\mathbf{f}^0(t) = b\sigma_{xy}^0(\sin\theta(t), -\cos\theta(t))$ . (A.3) reduces to

$$- \int_A^B b\sigma_{xy}^0(\sin\theta\delta x - \cos\theta\delta z) ds \quad (\text{A.4})$$

The variation of total energy  $\delta U^{\text{tot}} = 0$  corresponds to

$$\delta U^{\text{tot}} = \delta U^d - \int_A^B \mathbf{f}^0(t) \cdot \delta \mathbf{r}(t) ds = 0 \quad (\text{A.5})$$

The variation in  $\delta U^d$  is (using  $s'(t) = [x'(t)^2 + z'(t)^2]^{1/2}$ )

$$\begin{aligned} \delta U^d &= \int_0^1 \delta \left\{ E[\theta(t)] \frac{ds}{dt} \right\} dt \\ &= \int_0^1 \delta \{ E[\theta(t)] \} \frac{ds}{dt} + E[\theta(t)] \delta \left\{ \frac{ds}{dt} \right\} dt \\ &= \int_0^1 \left\{ E'(\theta) \delta \theta(t) [x'(t)^2 + z'(t)^2]^{1/2} + E(\theta) \delta [x'(t)^2 + z'(t)^2]^{1/2} \right\} dt \end{aligned} \quad (\text{A.6})$$

To derive the variation  $\delta \theta(t)$  we use the geometry relation (taking variation at both sides)

$$\tan \theta = \frac{z'}{x'} \Rightarrow \frac{1}{\cos^2 \theta} \delta \theta = \frac{(\delta z')x' - z'(\delta x')}{x'^2} \quad (\text{A.7})$$

Noting the following relation

$$\frac{z'}{\sqrt{x'^2 + z'^2}} = \sin \theta, \quad \frac{x'}{\sqrt{x'^2 + z'^2}} = \cos \theta \quad (\text{A.8})$$

We simplify (A.6) by using (A.7) and (A.8)

$$\begin{aligned} \delta U^d &= \int_0^1 \left\{ E'(\theta) \delta \theta(t) [x'(t)^2 + z'(t)^2]^{1/2} + E(\theta) \delta [x'(t)^2 + z'(t)^2]^{1/2} \right\} dt \\ &= \int_0^1 \left\{ E'(\theta) \frac{x' \delta z' - z' \delta x'}{x'^2 + z'^2} [x'^2 + z'^2]^{1/2} + E(\theta) \left[ \frac{x' \delta x'}{\sqrt{x'^2 + z'^2}} + \frac{z' \delta z'}{\sqrt{x'^2 + z'^2}} \right] \right\} dt \\ &= \int_0^1 \left\{ E'(\theta) (\cos \theta \delta z' - \sin \theta \delta x') + E(\theta) (\cos \theta \delta x' + \sin \theta \delta z') \right\} dt \\ &= \int_0^1 \left\{ [E(\theta) \cos \theta - E'(\theta) \sin \theta] \delta x' + [E(\theta) \sin \theta + E'(\theta) \cos \theta] \delta z' \right\} dt \end{aligned} \quad (\text{A.9})$$

Integrate by parts and use  $\delta x, \delta z = 0$  at  $t = 0, 1$ . The first term is written as

$$\begin{aligned} & \int_0^1 [E(\theta) \cos \theta - E'(\theta) \sin \theta] \delta x' dt \\ &= [E(\theta) \cos \theta - E'(\theta) \sin \theta] \delta x \Big|_0^1 - \int_0^1 [E(\theta)(-\sin \theta) - E''(\theta) \sin \theta] \frac{d\theta}{dt} \delta x dt \\ &= \int_0^1 [E(\theta) + E''(\theta)] \sin \theta \delta x \left( \frac{d\theta}{dt} \right) dt \end{aligned} \quad (\text{A.10})$$

The same calculation applies to the second term in (A.9). Then (A.9) is reduced to

$$\begin{aligned} \delta U^d &= \int_0^1 [E(\theta) + E''(\theta)] [\sin \theta \delta x - \cos \theta \delta z] \left( \frac{d\theta}{dt} \right) dt \\ &= \int_A^B [E(\theta) + E''(\theta)] [\sin \theta \delta x - \cos \theta \delta z] \left( \frac{d\theta}{ds} \right) ds \end{aligned} \quad (\text{A.11})$$

Then (A.5) can be simplified as

$$\delta U^{\text{tot}} = \int_A^B \left\{ [E(\theta) + E''(\theta)] \left( \frac{d\theta}{ds} \right) - b\sigma_{xy}^0 \right\} [\sin \theta \delta x - \cos \theta \delta z] ds \quad (\text{A.12})$$

for all variation  $\delta x, \delta z$  satisfying the boundary condition. Hence

$$[E(\theta) + E''(\theta)] \left( \frac{d\theta}{ds} \right) = b\sigma_{xy}^0 \quad (\text{A.13})$$

So a local definition of line tension can be

$$T = E(\theta) + E''(\theta) \quad (\text{A.14})$$

noting the curvature is also embedded in (A.13) as  $\frac{d\theta}{ds} = \frac{1}{r}$ . So the simple local form  $T = \tau br$  is also recovered.

In the context of anisotropic elasticity, the infinite straight dislocation self energy per unit length is

$$E(\theta) = K(\theta) \ln \left( \frac{R}{r_c} \right) + E_c(\theta) \Big|_{r_c} \quad (\text{A.15})$$

In an infinite elastic medium, the dislocation self energy of a finite segment is

$$W(\theta) = L \left( K(\theta) \ln \left( \frac{L}{\rho} \right) + E_c(\theta) \Big|_{r_c} \right) \quad (\text{A.16})$$

To make the dislocation energy consistent, the interaction cutoff  $\rho = r_c/2$  [49]. Hence with the definition in (A.14) we have the estimation of line tension per unit length of a dislocation due to its self energy as

$$T_{\text{self}} = (K(\theta) + K''(\theta)) \ln \left( \frac{L}{\rho} \right) + (E_c(\theta) + E_c''(\theta)) \Big|_{r_c} \quad (\text{A.17})$$

## Appendix A. List of Line Tensions

For isotropic elasticity, this expression is simplified as  $(K(\theta) = \frac{\mu b^2}{4\pi} \left( \cos^2 \theta + \frac{\sin^2 \theta}{1-\nu} \right))$

$$T_{\text{self}}^{\text{iso}} = \frac{\mu b^2}{4\pi(1-\nu)} \left[ (1+\nu) \cos^2 \theta + (1-2\nu) \sin^2 \theta \right] \ln \left( \frac{L}{\rho} \right) + (E_c(\theta) + E_c''(\theta))|_{r_c} \quad (\text{A.18})$$

### Line Tension of Different Geometries

The above derived dislocation line tension is based only on the dislocation self energy (including both elastic self energy and dislocation core energy). However, different parts of dislocation curve can interact with each other and hence change the overall dislocation line tension. So more precise definition of dislocation line tension involves dislocation geometry  $X$  and the energy variation due to the perturbation of a given geometry as given in Section 2.3.

$$T_x = \frac{\delta W}{\delta L} \quad (\text{A.19})$$

In [49, 68] the authors have derived line tension expressions for different typical geometries. We list them here and compare them for different characteristic lengths.

#### Small Triangular Bowout

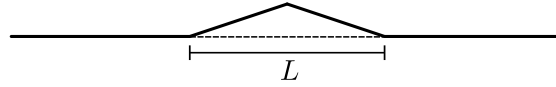


Figure A.2 – Small bowout of length  $L$ . Left and right arms are infinite long.

The geometry is shown in Figure A.2 and the line tensions for initially screw and edge are

$$\begin{aligned} T^{\text{screw}} &= \frac{\mu b^2}{4\pi(1-\nu)} \left[ (1+\nu) \ln \frac{L}{\rho} - 1.89\nu - 2.89 \right] \\ T^{\text{edge}} &= \frac{\mu b^2}{4\pi(1-\nu)} \left[ (1-2\nu) \ln \frac{L}{\rho} + 4.78\nu - 2.89 \right] \end{aligned} \quad (\text{A.20})$$

#### Large Semi-hexagonal Bowout

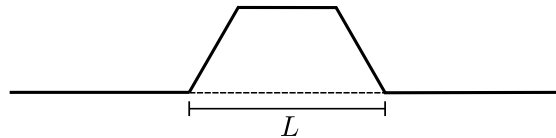


Figure A.3 – Large bowout of length  $L$  (semi-hexagon) . Left and right arms are infinite long.

The large semi-hexagonal bowout involves character angle of  $60^\circ$ . In [49] the expressions of energy change from an initially straight dislocation to the large bowout geometry is given. The derivatives of the energy change with respect to the characteristic length  $L$  is then the line

tension.

$$\begin{aligned} T^{\text{screw}} &= \frac{\mu b^2}{4\pi(1-\nu)} \left[ \left(1 + \frac{\nu}{2}\right) \ln \frac{L}{\rho} + 0.46\nu - 1.05 \right] \\ T^{\text{edge}} &= \frac{\mu b^2}{4\pi(1-\nu)} \left[ \left(1 - \frac{3\nu}{2}\right) \ln \frac{L}{\rho} + 0.50\nu - 1.05 \right] \end{aligned} \quad (\text{A.21})$$

### Sinusoidal Bowout

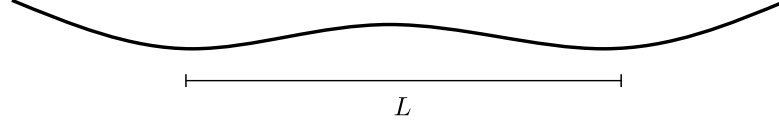


Figure A.4 – Periodic sinusoidal bowout of length  $L$ .

The line tension of sinusoidal bowout geometry is presented in [68] for screw dislocation. Changing the prefactor carefully, we can also obtain the corresponding line tension for edge dislocation. Such line tension can also be derived in the context of non-singular theory as given in the supplementary document of [44]. This sort of bowout geometry is still a small bowout but involves interaction with neighboring sections.

$$\begin{aligned} T^{\text{screw}} &= \frac{\mu b^2}{4\pi(1-\nu)} \left[ (1+\nu) \ln \frac{L}{r_c} - 1.221\nu - 2.221 \right] \\ T^{\text{edge}} &= \frac{\mu b^2}{4\pi(1-\nu)} \left[ (1-2\nu) \ln \frac{L}{r_c} + 3.942\nu - 2.221 \right] \end{aligned} \quad (\text{A.22})$$

### BKS Line Tension

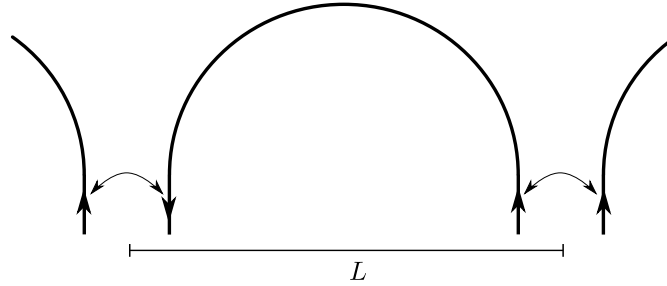


Figure A.5 – BKS bowout geometry with interacting neighboring arms.

The BKS line tension is formulated in [9], but it is a postulation that has never been proven. It accounts for the neighboring branch interaction and is justified by various simulations [9].

$$\begin{aligned} T^{\text{screw}} &= \frac{\mu b^2}{4\pi(1-\nu)} \left[ \ln \frac{\bar{D}}{b} + B \right] \\ T^{\text{edge}} &= \frac{\mu b^2}{4\pi(1-\nu)} \left[ (1-\nu) \ln \frac{\bar{D}}{b} + B \right] \end{aligned} \quad (\text{A.23})$$

### Comparison

Using a Bacon-Scattergood effective moduli  $\mu = 29.6$  GPa,  $\nu = 0.35$  based on DFT Al properties, we can compare different line tensions (Figure A.6). The core related  $(E_c + E_c'')|_b$  line tension is derived from the NNP16 core energies. To be consistent in the analysis, we set  $r_c = b$ , then  $\rho = 0.5b$ . The constant  $B$  in BKS line tension is ignored. And a typical precipitate dimension  $D = 3$  nm is chosen. The comparison in Figure A.6 shows that (i) for the same  $L$  the screw line tension is much larger than the corresponding edge case, (ii) small triangular bowout and sinusoidal bowout has very similar  $T$ , while the BKS and large bowout has a different scaling, (iii) BKS  $T$  varies slowly with  $\ln(L)$  due to harmonic average of  $D$  and  $L$ , (iv) in all cases core contribution to  $T$  should be included for its comparable values. For a specific problem, we then need to choose an appropriate line tension formula and possibly matching the underlying atomistic behavior.

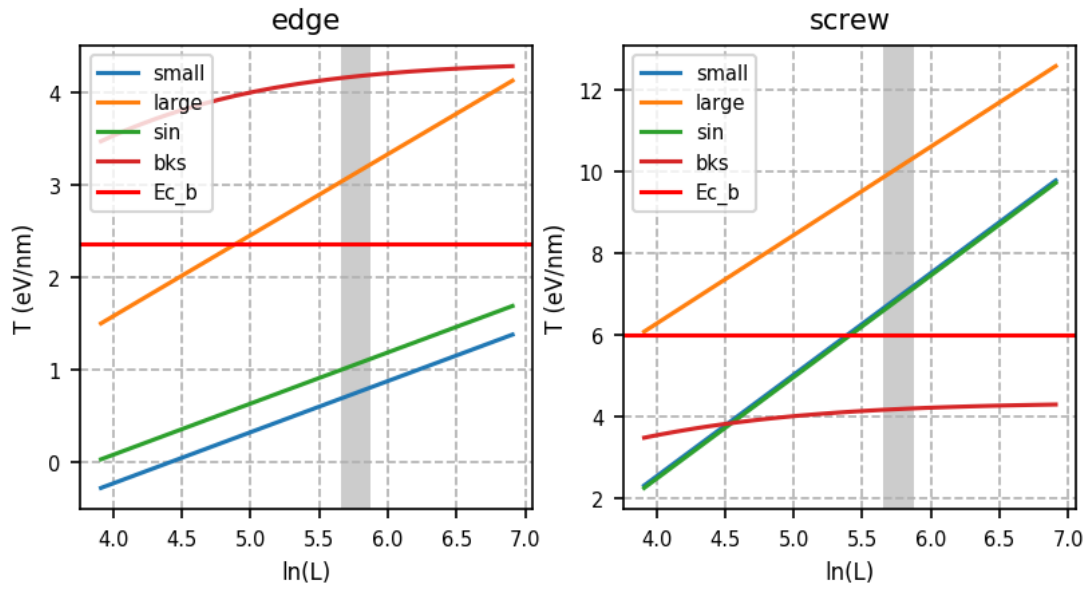


Figure A.6 – Different line tensions using for edge/screw. The gray area is for  $L = 100b \sim 125b$ , relevant to the current precipitation strengthening problem.

## B Introduction of FFT method

For the elastic misfit stress calculations, we use a variational FFT-based method to approximate the solution to the equilibrium equations on a regular periodic pixel or voxel grid [130] as in the open source package  $\mu$ Spectre [59].

The basic idea of the method is to use the discrete Fourier transform basis functions  $\varphi_{\mathbf{q}_m}(\mathbf{x})$  as shape functions for a Galerkin discretization of the periodic domain,

$$\varphi_{\mathbf{q}_m}(\mathbf{x}) = \exp(2\pi i \mathbf{q}_m \cdot \mathbf{x}), \quad (\text{B.1})$$

where  $\mathbf{q}_m$  is the normalized wave vector of the  $m$ -th Fourier space grid point. These basis functions are interpolatory and constitute a partition of unity.

Standard Galerkin discretization then allows for a determination of the stiffness matrix  $\mathbf{C}$  of the discretized problem and for the solution of the linear elasticity problem as

$$\mathbf{C}\mathbf{u} = -\mathbf{C}\mathbf{u}_{\text{ref}}, \quad (\text{B.2})$$

where  $\mathbf{u}$  is the vector of nodal displacements and  $\mathbf{u}_{\text{ref}}$  is a uniform displacement due to applied strain boundary conditions. One can also express the stiffness matrix  $\mathbf{C}_{\text{ref}}$  of a replacement problem with the same discretization grid, but uniform material properties. This reference stiffness matrix  $\mathbf{C}_{\text{ref}}$  corresponds a convolution and can therefore be expressed *and inverted* in Fourier space at low computational cost. The inverse  $\Gamma = \mathbf{C}_{\text{ref}}^{-1}$  corresponds to the discretized Greens function of the problem and happens to be a preconditioner to the problem (B.2) with excellent spectral properties.

The preconditioned problem

$$\Gamma \mathbf{C}\mathbf{u} = -\Gamma \mathbf{C}\mathbf{u}_{\text{ref}}, \quad (\text{B.3})$$

can be solved very efficiently using projection-based solvers such as the conjugate gradient method.

---

This chapter is written with the help of Dr. T. Junge

## Appendix B. Introduction of FFT method

---

Note that the formulation in [130] makes a modification to the stiffness matrix such that the unknowns are strains  $\boldsymbol{\varepsilon}$  instead of  $\mathbf{u}$ , leading to the main equation

$$\mathbf{G}\mathbf{K}\boldsymbol{\varepsilon} = -\mathbf{G}\boldsymbol{\sigma}, \quad (\text{B.4})$$

where  $\mathbf{G}$  and  $\mathbf{K}$  correspond to the modified Greens function matrix  $\Gamma$  and the modified stiffness matrix  $\mathbf{C}$ , and  $\boldsymbol{\sigma}$  corresponds Cauchy stress. The modifications are straight-forward and omitted here for brevity. The interested reader will find them well explained in Zeman et al. [130].

In Figure B.1 we list the misfit stress calculations of precipitate using FFT and FEM. Efficient FFT calculation shows a higher resolution.

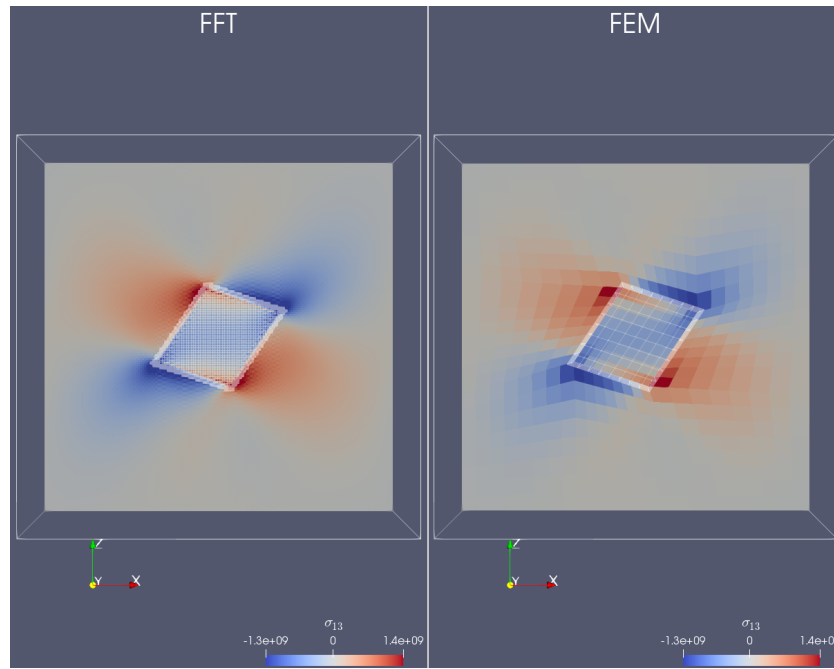


Figure B.1 – Example FFT calculation compared with FEM.



# C Behler-Parrinello Neural Network Potential

In Behler-Parrinello Neural Network Potential [11], the interatomic potential is constructed via a feedforward artificial neural network. While the structure of a Neural Network Potential (NNP) is fairly standard, the most critical part of a NNP is the input layer. The input layer of the Behler-Parrinello NNP consists of carefully selected symmetry functions which encode the multibody interactions in an atomistic environment and preserve the invariance under rotation etc. The relevant radial and angular symmetry functions are [58]

$$G_i^{\text{radial}} = \sum_{j \neq i} e^{-\eta(R_{ij}-R_s)^2} f_c(R_{ij}) \quad (\text{C.1})$$

$$G_i^{\text{angular}} = 2^{1-\zeta} \sum_{j,k \neq i} \left[ (1 + \lambda \cos \theta_{ijk})^\zeta e^{-\eta(R_{ij}^2 + R_{ik}^2 + R_{jk}^2)} f_c(R_{ij}) f_c(R_{ik}) f_c(R_{jk}) \right] \quad (\text{C.2})$$

where  $\lambda = +1, -1$ ,  $\eta$ , and  $\zeta$  are parameters.  $\mathbf{R}_{ij} = \mathbf{R}_i - \mathbf{R}_j$  and  $\theta_{ijk} = \mathbf{R}_{ij} \cdot \mathbf{R}_{ik} / (R_{ij} R_{ik})$ . The cutoff function  $f_c(R_{ij})$  can be chosen as

$$f_c(R_{ij}) = \begin{cases} \tanh^3 \left[ 1 - \frac{R_{ij}}{r_c} \right] & \text{for } R_{ij} \leq r_c \\ 0 & \text{for } R_{ij} > r_c \end{cases} \quad (\text{C.3})$$

In the current Al-Mg-Si, we have the following form for energy per atom

$$E_i^{\text{atom}} = f_a \left\{ b_1^3 + \sum_{k=1}^{24} a_{k,1}^3 f_a \left[ b_k^2 + \sum_{j=1}^{24} a_{j,k}^2 f_a \left( b_j^1 + \sum_{\mu=1}^{64} a_{\mu,j}^1 G_i^\mu \right) \right] \right\} \quad (\text{C.4})$$

Here  $\{G_i^\mu\}$  is the set of symmetry functions for atom  $i$ , and we carefully chose 64 symmetry functions either in radial form (C.1) or angular form (C.2). In such representation, we have actually two hidden layer, each with 24 nodes. And the activation function  $f_a$  is the softplus function. Coefficients  $a_{m,n}^l$  and bias  $b_m^l$  are the parameters to be sought for in the optimization

## Appendix C. Behler-Parrinello Neural Network Potential

process. With the energy per atom, we write the total energy per structure as

$$E^s = \sum_{i=1}^N E_i^{\text{atom}} \quad (\text{C.5})$$

In the training, a mean square loss function as a combination of energy and force is set up

$$\Gamma^{\text{loss}} = \frac{1}{n} \sum \left[ (E^{s,\text{NNP}} - E^{s,\text{DFT}})^2 + \frac{\alpha}{3N_s} \sum_{i=1}^{3N_s} (F_i^{s,\text{NNP}} - F_i^{s,\text{DFT}})^2 \right] \quad (\text{C.6})$$

with  $\alpha$  as the parameter balancing the weight of energy and force. The optimizer in the training is Kalman filter based method to avoid local minima. For further parameters and details, we recommend to refer to [58].

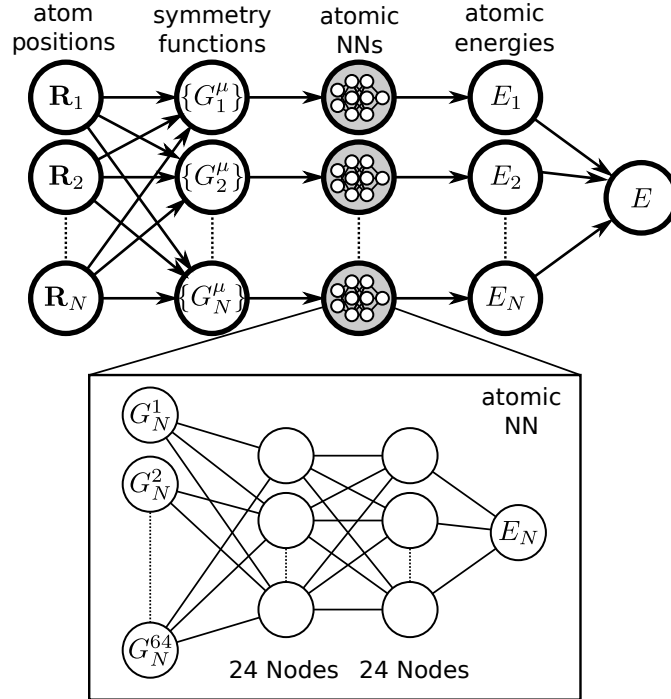


Figure C.1 – Neural Network Potential structure for an atomic environment with  $N$  atoms.

In the simulation, we use the LAMMPS interface of n2p2. One practical detail to point out is that although the energy is well defined, the Potential Energy Surface (PES) can be rough, cf. GSFE of precipitates in [58]. More problematic is that we may encounter a lot of Extrapolation Warning (EW) during the run, and for certain situations the number of EW can explode and so with the force. To restrict the simulation system in a reasonable regime (interpolation), we can add a moderate Lennard-Jones (LJ) potentials in the simulation. This technique is also documented in [58].

## D Simulation with ParaDiS

ParaDiS is an open source Discrete Dislocation Dynamics code [7] based on the non-singular theory [20]. It has a lot of nice feature and can solve a lot of mesoscale problems [16, 17, 31]. In this section, we cover some relevant implementation issue for our research and some subtleties that needs caution when performing simulations.

### Dislocation Nodal Force due to Core Energy

As is introduced in Section 1.2.2, for a dislocation segment with line vector  $\mathbf{l}$  (unit line direction vector  $\mathbf{t}$ ) and Burgers vector  $\mathbf{b}$  and dislocation core energy per unit length as  $E_c(\mathbf{b}, \mathbf{t})$ . Then the induced core force is (the node subscripts are ignored here)

$$\mathbf{f}^{\text{core}} = - \frac{\partial E_c(\mathbf{b}, \mathbf{t}) \|\mathbf{l}\|}{\partial \mathbf{l}} \quad (\text{D.1})$$

With careful derivation , we obtain the core force expression

$$\mathbf{f}^{\text{core}} = -E_c(\mathbf{b}, \mathbf{t}) \mathbf{t} - (\mathbf{I} - \mathbf{t} \otimes \mathbf{t}) \cdot \frac{\partial E_c(\mathbf{b}, \mathbf{t})}{\partial \mathbf{t}} \quad (\text{D.2})$$

In ParaDiS the default form of dislocation core energy is

$$E_c = E_{\text{core}} \left( b_s^2 + \frac{b_e^2}{1 - \nu} \right) \quad (\text{D.3})$$

If no  $E_{\text{core}}$  is specified in the simulation, a value of  $E_{\text{core}} = \mu / (4\pi) \ln(a/0.1)$  is then declared (all the geometry quantity is in  $b$  in ParaDiS, hence all normalized by  $b$ ). Such a core energy leads to the core force as

$$\mathbf{f}^{\text{core}} = E_{\text{core}} \left[ 2b_s \frac{\nu}{1 - \nu} \mathbf{b}_e - \left( b_s^2 + \frac{b_e^2}{1 - \nu} \right) \mathbf{t} \right] \quad (\text{D.4})$$

For a higher order core energy (already subtracted with the extra non-singular terms) as

$$E_c(\theta) = a_n(\cos^2 \theta)^n + a_{n-1}(\cos^2 \theta)^{n-1} + \dots + a_0 \quad (\text{D.5})$$

The core force is implemented as

$$\mathbf{f}^{\text{core}} = -E'_c(\theta) \frac{\mathbf{b}_e}{b_e} - E_c(\theta) \mathbf{t} \quad (\text{D.6})$$

## Loading Type

Due to the complicated interactions and geometrical operations (refine, coarsen, merge and split) the nodal positions can oscillate during integration of the governing equations [108]. This effect does not vanish even with an advanced integrator [109]. As a result, the positional oscillation can lead to oscillation of the nodal forces, hence impossible to set a force tolerance criterion, if a stable (or converged) configuration is sought after. One remedy for finding a converged solution is to use a fixed loading and monitor the plastic strain. The plastic strain can be regarded as overall displacement. Such a “displacement” approaching zero means a converged configuration. The corresponding settings are `loadType=0` and `saveprop=1`.

In CRSS calculation, one can load the system incrementally, once a converged state is attained, the current loading is a lower bound of CRSS. If the mobile dislocation pass the obstacle array, then the current load is an upper bound. Alternatively, we can use a constant strain loading, i.e. `loadType=1` and monitor the stress-strain curve. The maximum load is the CRSS. And a convergence test is needed for finding an appropriate strain rate.

## Regularization Parameter $a$

As is presented in Section 1.2.1 and Section 2.2, the dislocation energy should not depend on how the core energy is partitioned. Furthermore, the CRSS calculation of 1D periodic model in Section 2.7.2 shows that the CRSS does not change with regularization parameter  $a$ , once we have a full energetic description. However, we should be careful about the choice of  $a$ , since too small  $a$  can lead to local instability, when the full energetics is used (elasticity + core energy). This will then end with non effective blocking when the Orowan mechanism is simulated. Thus, initial test should be carried out and a slightly higher  $a$  such as  $a = 5.4b$  is preferred. The local instability might be linked with the discretization of the network. For a small segment, a very small  $a$  may not support its geometry. The local instability and non effective blocking are listed in Figure D.1.

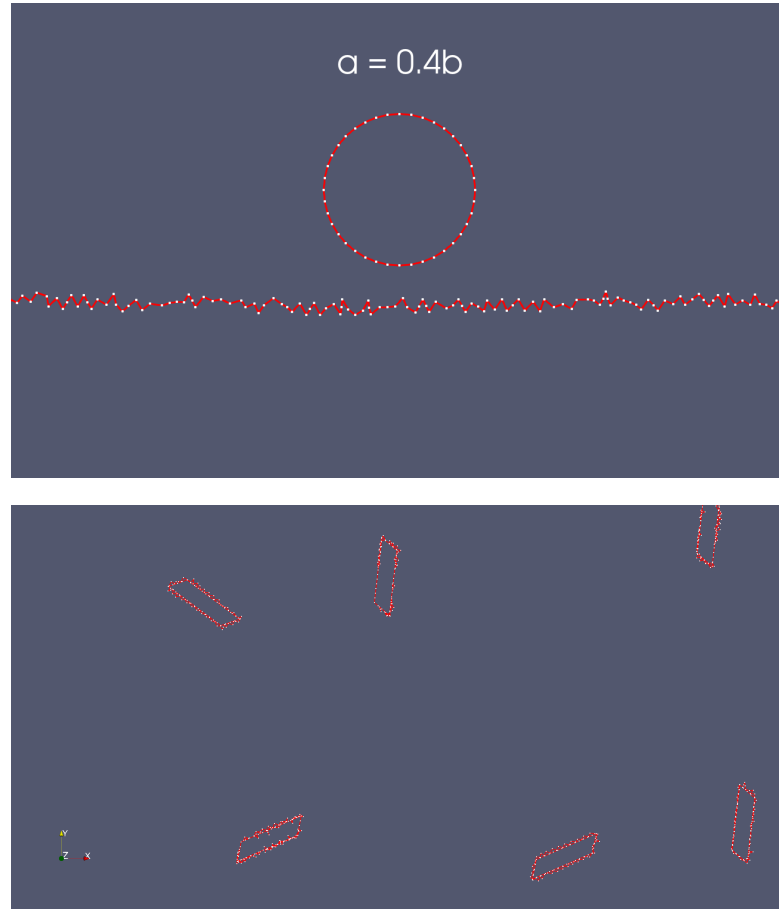


Figure D.1 – Unstable geometry due to small  $a$ . Above: local instability, below: zigzag pattern and non-effective blocking.

## Discretization and Effective Blocking

Discretization of dislocation network and precipitate geometry is important in the simulation. A coarse precipitate mesh will not block the dislocation network effectively, as is shown in Figure D.2. It is because the current dislocation-precipitate interaction algorithm is based on segment-segment collision detection supported by ParaDiS. Advance computational geometry algorithm can be implemented, but is out of scope of the current research. With a proper discretization, multiple dislocation looping can be realized in Figure D.3.

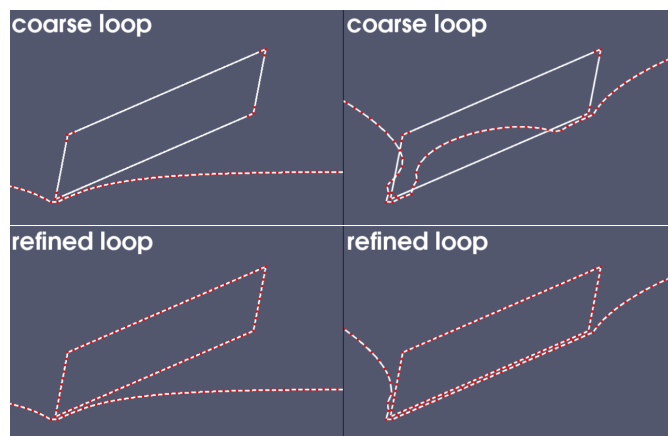


Figure D.2 – Finer discretization of precipitate is needed for effective dislocation-precipitate interaction in Orowan mechanism.

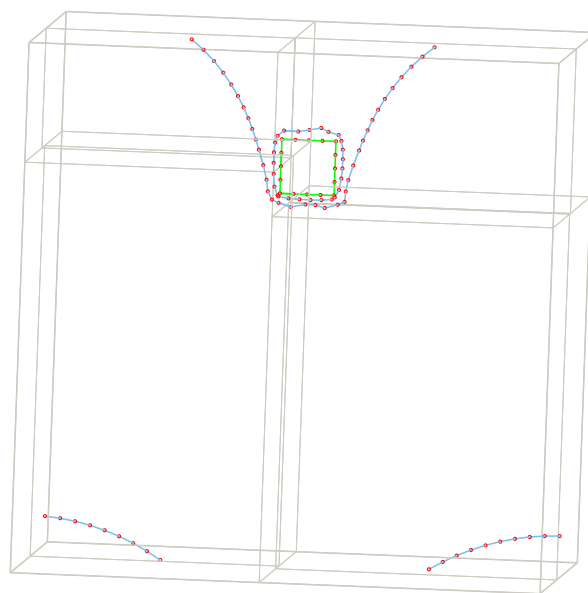


Figure D.3 – The implemented algorithm is robust to capture dislocation-precipitate interaction for multiple times.

### Image Effect and Accuracy

One weird phenomenon from ParaDiS simulation is that an infinite long dislocation line can move automatically in a small periodic box without any loading (also for very fine discretization). Fortunately, such spurious image effect is vanishing when increasing the simulation

---

box size. We can output sum of all the nodal forces and average them to estimate the spurious stress. This quantity is decreasing when increase the box size. So a relative large box size is recommended and the spurious image effect estimation can be made based on an infinite long dislocation geometry. One reason for the image effect may be the inaccurate evaluation of the interaction. Limited Taylor expansion and multiple expansion are used. However, a higher order for interaction calculation and FMM can quickly increase the burden of calculation [7].

## Extra Implemented Functionalities

For the current thesis, we extend ParaDiS with some new functionalities,

- high order dislocation core energy and automatic subtraction of extra terms in non-singular theory
- read in precipitate misfit stress field
- add labels for precipitate node and precipitate-colliding node
- collision detection with precipitate nodes
- automatic stopping when mobile dislocation reaches the box boundary

Added parameters in ParaDiS are listed below.

```
#### Yi core setting ####
rc = 5.4
coreYi = 1
coreYi_order = 3
Ecore_x = [ 8.50188829e9 -1.92529106e9 0.76495792e9 -0.71979278e9
  0. 0. 0. 0. 0. ]
#####

#### Yi precip para ####
precipYi = 5
precipCase = 1 # 1->screw, 0->edge
precipNoStress = 0
precipStressFile = "${stress_file}"
precipStressTxN = 0
precipStressTyN = 10
precipStressOrig = [-28.87 -500]
collisionMethod = 4 # 1 is proximity, 5 is retroactive
precipPinDist = 0.2 # 0.2-0.25, precip collide dist
precipSlowFact = 1e-11
```

## Appendix D. Simulation with ParaDiS

---

```
precipBowTol = 0.1 # very conservative val
precipBowCheckFreq = 50 # we use this para to check pass bound
precipLoadDelta = [0. 0. 0. 0. 1e6 0.] # screw positive, edge negative
#####
```



# Bibliography

- [1] L. K. Aagesen, J. Miao, J. E. Allison, S. Aubry, and A. Arsenlis. Prediction of Precipitation Strengthening in the Commercial Mg Alloy AZ91 Using Dislocation Dynamics. Metallurgical and Materials Transactions A, 49(5):1908–1915, May 2018. ISSN 1543-1940. doi: 10.1007/s11661-018-4530-6.
- [2] G. Anciaux, T. Junge, M. Hodapp, J. Cho, J. F. Molinari, and W. A. Curtin. The Coupled Atomistic/Discrete-Dislocation method in 3d part I: Concept and algorithms. Journal of the Mechanics and Physics of Solids, 118:152–171, Sept. 2018. ISSN 0022-5096. doi: 10.1016/j.jmps.2018.05.004.
- [3] S. J. Andersen, H. W. Zandbergen, J. Jansen, C. Træholt, U. Tundal, and O. Reiso. The crystal structure of the  $\beta''$  phase in Al–Mg–Si alloys. Acta Materialia, 46(9):3283–3298, May 1998. ISSN 1359-6454. doi: 10.1016/S1359-6454(97)00493-X.
- [4] S. J. Andersen, C. D. Marioara, J. Friis, S. Wenner, and R. Holmestad. Precipitates in aluminium alloys. Advances in Physics: X, 3(1):1479984, Jan. 2018. ISSN null. doi: 10.1080/23746149.2018.1479984.
- [5] A. J. Ardell. Precipitation hardening. Metallurgical Transactions A, 16(12):2131–2165, Dec. 1985. ISSN 1543-1940. doi: 10.1007/BF02670416.
- [6] A. S. Argon. Strengthening Mechanisms in Crystal Plasticity. Number 4 in Oxford Series on Materials Modelling. Oxford University Press, Oxford ; New York, 2008. ISBN 978-0-19-851600-2.
- [7] A. Arsenlis, W. Cai, M. Tang, M. Rhee, T. Oppelstrup, G. Hommes, T. G. Pierce, and V. V. Bulatov. Enabling strain hardening simulations with dislocation dynamics. Modelling and Simulation in Materials Science and Engineering, 15(6):553, 2007. ISSN 0965-0393. doi: 10.1088/0965-0393/15/6/001.
- [8] Asm. ASM Handbook: volume 4: Heat Treating. ASM International, Materials Park, Ohio, tenth edition, 1991. ISBN 978-0-87170-379-8.
- [9] D. J. Bacon, U. F. Kocks, and R. O. Scattergood. The effect of dislocation self-interaction on the orowan stress. Philosophical Magazine, 28(6):1241–1263, Dec. 1973. ISSN 0031-8086. doi: 10.1080/14786437308227997.

## Bibliography

---

- [10] D. Bardel, M. Perez, D. Nelias, A. Deschamps, C. R. Hutchinson, D. Maisonnette, T. Chaise, J. Garnier, and F. Bourlier. Coupled precipitation and yield strength modelling for non-isothermal treatments of a 6061 aluminium alloy. *Acta Materialia*, 62:129–140, Jan. 2014. ISSN 1359-6454. doi: 10.1016/j.actamat.2013.09.041.
- [11] J. Behler and M. Parrinello. Generalized Neural-Network Representation of High-Dimensional Potential-Energy Surfaces. *Physical Review Letters*, 98(14):146401, Apr. 2007. doi: 10.1103/PhysRevLett.98.146401.
- [12] N. Bertin and L. Capolungo. A FFT-based formulation for discrete dislocation dynamics in heterogeneous media. *Journal of Computational Physics*, 355:366–384, Feb. 2018. ISSN 0021-9991. doi: 10.1016/j.jcp.2017.11.020.
- [13] N. Bertin, S. Aubry, A. Arsenlis, and W. Cai. GPU-accelerated dislocation dynamics using subcycling time-integration. *Modelling and Simulation in Materials Science and Engineering*, 27(7):075014, Aug. 2019. ISSN 0965-0393. doi: 10.1088/1361-651X/ab3a03.
- [14] M. Boleininger, T. D. Swinburne, and S. L. Dudarev. Atomistic-to-continuum description of edge dislocation core: Unification of the Peierls-Nabarro model with linear elasticity. *Physical Review Materials*, 2(8):083803, Aug. 2018. doi: 10.1103/PhysRevMaterials.2.083803.
- [15] V. Bulatov and W. Cai. *Computer Simulations of Dislocations*. OUP Oxford, Nov. 2006. ISBN 978-0-19-151366-4.
- [16] V. Bulatov, F. F. Abraham, L. Kubin, B. Devincere, and S. Yip. Connecting atomistic and mesoscale simulations of crystal plasticity. *Nature*, 391(6668):669–672, Feb. 1998. ISSN 0028-0836. doi: 10.1038/35577.
- [17] V. V. Bulatov, L. L. Hsiung, M. Tang, A. Arsenlis, M. C. Bartelt, W. Cai, J. N. Florando, M. Hiratani, M. Rhee, G. Hommes, T. G. Pierce, and T. D. de la Rubia. Dislocation multi-junctions and strain hardening. *Nature*, 440(7088):1174–1178, Apr. 2006. ISSN 0028-0836, 1476-4687. doi: 10.1038/nature04658.
- [18] W. Cai and W. D. Nix. *Imperfections in Crystalline Solids*. Cambridge University Press, Cambridge, first edition, 2016. ISBN 978-1-107-12313-7.
- [19] W. Cai, V. V. Bulatov, J. Chang, J. Li, and S. Yip. Periodic image effects in dislocation modelling. *Philosophical Magazine*, 83(5):539–567, Jan. 2003. ISSN 1478-6435, 1478-6443. doi: 10.1080/0141861021000051109.
- [20] W. Cai, A. Arsenlis, C. R. Weinberger, and V. V. Bulatov. A non-singular continuum theory of dislocations. *Journal of the Mechanics and Physics of Solids*, 54(3):561–587, Mar. 2006. ISSN 0022-5096. doi: 10.1016/j.jmps.2005.09.005.
- [21] D. Caillard and J. Martin. *Thermally Activated Mechanisms in Crystal Plasticity*, volume 30. Pergamon Press, Jan. 2003.

- [22] J. Cho, J.-F. Molinari, W. A. Curtin, and G. Anciaux. The coupled atomistic/discrete-dislocation method in 3d. Part III: Dynamics of hybrid dislocations. Journal of the Mechanics and Physics of Solids, 118:1–14, Sept. 2018. ISSN 0022-5096. doi: 10.1016/j.jmps.2018.05.005.
- [23] E. Christiansen, C. D. Marioara, B. Holmedal, O. S. Hopperstad, and R. Holmestad. Nano-scale characterisation of sheared  $\beta''$  precipitates in a deformed Al-Mg-Si alloy. Scientific Reports, 9(1):1–11, Nov. 2019. ISSN 2045-2322. doi: 10.1038/s41598-019-53772-4.
- [24] E. Christiansen, C. D. Marioara, I. G. Ringdalen, R. Bjørge, B. Holmedal, O. S. Hopperstad, and R. Holmestad. Detailed investigation of the shearing mechanism of  $\beta''$  precipitates in Al-Mg-Si alloys. MATEC Web of Conferences, 326:01005, 2020. ISSN 2261-236X. doi: 10.1051/mateconf/202032601005.
- [25] E. Christiansen, I. G. Ringdalen, R. Bjørge, C. D. Marioara, and R. Holmestad. Multislice image simulations of sheared needle-like precipitates in an Al-Mg-Si alloy. Journal of Microscopy, 279(3):265–273, 2020. ISSN 1365-2818. doi: 10.1111/jmi.12901.
- [26] E. Clouet, L. Ventelon, and F. Willaime. Dislocation Core Energies and Core Fields from First Principles. Physical Review Letters, 102(5):055502, Feb. 2009. doi: 10.1103/PhysRevLett.102.055502.
- [27] W. A. Curtin. The X-Mechanics Toolbox to Solve Y-Mechanics Problems. Procedia IUTAM, 21:2–10, Jan. 2017. ISSN 2210-9838. doi: 10.1016/j.piutam.2017.03.030.
- [28] W. A. Curtin. Mechanics of Dislocations EPFL EDME. September 2020.
- [29] W. A. Curtin and R. E. Miller. Atomistic/continuum coupling in computational materials science. Modelling and Simulation in Materials Science and Engineering, 11(3):R33–R68, May 2003. ISSN 0965-0393, 1361-651X. doi: 10.1088/0965-0393/11/3/201.
- [30] B. Devincre and M. Condat. Model validation of a 3D simulation of dislocation dynamics: Discretization and line tension effects. Acta Metallurgica et Materialia, 40(10):2629–2637, Oct. 1992. ISSN 0956-7151. doi: 10.1016/0956-7151(92)90332-9.
- [31] J. A. El-Awady. Unravelling the physics of size-dependent dislocation-mediated plasticity. Nature Communications, 6(1):5926, Jan. 2015. ISSN 2041-1723. doi: 10.1038/ncomms6926.
- [32] F. Ercolessi and J. B. Adams. Interatomic Potentials from First-Principles Calculations: The Force-Matching Method. EPL (Europhysics Letters), 26(8):583, 1994. ISSN 0295-5075. doi: 10.1209/0295-5075/26/8/005.
- [33] A. C. Eringen. Screw dislocation in non-local elasticity. Journal of Physics D: Applied Physics, 10(5):671, 1977. ISSN 0022-3727. doi: 10.1088/0022-3727/10/5/009.

## Bibliography

---

- [34] S. Esmaeili, D. J. Lloyd, and W. J. Poole. A yield strength model for the Al-Mg-Si-Cu alloy AA6111. *Acta Materialia*, 51(8):2243–2257, May 2003. ISSN 1359-6454. doi: 10.1016/S1359-6454(03)00028-4.
- [35] G. Esteban-Manzanares, A. Ma, I. Papadimitriou, E. Martínez, and J. LLorca. Basal dislocation/precipitate interactions in Mg-Al alloys: An atomistic investigation. *Modelling and Simulation in Materials Science and Engineering*, 27(7):075003, Oct. 2019. ISSN 0965-0393, 1361-651X. doi: 10.1088/1361-651X/ab2de0.
- [36] G. Esteban-Manzanares, E. Martínez, J. Segurado, L. Capolungo, and J. LLorca. An atomistic investigation of the interaction of dislocations with Guinier-Preston zones in Al-Cu alloys. *Acta Materialia*, 162:189–201, Jan. 2019. ISSN 13596454. doi: 10.1016/j.actamat.2018.09.052.
- [37] H. Fan, Q. Wang, J. A. El-Awady, D. Raabe, and M. Zaiser. Strain rate dependency of dislocation plasticity. *Nature Communications*, 12(1):1845, Dec. 2021. ISSN 2041-1723. doi: 10.1038/s41467-021-21939-1.
- [38] S. P. Fitzgerald and S. Aubry. Self-force on dislocation segments in anisotropic crystals. *Journal of Physics: Condensed Matter*, 22(29):295403, 2010. ISSN 0953-8984. doi: 10.1088/0953-8984/22/29/295403.
- [39] M. C. Fivel. Discrete dislocation dynamics: An important recent break-through in the modelling of dislocation collective behaviour. *Comptes Rendus Physique*, 9(3):427–436, Apr. 2008. ISSN 1631-0705. doi: 10.1016/j.crhy.2007.11.005.
- [40] A. J. E. Foreman. The bowing of a dislocation segment. *Philosophical Magazine*, 15(137):1011–1021, May 1967. ISSN 0031-8086. doi: 10.1080/14786436708221645.
- [41] A. J. E. Foreman and M. J. Makin. Dislocation movement through random arrays of obstacles. *Philosophical Magazine*, 14(131):911–924, Oct. 1966. ISSN 0031-8086. doi: 10.1080/14786436608244762.
- [42] J. Friedel. *Dislocations*. Pergamon Press, 1967.
- [43] S. Gao, M. Fivel, A. Ma, and A. Hartmaier. Influence of misfit stresses on dislocation glide in single crystal superalloys: A three-dimensional discrete dislocation dynamics study. *Journal of the Mechanics and Physics of Solids*, 76(Supplement C):276–290, Mar. 2015. ISSN 0022-5096. doi: 10.1016/j.jmps.2014.11.015.
- [44] P.-A. Geslin and D. Rodney. Thermal fluctuations of dislocations reveal the interplay between their core energy and long-range elasticity. *Physical Review B*, 98(17):174115, Nov. 2018. doi: 10.1103/PhysRevB.98.174115.
- [45] P.-A. Geslin, R. Gatti, B. Devincere, and D. Rodney. Implementation of the nudged elastic band method in a dislocation dynamics formalism: Application to dislocation nucleation. *Journal of the Mechanics and Physics of Solids*, 108(Supplement C):49–67, Nov. 2017. ISSN 0022-5096. doi: 10.1016/j.jmps.2017.07.019.

- 
- [46] D. Giofr , T. Junge, W. A. Curtin, and M. Ceriotti. Ab initio modelling of the early stages of precipitation in Al-6000 alloys. Acta Materialia, 140(Supplement C):240–249, Nov. 2017. ISSN 1359-6454. doi: 10.1016/j.actamat.2017.08.017.
- [47] B. Gurrutxaga-Lerma and J. Verschueren. Elastic models of dislocations based on atomistic Kanzaki forces. Physical Review B, 98(13):134104, Oct. 2018. doi: 10.1103/PhysRevB.98.134104.
- [48] P. Hirel. AtomsK: A tool for manipulating and converting atomic data files. Computer Physics Communications, 197:212–219, Dec. 2015. ISSN 0010-4655. doi: 10.1016/j.cpc.2015.07.012.
- [49] J. P. Hirth and J. Lothe. Theory of Dislocations. Krieger Publishing Company, 1982. ISBN 978-0-89464-617-1.
- [50] J. P. Hirth, T. Jo/ssang, and J. Lothe. Dislocation Energies and the Concept of Line Tension. Journal of Applied Physics, 37(1):110–116, Jan. 1966. ISSN 0021-8979. doi: 10.1063/1.1707791.
- [51] M. Hodapp, G. Anciaux, J. F. Molinari, and W. A. Curtin. Coupled atomistic/discrete dislocation method in 3D Part II: Validation of the method. Journal of the Mechanics and Physics of Solids, 119:1–19, Oct. 2018. ISSN 0022-5096. doi: 10.1016/j.jmps.2018.05.003.
- [52] Y. Hu and W. A. Curtin. Modeling peak-aged precipitate strengthening in Al–Mg–Si alloys. Journal of the Mechanics and Physics of Solids, 151:104378, June 2021. ISSN 0022-5096. doi: 10.1016/j.jmps.2021.104378.
- [53] Y. Hu, B. A. Szajewski, D. Rodney, and W. A. Curtin. Atomistic dislocation core energies and calibration of non-singular discrete dislocation dynamics. Modelling and Simulation in Materials Science and Engineering, 28(1):015005, Nov. 2019. ISSN 0965-0393. doi: 10.1088/1361-651X/ab5489.
- [54] D. Hull. Introduction to Dislocations. Butterworth-Heinemann, Amsterdam Heidelberg, fifth edition, Apr. 2011. ISBN 978-0-08-096672-4.
- [55] A. M. Hussein, S. I. Rao, M. D. Uchic, T. A. Parthasarathy, and J. A. El-Awady. The strength and dislocation microstructure evolution in superalloy microcrystals. Journal of the Mechanics and Physics of Solids, 99(Supplement C):146–162, Feb. 2017. ISSN 0022-5096. doi: 10.1016/j.jmps.2016.11.014.
- [56] M. J. Hytch, J.-L. Putaux, and J.-M. P nisson. Measurement of the displacement field of dislocations to 0.03   by electron microscopy. Nature, 423(6937):270–273, May 2003. ISSN 1476-4687. doi: 10.1038/nature01638.
- [57] A. C. P. Jain, D. Marchand, A. Glensk, M. Ceriotti, and W. A. Curtin. Machine learning for metallurgy: A neural network potential for Al-Mg-Si, 2021.

## Bibliography

---

- [58] A. C. P. Jain, D. Marchand, A. Glensk, M. Ceriotti, and W. A. Curtin. Machine learning for metallurgy III: A neural network potential for Al-Mg-Si. Physical Review Materials, 5(5): 053805, May 2021. doi: 10.1103/PhysRevMaterials.5.053805.
- [59] T. Junge, A. F. N. Richart, L. Pastewka, R. Leute, J. Zeman, M. Doškář, M. Ladecký, and I. Pultarova.  $\mu$ Spectre, open-source platform for efficient FFT-based continuum mesoscale modelling. <https://gitlab.com/muspectre/muspectre>, 2020.
- [60] R. Kobayashi, D. Giofré, T. Junge, M. Ceriotti, and W. A. Curtin. Neural network potential for Al-Mg-Si alloys. Physical Review Materials, 1(5), Oct. 2017. ISSN 2475-9953. doi: 10.1103/PhysRevMaterials.1.053604.
- [61] U. F. Kocks. Statistical treatment of penetrable obstacles. Canadian Journal of Physics, 45(2):737–755, Feb. 1967. ISSN 0008-4204. doi: 10.1139/p67-056.
- [62] U. F. Kocks, A. S. Argon, and M. F. Ashby. Thermodynamics and Kinetics of Slip, volume Progressive in material science. Pergamon Press, 1975.
- [63] V. S. Krasnikov, A. E. Mayer, V. V. Pogorelko, F. T. Latypov, and A. A. Ebel. Interaction of dislocation with GP zones or  $\theta''$  phase precipitates in aluminum: Atomistic simulations and dislocation dynamics. International Journal of Plasticity, 125:169–190, Feb. 2020. ISSN 0749-6419. doi: 10.1016/j.ijplas.2019.09.008.
- [64] R. W. Lardner. Mathematical Theory of Dislocations and Fracture. University of Toronto Press, Dec. 1971. ISBN 978-1-4875-8685-0.
- [65] A. Lehtinen, F. Granberg, L. Laurson, K. Nordlund, and M. J. Alava. Multiscale modeling of dislocation-precipitate interactions in Fe: From molecular dynamics to discrete dislocations. Physical Review E, 93(1):013309, Jan. 2016. doi: 10.1103/PhysRevE.93.013309.
- [66] J. Li, C.-Z. Wang, J.-P. Chang, W. Cai, V. V. Bulatov, K.-M. Ho, and S. Yip. Core energy and Peierls stress of a screw dislocation in bcc molybdenum: A periodic-cell tight-binding study. Physical Review B, 70(10):104113, Sept. 2004. doi: 10.1103/PhysRevB.70.104113.
- [67] H. Liu, I. Papadimitriou, F. X. Lin, and J. LLorca. Precipitation during high temperature aging of Al-Cu alloys: A multiscale analysis based on first principles calculations. Acta Materialia, 167:121–135, Apr. 2019. ISSN 1359-6454. doi: 10.1016/j.actamat.2019.01.024.
- [68] J. Lothe. Chapter 2 - Dislocations in Continuous Elastic Media. In V. Indenbom and J. Lothe, editors, Elastic Strain Fields and Dislocation Mobility, volume 31 of Modern Problems in Condensed Matter Sciences, pages 175–235. Elsevier, 1992. doi: 10.1016/B978-0-444-88773-3.50008-X.
- [69] R. Madec, B. Devincre, L. Kubin, T. Hoc, and D. Rodney. The role of collinear interaction in dislocation-induced hardening. Science, 301(5641):1879–1882, 2003.

- 
- [70] D. Maisonnette, M. Suery, D. Nelias, P. Chaudet, and T. Epicier. Effects of heat treatments on the microstructure and mechanical properties of a 6061 aluminium alloy. Materials Science and Engineering: A, 528(6):2718–2724, Mar. 2011. ISSN 0921-5093. doi: 10.1016/j.msea.2010.12.011.
- [71] D. Marchand, A. Jain, A. Glensk, and W. A. Curtin. Machine learning for metallurgy I. A neural-network potential for Al-Cu. Physical Review Materials, 4(10):103601, Oct. 2020. doi: 10.1103/PhysRevMaterials.4.103601.
- [72] C. D. Marioara, S. J. Andersen, H. W. Zandbergen, and R. Holmestad. The influence of alloy composition on precipitates of the Al-Mg-Si system. Metallurgical and Materials Transactions A, 36(3):691–702, Mar. 2005. ISSN 1543-1940. doi: 10.1007/s11661-005-0185-1.
- [73] C. D. Marioara, H. Nordmark, S. J. Andersen, and R. Holmestad. Post- $B''$  phases and their influence on microstructure and hardness in 6xxx Al-Mg-Si alloys. Journal of Materials Science, 41(2):471–478, Jan. 2006. ISSN 1573-4803. doi: 10.1007/s10853-005-2470-1.
- [74] C. D. Marioara, S. J. Andersen, T. N. Stene, H. Hasting, J. Walmsley, A. T. J. V. Helvoort, and R. Holmestad. The effect of Cu on precipitation in Al-Mg-Si alloys. Philosophical Magazine, 87(23):3385–3413, Aug. 2007. ISSN 1478-6435. doi: 10.1080/14786430701287377.
- [75] E. Martínez, J. Marian, A. Arsenlis, M. Victoria, and J. M. Perlado. Atomistically informed dislocation dynamics in fcc crystals. Journal of the Mechanics and Physics of Solids, 56(3):869–895, Mar. 2008. ISSN 0022-5096. doi: 10.1016/j.jmps.2007.06.014.
- [76] Y. Mishin, D. Farkas, M. J. Mehl, and D. A. Papaconstantopoulos. Interatomic potentials for monoatomic metals from experimental data and ab initio calculations. Physical Review B, 59(5):3393–3407, Feb. 1999. doi: 10.1103/PhysRevB.59.3393.
- [77] V. Mohles and E. Nembach. The peak- and overaged states of particle strengthened materials: Computer simulations. Acta Materialia, 49(13):2405–2417, Aug. 2001. ISSN 1359-6454. doi: 10.1016/S1359-6454(01)00153-7.
- [78] V. Mohles, D. Rönnpagel, and E. Nembach. Simulation of dislocation glide in precipitation hardened materials. Computational Materials Science, 16(1):144–150, Dec. 1999. ISSN 0927-0256. doi: 10.1016/S0927-0256(99)00056-7.
- [79] G. Monnet. Multiscale modeling of irradiation hardening: Application to important nuclear materials. Journal of Nuclear Materials, 508:609–627, Sept. 2018. ISSN 0022-3115. doi: 10.1016/j.jnucmat.2018.06.020.
- [80] G. Monnet, S. Naamane, and B. Devincre. Orowan strengthening at low temperatures in bcc materials studied by dislocation dynamics simulations. Acta Materialia, 59(2):451–461, Jan. 2011. ISSN 1359-6454. doi: 10.1016/j.actamat.2010.09.039.

## Bibliography

---

- [81] T. Mura. Micromechanics of Defects in Solids. Mechanics of Elastic and Inelastic Solids. Springer Netherlands, second edition, 1987. ISBN 978-90-247-3256-2. doi: 10.1007/978-94-009-3489-4.
- [82] O. R. Myhr, Ø. Grong, and S. J. Andersen. Modelling of the age hardening behaviour of Al–Mg–Si alloys. Acta Materialia, 49(1):65–75, Jan. 2001. ISSN 1359-6454. doi: 10.1016/S1359-6454(00)00301-3.
- [83] O. R. Myhr, O. S. Hopperstad, and T. Børvik. A Combined Precipitation, Yield Stress, and Work Hardening Model for Al–Mg–Si Alloys Incorporating the Effects of Strain Rate and Temperature. Metallurgical and Materials Transactions A, 49(8):3592–3609, Aug. 2018. ISSN 1543-1940. doi: 10.1007/s11661-018-4675-3.
- [84] E. Nembach. Particle Strengthening of Metals and Alloys. Wiley, New York, 1997. ISBN 978-0-471-12072-8.
- [85] J. Nie. Effects of precipitate shape and orientation on dispersion strengthening in magnesium alloys. Scripta Materialia, 48(8):1009–1015, Apr. 2003. ISSN 13596462. doi: 10.1016/S1359-6462(02)00497-9.
- [86] J.-F. Nie. 20 - Physical Metallurgy of Light Alloys. In D. E. Laughlin and K. Hono, editors, Physical Metallurgy (Fifth Edition), pages 2009–2156. Elsevier, Oxford, Jan. 2014. ISBN 978-0-444-53770-6. doi: 10.1016/B978-0-444-53770-6.00020-4.
- [87] P. H. Ninive, A. Strandlie, S. Gulbrandsen-Dahl, W. Lefebvre, C. D. Marioara, S. J. Andersen, J. Friis, R. Holmestad, and O. M. Løvvik. Detailed atomistic insight into the  $\beta''$  phase in Al–Mg–Si alloys. Acta Materialia, 69(Supplement C):126–134, May 2014. ISSN 1359-6454. doi: 10.1016/j.actamat.2014.01.052.
- [88] T. Nogaret and D. Rodney. Finite-size effects in dislocation glide through random arrays of obstacles: Line tension simulations. Physical Review B, 74(13):134110, Oct. 2006. ISSN 1098-0121, 1550-235X. doi: 10.1103/PhysRevB.74.134110.
- [89] D. L. Olmsted, L. G. Hector Jr, W. A. Curtin, and R. J. Clifton. Atomistic simulations of dislocation mobility in Al, Ni and Al/Mg alloys. Modelling and Simulation in Materials Science and Engineering, 13(3):371–388, Mar. 2005. ISSN 0965-0393. doi: 10.1088/0965-0393/13/3/007.
- [90] G. B. Olson. Designing a New Material World. Science, 288(5468):993–998, May 2000. doi: 10.1126/science.288.5468.993.
- [91] Y. N. Osetsky and D. J. Bacon. An atomic-level model for studying the dynamics of edge dislocations in metals. Modelling and Simulation in Materials Science and Engineering, 11(4):427, 2003. ISSN 0965-0393. doi: 10.1088/0965-0393/11/4/302.
- [92] F. Ozturk, A. Sisman, S. Toros, S. Kilic, and R. C. Picu. Influence of aging treatment on mechanical properties of 6061 aluminum alloy. Materials & Design, 31(2):972–975, Feb. 2010. ISSN 0261-3069. doi: 10.1016/j.matdes.2009.08.017.



- [93] F. Pavia and W. A. Curtin. Parallel algorithm for multiscale atomistic/continuum simulations using LAMMPS. Modelling and Simulation in Materials Science and Engineering, 23(5):055002, July 2015. ISSN 0965-0393, 1361-651X. doi: 10.1088/0965-0393/23/5/055002.
- [94] S. Plimpton. Fast Parallel Algorithms for Short-Range Molecular Dynamics. Journal of Computational Physics, 117(1):1–19, Mar. 1995. ISSN 0021-9991. doi: 10.1006/jcph.1995.1039.
- [95] G. Po, M. Lazar, D. Seif, and N. Ghoniem. Singularity-free dislocation dynamics with strain gradient elasticity. Journal of the Mechanics and Physics of Solids, 68:161–178, Aug. 2014. ISSN 0022-5096. doi: 10.1016/j.jmps.2014.03.005.
- [96] G. Po, M. S. Mohamed, T. Crosby, C. Erel, A. El-Azab, and N. Ghoniem. Recent Progress in Discrete Dislocation Dynamics and Its Applications to Micro Plasticity. JOM, 66(10): 2108–2120, Oct. 2014. ISSN 1047-4838, 1543-1851. doi: 10.1007/s11837-014-1153-2.
- [97] W. J. Poole, X. Wang, D. J. Lloyd, and J. D. Embury. The shearable–non-shearable transition in Al–Mg–Si–Cu precipitation hardening alloys: Implications on the distribution of slip, work hardening and fracture. Philosophical Magazine, 85(26-27):3113–3135, Sept. 2005. ISSN 1478-6435. doi: 10.1080/14786430500154935.
- [98] S. Queyreau and B. Devincre. Bauschinger effect in precipitation-strengthened materials: A dislocation dynamics investigation. Philosophical Magazine Letters, 89(7):419–430, July 2009. ISSN 0950-0839, 1362-3036. doi: 10.1080/09500830903005433.
- [99] J. D. Robson, N. Stanford, and M. R. Barnett. Effect of Precipitate Shape and Habit on Mechanical Asymmetry in Magnesium Alloys. Metallurgical and Materials Transactions A, 44(7):2984–2995, July 2013. ISSN 1073-5623, 1543-1940. doi: 10.1007/s11661-012-1466-0.
- [100] D. Rodney and R. Phillips. Structure and strength of dislocation junctions: An atomic level analysis. Physical Review Letters, 82(8):1704, 1999.
- [101] H. Salmenjoki, A. Lehtinen, L. Laurson, and M. J. Alava. Plastic yielding and deformation bursts in the presence of disorder from coherent precipitates. Physical Review Materials, 4(8):083602, Aug. 2020. doi: 10.1103/PhysRevMaterials.4.083602.
- [102] R. Santos-Güemes, G. Esteban-Manzanares, I. Papadimitriou, J. Segurado, L. Capolungo, and J. LLorca. Discrete dislocation dynamics simulations of dislocation- $\Theta'$  precipitate interaction in Al-Cu alloys. Journal of the Mechanics and Physics of Solids, 118:228–244, Sept. 2018. ISSN 0022-5096. doi: 10.1016/j.jmps.2018.05.015.
- [103] R. Santos-Güemes, B. Bellón, G. Esteban-Manzanares, J. Segurado, L. Capolungo, and J. LLorca. Multiscale modelling of precipitation hardening in Al–Cu alloys: Dislocation dynamics simulations and experimental validation. Acta Materialia, 188:475–485, Apr. 2020. ISSN 1359-6454. doi: 10.1016/j.actamat.2020.02.019.

## Bibliography

---

- [104] R. Santos-Güemes, L. Capolungo, J. Segurado, and J. LLorca. Dislocation dynamics prediction of the strength of Al-Cu alloys containing shearable  $\Theta''$  precipitates. Journal of the Mechanics and Physics of Solids, page 104375, Mar. 2021. ISSN 0022-5096. doi: 10.1016/j.jmps.2021.104375.
- [105] S. Saroukhani, L. D. Nguyen, K. W. K. Leung, C. V. Singh, and D. H. Warner. Harnessing atomistic simulations to predict the rate at which dislocations overcome obstacles. Journal of the Mechanics and Physics of Solids, 90(Supplement C):203–214, May 2016. ISSN 0022-5096. doi: 10.1016/j.jmps.2016.02.016.
- [106] R. O. Scattergood and D. J. Bacon. The Orowan mechanism in anisotropic crystals. Philosophical Magazine, 31(1):179–198, Jan. 1975. ISSN 0031-8086. doi: 10.1080/14786437508229295.
- [107] R. B. Sills and S. Aubry. Line Dislocation Dynamics Simulations with Complex Physics. In W. Andreoni and S. Yip, editors, Handbook of Materials Modeling, pages 1–23. Springer International Publishing, Cham, 2018. ISBN 978-3-319-42913-7. doi: 10.1007/978-3-319-42913-7\_19-1.
- [108] R. B. Sills and W. Cai. Efficient time integration in dislocation dynamics. Modelling and Simulation in Materials Science and Engineering, 22(2):025003, 2014. ISSN 0965-0393. doi: 10.1088/0965-0393/22/2/025003.
- [109] R. B. Sills, A. Aghaei, and W. Cai. Advanced time integration algorithms for dislocation dynamics simulations of work hardening. Modelling and Simulation in Materials Science and Engineering, 24(4):045019, 2016. ISSN 0965-0393. doi: 10.1088/0965-0393/24/4/045019.
- [110] R. B. Sills, W. P. Kuykendall, A. Aghaei, and W. Cai. Fundamentals of Dislocation Dynamics Simulations. In C. R. Weinberger and G. J. Tucker, editors, Multiscale Materials Modeling for Nanomechanics, volume 245, pages 53–87. Springer International Publishing, Cham, 2016. ISBN 978-3-319-33478-3 978-3-319-33480-6. doi: 10.1007/978-3-319-33480-6\_2.
- [111] C. V. Singh and D. H. Warner. Mechanisms of Guinier–Preston zone hardening in the athermal limit. Acta Materialia, 58(17):5797–5805, Oct. 2010. ISSN 1359-6454. doi: 10.1016/j.actamat.2010.06.055.
- [112] C. V. Singh and D. H. Warner. An Atomistic-Based Hierarchical Multiscale Examination of Age Hardening in an Al-Cu Alloy. Metallurgical and Materials Transactions A, 44(6): 2625–2644, June 2013. ISSN 1073-5623, 1543-1940. doi: 10.1007/s11661-013-1614-1.
- [113] A. Singraber, J. Behler, and C. Dellago. Library-Based LAMMPS Implementation of High-Dimensional Neural Network Potentials. Journal of Chemical Theory and Computation, 15(3):1827–1840, Mar. 2019. ISSN 1549-9618. doi: 10.1021/acs.jctc.8b00770.

- [114] R. Smallman and A. H. W. Ngan. Modern Physical Metallurgy. Butterworth-Heinemann, Oxford ; Waltham, MA, eighth edition, 2013. ISBN 978-0-08-098204-5.
- [115] A. N. Stroh. Dislocations and Cracks in Anisotropic Elasticity. Philosophical Magazine, 3(30):625–646, June 1958. ISSN 0031-8086. doi: 10.1080/14786435808565804.
- [116] A. Stukowski. Visualization and analysis of atomistic simulation data with OVITO—the Open Visualization Tool. Modelling and Simulation in Materials Science and Engineering, 18(1):015012, Dec. 2009. ISSN 0965-0393. doi: 10.1088/0965-0393/18/1/015012.
- [117] B. A. Szajewski and W. A. Curtin. Analysis of spurious image forces in atomistic simulations of dislocations. Modelling and Simulation in Materials Science and Engineering, 23(2):025008, Mar. 2015. ISSN 0965-0393, 1361-651X. doi: 10.1088/0965-0393/23/2/025008.
- [118] B. A. Szajewski, F. Pavia, and W. A. Curtin. Robust atomistic calculation of dislocation line tension. Modelling and Simulation in Materials Science and Engineering, 23(8):085008, Dec. 2015. ISSN 0965-0393, 1361-651X. doi: 10.1088/0965-0393/23/8/085008.
- [119] B. A. Szajewski, A. Hunter, D. J. Luscher, and I. J. Beyerlein. The influence of anisotropy on the core structure of Shockley partial dislocations within FCC materials. Modelling and Simulation in Materials Science and Engineering, 26(1):015010, 2018. ISSN 0965-0393. doi: 10.1088/1361-651X/aa9758.
- [120] A. Vaid, J. Guénolé, A. Prakash, S. Korte-Kerzel, and E. Bitzek. Atomistic simulations of basal dislocations in Mg interacting with Mg17Al12 precipitates. Materialia, 7:100355, Sept. 2019. ISSN 2589-1529. doi: 10.1016/j.mtla.2019.100355.
- [121] C. Varvenne, G. P. M. Leyson, M. Ghazisaeidi, and W. A. Curtin. Solute strengthening in random alloys. Acta Materialia, 124:660–683, Feb. 2017. ISSN 1359-6454. doi: 10.1016/j.actamat.2016.09.046.
- [122] D. Warner and W. Curtin. Origins and implications of temperature-dependent activation energy barriers for dislocation nucleation in face-centered cubic metals. Acta Materialia, 57(14):4267–4277, Aug. 2009. ISSN 13596454. doi: 10.1016/j.actamat.2009.05.024.
- [123] S. Wenner and R. Holmestad. Accurately measured precipitate–matrix misfit in an Al–Mg–Si alloy by electron microscopy. Scripta Materialia, 118:5–8, June 2016. ISSN 1359-6462. doi: 10.1016/j.scriptamat.2016.02.031.
- [124] S. Wenner, C. D. Marioara, S. J. Andersen, and R. Holmestad. Effect of room temperature storage time on precipitation in Al–Mg–Si(–Cu) alloys with different Mg/Si ratios. International Journal of Materials Research, 103(8):948–954, Aug. 2012. ISSN 1862-5282, 2195-8556. doi: 10.3139/146.110795.

- [125] D. Weygand, L. H. Friedman, E. V. der Giessen, and A. Needleman. Aspects of boundary-value problem solutions with three-dimensional dislocation dynamics. Modelling and Simulation in Materials Science and Engineering, 10(4):437–468, June 2002. ISSN 0965-0393. doi: 10.1088/0965-0393/10/4/306.
- [126] Z. Wu and W. A. Curtin. Mechanism and energetics of  $\langle c + a \rangle$  dislocation cross-slip in hcp metals. Proceedings of the National Academy of Sciences, 113(40):11137–11142, Oct. 2016. ISSN 0027-8424, 1091-6490. doi: 10.1073/pnas.1603966113.
- [127] Z. Wu, B. Yin, and W. A. Curtin. Energetics of dislocation transformations in hcp metals. Acta Materialia, 119:203–217, Oct. 2016. ISSN 1359-6454. doi: 10.1016/j.actamat.2016.08.002.
- [128] L. Xiong, Q. Deng, G. Tucker, D. L. McDowell, and Y. Chen. A concurrent scheme for passing dislocations from atomistic to continuum domains. Acta Materialia, 60(3): 899–913, Feb. 2012. ISSN 1359-6454. doi: 10.1016/j.actamat.2011.11.002.
- [129] S. Xu, L. Xiong, Y. Chen, and D. L. McDowell. An analysis of key characteristics of the Frank-Read source process in FCC metals. Journal of the Mechanics and Physics of Solids, 96:460–476, Nov. 2016. ISSN 0022-5096. doi: 10.1016/j.jmps.2016.08.002.
- [130] J. Zeman, T. W. J. de Geus, J. Vondřejc, R. H. J. Peerlings, and M. G. D. Geers. A finite element perspective on nonlinear FFT-based micromechanical simulations. International Journal for Numerical Methods in Engineering, vol. 111, issue 10, pp. 903-926, 111:903–926, sep 2017. doi: 10.1002/nme.5481.
- [131] L. A. Zepeda-Ruiz, A. Stukowski, T. Oppelstrup, and V. V. Bulatov. Probing the limits of metal plasticity with molecular dynamics simulations. Nature, 550(7677):492–495, Oct. 2017. ISSN 1476-4687. doi: 10.1038/nature23472.
- [132] X. W. Zhou, R. B. Sills, D. K. Ward, and R. A. Karnesky. Atomistic calculations of dislocation core energy in aluminium. Physical Review B, 95(5), Feb. 2017. ISSN 2469-9950. doi: 10.1103/physrevb.95.054112.

# YI HU

✉ yi.hu@epfl.ch  
☎ +41 (0)78 693 64 50  
✉ 72, Route de la Maladière 6,  
1022 Chavannes-près-Renens, Suisse



## EDUCATION

2016–2021	École Polytechnique Fédérale de Lausanne, Ph.D. Mechanical Engineering
2014–2016	Universität Stuttgart, M.Sc. Simulation Technology, GPA: 1.2/1
2009–2014	Tongji University, B.E. Civil Engineering, GPA: 4.38/5
2011–2012	Hong Kong Polytechnic University, Exchange Program

## RESEARCH & WORK EXPERIENCE

11/2016–11/2021	Ph.D. Thesis: "Precipitation Strengthening in Al-Mg-Si Alloys" <ul style="list-style-type: none"><li>• Supervisor: Prof. W. A. Curtin</li></ul>
06/2018–06/2020	Teaching Assistant (3 semesters): "Solid Mechanics" <ul style="list-style-type: none"><li>• Problem set design, tutorial sessions for exercises</li></ul>
09/2017–09/2019	Research member of MARVEL, National Center of Competence in Research, Switzerland <ul style="list-style-type: none"><li>• Posters in 2018, 2019, and 2021 of MARVEL Site Visit, Lausanne</li></ul>
02/2016–07/2016	Master Thesis: "Phase field approaches to topology optimization" <ul style="list-style-type: none"><li>• Supervisor: Prof. Marc-André Keip</li></ul>
10/2015–02/2016	Course Thesis: "Homogenization for multi-field modeling"
02/2014–06/2014	Bachelor Thesis: "Damage simulation of concrete tunnel segment lining" <ul style="list-style-type: none"><li>• Supervisor: Prof. Xiaoying Zhuang</li></ul>

## PAPER & CONFERENCE

- Yi Hu, W. A. Curtin. "Near-chemically-accurate modeling of precipitate strengthening in Al-6xxx alloys.", (in preparation)
- Yi Hu, W. A. Curtin. "Modeling peak-aged precipitate strengthening in Al-Mg-Si alloys.", Journal of the Mechanics and Physics of Solids, 2021.
- Yi Hu. "Modeling Orowan strengthening in Al-Mg-Si alloys.", Material Science and Engineering Congress, Darmstadt (Germany), 2020
- Yi Hu, B. A. Szajewski, D. Rodney, and W. A. Curtin. "Atomistic dislocation core energies and calibration of Non-singular Discrete Dislocation Dynamics." Modelling and Simulation in Materials Science and Engineering, 2019
- Yi Hu. "Atomistic dislocation core energies and the calibration to Discrete Dislocation Dynamics.", 13th World Congress on Computational Mechanics, New York City, 2018
- Yi Hu, X. Ren. "XFEM Based Discontinuity Simulation for Saturated Soil.", 6th International Conference on Nonlinear Mechanics, Shanghai, 2013

## SKILLS

Programming	Python, C/C++, Matlab, CUDA, OpenACC
Data analysis	PyTorch, Numpy, Pandas, Matplotlib, SQLite
FEM software	Ansys, Abaqus
Open source	LAMMPS, ParaDiS, FEniCS, deal.II
Graphic modeling	AutoCAD, Gmsh, ParaView, OVITO
Office	MS Office, LaTeX, Inkscape
Other	Linux, High Performance Computing
Language	Chinese (mother tongue)      English (working proficiency) German (TestDaF 19/20)      French B1
Expertise	Mechanics, Materials, Machine Learning, Numerical Methods